A Broadband Approach to Measuring Acoustic Impedance and Roughness using Spherical Hydrophones

Mark Noonchester
(B.S.E.E.)

A thesis presented for the degree of
Doctor of Philosophy
in
Electrical and Computer Engineering
at the
University of Canterbury,
Christchurch, New Zealand.

6 August 2010

ABSTRACT

The ARG (Acoustic Research Group) at the University of Canterbury has a goal to image objects buried under the seafloor. In order to image these objects, accurate models and a good understanding of the acoustic parameters of the seafloor are needed. The relevant acoustic parameters to model the seafloor include: physical classification, speed of sound, acoustic impedance, density, and roughness.

Acquiring accurate acoustic parameters for the seafloor is a challenging task that requires different approaches depending on the environment, especially in locations with low visibility. This thesis looks at a non-invasive method of acoustically examining the roughness spectrum and acoustic impedance of the seafloor. To achieve these goals, spherical transducers with a continuous bandwidth between 30 kHz and 130 kHz were chosen to examine the frequency dependent specular and diffused components of the reflection from rough seafloor surfaces.

Using spherical transducers allows the surface scattering to be examined independently of the transducer beam-pattern. This thesis examines the range and validity of the tools required to make these measurements and presents empirical results measured in the controlled environment of a cylindrical 3.5 m diameter by 2 m deep sonar test tank. Using results from the sonar test tank, this thesis demonstrates that the acoustic impedance, speed of sound, and density of the material of the seafloor can be measured from a single seafloor realisation measured at multiple angles, provided the seafloor material has a critical angle. Additionally, this thesis demonstrates that the spectrum of the specular and diffused components of the rough-surface reflection requires averaging multiple seafloor realisations to be statistically relevant. As well as describing the benefits of using spherical transducers, this thesis presents some of the problems and potential solutions for future applications.

ACKNOWLEDGEMENTS

Thanks to everyone in the Electrical and Computer Engineering Department at the University of Canterbury. I would also like to thank the 'R9' crew: Alan Hunter, Phil Barclay, Ed Pilbrow, Stewart Hardie, and Blair Bonnett. It was sad to see 'R9' dwindle and then be remodelled into the power electronics room after three generations of sonar research. I have to thank the many people that have been friends and maintained contact as I have hidden away working on something they do not understand. I have to thank Anthony Lyons for his long hours on the phone, listening to my ideas and offering words of encouragement, and yes Anthony, cafe 360 does have the best coffee. I am grateful for the work of the sand crew who helped me endure the daunting task of hauling three tons of sand from the beach to the sonar tank: Blair Bonnett, Andrew Clow, and Volker Nock. I would also like to thank my proof readers: Ciaran Moore, Debra Hoult, Antony Liken, Alan Hunter, and Steve Weddell for their valuable feed back. Last but not least, I would like to thank my supervisory team: Peter Gough and Michael Hayes.

PREFACE

This thesis considers the problem of surface roughness, its measurement, and its effects on specular and diffused scattering. The initial work for this thesis was performed on the Kiwi-SAS (a synthetic aperture sonar system developed at Canterbury University) [Hawkins 1996], using its ability to transmit at 30 kHz and 100 kHz, for analyses of the frequency dependent scattering of the seafloor. It was discovered that the Kiwi-SAS system was not configured properly for this purpose due to beam-pattern issues; At 100 kHz, the side-lobe is in the middle of the range of interest [Gough et al. 2006c]. As a consequence, the focus changed to spherical transducers to study specular and diffused scattering independent of transducer beam-patterns. With the change to spherical transducers, the work was also moved to a cylindrical 3.5 m diameter by 2 m deep sonar test tank to provide a controlled environment to conduct the tests.

By employing spherical transducers in conjunction with a new test environment, new hardware and software systems were required to provide: signal generation, data acquisition, and ground-truth measurements. Additionally, the simulation software developed by Hunter [2006] was found to be inappropriate for the new environment and configuration, and hence, the development of new simulation software was also required. At this point, development was initiated on: new tools, a new test environment, and a new method of measuring the acoustic impedance and surface roughness. This thesis describes the process of measuring the acoustic impedance with individual surface realisations. Additionally this thesis uses a broadband pulse to explores the spectral analysis of rough surface scattering by taking advantage of the 30 kHz to 130 kHz continuous bandwidth available from ITC-1042 transducers.

Chapter 1 provides a general overview of the problem including: the problem description and the differences between spherical-wave and plane-wave reflection coefficients. Chapter 2 describes the acoustic modelling and the use of those models to both simulate and statistically analyse acoustic rough surfaces. This chapter also describes the simulator developed for the roughness analysis. Chapter 3 describes the sonar test tank environment and the hardware used to make the acoustic and optical measurements. Chapter 4 uses the models in Chapter 2, and the hardware and test environment described in Chapter 3, to analyse both simulated and real surfaces. This chapter demonstrates the method of measuring acoustic impedance

using spherical transducers, as well as using the simulations to show how the roughness spectrum can be analysed. Chapter 5 provides an overview of the results and what is required to extend the system.

PUBLICATIONS

A local and an international conference were attended during the course of research. The authored and co-authored papers are listed here in order of presentation: [Gough et al. 2006a],[Gough et al. 2006b], [Gough et al. 2006c], and [Noonchester et al. 2007].

ASSUMED KNOWLEDGE

It is assumed that the reader of this thesis has an understanding of partial differential calculus, Fourier methods, signal processing, and acoustic wave equations. The reader is also assumed to be familiar with acoustic scattering and reflection of sound from rough surfaces. Suggested background reading includes [Simmons 1975] for partial differential calculus, [Bracewell 1986, Goodman 2005, Williams 1999] for Fourier methods, [Ambardar 1999] for signal processing, and [Ziomek 1995] for an understanding of the acoustic wave equations. However, there are many texts on these subjects. The subject of the acoustic scattering and reflection from rough surfaces is an ever changing field, however, a general overview is provided in [Jackson and Richardson 2007] and [Clay et al. 1973]. With the help of these references as well as the background material provided in Appendix A to Appendix C an informed reader may better comprehend the information presented in this thesis.

AUTHOR'S CONTRIBUTIONS

This thesis presents a number of original contributions to the field of acoustic wave scattering and reflection from rough surfaces using spherical transducers.

Broadband acoustic measurements

A major contribution of this thesis is in the methodology used to perform broadband acoustic measurements of surface scattering, over 30 kHz to 130 kHz continuous bandwidth, on the ITC-1042 transducers. This bandwidth is used by transmitting an impulse on the transducer and then the received signal is deconvolved by its ideal signal using a Wiener filter, as described in Sections 3.1.1 and 3.1.2. This deconvolved signal can then either be used as an impulse response to perform broadband analysis of the surface or to analyse the spectral response of the surface. The broadband pulse is used to analyse individual features such as the multi-layer reflections, as shown in Section 3.2, and the reflection coefficient, as shown in Section 4.4.1. The

temporal spectrum is used to analyse the diffused and scattered components of the reflection from a rough surface, as shown in Section 4.5.1.

Measurement of acoustic impedance from a rough surface

This thesis shows that the acoustic impedance, speed of sound, and density of the material of the seafloor can be determined using a single surface realisation evaluated at multiple angles, as shown Section 4.4.1. This method can be used to non-invasively measure the acoustic impedance of the surface.

Broadband analysis of surface scattering

This thesis demonstrates that when using spherical transducers, the specular and diffused components of the reflection from a rough surface need multiple realisations to be evaluated, as shown in Section 4.5.1. The initial restriction of three realisations, described in Section 1.1, only works on relatively smooth surfaces, e.g., a power law surface with a peak roughness of -100 dB at 10 cycles m^{-1} and a roll-off of -25 dB per decade. However, the spectrum of the specular and diffused components of the reflection from a rough surface can be analysed with 12 or more realisations, depending on the surface roughness.

CONTENTS

Chapter 1

INTRODUCTION

Obtaining accurate ground truth information about a specific area of the seafloor can be a challenging task that requires different approaches depending on the optical visibility [Jackson and Richardson 2007]. In areas of good visibility, only a few physical samples of the seafloor may be required, since a visual inspection can give an indication of how representative the specific sample may be. In areas of moderate visibility, divers, ROVs (Remotely Operated Vehicle), or AUVs (Autonomous Underwater Vehicle) can be employed with cameras to take images and to bring up physical samples from the selected area. In areas of poor visibility, i.e., less than one metre (such as Lyttelton Harbour in New Zealand, and most other harbours), alternative techniques are required. Divers can still descend to the sample site but visual inspection and the use of cameras becomes difficult. An accurate non-invasive method of classifying the seafloor would be of value in areas of low visibility.

1.1 PROBLEM OUTLINE

The ARG (Acoustic Research Group) has a goal to image objects buried under the seafloor. In order to accurately image these objects, a good understanding of the acoustic parameters of the seafloor is needed. With this goal in mind, ground truth data and physical samples have been collected by the ARG using a variety of methods, including: core sampling, scoops, and a diver. Samples were then analysed to determine the relevant parameters, including: physical classification, speed of sound, acoustic impedance, density, and roughness. These parameters can be used as input parameters for scattering models in order to estimate signal return strength. The estimated return strength can be used to analyse the SAS (Synthetic Aperture Sonar) images from the same areas, providing a better understanding of what is being imaged.

There are many useful references on the physical parameters relevant to seafloor acoustic response, e.g., the speed of sound and density of different media [Hamilton et al. 1956, Jackson and Richardson 2007] but the data varies greatly between references and even within the same reference. For example, there are an

estimated thirty different published speed of sound values for fine sand, which differ by greater than 15%; each value, however, is relevant to a specific environment. The physical parameters provide a great deal of information about the samples but not the information required to specify the acoustic behaviour of the sample. The acoustic behaviour of different media can be affected by roughness, temperature, and gas trapped in the media. In the case of gas trapped in the media, the act of taking a physical sample, i.e., scooping up a core sample of the seafloor, can change it's behaviour by changing the bubble size and distribution. The act of taking physical samples also changes the roughness of the sea-surface. Therefore, in cases where taking physical measurements will change the acoustic behaviour of the sample, the measurements need to be taken in the environment (or a similar environment) to be accurate.

The simulations, outlined in Section 2.2.1, Section 2.3, and Section 4.5.1, demonstrate that density, speed of sound, and roughness are the primary parameters required to characterise the acoustic behaviour of the seafloor. However, determining roughness can be difficult [Chotiros et al. 2007, Jackson and Richardson 2007]. While speed of sound and density can be found using core samples, roughness requires a different method. Three methods for determining roughness used by the ARG include: inferring samples of the seafloor from the shore, using underwater cameras to measure the roughness, or using divers to take manual measurements. Inferring the seafloor from shore measurements assumes that seafloor conditions match the shore conditions. This was found to be false in Lyttelton Harbour, New Zealand, i.e., rocky beaches were found in areas where the seafloor was muddy. The assumption that the entire harbour has a muddy bottom was found to be equally false given that a number of bays that have a sandy bottom, as verified by industrial divers who installed moorings in those bays. The use of underwater cameras in Lyttelton Harbour was found to be impossible due to sub-metre visibility. In areas of low visibility, the measurement of roughness by divers becomes more qualitative (touching the bottom to feel the overall roughness as well as taking some limited visual measurements using a ruler). In environments of low visibility, only one or two samples may be taken to represent an entire sea trial which could cover several, square kilometres. Since direct measurement of the roughness (as well as speed of sound and density) requires considerable time and is often difficult, too few samples are taken. In many cases, this forces models to be based on possibly unrepresentative seafloor parameters. A non-invasive method of determining the roughness and impedance of the seafloor would be of great use for site surveys and could greatly lessen the amount of under-sampling. This thesis describes a non-invasive acoustic method of determining the roughness and the impedance of the seafloor using three identical spherical acoustic transducers.

The transducer system, shown in Figure 1.1 and described in Section 3.1, is

Figure 1.1: The transducer system used in this thesis and described in Section 3.1.

made up of three identical spherical transducers in a frame separated by 1 m. This system is raised and lowered to vary the transducer's distance above the seafloor to produce bi-static angles between 30° and 70° (with respect to the surface normal). This system produces three independent bi-static acoustic angular readings and three independent mono-static acoustic readings at 0°. From these six acoustic readings, taken at various heights, the acoustic impedance of the seafloor can be determined. However, it was found that 12 or more realisations of the seafloor are required to determine the roughness of the seafloor, as described in Section 4.5. One of the primary restrictions of this system is that acoustic readings are limited to three realisations of seafloor roughness at any angle. This restriction was imposed and maintained by the senior member of the supervisory team Professor Peter Gough. This simplification was imposed so the system so it could be deployed over the side of a boat. The sonar system is described in more detail in Section 3.1.

Before examining the complete three spherical transducer system, it is useful to firstly discuss a simple acoustic measurement system. An acoustic measurement system is defined as consisting of three parts: a transmitting transducer (the projector), a receiving transducer (the hydrophone), and a discontinuity in the media known as a scattering surface. The projector and hydrophone are electromechanical devices that translate acoustic energy, from and to, electrical energy, respectively. The scattering surface has an impedance mismatch, such as the air bladder of a fish in water, the air-water interface at the surface of the sea, or the water-sand interface on the seafloor. The signal strength reflected from the scattering surface

is dependent on four parameters: the acoustic impedance of the surface, the roughness of the surface, the shape of the surface, and the location and orientation of the surface with respect to the projector and hydrophone. The models for analysing the acoustic impedance are described in Section 2.1, and the models for analysing the scattering effects are described in Section 2.2.

1.2 PREVIOUS WORK

Many uses of remote sensing using sound can be found in nature by animals such as bats, beluga whales, and dolphins. Man has most likely used some form of echo location since before recorded history, but there is evidence that Phoenician fishermen (circa 500 B.C.) used echo location, i.e., ringing bells, to avoid headlands concealed by fog [Kaharl 2003]. More recently echo location has been used to detect and avoid icebergs,; this was patented in 1911, two weeks after the sinking of the Titanic [Urick 1983]. The use of underwater echo location and more complicated forms of sonar grew in part because of the advent of submarine warfare in World War I and from that time sonar applications have continued to evolve [Urick 1983].

As technology has advanced, so have the uses of sonar. Early applications of sonar were little more than an echo location system which allows measurement of the distance between sonar and the reflecting object(s). It was soon discovered that a great deal of information about the object can be inferred from an echo response, i.e., the shape, roughness and the acoustic impedance. Modern synthetic aperture sonar (SAS), or side scan sonar system, can be used to image the seafloor or objects on it, with resolutions limited only by the frequencies being used [Jackson and Richardson 2007]. Both SAS and side scan sonar imaging use back scattering to image and their performance is enhanced by surface roughness. The analytical modelling of the surface roughness is commonly done using the Kirchhoff approximation and small-roughness perturbation method, as discussed in Section 2.2. The Kirchhoff approximation assumes that plane-wave reflection coefficients can be used in the integral (2.20) for rough surfaces and spherical waves [Clay and Medwin 1977].

The use of the Kirchhoff approximation to model acoustic scattering from a rough sea-surface can be traced back to Eckart [1953]. The use of the Kirchhoff approximation for electromagnetic scattering from rough surfaces was applied to radio waves by Beckmann and Spizzichino [1963] and in the visual spectrum by Goodman [1968]. A series of empirical measurements of the sea-surface scattering, i.e., a tank with a fan to generate the waves, was conducted showing a good match between the empirical and theoretical until shadowing occurs, assuming a Gaussian height PDF (probability distribution function) [Medwin 1967, Medwin and Clay 1970, Clay and Medwin 1970, Clay et al. 1973]. The modelling and validation of this work was limited by the data acquisition and computational efficiencies of the time. These

limitations applied to both the ground-truth measurements and the acoustic measurements. The ground-truth of these early experiments used a partially immersed two-wire resistance probe to determine the PDF of the surface of the tank [Clay et al. 1973]. The acoustic data was analysed in realtime using an oscilloscope. Since the time of these initial experiments, the measurements of both the ground-truth and acoustic roughness measurements have improved. Section 1.2.1 describes some of the modern methods of measuring the ground-truth. Section 1.2.2 describes some of the modern acoustic scattering analysis methods using the Kirchhoff approximation.

1.2.1 Ground-truth methods

One of the problems with any experiment is validation of the experimental measurements. The ground-truth method chosen for the experiments in this thesis was stereo-photography. This stereo-photography configuration uses two calibrated cameras mounted in a fixed configuration to generate surface height maps with a xy resolution of $\pm 0.25\,\text{mm}$ and a z (height) resolution of $\pm 0.13\,\text{mm}$, as described in Section 3.4. The goal of the ground-truth measurements is to generate a 2D height spectrum and a 2D height map. Previous work has used: divers using a yard stick [Lyons and Pouliquen 2004], stereo photography [Gerig et al. 2009, Lyons and Pouliquen 2004, Tang 2004, Lyons et al. 2002, Briggs 1989], laser line scanning [Moore and Jaffe 2002], laser imaging [Richardson et al. 2001], ultrasound profiling [Jackson et al. 1986a], towed acoustic multi-beam and side-scan sonar [Stewart et al. 1994, Briggs et al. 2005], and bottom-mounted sector-scanning and pencil beam sonar [Irish et al. 1999], to determine the 1D height spectrum and a 2D height map of the seafloor [Jackson and Richardson 2007]. One of the problems when examining the roughness effect on acoustic measurement is that the determination of the roughness is not a trivial task. One of the main difficulties with stereo-photography is water clarity. This method would be unusable in Lyttelton Harbour, which has under 1 m visibility, but was appropriate in the sonar test tank environment. The test system used in this thesis is described in Section 3.4.

1.2.2 Acoustic scattering using the Kirchhoff approximation

Since the early work using the Kirchhoff approximation for the rough surface acoustic scattering problem, several advances have been made. These advances have been in: the understanding of seafloor roughness, understanding of the acoustic impedance, and methods employed to analyse the data [Clay et al. 1973, Pouliquen et al. 1999, Bergem et al. 1999, Jackson and Richardson 2007].

The understanding of seafloor roughness has improved with better methods of acquiring and analysing the roughness of the seafloor, as described in Section 1.2.1. The principal change that this improved roughness analysis has made is

the determination that the seafloor roughness has a power law spectrum (fractal) rather than a simple Gaussian distribution [Berkson and Matthews 1983, Fox and Hayes 1985, Jackson et al. 1986b, Jackson and Richardson 2007]. Additional analysis of the seafloor roughness spectrum has indicated that it has a different spectral slope for surface features above 1 m, between 1 m and 0.10 m, and below 0.10 m [Jackson et al. 1986b, Jackson and Richardson 2007]. The spectrum below 0.10 m may be biogenic in origin, the spectrum between 0.10 m and 1 m corresponds to the wave-generated ripples that can vary greatly with time, and the spectrum above 1 m corresponds to long lived morphological features [Briggs et al. 2005, Jackson and Richardson 2007]. The seafloor roughness spectrum between 0.005 m and 0.15 m is the primary range of interest for the experiments conducted in this thesis.

The initial applications of the Kirchhoff approximation were for fluid theory scattering problems [Eckart 1953], which closely matches the electromagnetic scattering problem [Beckmann and Spizzichino 1963]. Dacol [1990] expand the application of Kirchhoff approximation by applying it to elastic theory, which allows more accurate modelling of some seafloor interfaces. The development of more accurate reflection coefficient models is an ongoing process, where no model is accurate for all seafloor types as discussed in Section 2.1. In this thesis the fluid theory model is used and should be accurate for the frequency range of interest, i.e., 30 kHz -130 kHz, as discussed in Section 2.1.4.

Early analysis of seafloor scattering, both simulated and experimental, was primarily limited by the computing power of the time. Acoustic scattering simulations of 1D height maps required super computers [Thorsos 1988] whereas today, a low cost computing clusters can meet or exceed the computing power of modern super computers [Katz et al. 2002, Sacerdoti et al. 2004]. An example of using a computing cluster to perform 2D acoustic scattering simulations is shown in Hunter [2006]. Similarly, acoustic data acquisition and analysis has improved. Early work consisted of analogue signal processing and observing the results on an oscilloscope or chart-records [Eckart 1953, Clay et al. 1973], whereas today the raw waveform can be captured and analysed, as described in Section 3.3.2. Many of the advances in acoustic scattering analysis are taking advantage of the technological advances and leveraging the earlier research. Much of the earlier work was limited to statistical analysis of the surfaces and their scattering. This thesis takes advantage of the available computing power to perform modelling of 2D height maps with 1 mm resolution as discussed in Section 2.2.4, as well as the statistical analysis discussed in Section 2.3.

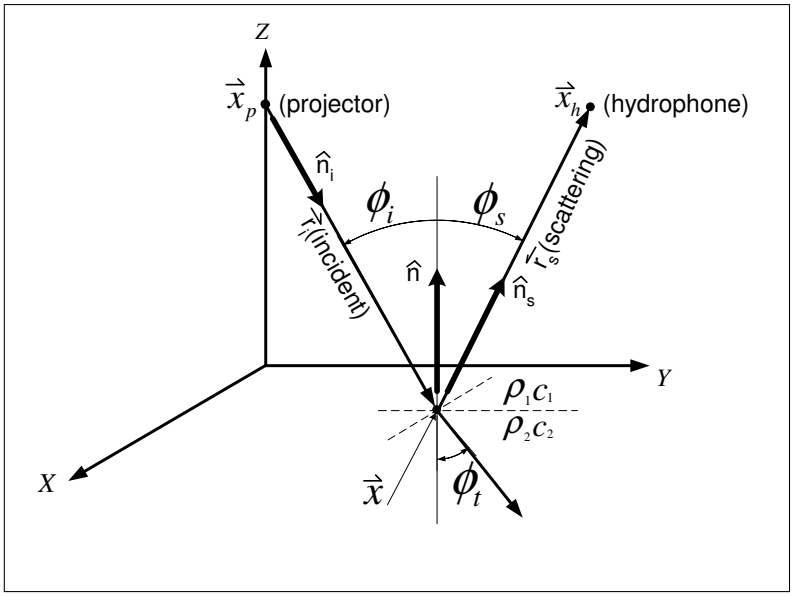

Figure 1.2: Bi-static transducer configuration reflecting off a planer surface.

1.3 SPHERICAL WAVE LIMITATIONS

Spherical wave reflection coefficients and scatter can be approximated by their plane wave equivalents, however, this is not valid in all cases. When the plane wave equivalents are not valid, there are added frequency dependencies [Brekhovskikh 1980]. In the cases that these frequency dependencies are present, then one of the primary reasons for using the spherical transducers is invalid. The primary reasons that spherical transducers were used in this thesis was to make use of the frequency independent response and wide bandwidth to analyse the surface roughness. The experiments in this thesis use a pulse with a 100 kHz bandwidth and a frequency range between 30 kHz and 130 kHz. Over this frequency range the transducers have beam pattern and frequency variations of less than 3 dB. Most directional transducers do not have a continuous operational frequency range from 30 kHz to 130 kHz. Even if directional transducers could produce a pulse over this frequency range, the transducer's beam pattern effects would be greater than 3 dB. To make use of spherical transducers and spherical waves, their behaviour must be understood.

The frequency, angle, and range dependencies of spherical waves can be modelled using the stationary phase approximation [Brekhovskikh 1980]. (The equations and limitations of this approximation are described in Appendix C.2.4.) Figure 1.3 shows a comparison between a planar reflection coefficient and the spherical wave reflection coefficient using this approximation for sand and for concrete. The geometry of the test set-up is shown in Figure 1.2. The test set-up requires the transducers to be at a fixed separation of 1 m. Their height is varied to produce the required incidence angle. A plot of the resulting height-angle relationship is shown in Figure 1.3 (c). Figure 1.3 (a), (b), (e), and (f) have several points where the

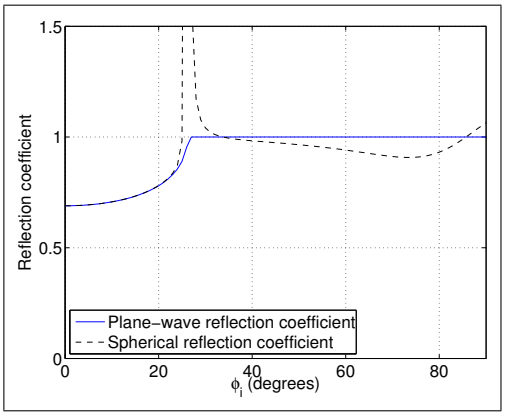

(a) The plane wave and spherical wave reflection coefficients for concrete compared at 10 kHz. The parameters for the first and second media are $\rho_1 = 1000$, $c_1 = 1456$ and $\rho_2 = 2400$, $c_2 = 3300$.

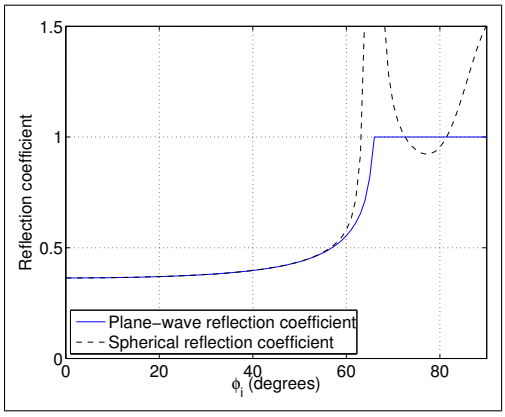

(b) The plane wave and spherical reflection coefficients for sand compared at 10 kHz. The parameters for the first and second media are $\rho_1 = 1000$, $c_1 = 1456$ and $\rho_2 = 2000$, $c_2 = 1750$.

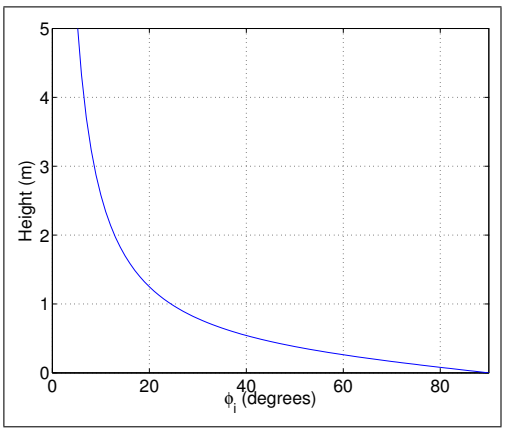

(c) This figure show the transducer height measurements used for the angular reflection coefficient measurements. The transducer separation is fixed at 1 m the transducer height is varied to produce the appropriate value of ϕ_i.

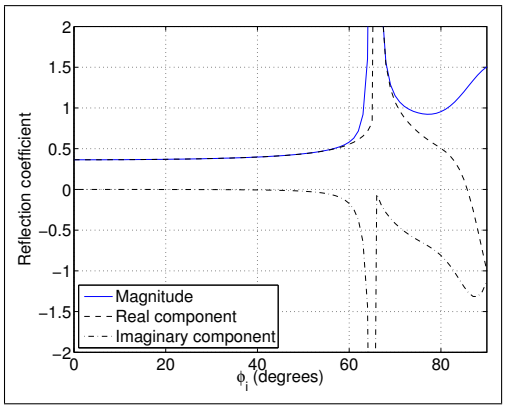

(d) The spherical reflection coefficient for sand at 10 kHz with real and imaginary components separated.

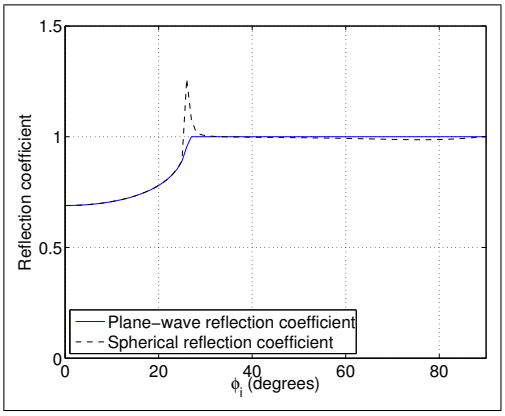

(e) The plane wave and spherical reflection coefficients for concrete compared at 80 kHz.

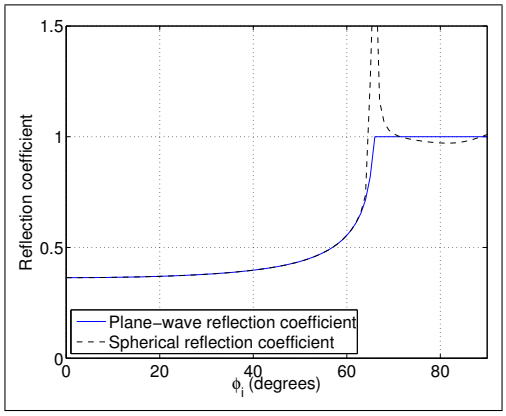

(f) The plane wave and spherical reflection coefficients for sand compared at 80 kHz.

Figure 1.3: Spherical-wave reflection coefficients derived using the stationary phase approximation and compared to plane-wave reflection coefficients. Note this figure is repeated in Figure C.4.

approximated reflection coefficient is greater than 1. These points are invalid points for the approximation. The reflection coefficient exceeds 1 at points near 90°, where the height approaches a wave length, and at the critical angles of 26.2° and 56.3° for concrete and sand. Excluding the invalid regions, the maximum differences between the spherical and planar reflection coefficients for concrete and sand are -0.08 and -0.10 for 10 kHz and 0.01 and 0.02 for 80 kHz as shown in Figure 1.3 (a), (b), (e), and (f). With this configuration, there are three areas where the plane wave coefficient does not apply to spherical waves: close ranges, near the critical angle, and in the case of total internal reflection, i.e., when ϕ_i > critical angle. In these areas the plane wave reflection is not valid for spherical waves and so neither is the Kirchhoff approximation. In the areas where the plane wave reflection coefficient is valid for spherical wave reflections any of the different plane wave acoustic models (discussed in Section 2.1) are equally valid.

Chapter 2

ACOUSTIC MODELLING

This section presents more complicated models for approximating surface reflection coefficients, surface scattering, and their regions of validity. Section 2.1 describes the most common methods for approximating plane-wave reflection coefficients. Section 2.2 and Section 2.3 describe methods for modelling surface scattering from rough surfaces. Section 2.2 presents methods of the modelling of surface scattering from individual rough surfaces and Section 2.3 the statistical analysis of the scattering from both Gaussian and power-law surfaces.

2.1 MODELS FOR PLANE WAVE REFLECTIONS FROM A PLANAR INTERFACE

So far the acoustic model that has been used for the reflection coefficient, $\mathscr{R}$, has been the fluid model. Acoustically, the major difference between fluids and solids is that solids support shear waves but fluids do not. As an example, a granite bolder is a solid and supports shear waves. A bucket of water saturated sand, made up of small grains of the granite boulder, supports shear waves but to a lesser extent than the granite bolder. Hence, the bucket of water and sand has acoustic aspects of both a solid and a liquid. To deal with materials (such as sand, clay, and mud) that do not fit completely into the acoustic category of fluid or solid, a number of different acoustic models have been developed. As with most models, the trade-off is complexity for accuracy with some exceptions, i.e., sometimes a simple model can be accurate for a specific application. When choosing a model, it is expedient to choose the simplest model that yields accurate results for the application and that is accepted and well understood. There are three well-known acoustic models for describing sound waves in a fluid environment. In order of increasing complexity they are: fluid, elastic, and poroelastic theories [Jackson and Richardson 2007]. Table 2.1 is a summary of the physical and geo-acoustical properties required to implement the different acoustical models. Note that most of the models use different subsets of the parameters provided in Table 2.1. In some cases the parameters are not directly measurable and must be derived from the available measurements. The measurement

of some of these parameters is far from straightforward. For example, to determine porosity requires the drying of the physical sample [Jackson and Richardson 2007], whereas, to determine grain size may require sorting and statistical analysis. It is reasonable to conclude that the simpler the measurements required to implement a model, the more accessible the model. Another advantage of using a simpler model is that more data-sets are available, e.g., many of the older measurements include only the speed of sound, attenuation, bulk density, and the reflection coefficient for comparison [Hamilton et al. 1956]. A secondary consideration is which parameters can be measured in the test environment. It is useful to have a comprehensive and accurate model but if the data required to implement the model is either unavailable or inaccurate then the model is of little use.

Site	c_t	a_t	α_t	M_z	η	ρ	k	IOI	Sediment
SA Bay	1518.9	0.993	38.7	10.94	89.14	1.170	0.097	1.162	clay
Diga	1480.4	0.968	58.0	10.05	69.12	1.506	0.145	1.458	silty clay
Orcas	1511.9	0.988	179.1	8.08	75.22	1.403	0.448	1.387	clayey sand
JDF4	1521.7	0.995	206.8	6.93	74.35	1.470	0.517	1.462	glacial till
VAzzura	1686.4	1.102	156.5	4.14	45.17	1.911	0.391	2.106	muddy sand
PCB99	1764.2	1.153	133.5	2.24	39.33	2.020	0.334	2.329	fine sand
T Bay/crse	1754.2	1.147	610.2	1.36	44.85	1.966	1.526	2.254	coarse/fine sand
Hood Canal	1767.1	1.155	184.6	1.34	36.46	2.108	0.462	2.435	medium sand
SAX99	1766.3	1.154	177.5	1.27	37.27	2.066	0.444	2.385	medium sand
PC93	1708.5	1.117	404.0	0.98	40.93	2.008	1.010	2.242	coarse sand

Table 2.1: Summary of the physical and geo-acoustic properties of the sediment from 10 siliciclastic sites. These properties consist of sound speed (c_t, $\mathrm{m\,s^{-1}}$), sound speed ratio c_t/c_w (a_t, no units), attenuation (α_t $\mathrm{dB\ m^{-1}}$), mean grain size (M_z, ϕ), porosity (η, %), bulk density (ρ, g $\mathrm{cm^{-3}}$), attenuation factor (k, $\mathrm{dB\ m^{-1}\ kHz^{-1}}$), index of impedance (IOI, g $\mathrm{cm^{-3}}$), and sediment type. Values of all acoustic parameters were determined at 400 kHz The subscript t indicates that the parameter is for the transmitted wave in the second medium [Jackson and Richardson 2007].

2.1.1 Fluid theories

Fluid theory without attenuation is by far the simplest theory to implement, as it only requires two parameters for each medium: the speed of sound as a real constant c ($\mathrm{m\,s^{-1}}$) and bulk density ρ ($\mathrm{kg\,m^{-3}}$). The reflection coefficient for a smooth surface, which is described in more detail in Section C.1, is

$$\mathscr{R}_{12} = \frac{p_s}{p_i} = \frac{\rho_2 c_2 \cos\phi_i - \rho_1 c_1 \cos\phi_t}{\rho_2 c_2 \cos\phi_i + \rho_1 c_1 \cos\phi_t} = \frac{\rho_2 k_1 \cos\phi_i - \rho_1 k_2 \cos\phi_t}{\rho_2 k_1 \cos\phi_i + \rho_1 k_2 \cos\phi_t}. \tag{2.1}$$

where p_s and p_i are the incident and scattering sound pressures, c_1 and c_2 are the sound speeds of the first and second media, ρ_1 and ρ_2 are the densities of the first and second media, and $k_1 = 2\pi\, f/c_1$ and $k_2 = 2\pi\, f/c_2$ are the wave numbers for the

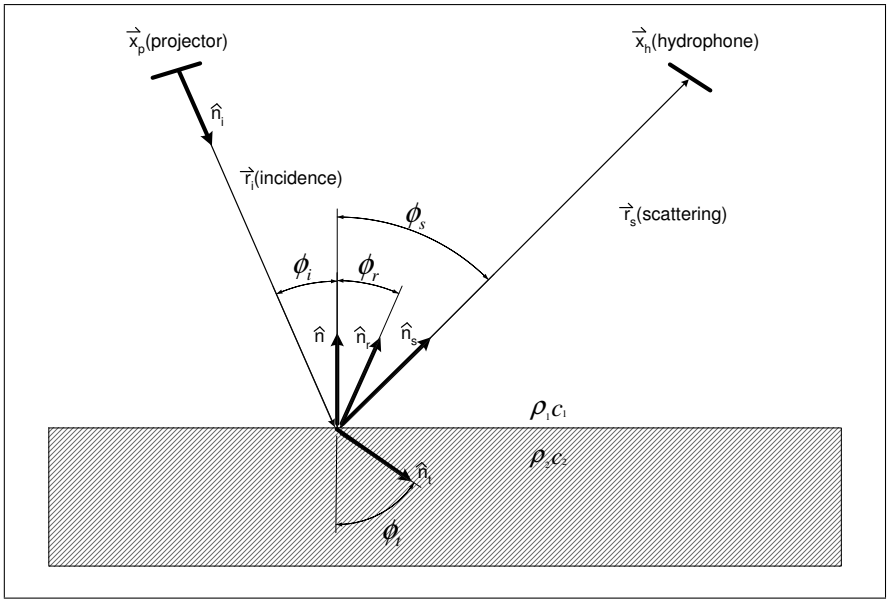

Figure 2.1: Two-dimensional representation of the planar boundary.

first and second media. The relationship between ϕ_i and ϕ_t can be determined from

$$\frac{\sin\phi_i}{c_1} = \frac{\sin\phi_t}{c_2} \quad \text{or} \quad \frac{\sin\phi_i}{k_2} = \frac{\sin\phi_t}{k_1} \tag{2.2}$$

The relationship between angles, vectors and media for (2.1) is shown in Figure 2.1. Equation (2.1) is valid for a lossless interface between the two media with no frequency dependance. This model is the most relevant when dealing with two fluids [Jackson and Richardson 2007].

2.1.1.1 Fluid theory with attenuation

It is well known that even distilled water has a non-zero attenuation α (dB m^{-1}) [Urick 1983]. However, for most water applications, α is small enough to be ignored. When dealing with mud, clay, or sand; α_p becomes significant. Table 2.1 shows some representative values of α_p for different materials. Acoustic loss can be applied to fluid theory by replacing the wave-number, k, with a complex wave-number, i.e.,

$$\mathbf{K} = k + j\,\alpha, \tag{2.3}$$

where k is the wave-number and α is the attenuation taken from Table 2.1. The complex wave number $\mathbf{K}$ can then be used to replace the real wave number k in the equations described in Section C.1. If it is assumed that media 1 is lossless and media 2 is lossy, only k_2 needs to be substituted with $\mathbf{K_2}$ in (2.1) and (2.2) resulting

in

$$\mathscr{R}_{12} = \frac{p_s}{p_i} = \frac{\rho_2 k_1 \cos\phi_i - \rho_1 \mathbf{K_2} \cos\phi_t}{\rho_2 k_1 \cos\phi_i + \rho_1 \mathbf{K_2} \cos\phi_t}. \tag{2.4}$$

and

$$\frac{\sin\phi_i}{|\mathbf{K_2}|} = \frac{\sin\phi_t}{k_1}. \tag{2.5}$$

The derivations of (2.3)-(2.5) are from Ziomek [1995]. The performance of the fluid theory with respect to other theories is discussed in Section 2.1.4. The fluid model (with attenuation) compared with the measured sand data, e.g., from SAX99, has a good match between the measured results and the predicted results between 20 kHz and 80 kHz [Williams et al. 2002b].

2.1.2 Elastic theories

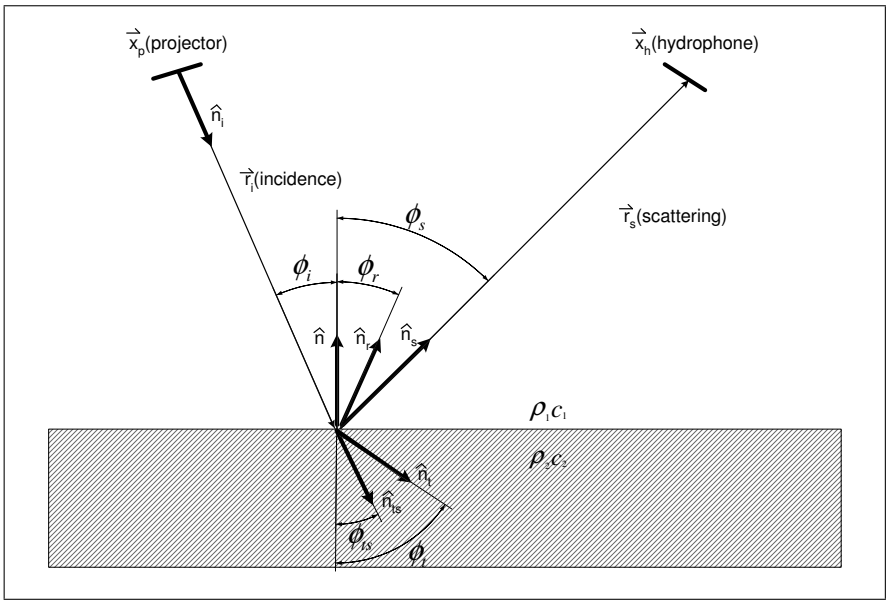

Figure 2.2: Two-dimensional representation of the planar boundary with the shear vector included.

Fluid theory works best for materials that acoustically resemble fluids, i.e., those materials that do not support shear waves, such as mud. A more complicated theory, such as elastic theory, is required as materials acoustically start to resemble solids, i.e., materials able to support shear waves such as sand. The problem is that a material such as sand is more complicated than a rigid solid. Shear waves are not fully supported and there are extra losses. Both Gassmann's equations, Section 2.1.2.2, and Buckingham's theory, Section 2.1.2.3 are based on elastic theory and account for shear wave interaction. However, Buckingham's theory also accounts for the interaction between the particles in the media based on the particle

size and weight and then relate these parameters to the elastic theory parameters, Gassmann's equations do not account for these losses [Jackson and Richardson 2007]. The reflection coefficient for elastic theory is determined by solving for $\mathscr{R}_{12} = p_s/p_i$, as described in Section C.1. The solution (2.6) is the same as fluid theory, except that there are additional relationships between p_i, p_s, p_{ts}, and p_t. Equation (2.6) to (2.19) are a summary of the Jackson and Richardson [2007] derivation of the elastic reflection coefficient from first principles. The reflection coefficient for elastic theory is

$$\mathscr{R}_{12} = \frac{p_s}{p_i} = \frac{z_e(\phi_i) - 1}{z_e(\phi_i) + 1}, \tag{2.6}$$

where the normalised acoustic impedance $z_e(\phi_i)$ is given by

$$z_e(\phi_i) = z_{wt} \cos^2 2\,\phi_{ts} + z_{wts} \sin^2 2\,\phi_{ts}. \tag{2.7}$$

The angles ϕ_i, ϕ_t, and ϕ_{ts} have the relationship of

$$\cos\phi_i = \frac{\cos\phi_t}{a_t} = \frac{\cos\phi_{ts}}{a_{ts}}, \tag{2.8}$$

where a_t and a_{ts} are the bulk transmitted (compressional) and transmitted (shear) sound speeds normalised with respect to c_w, the water sound speed, and have the relationships

$$a_t = \frac{c_t}{c_w} \tag{2.9}$$

and

$$a_{ts} = \frac{c_{ts}}{c_w}. \tag{2.10}$$

c_t and c_{ts}, the transmitted (compressional) and transmitted (shear) wave speeds, are:

$$c_t = \sqrt{\frac{\lambda + 2\,\mu}{\rho}} \tag{2.11}$$

and

$$c_{ts} = \sqrt{\frac{\mu}{\rho}}, \tag{2.12}$$

where ρ is the density (shown in Table 2.1), λ[1] is Lame's first parameter, and μ is the shear modulus or Lame's second parameter. Determination of λ and μ is based on

[1]Note that only in this section is λ Lame's first parameter. In all other parts of this thesis λ represents the wavelength.

the elastic theory that is chosen and can be found in a number of sources [Jackson and Richardson 2007]. The application of both Buckingham's theory and Gassmann's equations start with shear and compressional wave for the transmitted component shown in Figure 2.2, but the determination of the relationship between these is where they diverge. The impedance $z_{wt}(\phi_i)$ is the transmitted (compressional) impedance normalised with respect to water and has the relationship

$$z_{wt}(\phi_i) = \frac{a_\rho a_t \sin\phi_i}{\sin\phi_t}. \tag{2.13}$$

The impedance $z_{wts}(\phi_i)$ is the transmitted (shear) impedance normalised with respect to water, and has the relationship

$$z_{wts}(\phi_i) = \frac{a_\rho a_{ts} \sin\phi_i}{\sin\phi_{ts}}. \tag{2.14}$$

and a_ρ, the normalised density, is

$$a_\rho = \frac{\rho}{\rho_w}, \tag{2.15}$$

where ρ_w is the density of water. These equations deal with additional losses due to shear forces but do not add the frequency dependent losses. Note when $c_{ts} = 0$, this causes $a_{ts} = 0$ and $z_{wts} = 0$ resulting in $\mathscr{R}_{12}$ of (2.6) give the same result as fluid theory (2.4).

2.1.2.1 Elastic theory with attenuation

The frequency dependent losses are treated as described in Section 2.1.1.1 by using complex wave numbers and thus the complex sound speeds. The normalised complex sound speeds from Jackson and Richardson [2007] are

$$a_t = \frac{c_t}{c_w} = \frac{v_t}{1 + j\,\delta_t} \tag{2.16}$$

and

$$a_{ts} = \frac{c_{ts}}{c_w} = \frac{v_{ts}}{1 + j\,\delta_{ts}}, \tag{2.17}$$

where v_t and v_{ts} are the sediment/water phase speed ratios for the transmitted (compressional) and transmitted (shear) waves, and δ_t and δ_{ts} are the loss parameters for the transmitted and transmitted (shear) waves, obtained from

$$\delta_t = \frac{\alpha_t\, v_t\, c_w \ln(10)}{40\,\pi\, f} \tag{2.18}$$

and

$$\delta_{ts} = \frac{\alpha_{ts}\, v_{ts}\, c_w \ln(10)}{40\,\pi\, f}. \tag{2.19}$$

A comparison of the performance of the different theories is covered in Section 2.1.4.

2.1.2.2 Gassmann's equations

Gassmann's equations relate the shear waves and compressional waves to measurable physical parameters using two equations [Jackson and Richardson 2007]. These equations relate the fractional porosity β, the bulk modulus of the individual sediment grains K_g (Pa), the bulk modulus of the pore water (the water contained in the sediment), K_w (Pa), and the bulk modulus of the frame (drained of water) K_f (Pa), to λ and μ (Pa) to determine c_t and c_{ts} using (2.11) and (2.12), respectively. Gassmann's equations work well with materials such as mud and clay, where the frame modulus (the particles) and the pore water do not react separately, i.e., in mud the water is not separate as it is with sand where the water is between the grains of sand coupling them together. However, Gassmann's equations perform poorly with materials such as sand, where the frame modulus and the pore water react separately [Stoll and Bautista 1998]. Gassmann's equations are an improvement over fluid theory for simple materials, such as mud, but for more complex materials, such as sand, Buckingham's or Biot theories perform better [Jackson and Richardson 2007].

2.1.2.3 Buckingham's theory

Buckingham's theory is more complicated than that based on Gassmann's equations but far simpler than the Biot theory [Jackson and Richardson 2007]. Buckingham's theory is an empirical approach in that it relates the measured physical parameters of the shear attenuation η, the transmitted relaxation coefficient γ_t, and the transmitted (shear) relaxation coefficient γ_{ts}, measured at a single frequency to determine the two sound speeds c_t and c_{ts}. Buckingham's theory predicts that acoustic impedance will have an approximately linear increase with frequency and that sound speed will increase slowly with respect to frequency [Williams et al. 2002b, Jackson and Richardson 2007]. Buckingham's theory seems to excel when dealing with simple sands and is as good as Gassmann's equations and fluid theory when dealing with mud or other soft sediments [Jackson and Richardson 2007].

2.1.3 Poroelastic theory

The poroelastic theories, the most common of which is Biot theory, combines the porosity and the elastic physical properties of the material being modelled [Jackson

and Richardson 2007]. The Biot theory is a model based approach, as such, it is by far the most intellectually satisfying theory, given that all the losses are accounted for by the physical interaction between the particles with empirically determined numbers. However, it is by far the most complicated theory and not necessarily the most relevant theory given that better matches to empirical data have been achieved using Buckingham's theory [Williams et al. 2002b]. The concept of Biot theory is that sediments such as sand are porous and the gaps between particles are filled with water and when the sediment is acoustically excited, the response is governed by its porous gaps and elastic properties. The porous effects are most notable in materials such as sand and less so in materials such as mud or clay [Jackson and Richardson 2007]. Biot theory requires seven different parameters in contrast to the two or three required for the other models. Typical Biot theory parameters for sand are shown in Table 2.2. This theory has had limited success which may be due in part to the complexity of the model and inaccessibility of some of the parameters required to implement the model [Jackson and Richardson 2007].

Parameter	Symbol	Units	Value
Bulk Modulus of Grains	K_g	Pa	3.2 x 10^{10}
Permeability	κ	m^2	2.5 x 10^{-11}
Tortuosity	α	Dimensionless	1.35
Porosity	β	Dimensionless	0.385
Dynamic Viscosity of Water	K_w	Pa	2.395 x 10^9
Mass Density of Water	ρ_w	kg m^{-3}	1023
Shear Modulus of Frame	μ	Pa	(2.92 - j0.18) x 10^7
Bulk Modulus of Frame	K_f	Pa	(4.360 - j0.208) x 10^7
Pore Size	a	m	2.65 x 10^{-5}

Table 2.2: Typical acoustic parameters of sand for for the fluid, Buckingham, and Biot theories. [Williams et al. 2002a]. Note that the fluid and Buckingham theories only require a subset of these parameters.

2.1.4 Summary of acoustic models

Of the three acoustic theories, the fluid theory is the simplest, the Biot theory is the most complicated and not necessarily the most accurate, and Buckingham's theory seems to be a good compromise between simplicity and accuracy. For sediments such as mud, clay, and sand elastic theories only provide a minor improvement of the reflection coefficient over fluid theory [Jackson and Richardson 2007]. For sand surface interaction i.e., reflection, fluid theory is appropriate. However, for sand subsurface interaction, transmission and conductance, elastic theories can provide more accurate models and Biot theory provides the most complete model for the subsurface interactions [Jackson and Richardson 2007]. Fluid theory is most appropriate for the experiments in this thesis given that it focuses on the surface interactions

and the additional complexity of the elastic theories provide little gain.

2.2 ROUGH SURFACE SCATTERING AND REFLECTION MODELS

There are three main analytical roughness scattering models: small-roughness perturbation method (sometimes known as Rayleigh-Rice perturbation theory), Kirchhoff approximation (also known as the tangent-plane approximation), and small-slope approximation. These models are general and are applicable for fluid, elastic, and poroelastic theories [Jackson and Richardson 2007]. All three models assume a homogeneous medium and assume far-field approximations. The far-field approximations makes these models independent of the transducer type, e.g., spherical, cylindrical, or planar [Jackson and Richardson 2007]. Most widely used are the Kirchhoff approximation and small-roughness perturbation method. Each has its domain of validity: small-roughness perturbation method is most accurate for scattering at wide angles relative to the specular (flat-interface reflection)[Thorsos and Jackson 1989]; while the Kirchhoff approximation is most accurate for scattering at incidence angles near the specular direction [Thorsos 1990]. For a water/sand interface[2] the Kirchhoff approximations start producing diffused scattering responses that are too high at an incidence angle of 70° [Jackson and Richardson 2007]. The tank test set-up, discribed in Section 3.1, has angles of interest between 70° and 0° (with respect to the surface normal) making the Kirchhoff approximation the best modelling choice to analyse the experimental data. As well as the angular limitations, the Kirchhoff approximation is valid only when the planar and spherical reflection coefficients match, as described in Section 1.3 and Brekhovskikh [1980].

In the past, the Kirchhoff approximation has been used to solve rough surface scattering for electromagnetics [Beckmann and Spizzichino 1963, Ogilvy 1991, Ishimaru 1997], optical [Goodman 1968], and acoustic problems using fluid theory [Eckart 1953] and more recently it has been applied to acoustic problems using elastic theory [Dacol 1990]. The Kirchhoff approximation allows plane wave reflection coefficients to be applied to non-planar surfaces. Modelling a plane wave interacting with a smooth planar surface is straightforward, and is covered in Appendix C.1. Modelling a spherical wave interacting with a smooth planar surface is slightly more complicated and is covered in Appendix C.2. Modelling a plane or spherical wave interacting with a rough surface, rather than a smooth surface, requires a more complicated model, e.g., the Kirchhoff approximation. The Kirchhoff approximation produces an integral that is evaluated over the surface of interest. This problem can be addressed by a number of different methods including statistical analysis of the

[2]The parameters of the water/sand interface are: ρ_1=1000 kg m^{-3}, c_1=1550 m s^{-1}, ρ_2 = 1845 kg m^{-3}, and c_2=1826 m s^{-1}.

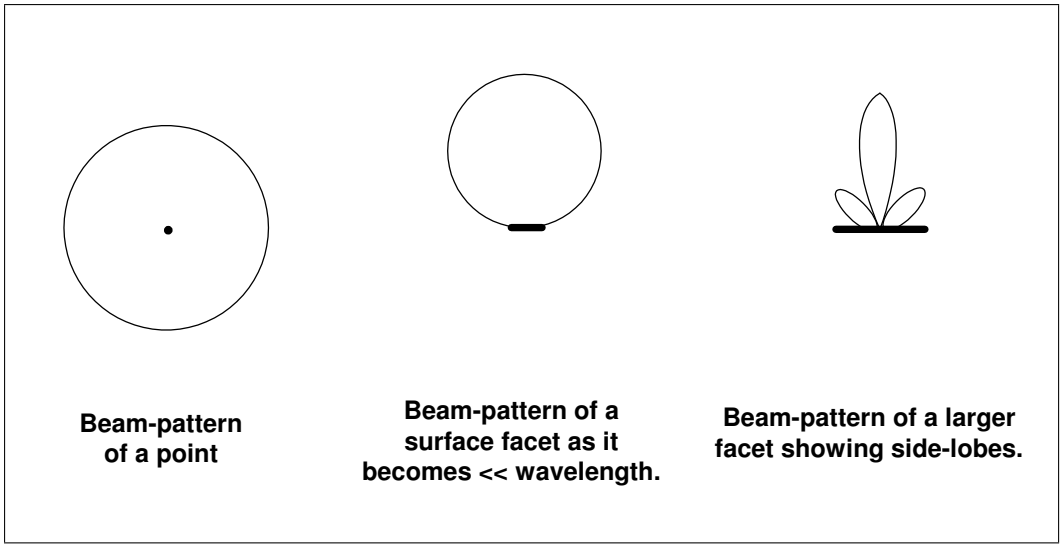

Figure 2.3: The normal incident beam-patterns of a single isolated point, a small surface facet, and a larger surface facet.

surface using the Kirchhoff approximation (described in Section 2.3), or discrete solutions of the Kirchhoff approximation using either point or facet simulations. Each of the two discrete solutions has its trade-offs. The point simulation divides the seafloor[3] into many small points about a 1/10 of a wavelength apart, whereas the facet simulation divides the seafloor into many small facets which can have a large range in sizes, e.g., the Kiwi SAS simulator uses facets ranging from 1 m to 1 mm [Hunter 2006].

The major trade-off between point simulation and a facet simulation is simplicity versus accuracy. Most point simulations assume that the point has no directional component and its weighting is constant. The weighting of the points is based on the area of the simulation divided by the number of points, i.e., the equivalent facet area. A facet simulation needs the direction, the beam-pattern and the area to be calculated for each facet. This means that a facet simulation requires more computing power than a point simulation for a given resolution. However, facet simulations do not require the same resolution as point simulations; their spacing is dictated by the spatial spectrum of the surface, e.g., a smooth surface could be represented by a single facet, provided that far-field approximations are still valid, whereas the same surface would spaced at approximately 1/10 of a wavelength for a point simulation. This allows for computational gains due to the use of larger facets. The use of rough facet simulations is demonstrated by Hunter [2006] and allows a large facet to represent objects with fine scale roughness.

[3]The seafloor is defined as the interface at the bottom, which in most cases is a water/sand interface. The sea-surface is defined as the interface at the top, which, for these experiments, is a water/air interface.

Rather than using large facets and applying them with fine scale roughness, small facets, i.e., 1 mm or smaller, can be used to model fine scale roughness. It is important to note that as a facet approaches a point, its scattered field still has direction due to the obliquity factor and does not reduce to a point source, i.e., an omni-directional scatterer. Figure 2.3 shows a comparison of the beam-patterns of a single point source, a small surface facet, and a larger surface facet. One advantage of a directional scatterer is that a reflection coefficient can be applied to each facet. The plane-wave reflection coefficient can be applied to each individual facet allowing a rough, sandy seafloor to be modelled.

2.2.1 3D modelling simulation

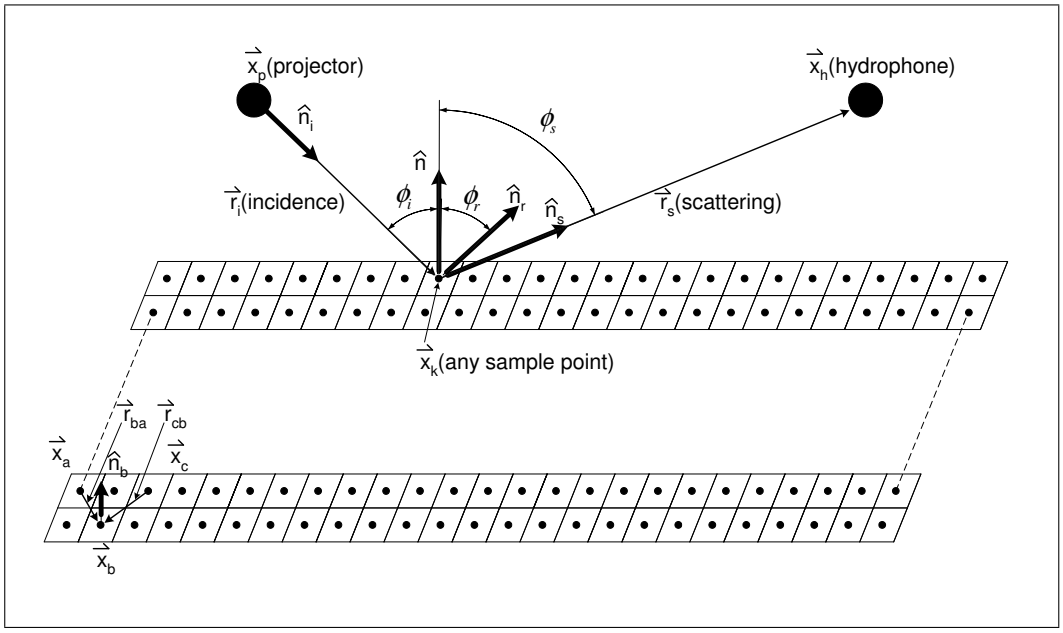

Figure 2.4: Approximate geometry of a facet and point simulation setups.

3D simulations have several advantages over 2D simulations (discussed in Section 2.2.5) but they require the facet to have a shape, i.e., a 2D simulation facet simulation will use a line. Any shape can be used but a single simple shape, such as a triangle or rectangle, is preferred to simplify the computation. The best shape to use is a triangle, given that any continous surface can be made up of small triangles. Unfortunately, this requires the computationally intensive process of tessellating the surface into those small triangles. Hunter used this process for his simulations [Hunter 2006].

On the other hand, the simplest shape to implement is a rectangular facet using a fixed xy axis sampling rate with variable area. The rectangular facet has one important drawback over the triangular facet, namely, not all surfaces can be

fully enclosed by rectangles, i.e. there will be small gaps between the facets. This problem can be minimised by making the facet sampling rate or resolution small with respect to the roughness of the surface, i.e., if the gaps between the facets are 1/10 of the facet size and the facet size is 1/10 of a wave length then the gaps between the facets are 1/100 of a wavelength having minimal contribution [Hunter 2007]. For these reasons, a rectangular facet with a 1 mm sample rate has been chosen to perform the rough surface simulations.

2.2.2 Kirchhoff facet simulation

The facet simulation is derived from the basic Kirchhoff approximation of the acoustic velocity potential as given by Clay and Medwin [1977] is,

$$\varphi_s(\vec{\boldsymbol{x}}_p, \vec{\boldsymbol{x}}_h, f) = \frac{1}{4\pi} \iint_{\Omega} \mathscr{R}_{12}\big(\widehat{\boldsymbol{n}}_r, \widehat{\boldsymbol{n}}_s, f\big) \times \frac{\partial}{\partial\, \widehat{\boldsymbol{n}}} \left(\varphi_i(|\vec{\boldsymbol{x}} - \vec{\boldsymbol{x}}_p|, f)\ \frac{\exp\big[-jk|\vec{\boldsymbol{x}}_h - \vec{\boldsymbol{x}}|\big]}{|\vec{\boldsymbol{x}}_h - \vec{\boldsymbol{x}}|} \right) \mathrm{d}x\ \mathrm{d}y \quad \Big(\mathrm{m}^2\Big), \tag{2.20}$$

where the geometry of the configuration is shown in Figure 2.4, Ω denotes the surface being evaluated, and $\vec{\boldsymbol{x}}_h$, $\vec{\boldsymbol{x}}_p$ and $\vec{\boldsymbol{x}} = (x, y, z)$ are the vector locations of the projector, hydrophone, and an arbitrary surface location (x, y). The unit vector in the direction of the incident field is

$$\widehat{\boldsymbol{n}}_i = \widehat{\boldsymbol{n}}_i\big(x, y\big) = \frac{\vec{\boldsymbol{x}} - \vec{\boldsymbol{x}}_p}{|\vec{\boldsymbol{x}} - \vec{\boldsymbol{x}}_p|}, \tag{2.21}$$

the unit vector in the direction of the scattering field is

$$\widehat{\boldsymbol{n}}_s = \widehat{\boldsymbol{n}}_s\big(x, y\big) = \frac{\vec{\boldsymbol{x}}_h - \vec{\boldsymbol{x}}}{|\vec{\boldsymbol{x}}_h - \vec{\boldsymbol{x}}|}, \tag{2.22}$$

and $\mathscr{R}_{12}\big(\widehat{\boldsymbol{n}}_r, \widehat{\boldsymbol{n}}_s, f\big)$ is the plane wave reflection coefficient as given by (C.14) for the reflected unit vector:

$$\widehat{\boldsymbol{n}}_r = \widehat{\boldsymbol{n}}_r\big(x, y\big) = \widehat{\boldsymbol{n}}_i - 2\Big[\widehat{\boldsymbol{n}}_i \cdot \widehat{\boldsymbol{n}}\Big]\widehat{\boldsymbol{n}}, \tag{2.23}$$

where $\widehat{\boldsymbol{n}} = \widehat{\boldsymbol{n}}\big(x, y\big)$ is the normal of the surface at a location (x, y). Equation (2.20) is derived for a point source but can be generalised for an arbitrary source with a projector who's transmitted waveform has a spectrum $S(f)$ and its projector beam pattern is $B_p\big(\widehat{\boldsymbol{n}}_i, \widehat{\boldsymbol{n}}_p, f\big)$, resulting in

$$\varphi_s(\vec{\boldsymbol{x}}_p, \vec{\boldsymbol{x}}_h, f) \approx S(f) \frac{1}{(4\pi)^2} \iint_{\Omega} \mathscr{R}_{12}\big(\widehat{\boldsymbol{n}}_r, \widehat{\boldsymbol{n}}_s, f\big) B_p\big(\widehat{\boldsymbol{n}}_i, \widehat{\boldsymbol{n}}_p, f\big) \times \frac{\exp\Big[-j\,k\,\big(|\vec{\boldsymbol{x}} - \vec{\boldsymbol{x}}_p| + |\vec{\boldsymbol{x}}_h - \vec{\boldsymbol{x}}|\big)\Big]}{|\vec{\boldsymbol{x}} - \vec{\boldsymbol{x}}_p| \cdot |\vec{\boldsymbol{x}}_h - \vec{\boldsymbol{x}}|}\, \mathrm{d}x\ \mathrm{d}y \qquad \Big(\mathrm{m}^2\Big), \tag{2.24}$$

where $\widehat{\boldsymbol{n}}_p$ is the normal of the projector [Hunter 2006]. Note the beam-pattern of the hydrophone is not included because it is not part of the scattering field, but to simulate an entire system it should be included. For the case of spherical transducers, the $B_p\big(\widehat{\boldsymbol{n}}_i, \widehat{\boldsymbol{n}}_p, f\big) \approx 1$. This is not true in all cases since spherical transducers can still have significant beam patterns as discussed in Section 3.1.3. If (2.24) is evaluated over a single facet then, using superposition (2.24) can simplified to represent a surface made up of a field of facets

$$\varphi_s(\vec{\boldsymbol{x}}_p, \vec{\boldsymbol{x}}_h, f) \approx \sum_{k=1}^{N_f} \varphi_{sk}(\vec{\boldsymbol{x}}_k, \vec{\boldsymbol{x}}_p, \vec{\boldsymbol{x}}_h, f), \tag{2.25}$$

where N_f is the number of facets comprising the surface and $\varphi_{sk}(\vec{\boldsymbol{r}}_{ik}, \vec{\boldsymbol{r}}_{sk}, f)$ is a solution of (2.24) for a single facet assuming the Fraunhoffer approximation

$$\begin{aligned}\varphi_{sk}(\vec{\boldsymbol{x}}_k, \vec{\boldsymbol{x}}_p, \vec{\boldsymbol{x}}_h, f) \approx & A_f\, S(f) \frac{j\,2\pi}{\lambda} \frac{1}{(4\pi)^2} \mathscr{R}_{12}\big(\widehat{\boldsymbol{n}}_{rk}, \widehat{\boldsymbol{n}}_{sk}, f\big) B\big(\widehat{\boldsymbol{n}}_{rk}, \widehat{\boldsymbol{n}}_{sk}, f\big) B_p\big(\widehat{\boldsymbol{n}}_{ik}, \widehat{\boldsymbol{n}}_p, f\big) \\ & \times \frac{\big[(\widehat{\boldsymbol{n}}_{ik} + \widehat{\boldsymbol{n}}_{sk}) \cdot \widehat{\boldsymbol{n}}_k\big]}{2} \frac{\exp\Big[-j\,k\,\big(|\vec{\boldsymbol{x}}_k - \vec{\boldsymbol{x}}_p| + |\vec{\boldsymbol{x}}_h - \vec{\boldsymbol{x}}_k|\big)\Big]}{|\vec{\boldsymbol{x}}_k - \vec{\boldsymbol{x}}_p| \cdot |\vec{\boldsymbol{x}}_h - \vec{\boldsymbol{x}}_k|} \qquad \Big(\mathrm{m}^2\Big).\end{aligned} \tag{2.26}$$

Here A_f is the area of the facet, $\vec{\boldsymbol{x}}_k = (x_k, y_k, z_k)$ are the coordinates of the facet centre, and $B\big(\widehat{\boldsymbol{n}}_{rk}, \widehat{\boldsymbol{n}}_{sk}, f\big)$ is the beam pattern of that facet (described in more detail in Section 2.2.3), $\widehat{\boldsymbol{n}}_{sk}$, $\widehat{\boldsymbol{n}}_{ik}$, $\widehat{\boldsymbol{n}}_{rk}$, and $\widehat{\boldsymbol{n}}_k$ are the scattering, incident and reflecting unit vectors, and the facet normal at the facet centre. The derivation of (2.26) is covered in detail in Hunter [2006]. It is important to note that even though N_f

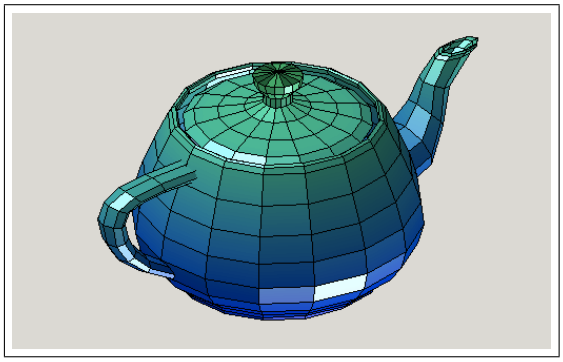

Figure 2.5: The "teapotdemo" from MATLAB showing a teapot tessellated with quadrilaterals.

covers the entire surface, the x_k, y_k and z_k dimensions are no longer continuous but are based on the location of the facets centres. The (x,y) spatial sampling of the facets is not necessarily at a constant rate. This is particularly true for tessellated surfaces, which can be clearly seen in the MATLAB demo "teapotdemo", shown in Figure 2.5. In this figure the facets on the edges of the teapot have a much

finer x, y resolution than the facets on the top. This is because when the slope is steeper, the facet centres have a finer x, y. On the bottom half of the teapot, there are facets at the same x, y location as on the top half of the teapot. At this point a simple surface integral, for (2.20), is not an appropriate solution for the Kirchhoff approximation given that occlusions and multiple scattering occur. The Kiwi SAS simulator solved the occlusion and multiple scatter problem by testing the ray path for each facet [Hunter 2006]. This limitation can also be solved by choosing a surface that is unlikely to have these issues. This can be done by limiting the spacial frequencies of the surface and limiting the transducer geometry to angles of low incidence, i.e., 70° to 90°. If these limitations are dealt with then (2.26) can accurately represent an arbitrary surface. The derivation of (2.26) is covered in great detail in Hunter [2006] and in somewhat less detail in Goodman [2005] and Beckmann and Spizzichino [1963].

2.2.3 Facet beam-patterns

Equation (2.26) can use any shape for the facet. The beam pattern for a rectangular facet is

$$\begin{aligned} B_r(\widehat{\boldsymbol{n}}_s, \widehat{\boldsymbol{n}}_r, f) =& (n_{sz} + n_{rz}) \\ & \operatorname{sinc}\Big(L_x \frac{f}{c}(n_{rx} - n_{sx})\Big) \operatorname{sinc}\Big(L_y \frac{f}{c}(n_{ry} - n_{sy})\Big) \end{aligned} \tag{2.27}$$

where L_x and L_y are the length of the facet in the x and y directions, n_{sx}, n_{sy}, and n_{sz} are the x, y, and z components of $\widehat{\boldsymbol{n}}_s$, the scattering unit vector, and n_{rx}, n_{ry}, and n_{rz} are the x, y, and z components of $\widehat{\boldsymbol{n}}_r$, the reflecting unit vector. The beam-pattern of a unit right-angle triangle is

$$\begin{aligned} B_t(\widehat{\boldsymbol{n}}_s, \widehat{\boldsymbol{n}}_r, f) =& \frac{n_{sz} + n_{rz}}{n_{sx} + n_{rx}} \exp\left[j\pi \frac{1}{3} \frac{f}{c} \Big(L_x(n_{rx} - n_{sx}) - L_y(n_{ry} - n_{sy}) \Big) \right] \\ & \times \left(\exp\left[L_x \, j\pi \frac{f}{c}(n_{sx} - n_{rx}) \right] \operatorname{sinc}\Big(L_y \frac{f}{c}(n_{ry} - n_{sy}) \Big) \right. \\ & \left. - \operatorname{sinc}\Big(\frac{f}{c} \Big(L_x(n_{rx} - n_{sx}) + L_y(n_{ry} - n_{sy}) \Big) \Big) \right). \end{aligned} \tag{2.28}$$

Most surfaces can be approximated using either of these shapes. The derivations of the rectangular and triangular beam-patterns are covered in [Hunter 2006]. The numerical approximation of the beam-pattern of an arbitrary shape using the FFT is covered in [Bracewell 1986].

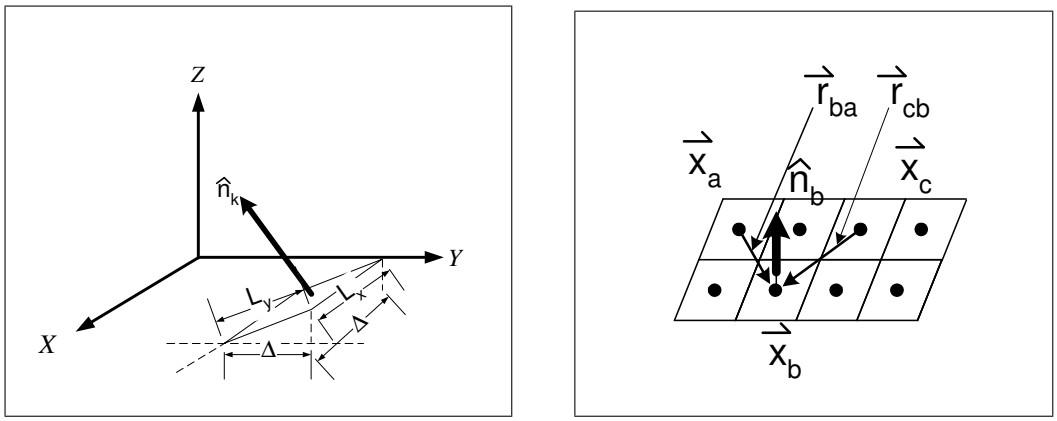

(a) Facet length vs Δ

(b) Locations of $\vec{\boldsymbol{x}}_a$, $\vec{\boldsymbol{x}}_b$, and $\vec{\boldsymbol{x}}_c$ are required determine to the facet normal $\widehat{\boldsymbol{n}}_b$.

Figure 2.6: Geometry of the rectangular simulation used in Section 2.2.4.

2.2.4 Simulation implementation

Tessellating a surface has been found to be computationally intensive and is not required for this simulation implementation. The main reason the rectangular facets were chosen is to minimise the computational requirements and still allow the analysis of fine scale roughness. Rectangular facets with constant centre spacing were chosen to simulate the surfaces. These facets have both a variable area and a beam pattern. The spacing of the facet centres is 1 mm in the x and y directions. Because the facet dimension are under 1/10 of a wavelength, the beam-pattern of the facet simplifies to the obliquity factor, reducing (2.27) to

$$B_r(\widehat{\boldsymbol{n}}_s, \widehat{\boldsymbol{n}}_r, f) = (n_{sz} + n_{rz}). \tag{2.29}$$

If the projector is assumed to be spherical and the facet being simulated is a rectangle facet of less than 1/10 of a wavelength, then (2.26) can be simplified by substituting $B_p\big(\widehat{\boldsymbol{n}}_{ik}, \widehat{\boldsymbol{n}}_p, f\big) = 1$,(2.29), and $A_f = L_x\, L_y$ yielding

$$\begin{aligned}\varphi_{sk}(\vec{\boldsymbol{x}}_k, \vec{\boldsymbol{x}}_p, \vec{\boldsymbol{x}}_h, f) \approx & L_x\, L_y\, S(f) \frac{j\,2\pi}{\lambda} \frac{1}{(4\pi)^2} \mathscr{R}_{12}\big(\widehat{\boldsymbol{n}}_{rk}, \widehat{\boldsymbol{n}}_{sk}, f\big)(n_{sz} + n_{rz}) \\ & \times \frac{\big[(\widehat{\boldsymbol{n}}_{ik} + \widehat{\boldsymbol{n}}_{sk}) \cdot \widehat{\boldsymbol{n}}_k\big]}{2} \frac{\exp\Big[- j\,k\,\big(|\vec{\boldsymbol{x}}_k - \vec{\boldsymbol{x}}_p| + |\vec{\boldsymbol{x}}_h - \vec{\boldsymbol{x}}_k|\big)\Big]}{|\vec{\boldsymbol{x}}_k - \vec{\boldsymbol{x}}_p| \cdot |\vec{\boldsymbol{x}}_h - \vec{\boldsymbol{x}}_k|} \qquad \Big(\mathrm{m}^2\Big),\end{aligned} \tag{2.30}$$

where L_x and L_y, shown in Figure 2.6 (a), are the length and width of the facet:

$$L_x = \frac{\Delta}{\widehat{\boldsymbol{n}}_k \cdot \widehat{\boldsymbol{x}}}, \tag{2.31}$$

and

$$L_y = \frac{\Delta}{\widehat{\boldsymbol{n}}_k \cdot \widehat{\boldsymbol{y}}}. \tag{2.32}$$

(Note this methode of calcuating L_x and L_y assumes constant centre spacing and that adjacent facets touch; therefore, it will fail if $\widehat{\boldsymbol{n}}_k \cdot \widehat{\boldsymbol{x}}$ or $\widehat{\boldsymbol{n}}_k \cdot \widehat{\boldsymbol{y}}$ are zero.) Here Δ is the spatial sampling distance in both x and y, $\widehat{\boldsymbol{n}}_k$ is the facet normal, $\widehat{\boldsymbol{x}}$ and $\widehat{\boldsymbol{y}}$ are the unit vectors in the x and y directions. The value of $\widehat{\boldsymbol{n}}_k$ for a facet can be determined using the cross product of three arbitrary surface locations:

$$\widehat{\boldsymbol{n}}_k = \widehat{\boldsymbol{n}}_k\big(x_k, y_k\big) = \frac{(\vec{\boldsymbol{x}}_a - \vec{\boldsymbol{x}}_b) \times (\vec{\boldsymbol{x}}_c - \vec{\boldsymbol{x}}_b)}{|(\vec{\boldsymbol{x}}_a - \vec{\boldsymbol{x}}_b) \times (\vec{\boldsymbol{x}}_c - \vec{\boldsymbol{x}}_b)|} = \frac{\vec{\boldsymbol{r}}_{ba} \times \vec{\boldsymbol{r}}_{bc}}{|\vec{\boldsymbol{r}}_{ba} \times \vec{\boldsymbol{r}}_{bc}|}, \tag{2.33}$$

where the geometry of the points is shown in Figure 2.6 (b). The first point is at

$$\vec{\boldsymbol{x}}_a = \vec{\boldsymbol{x}}_k\big((x_k - \Delta), (y_k + \Delta)\big) = \big(x_a, y_a, z_a\big), \tag{2.34}$$

the second point is at

$$\vec{\boldsymbol{x}}_b = \vec{\boldsymbol{x}}_k\big(x_k, y_k\big) = \big(x_b, y_b, z_b\big), \tag{2.35}$$

and the third point is at

$$\vec{\boldsymbol{x}}_c = \vec{\boldsymbol{x}}_k\big((x_k + \Delta), (y_k + \Delta)\big) = \big(x_c, y_c, z_c\big). \tag{2.36}$$

This method of converting a surface to facets is only appropriate for spatially oversampled surfaces given that there will be gaps between facets. As the surface roughness increases with respect to the facet spacing these gaps will become significant. If the surface spectrum is limited then the gaps between facets are insignificant given that they are less than 1/100 of a wavelength. Tessellating the surface with triangles would be more accurate but more computationally intensive. Given that the standard surface used for the simulations is 3 m x 3 m with a 1 mm sampling rate, this would significantly increase the simulation time above the current 10 hours with little gain in accuracy [Hunter 2007].

2.2.5 2-D simulation limitations

When modelling a seafloor or other rough surface, one of the most common assumptions to be made is that a 2-D simulation is roughly equivalent to a 3-D simulation. This assumption can be seen in many acoustic and electromagnetic books [Clay and Medwin 1977, Beckmann and Spizzichino 1963, Jackson and Richardson 2007]. When comparing 2-D and 3-D simulations for spherical waves it is important to note that the mono-static and bi-static configurations are diffrent problems. For a mono-

static configuration with an isotropic surface circular symmetry is appropriate, as described in Section C.2.2 and

$$\varphi_i(\vec{\boldsymbol{r}}_i, f) = S(f)\frac{j}{4\,\pi}\int_0^\infty J_0(k_\rho, \rho)\frac{\exp\left[-j\,k_{z_1}|z - z_p|\right]}{k_{z_1}}k_\rho\,\mathrm{d}k_\rho \tag{2.37}$$

for the acoustic potential of the scattered field, where $z \leq 0$ and

$$k_{z1} = \begin{cases} \sqrt{k_1^2 - k_\rho}, & k_\rho^2 \leq k_1^2 \\ -j\sqrt{k_\rho - k_1^2}, & k_\rho^2 > k_1^2 \end{cases} \tag{2.38}$$

[Ziomek 1995]. Circular symmetry is also valid for bi-static reflection with spherical waves reflecting from a smooth surface [Jackson and Richardson 2007, Ziomek 1995, Brekhovskikh and Lysanov 2003]. However, circular symmetry is not valid for anisotropic surfaces [Jackson and Richardson 2007], nor is circular symmetry valid for bi-static scattering from a rough surface. The equations for dealing with bi-static scattering from rough surfaces is discussed in Section 2.3.2.

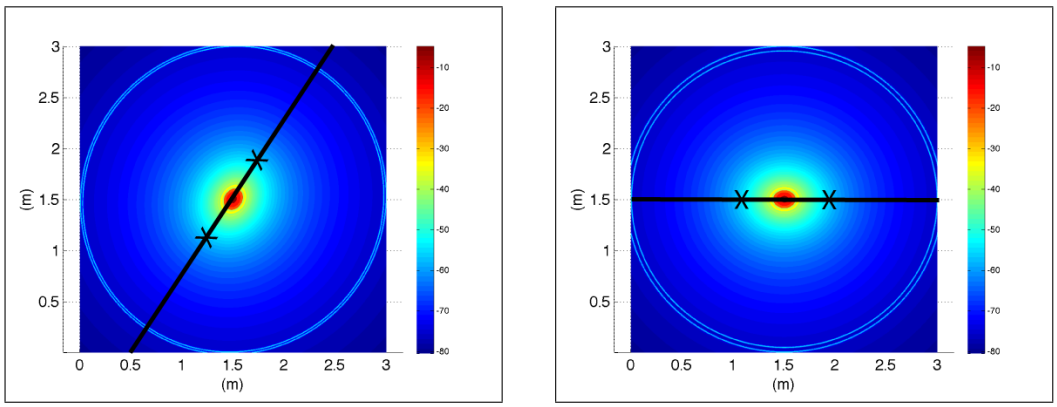

(a) 60° (b) 0°

Figure 2.7: Bi-static transducer configuration reflecting from a smooth seafloor. Note the dark lines indicate the transducer orientation. The transducers are orientated at 60° and 0°. The 60° orientation places the transducers at $1.333\,\mathrm{m}\,\widehat{\boldsymbol{x}} + 1.210\,\mathrm{m}\,\widehat{\boldsymbol{y}} + 0\,\mathrm{m}\,\widehat{\boldsymbol{z}}$ and $1.667\,\mathrm{m}\,\widehat{\boldsymbol{x}} + 1.890\,\mathrm{m}\,\widehat{\boldsymbol{y}} + 0\,\mathrm{m}\,\widehat{\boldsymbol{z}}$. The 0° orientation places the transducers at $1.165\,\mathrm{m}\,\widehat{\boldsymbol{x}} + 1.5\,\mathrm{m}\,\widehat{\boldsymbol{y}} + 0\,\mathrm{m}\,\widehat{\boldsymbol{z}}$ and $1.835\,\mathrm{m}\,\widehat{\boldsymbol{x}} + 1.5\,\mathrm{m}\,\widehat{\boldsymbol{y}} + 0\,\mathrm{m}\,\widehat{\boldsymbol{z}}$. Note the seafloor is located at -0.5 m $\widehat{\boldsymbol{z}}$ and the transducer separation is 77 cm.

In order for circular symmetry to be valid, the geometry that it is applied to needs to be circular or roughly circular. A bi-static configuration does not have circular symmetry but has elliptical symmetry. This can be seen in the bi-static simulation results shown in Figure 2.7. Figure 2.7 (a) and (b) clearly shows an elliptical return from the bi-static transducer configuration. What is shown in the figure is the signal strength in dB mapped onto the surface based on the time delay. The 3 m by 3 m surface has three main returns: the surface reflection, and two edge returns. The elliptical nature of the returns is also shown by the fact that there are

two edge returns rather than one. If the surface had spherical symmetry then there would only be one edge return. The effects of bi-static scattering are dealt with in more detail in Section 2.3.2.

2.3 SURFACE STATISTICS

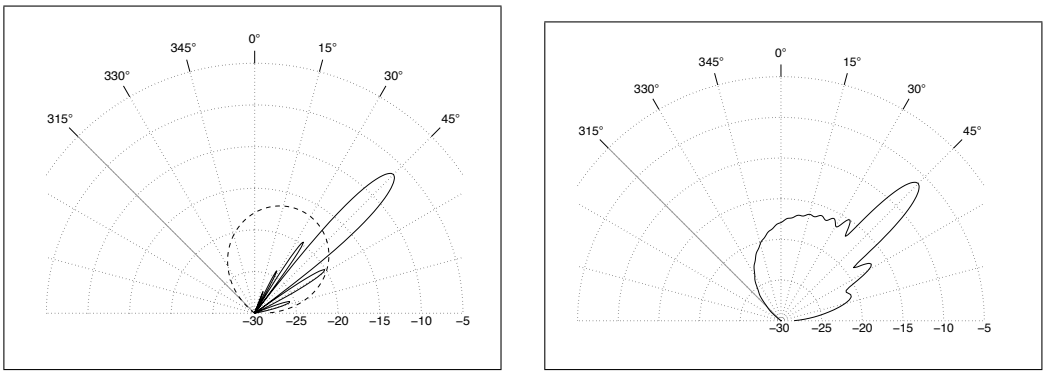

Figure 2.8: The mean intensity of the scattering pattern at 30 kHz for a 0.5 m x 0.5 m surface with a roughness of $\sigma = 5$ mm: (a) decomposition of the beam pattern into its specular (solid line) and diffuse (dashed line) components, (b) total beam-pattern intensity [Hunter 2006].

In acoustic applications, some systems make primary use of the reflected signals (specular reflection), e.g., an echo sounder on a boat, and others make primary use of the scattered signals (diffuse scattered), e.g., side scan sonar or SAS systems. Roughness affects both the specular reflection and diffuse scattered components of the reflected signal, shown in Figure 2.8. The effect of a Gaussian rough surface on the specular reflection is covered in Section 2.3.1 and the effect of a surface with a power-law roughness spectrum on both specular and diffuse scattered components is covered in Section 2.3.2. The reason that the two methods are covered is that Section 2.3.1 is more easily followed and can be applied to a power-law surface. Whereas Section 2.3.2 is simple to implement but the details behind the process are obscured.

2.3.1 Rough surface specular reflection coefficient

A better method of characterising the surface roughness allows improved analysis of the signals reflected back to the sonar. There are many references on the reflection generated by rough surfaces. The key references are: Jackson and Richardson [2007], Beckmann and Spizzichino [1963], Clay and Medwin [1977], Clay et al. [1973], and Spindel and Schultheiss [1972]. The following analysis is based on the work of Clay

and Medwin [1977]. In Section C.2.4 it is shown that, if the range is sufficient[4], then the sound pressure for a spherical wave reflected from a plane, with $\phi_s = \phi_i$, can be approximated as

$$p = p_s(\vec{\boldsymbol{r}}_i, \vec{\boldsymbol{r}}_s, f) \approx p_0\, r_0 \mathscr{R}(\phi_i) \frac{\exp\Big[- j\, k \left(|\vec{\boldsymbol{r}}_i| + |\vec{\boldsymbol{r}}_s| \right) \Big]}{\Big(|\vec{\boldsymbol{r}}_i| + |\vec{\boldsymbol{r}}_s| \Big)} \qquad \left(\frac{\text{Pa}}{\text{Hz}} \right), \tag{2.39}$$

where $\mathscr{R}(\phi_i) = \mathscr{R}_{12}(\phi_i)$ is the reflection coefficient as defined by (C.14); k is the wave-number, defined as ω/c, and $\omega = 2\,\pi\, f$; p_0 is the reference sound pressure at a range r_0 including the spectrum $S(f)$, at a range r_0; $p_s(\vec{\boldsymbol{r}}_i, \vec{\boldsymbol{r}}_s, f)$ is the sound pressure of the scattered field measured at a point $\vec{\boldsymbol{x}}_h$; and $\vec{\boldsymbol{r}}_i$, $\vec{\boldsymbol{r}}_s$ and ϕ_i, ϕ_s are the vectors and angles of incidence and scattering with their geometry defined in Figure 2.9 [Clay and Medwin 1977].

The equation for the reflection coefficient of a spherical wave from (2.39) is given as

$$\mathscr{R}(\phi_i) = p \frac{(r_i + r_s)}{p_0 r_0} \exp\Big[- j\, k \left(r_i + r_s \right) \Big], \tag{2.40}$$

where $r_i = |\vec{\boldsymbol{r}}_i|$ and $r_s = |\vec{\boldsymbol{r}}_s|$ are the incidence and scattering range of the projector and hydrophone. This equation works well with smooth surfaces [Clay and Medwin 1977], but when dealing with a rough surface, the sound pressure p varies greatly between surface realisations. When dealing with a rough surfaces the sound pressure is no-longer as simple as a smooth surface reflection. The received sound pressure, sometimes described as the scattering field, is now made up of diffuse and specular components, as shown in Figure 2.8. The diffuse component, described by the scattering strength, is discussed in Section 2.3.2. The specular component, described by the rough surface reflection coefficient is described in this section. Individual rough surface realisations can have sound pressures levels that are greater or less than the smooth surface sound pressure value, given by (2.39). However the average sound pressure from a rough surface will be smaller than the smooth surface sound pressure. The amount that the rough surface's average sound pressure decreases is dependent on the surface roughness statistics. Thus it is necessary to consider the average p rather than individual occurrences. This allows the analysis of the statistical response of the system, given by

$$\langle \mathscr{R}(\phi_i) \rangle = \left\langle p\, \frac{(r_i + r_s)}{p_0 r_0} \exp\Big[- j\, k \left(r_i + r_s \right) \Big] \right\rangle \tag{2.41}$$

[4]The effect of spherical-waves on the reflection coefficient is both range and frequency dependent. The effect of spherical-waves is greatest at minimum frequency and range. The reflection from sand will be effected by less than 5% for a frequency of 80 kHz and a range greater than 10 cm as shown in Figure C.4. Note the 10 cm range is at approximately 80° in Figure C.4 (f) with the transducers separated by 1 m.

and

$$\langle p \rangle = \left\langle \frac{p_0 r_0}{\mathscr{R}(\phi_i)\,(r_i + r_s)} \exp\left[j\,k\,\left(r_i + r_s\right)\right] \right\rangle \tag{2.42}$$

where $\langle \mathscr{R} \rangle$ and $\langle p \rangle$ are the average surface reflection coefficient and sound pressure. This can be computed by

$$\langle \mathscr{R}(\phi_i) \rangle = E[\mathscr{R}(\phi_i)] = E[\mathscr{R}(\langle \phi_i \rangle)] = \frac{1}{N} \sum_{n=1}^{N} \mathscr{R}_n(\langle \phi_i \rangle) \tag{2.43}$$

and

$$\langle p \rangle = E[p] = \frac{1}{N} \sum_{n=1}^{N} p_n, \tag{2.44}$$

where $E[\mathscr{R}(\langle \phi_i \rangle)]$ is the expectation or mean value of $\mathscr{R}(\langle \phi_i \rangle)$ and $\mathscr{R}_n(\langle \phi_i \rangle)$ denotes different and independent realisations $\mathscr{R}(\langle \phi_i \rangle)$. Likewise, $E[p]$ is the mean value of p and p_n denotes different and independent realisations of p. Equation (2.43) assumes the angle ϕ_i does not change significantly and therefore $\mathscr{R}(\phi_i)$ does not change significantly, allowing $\mathscr{R}(\phi_i) = \mathscr{R}(\langle \phi_i \rangle)$. If it is further assumed that the spreading losses are normalised, i.e., $1/A$ where

$$A = \frac{r_0}{(r_i + r_s)}, \tag{2.45}$$

then using (2.42)

$$p_n = p_0 \mathscr{R}_n(\langle \phi_i \rangle) = \mathscr{R}(\langle \phi_i \rangle) \exp[-j\,k(r_i + r_s)]. \tag{2.46}$$

This equation relies on several assumptions: firstly, that the roughness height is small compared to the total distance, therefore, allowing small differences in spreading loss to be ignored; secondly, that the beam-pattern and diffuse scattered components do not play a role in the reflection coefficient; and thirdly, that the major effect causing a reduction in the response of $\langle p \rangle$ is interference of the reflected signals. It is assumed that the roughness does not change the value of the reflection coefficient, instead it reduces the amount of signal returned in the specular direction by scattering else where rather than all in the specular direction. The analysis of the scattering effect of roughness is discussed in Section 2.3.2.

To relate the reflection coefficient to the surface height statistics, the roughness needs to be put in terms of height variance. Figure 2.9 shows the roughness measured as height variances, relating r_i and r_s to the height z from the surface. Assuming $\phi_i = \phi_s$ and the transducers are at equal height, r_i and r_s can be related

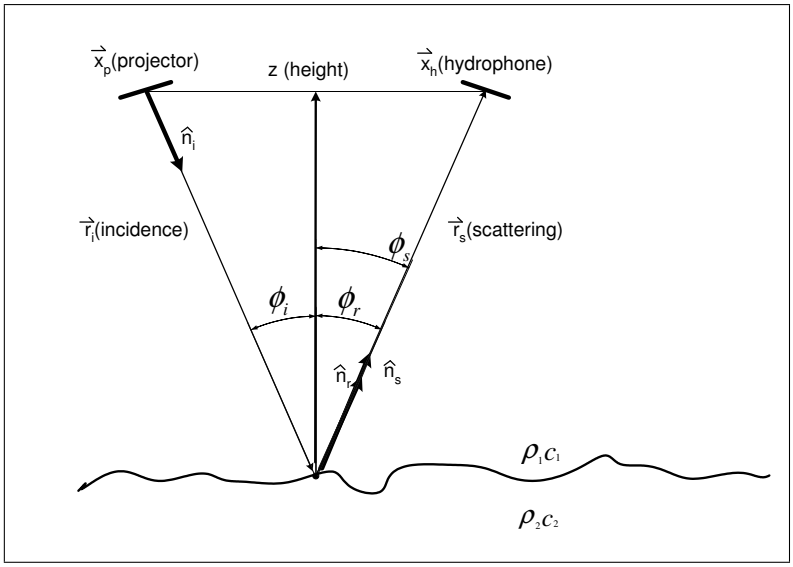

Figure 2.9: Configuration for measuring the average reflection coefficient of a randomly rough surface.

to z, giving

$$r_i = r_s = \frac{z}{\cos\phi_i}. \tag{2.47}$$

This implies that

$$r_i + r_s = 2\,\frac{z_n}{\cos\phi_i} \tag{2.48}$$

where z_n denotes different and independent realisations of z. Substituting (2.48) into (2.46) gives

$$p_n = p_0 \cdot \mathscr{R} \cdot \exp\left[-\,j\,k\,2\,\frac{z_n}{\cos\phi_i}\right]. \tag{2.49}$$

An analysis of (2.49) shows that the average distance $\langle z\rangle$ will not have an effect on the phase difference between values of p_n. To further simplify the analysis, let

$$\zeta \equiv \triangle z \equiv z_n - \langle z\rangle. \tag{2.50}$$

When the height differences are small, the path difference, $2\zeta_n\cos\phi_i$, may be substituted for the path and $\langle\mathscr{R}_{RND}\rangle$ can be expressed in terms of ζ_n yielding

$$\langle\mathscr{R}_{RND}(\zeta_n)\rangle = \left\langle\frac{p_n}{p_0}\right\rangle = \langle\mathscr{R}\cdot\exp[-j\,k\,2\zeta_n\cos\phi_i]\rangle. \tag{2.51}$$

$\mathscr{R}_{RND}(\zeta_n)$ represents an individual realisation of the reflection coefficient with re-

spect to ζ_n, with *RND* denoting random. $\langle \mathscr{R}_{RND} \rangle$ is the average specular reflection and may not match the specular reflection of a single seafloor realisation. The number of seafloor realisations required to match $\langle \mathscr{R}_{RND} \rangle$ is dependent on the statistics of the seafloor and is described in more detail in Section 4.4.1.

When the individual realisations are averaged, the small phase difference will result in destructive interference causing the reflection coefficient $\langle \mathscr{R}_{RND} \rangle$ to be degraded. The average value can be represented in the following form:

$$\langle g \rangle = E[g(X)] = \int_{-\infty}^{\infty} g(x)\, f_X(x)\, \mathrm{d}x, \tag{2.52}$$

where $E[g(X)]$ is the average value of the function $g(x)$ with a data set X, and $f_X(x)$ is the Probability Density Function (PDF) of x [Haykin 1994]. Substituting $\mathscr{R}_{RND}(\zeta)$ for $g(x)$ gives

$$\langle \mathscr{R}_{RND} \rangle = \int_{-\infty}^{\infty} \mathscr{R}_{RND}(\zeta)\, w_a(\zeta)\, \mathrm{d}\zeta, \tag{2.53}$$

where $w_a(\zeta)$ is the PDF for the height of the surface being analysed. Substituting (2.51) for $\mathscr{R}_{RND}(\zeta)$ in (2.53) yields

$$\langle \mathscr{R}_{RND} \rangle = \mathscr{R} \int_{-\infty}^{\infty} \exp[-2jk\zeta \cos\phi_i] w_a(\zeta) \mathrm{d}\zeta. \tag{2.54}$$

Given that $k = \omega/c$, it can be seen that (2.54) is frequency dependent and is in the form of a Fourier transform of $w_a(\zeta)$ evaluated at $k\omega\phi_i/\pi$. Averaging (2.51) yields

$$w_a(\zeta) = \frac{1}{\pi \mathscr{R}} \int_{-\infty}^{\infty} \langle \mathscr{R}_{RND} \rangle \exp[-2jk\zeta \cos\phi_i] w_a(\zeta) \mathrm{d}(k \cos\phi_i). \tag{2.55}$$

Equation (2.55) can then be solved for the more specific case of a Gaussian PDF by substituting $w_G(\zeta)$ for $w_a(\zeta)$ where

$$w_G(\zeta) = \sigma^{-1}(2\pi)^{-1/2} \exp\left[\frac{-\zeta^2}{2\sigma^2}\right] \tag{2.56}$$

for a height standard deviation σ. Substituting (2.56) for w_a in (2.55) and integrating gives

$$\frac{\langle \mathscr{R}_{RND} \rangle_G}{\mathscr{R}} = \exp[-2k^2\sigma^2 \cos^2\phi_i]. \tag{2.57}$$

Clay and Medwin [1973,1977] used this formula to determine σ of the sea-surface based on measurements of $\langle \mathscr{R}_{RND} \rangle_G$ and assuming $\mathscr{R} = 1$. Stanton [1984] expanded (2.57) to determine the roughness of the seafloor. The formulation of (2.57) is still referenced in recent texts such as Jackson and Richardson [2007] (13.14).

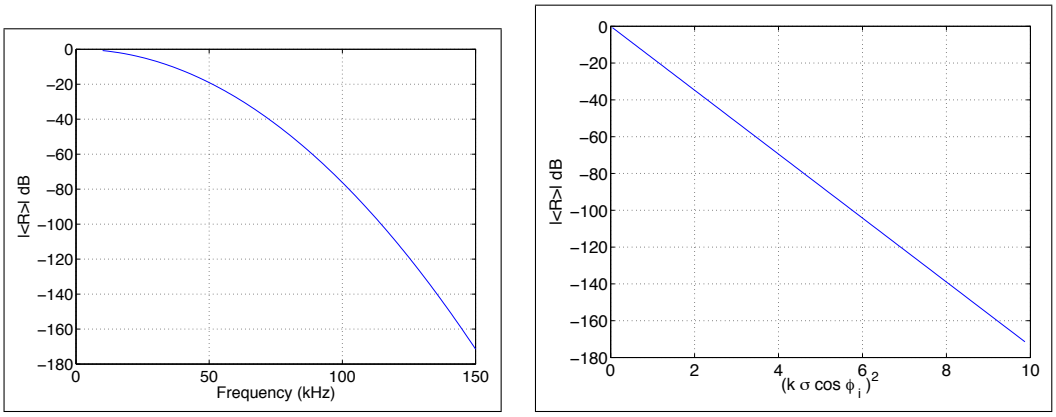

(a) $\langle \mathscr{R} \rangle_G$ dB vs frequency

(b) Linearized plot by substituting $(k\,\sigma\,\cos\phi_i)^2$ for Frequency

Figure 2.10: Coherent reflection coefficient $\langle \mathscr{R} \rangle_G$ vs frequency between 10 kHz and 150 kHz for $\sigma = 5$ mm, $\phi_i = 0$, and $\mathscr{R} = 1$.

Analysis of (2.57) identifies several limitations. For example, it assumes a Gaussian PDF. This has yielded inaccurate readings when σ is large. The reason for this inaccuracy is attributed to shadowing caused by the steepness of the surface roughness [Clay and Medwin 1977]. However, (2.57) yields some useful properties, such as a linearized frequency plot by plotting over $(k\,\sigma\cos\phi_i)^2$ rather than f, as seen in Figure 2.10. Ideally, this could be used to estimate $\mathscr{R}$ if its spectrum were flat. In practice, the seafloor has a to a power-law spectrum [Jackson and Richardson 2007], which is further discussed in Section 2.3.4. The reflection coefficient (specular reflection) and the diffuse scattered components are interrelated as shown in Figure 2.8. So far the effects of the diffuse scattered components have been ignored; these effects are covered in Section 2.3.2.

2.3.2 Roughness effect on scattering

There are two primary types of scattering: volume scattering and surface scattering. Volume scattering is caused by discontinuities inside the medium and surface scattering is caused by the interface discontinuity [Jackson and Richardson 2007]. Volume scattering tends to dominate for soft sediments, such as mud, where there is no critical angle, although this is not true at near vertical angles. Surface scattering tends to dominate for harder sediments, such as sand [Jackson and Richardson 2007]. The separation into surface scattering and volume scattering is not always clear due to the heterogeneity of the seafloor. This may be caused by bubbles, layering, or biology (both plants and animals) [Jackson and Richardson 2007][5]. The water/sand interface is used as the primary media for the experiments performed in this thesis.

[5]Heterogeneity issues, such as air in the sand, occurred in the the tank test environment and is discussed in Section 3.2.3.

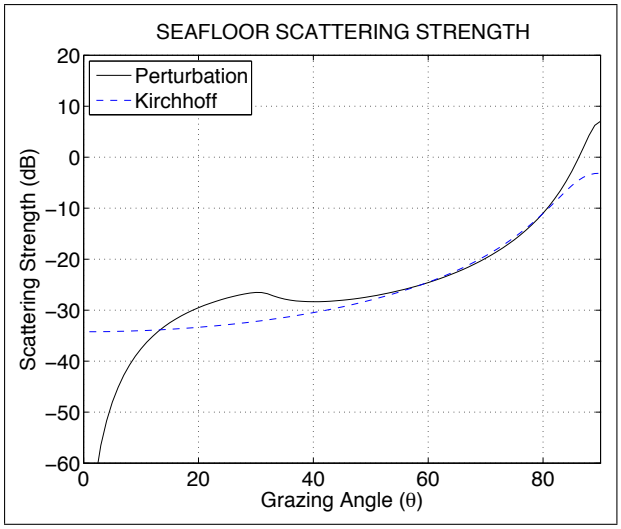

Figure 2.11: A comparison of the scattering strength S_b of the small-roughness perturbation method and the Kirchhoff approximation. These comparisons were made with a power-law surface with a density ratio of $a_\rho = \rho_2/\rho_1 = 1.845$, a sound speed ratio of $a_t = c_2/c_1 = 1.1782$, a spectral exponent of $\gamma_2 = 3.25$, a spectral strength of $\omega_2 = 0.000141$ and a centre frequency of $f = 30\,\text{kHz}$. An explanation of the power-law parameters, γ_2 and ω_2, and the acoustic parameters a_ρ and a_t are given in Section 2.3.4 and Section 2.1. This figure was generated using a MATLAB implementation of a numerical evaluation of (2.58) for (2.60) and its small-roughness perturbation equivalent from Jackson and Richardson [2007].

Therefore, surface scattering is a major area of focus for this thesis.

As discussed in Section 2.2, there are two primary scattering models: the small-roughness perturbation method and the Kirchhoff approximation. A comparison of the perturbation method and the Kirchhoff approximation is shown in Figure 2.11. The Kirchhoff approximation and perturbation method are complementary in their areas of validity. Figure 2.11 shows that the scattering strength S_b is too large for the perturbation method and grazing angles above 80°. Likewise, S_b is also too large for the Kirchhoff approximation for grazing angles below 10°. For angles between 10° and 80° both are equally valid [Jackson and Richardson 2007]. For the grazing angles of interest, i.e., 30° to 90°, the Kirchhoff approximation is appropriate. The perturbation method would be equally valid for grazing angles between 30° and 90° but is more complex and produces little or no gain in accuracy [Jackson and Richardson 2007].

The scattering strength S_b is used to evaluate the average scattered intensity in all directions for a rough surface, much like the reflection coefficient $\mathscr{R}_{12}$ is used to evaluate the reflected signal for a smooth surface. However, it is important to note that in the specular direction the coherent reflection component, discussed in Section 2.3.1, is not given by the scattered strength. The following description of the scattering strength is from [Jackson and Richardson 2007]. The scattering strength

is

$$S_b = 10 \log_{10} \sigma. \tag{2.58}$$

where σ is the proportionality factor. The scattering strength is related to the scattered sound pressure p_s by σ. The mean square value of scattered sound pressure is

$$< |p_s|^2 >= |p_i|^2 A\sigma \frac{1}{|\vec{\boldsymbol{r}}_s|^2}, \tag{2.59}$$

where p_i is the incident sound pressure, $\vec{\boldsymbol{r}}_i$ and $\vec{\boldsymbol{r}}_s$ are the incident and scattering vectors as defined in Figure 2.12, and A is the area of the seafloor being evaluated. The calculation of this area is described in Section 2.3.3. The proportionality factor

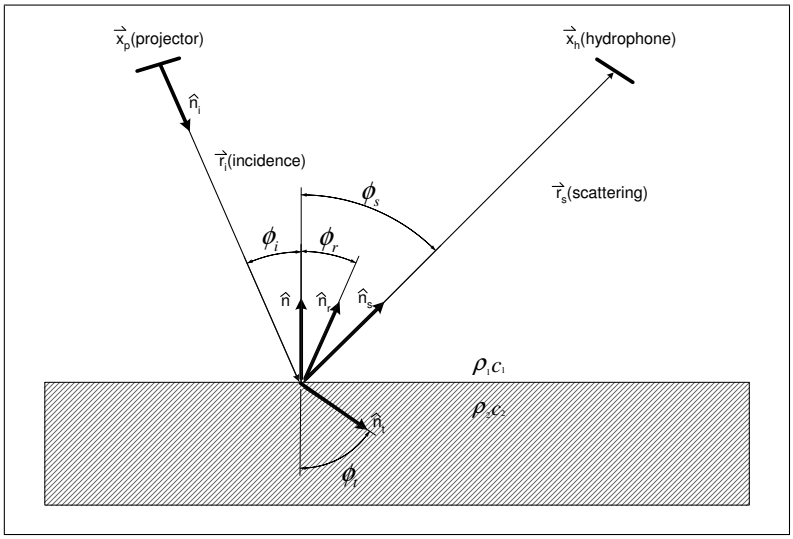

Figure 2.12: Two-dimensional representation of the transducer configuration.

determined by the Kirchhoff approximation is

$$\sigma = \frac{\mathscr{R}_{12}(\theta_{is})}{8\pi} \left(\frac{\Delta k^2}{\Delta K \Delta k_z} \right)^2 I_K, \tag{2.60}$$

where I_K is the Kirchhoff integral described by (2.65) through (2.67),

$$\theta_{is} = \arcsin \left(\frac{\Delta k}{2k_1} \right), \tag{2.61}$$

and $k_1 = 2\pi f/c_1$ is the wave number for the first medium, $\Delta k = |\Delta \vec{\boldsymbol{k}}|$ and $\Delta K = |\Delta \vec{\boldsymbol{K}}|$ are the magnitudes of the wave-number vectors. The wave number vectors are:

$$\begin{aligned} \Delta \vec{\boldsymbol{k}} &= \vec{\boldsymbol{k}}_s - \vec{\boldsymbol{k}}_i \qquad \text{and} \\ \Delta \vec{\boldsymbol{K}} &= \vec{\boldsymbol{K}}_s - \vec{\boldsymbol{K}}_i, \end{aligned} \tag{2.62}$$

and the wave number directional components are:

$$\begin{aligned} \Delta k_z &= k_{sz} - k_{iz} \qquad \text{and} \\ \Delta k^2 &= \Delta K^2 + \Delta k_z^2, \end{aligned} \tag{2.63}$$

where

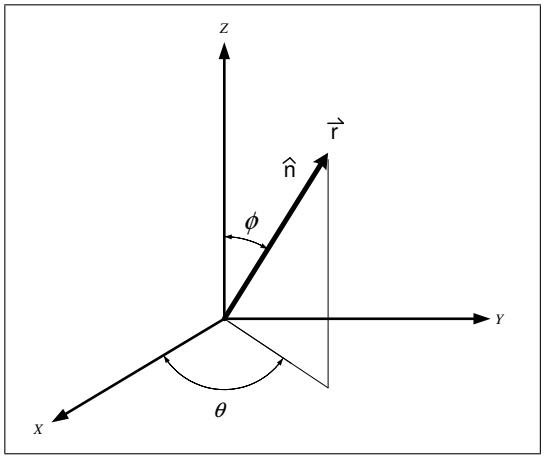

Figure 2.13: The unit normal $\widehat{\boldsymbol{n}}$ and vector $\vec{\boldsymbol{r}}$ with respect to angles θ and ϕ).

$$\begin{aligned} \vec{\boldsymbol{k}}_i &= k_1\big(\cos\theta_i \sin\phi_i\, \widehat{\boldsymbol{x}} + \sin\theta_i \sin\phi_i\, \widehat{\boldsymbol{y}} + \cos\theta_i\, \widehat{\boldsymbol{z}}\big), \\ \vec{\boldsymbol{k}}_s &= k_1\big(\cos\theta_s \sin\phi_s\, \widehat{\boldsymbol{x}} + \sin\theta_s \sin\phi_s\, \widehat{\boldsymbol{y}} + \cos\theta_s\, \widehat{\boldsymbol{z}}\big), \\ \vec{\boldsymbol{K}}_i &= k_1\big(\cos\theta_i \sin\phi_i\, \widehat{\boldsymbol{x}} + \sin\theta_i \sin\phi_i\, \widehat{\boldsymbol{y}}\big), \\ \vec{\boldsymbol{K}}_s &= k_1\big(\cos\theta_s \sin\phi_s\, \widehat{\boldsymbol{x}} + \sin\theta_s \sin\phi_s\, \widehat{\boldsymbol{y}}\big). \end{aligned} \tag{2.64}$$

The geometry of the incident angles, θ_i and ϕ_i, and scattering angles, θ_s and ϕ_s, are defined as shown in Figure 2.13. The Kirchhoff integral I_K for the general solution is

$$\begin{aligned} I_K = \frac{\Delta K^2}{2\pi} \iint \exp\Big[- j\Delta K \cdot \vec{\boldsymbol{R}}\Big] \\ \Big(\exp\Big[- 0.5\Delta k_z^2 S(\vec{\boldsymbol{R}})\Big] - \exp\Big[- \Delta k_z^2 h^2\Big] \Big) \mathrm{d}^2\vec{\boldsymbol{R}}, \end{aligned} \tag{2.65}$$

where h is the RMS interface roughness and $S(\vec{\boldsymbol{R}})$ is the structure function. If the seafloor is isotropic, i.e. has no directional ripples, then $S(\vec{\boldsymbol{R}})$ can be considered isotropic and (2.65) can be simplified to

$$I_K = \int_0^\infty J_0(u) \Bigg(\exp\Big[- 0.5\Delta k_z^2 S\Big(\frac{u}{\Delta K}\Big)\Big] - \exp\Big[- \Delta k_z^2 h^2\Big] \Bigg) u \, \mathrm{d}u, \tag{2.66}$$

where $J_0(u)$ is the zeroth-order Bessel function of the first kind. Equation (2.66)

can be further simplified, if $S(\vec{\boldsymbol{R}})$ is the power-law case, to

$$I_K = \int_0^\infty J_0(u)\left(\exp\left[-qu^{2\alpha}\right]\right)u\,\mathrm{d}u, \tag{2.67}$$

where

$$q = \frac{1}{2}C_h^2\Delta k_z^2\Delta K^{-2\alpha}. \tag{2.68}$$

The parameter α is the structure function exponent and C_h is the structure constant for the interface relief for power-law. These are given by

$$\alpha = \frac{\gamma_2}{2} - 1, \tag{2.69}$$

and

$$C_h^2 = \frac{2\pi\omega_2\Gamma(2-\alpha)2^{-2\alpha}}{\alpha(1-\alpha)\Gamma(1+\alpha)}, \tag{2.70}$$

where Γ is the gamma function, and ω_2 and γ_2 are the measured parameters of the spectral strength and the spectral exponent. Some typical measured values of γ_2 and ω_2 for sand and mud related to grain size are shown in Figure 2.14.

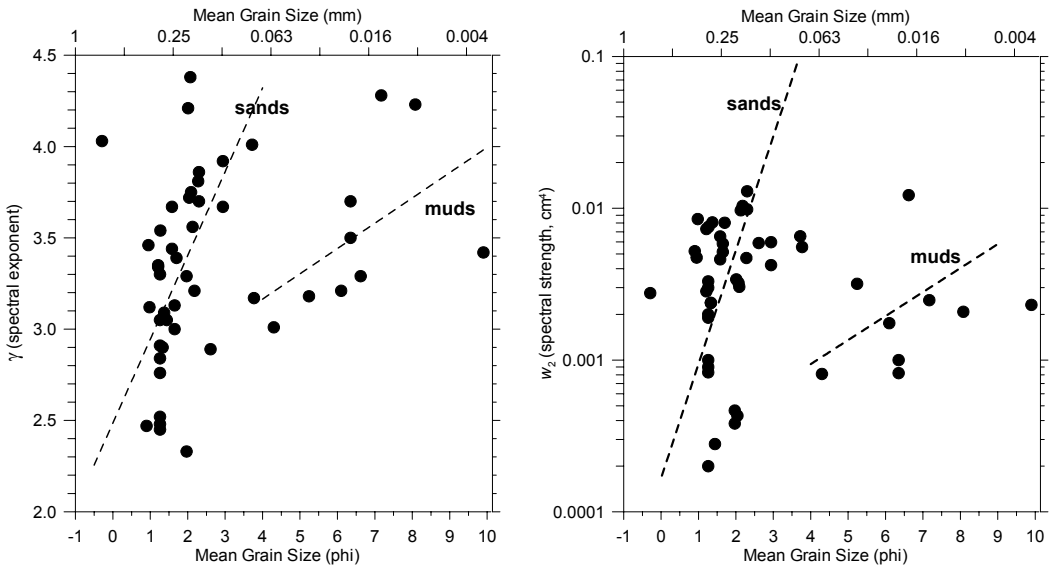

Figure 2.14: Plots of the 2-D seafloor roughness spectral exponent ($\gamma = \gamma_2$) and the spectral strength (ω_2) as a function of grain size. The units of grain size (phi) are $\log_2$(dia. in mm). These figures are from Briggs et al. [2005].

As shown in Figure 2.14, the correlation between grain size and the values of γ_2 and ω_2 are tenuous at best [Jackson and Richardson 2007, Briggs et al. 2001].

But there is a clustering of values based on material type, i.e., sand or mud [Jackson and Richardson 2007]. The power-law structural function γ_2 and ω_2 are discussed in more detail in Section 2.3.4.

2.3.3 Scattering area

In order to relate the proportionality factor σ to the scattered sound pressure the area A must be calculated as shown in (2.59). The size of the area is limited by factors such as: beam-pattern and pulse width. If the transmitted signal is monotonic then the limiting factor is the beam-pattern of the transducers. To include both the transmitted and received beam-patterns the following equations deal with transmitted and received, voltage signals rather than sound pressures. The mean square value of the received voltage for a monotonic signal is

$$< |V_{rr}(t)|^2 >= \frac{(s_0 s_r)^2 \exp[4k_w'' H]}{H^4} \iint \sigma(\phi_i, \phi_s) |b_r(\theta, \phi) b_x(\theta, \phi)|^2 \mathrm{d}^2 \vec{\boldsymbol{R}}, \qquad (2.71)$$

where $V_{rr}(t)$ is the voltage output of the receiver transducer related to the roughness scattering, k_w'' is the imaginary part of the water wave-number, ϕ_i and ϕ_s are the incident and scattering angles with respect to the z axis, θ is the azimuthal angle, s_0 is the RMS source pressure times range, s_r is the receiver sensitivity as a voltage/pressure ratio, H is the height of the transducers above the seafloor, $b_r(\theta, \phi)$ and $b_x(\theta, \phi)$ are the receiving and transmitting transducer beam-patterns, and $\vec{\boldsymbol{R}}$ is a two-dimensional horizontal position vector [Jackson and Richardson 2007].

The area insonified is limited by either the beam-pattern of the transducer or the pulse-width. If the pulse-width's spatial resolution, $\tau\, c_1$, where τ is the pulse-width, is the limiting factor then its effects must be added to (2.71). The mean squared value of the received, voltage including the pulse-width limitation, is

$$< |V_{rr}(t)|^2 >= \frac{(s_0 s_r)^2 \exp[4k_w'' H]}{H^4} \int_{-\pi}^{\pi} \int_{R_1}^{R_2} \sigma(\phi_i, \phi_s) |b_r(\theta, \phi) b_x(\theta, \phi)|^2 \vec{\boldsymbol{R}}\, \mathrm{d}\vec{\boldsymbol{R}}\, \mathrm{d}\theta, \qquad (2.72)$$

where R_1 and R_2 are the inner and outer radii of the insonified area. They are given by

$$R_1 = \left(\frac{R_0}{c_1} - \frac{\tau}{2} \right) c_1 \qquad (2.73)$$

and

$$R_2 = \left(\frac{R_0}{c_1} + \frac{\tau}{2} \right) c_1, \qquad (2.74)$$

where R_0 is the range at the centre of the insonified area [Jackson and Richardson 2007]. If the transducers are spherical, i.e., the beam-pattern can be assumed

to be $b_r(\theta,\phi) = b_x(\theta,\phi) = 1$, then (2.72) can be simplified to

$$< |V_{rr}(t)|^2 >= \frac{(s_0 s_r)^2 \exp[4k_w'' H]}{H^4} \int_{-\pi}^{\pi} \int_{R_1}^{R_2} \sigma(\phi_i, \phi_s) \vec{\boldsymbol{R}}\, \mathrm{d}\vec{\boldsymbol{R}}\, \mathrm{d}\theta. \tag{2.75}$$

The geometries for the mono-static and bi-static configurations are shown in Figures 2.15 and 2.16. Equation (2.75) can relate to the roughness scattering, for both configurations, to the output voltage of the receiver transducer. The equations governing the mono-static and bi-static configurations are given in Section 2.3.3.1 and Section 2.3.3.2. A comparison of the facet simulation of a power-law and the statistical analysis of the surface using (2.75) is presented in Section 4.5.1.

Several important aspects are unique to using a spherical transmitter and receiver. Firstly, independent of transducer orientation a directional surface will have a directional reflection, this is not true for directional transducers, this is because there is no beam-pattern to focus the sound waves in any one direction. Secondly, although the transducers still have beam-patterns, they are small enough to be ignored in some applications. However, this is not true in all cases. This is discussed in more detail in Section 3.1.3.

2.3.3.1 Mono-static geometry

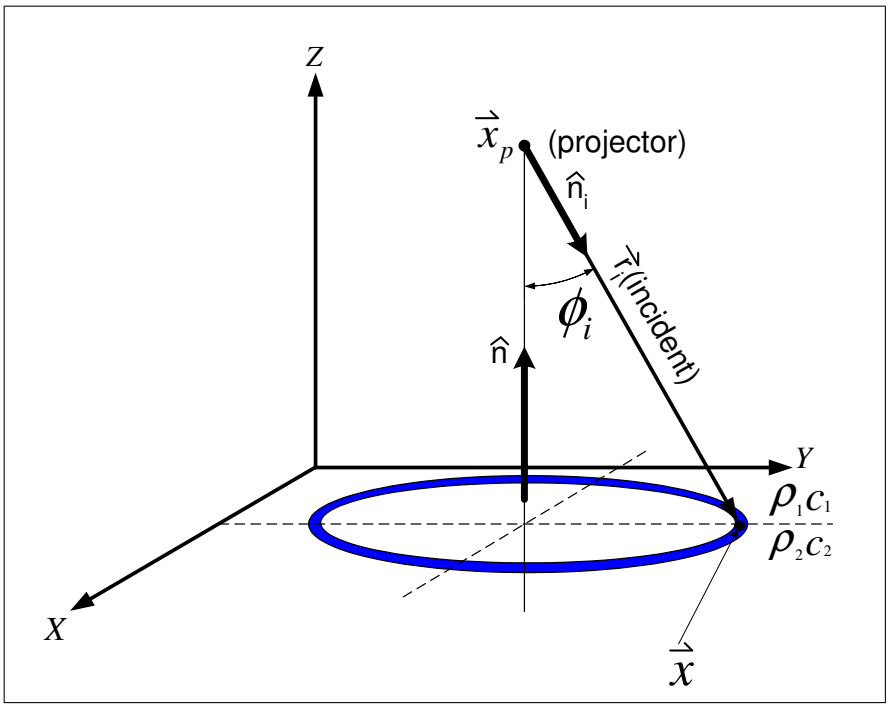

Figure 2.15: Mono-static scattering configuration.

The mono-static configuration has circular symmetry because the scattering area is a sphere intersecting a scattering surface that is assumed to be planar with

the transducer at the centre. Note for $2 < \gamma < 4$ the mono-static configuration does not require numeric integration of (2.67) as described by Mourad and Jackson [1989]. The geometry for the bi-static configuration is shown in Section 2.3.3.2. The relationship between x and y is dictated by the equation of a sphere

$$R = \sqrt{x^2 + y^2 + z^2} = \sqrt{x^2 + y^2 + H^2}. \tag{2.76}$$

Since the relationship between x and y has circular symmetry,

$$\phi = \phi_i = \phi_s = \tan^{-1}\left(\frac{H}{\sqrt{x^2 + y^2}}\right) \tag{2.77}$$

and

$$\theta = \tan^{-1}\left(\frac{y}{x}\right). \tag{2.78}$$

2.3.3.2 Bi-static geometry

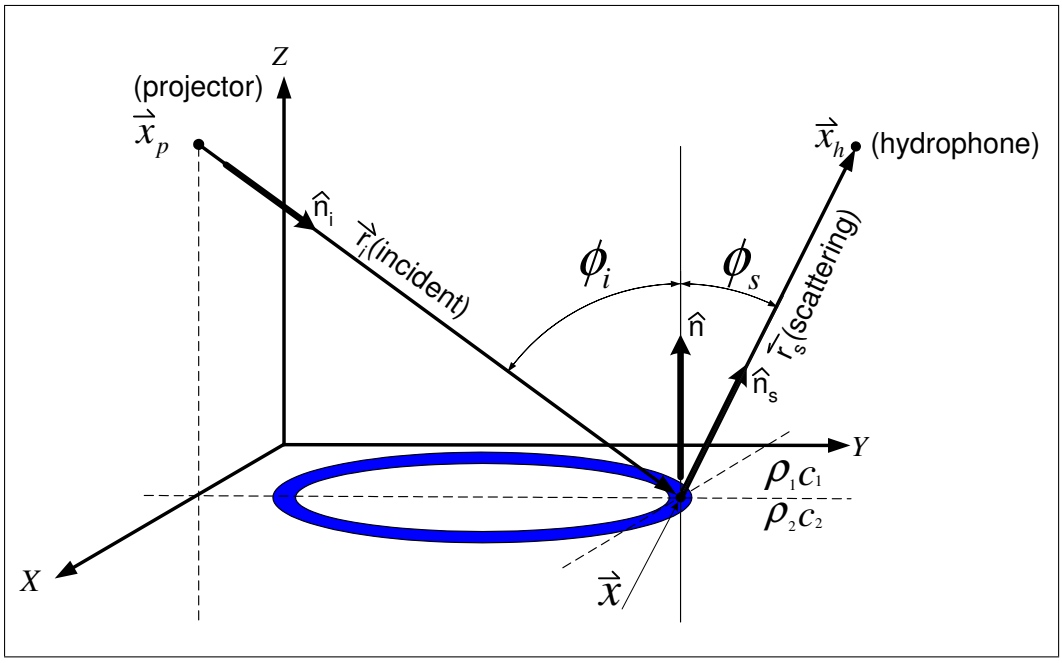

Figure 2.16: Bi-static scattering configuration.

The bi-static configuration does not have circular symmetry because the scattering area is an ellipsoid intersecting a scattering surface that is assumed to be planar with the two transducers at the foci. The bi-static geometry is shown in Figure 2.16. Unlike the mono-static configuration, the relationships between ϕ_i and ϕ_s with respect to θ are not independent. To allow elliptical symmetry, θ is assumed

to be measured with respect to the centre of the elipse and is given by

$$\theta = \tan^{-1}\left(\frac{y - \frac{S}{2}}{x}\right), \tag{2.79}$$

where S is the transducer separation. The projector is assumed to be at the origin, so the incident angle is

$$\phi_i = \tan^{-1}\left(\frac{H}{\sqrt{x^2 + y^2}}\right) \tag{2.80}$$

and the scattering angle is

$$\phi_s = \tan^{-1}\left(\frac{H}{\sqrt{x^2 + (y - S)^2}}\right), \tag{2.81}$$

with the hydrophone located on the x origin. The equation governing the relationship between x and y, with a set radius R and an intersecting plane at a depth of H is

$$\frac{x^2}{a^2} + \frac{y^2}{b^2} + \frac{z^2}{b^2} = \frac{x^2}{4R^2} + \frac{y^2}{4(R^2 - S^2)} + \frac{H^2}{4(R^2 - S^2)} = 1 \tag{2.82}$$

[Simmons 1975]. This equation can be factorised in terms of x and y:

$$x = \sqrt{\frac{R^2}{4} - \frac{y^2 R^2}{R^2 - S^2} - \frac{H^2 R^2}{R^2 - S^2}} \tag{2.83}$$

and

$$y = \sqrt{\frac{R^2 - S^2}{4} - \frac{x^2(R^2 - S^2)}{R^2} - H^2}. \tag{2.84}$$

Once (2.82) has been factorised then (2.83) and (2.84) can be used to numerically evaluate (2.71).

2.3.4 Power-law surfaces

The seafloor roughness statistics have been described in many different ways, ranging from Gaussian correlated to power-law [Jackson and Richardson 2007]. Gaussian statistics have been widely used to describe the seafloor for ease of the mathematical computations and because the experimental results have matched computational results [Jackson and Richardson 2007, Clay and Medwin 1977, Hunter 2006, Beckmann and Spizzichino 1963]. Detailed observations of the spatial spectrum of the seafloor, using various optical and acoustic methods, have shown that the seafloor can be more accurately described using the power-law spectral form [Jackson et al. 1996, Williams et al. 2002a, Lyons et al. 2002, Jackson and Richardson 2007]. For this reason the analysis and simulations assume a power-law spectrum unless otherwise stated.

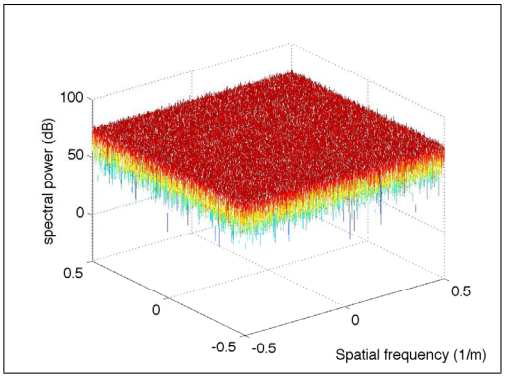

(a) Spectral power of Gaussian distributed random numbers generated with the randn function.

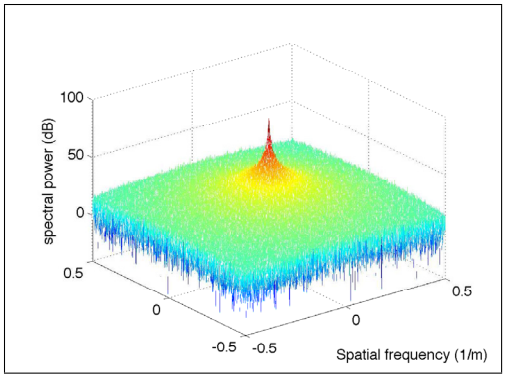

(b) Sprectral power of Gaussian distributed random numbers after they have been filtered by a 2-D 30 dB/decade spectral filter.

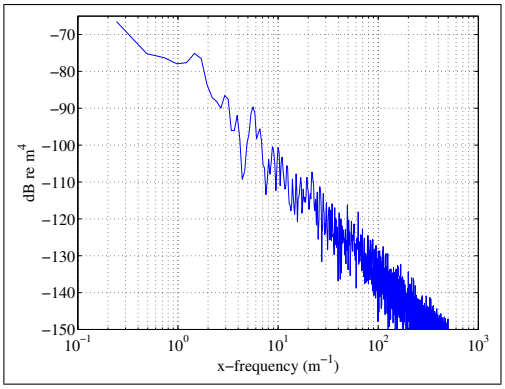

(c) The real part of the spectral power of a cross-section of the x-axis.

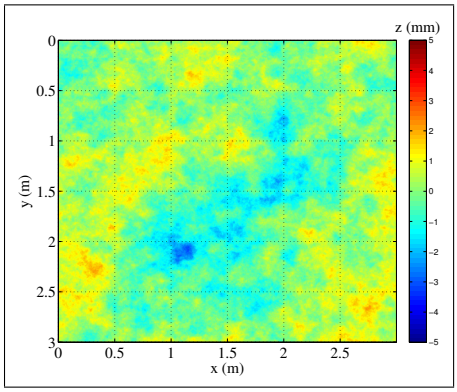

(d) The height map of a 3 m x 3 m power-law seafloor generated using this process.

Figure 2.17: A random power-law seafloor generated by filtering Gaussian distributed random numbers by 30 dB/decade using (2.87).

The power-law spectrum has a structure function of

$$S(\vec{\boldsymbol{R}}) = C_h^2 R^{2\alpha} \tag{2.85}$$

where $\vec{\boldsymbol{R}}$ is a two-dimensional "lag" vector, $R = |\vec{\boldsymbol{R}}|$ is the magnitude, α is the structure function exponent, and C_h is the structure constant described by (2.70) [Jackson and Richardson 2007]. The power-law spectrum of the structure function is

$$W(\vec{\boldsymbol{K}}) = \frac{\omega_2}{K^{\gamma_2}}, \tag{2.86}$$

where $\vec{\boldsymbol{K}} = (k_x, k_y)$ is a two-dimensional horizontal wave-number vector, $K = |\vec{\boldsymbol{K}}|$ is the magnitude of the wave-number vector, ω_2 is the spectral strength, and γ_2 is the spectral exponent. The power-law structure function parameters and the spectral structure function parameters are related by (2.69) and (2.70) in Section 2.3.2. The spectral exponent and spectral strength are measured parameters with some typical values shown in Figure 2.14.

Using typical values for γ_2 and ω_2, a simulated random seafloor can be generated as shown in Figure 2.17. The filter slope is 30 dB/decade, i.e., $\gamma_2 = 3$ and ω_2 was varied to compare the effects of different scaling factors. Note, the 30 dB/decade slope was chosen based on the work of Pouliquen and Lyons [2002] as a starting point. This surface was generated from a Gaussian random spectrum, shown in Figure 2.17 (a), filtered using a two-dimensional power-law slope, i.e., a cone shaped filter

$$W(\vec{\boldsymbol{K}}) = \frac{\omega_2}{(K^2 + 0.001^2)^{\gamma_2/2}}. \tag{2.87}$$

The resulting spectrum is shown in Figure 2.17 (b) and (c). Figure 2.17 (d) shows the resulting height map of a simulated power-law surface. This surface is not fully power-law due to limitations of the roll-off created by the filter roll-off, i.e., for $\gamma_2 = 1.5$ the denominator is $(K^2 + 0.001^2)^{1.5}$ rather than K^3. Equation (2.87) is know as the von Karman spectrum which sometimes used in scattering models [Jackson and Richardson 2007].

The low spatial frequency roll-off limitation is done for two reasons: firstly, to minimise slants and offsets of the surfaces; and secondly, to prevent infinite numbers when $K = 0$. The sample rate limitation is chosen due to the acoustic limitations of the frequency range of interest; this is covered in Section 2.2.4. These limitations should not affect the simulated surfaces since real seafloors have similar limitations. The slope of the spatial spectrum of real seafloors is dependent on many parameters: grain size of the sand, current, storms, plant life, and animal life [Jackson and Richardson 2007, Briggs et al. 2001, Pouliquen and Lyons 2002]. Briggs et al. [2001],

Jackson et al. [2009], and Gerig et al. [2009] showed that roughness of the seafloor has a large temporal component that in some cases is greater than the spatial component. This work consisted of a 30 day survey using both acoustic and visual verification of the spectrum. This work showed that storms and other hydrodynamic processes can generate directional ripples that are then eroded by animal activity. This dependence is verified by the work of Pouliquen and Lyons [2002] and also by a time-lapse video showing fish feeding causing the decay of the manmade ripples [Hay 2008].

The work presented in this thesis has eliminated the plant and animal dependence from the spatial spectrum by performing tests in a chlorinated test tank with 20 cm of beach sand on the bottom of the tank as described in Section 3.1. The ripples in the sand are generated both hydrodynamically and by raking the sand as described in Chapter 4. The spectrum of the sand is verified photo-grammetrically as described in Section 3.4. The results of this work are summarised in Chapter 5.

Chapter 3

TEST ENVIRONMENT AND HARDWARE

This chapter describes the test environment and the hardware used to make the empirical measurements of that environment. The sonar tank and the acoustic measurement methods are described in Section 3.1. The analysis of the acoustic properties of the floor of the sonar tank with and without sand as well as some of the spherical transducer measurement features are described in Section 3.2. The measurements of the sonar test tank were made both acoustically and optically. The acoustic system's hardware and software are described in Section 3.3 and, likewise, the hardware and software of the optical system are described in Section 3.4. This chapter provides a general overview of the test process and procedures. The full analysis of the acoustic and the optical test results are described in Chapter 4.

3.1 TANK SET-UP AND CONFIGURATION

The sonar test tank is a concrete water storage tank that has been in use at Canterbury University for nearly 40 years for various purposes. The tank is of concrete and rebar construction, sitting on a concrete pad, with a ladder and walkway on one side to allow access. The outside of the tank and walkway are pictured in Figure 3.1 (a). For reference, the front of the tank is the area closest to the walkway and the left side is assigned when facing the tank from the walkway. Figure 3.1 (b) shows the cross-section of the tank. Note that all features are symmetrical with the exceptions of the drain tap, 0.07 m from the bottom of the tank, and the overflow hole, 0.14 m from the top of the tank.

The transducers are held in the tank by a triangular frame shown in Figure 3.1 (c). Initially, PVC pipe was chosen for the frame since it is acoustically transparent. However, it was found that the PVC pipe or bubbles inside the pipe caused acoustic interference. To minimise these problems, the transducers are hung approximately 1 m below the frame by their cables, shown in Figure 3.1 (c). Their exact depth varies due to bowing of the transducer cables. The depth of the frame is controlled with a bolt and a chain, shown in Figure 3.1 (d). Each chain link provides 2.25 cm increments and allows all three adjustment points to be moved by

(a) Outside view of the sonar test tank.

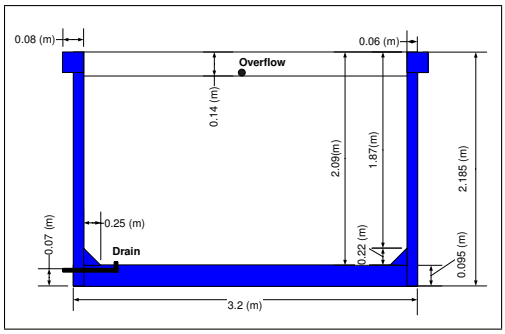

(b) Tank cross-section.

(c) Free hanging transducer configuration.

(d) Chain used to raise and lower transducers by increments of 2.25 cm.

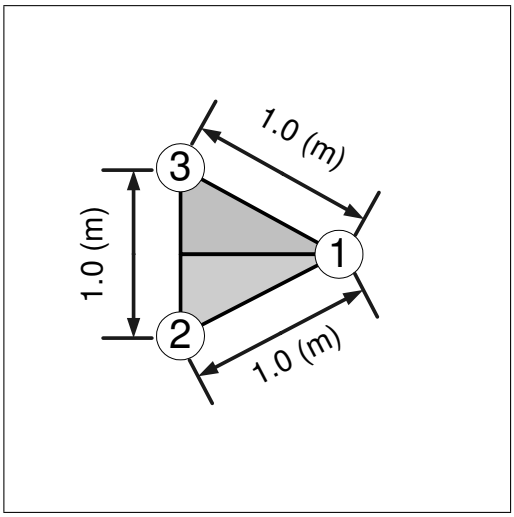

(e) Zoom view showing the transducer separation. All dimensions are ±3 cm.

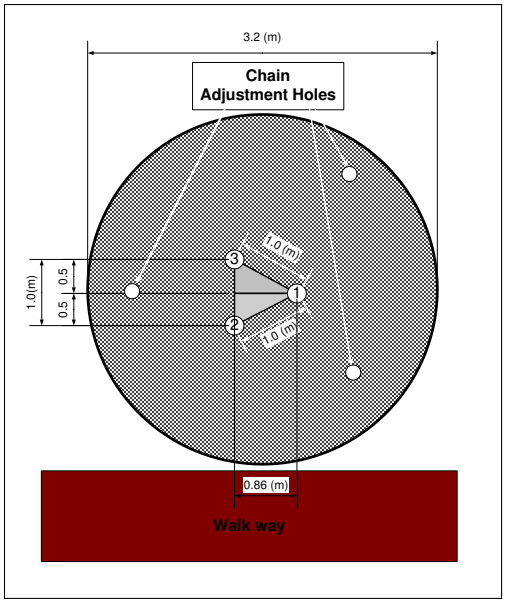

(f) Top view of the tank including the chain adjustment points and orientation of the transducers with respect to the walkway.

Figure 3.1: Tank set-up and orientation.

the same calibrated amount, shown in Figure 3.1 (f). To adjust the height of a single transducer with respect to the other two transducers requires an adjustment of all three chains. This is due to the mounting of the transducers in the triangular frame. Care must be taken not to twist the chain when raising or lowering a transducer otherwise height errors will occur. For this reason it was preferable to raise and lower a transducer in two link increments (approximately 5.49 cm). The transducers are 1 m ±3 cm apart, as shown in Figure 3.1 (c). The distance between the transducers can vary depending on how the cables hang, which can change over time. There are two transducers on the left side of the tank and one transducer on the right side shown in Figure 3.1 (f).

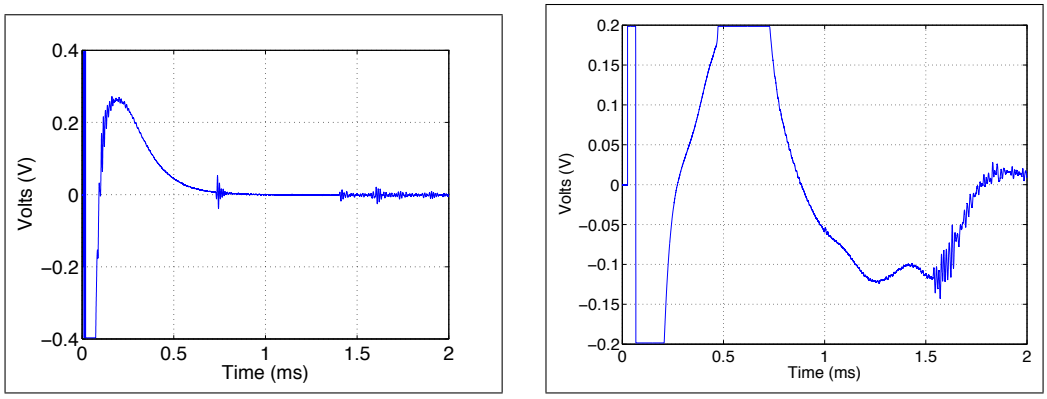

(a) The mono-static amplitude response for a short rectangular pulse 2.2 μs long.

(b) The mono-static amplitude response for a step input.

Figure 3.2: The mono-static system response for rectangular pulse and step inputs. The rectangular pulse and step waveforms were applied to the input of the power amplifier with the transducer 50 cm from the water's surface with the resulting acoustic responses shown in plots (a) and (b). Plot (b) clearly shows the step response is unsuitable for analysis of the mono-static return due to saturation. The reason for the saturation is not the transducer response but the electronic response. The design of the system, i.e., the TX/RX switch, power amplifier, and a pre-amplifier circuit, could have been changed to solve the saturation problem; however, it was unnecessary to change the design because this system worked with the rectangular pulse response. Note the acoustic hardware is described in more detail in Section 3.3. These plots are repeated in Figure 3.5 (a) and (b).

Each of the three transducers can both transmit and receive signals. The standard test involves transmitting on each transducer in turn and receiving on all three transducers. This produces three independent mono-static responses and six bi-static responses. Since reciprocity is assumed, there are two dependent realisations of three independent bi-static responses, i.e., transmitting on channel 1 and receiving on channel 2 (TX 1 RX 2) is equivalent to transmitting on channel 2 and receiving on channel 1 (TX 2 RX 1), after correcting for the differences of the individual channel's frequency response. The transmit signal is generated by

an arbitrary signal generator, discussed in Section 3.3.1. The broadest bandwidth signal possible can be achieved with either a step or impulse[1] excitation. Figure 3.2 shows the mono-static response of the step and impulse excitation.

The TX/RX switch causes a charge to remain on the transducer during the process of transmitting a waveform. Figure 3.2 (a) shows the charging and discharging process for the impulse excitation. It can be seen that the returns from the impulse excitation are much smaller than those from the step excitation but the exponential decay can be removed or filtered from the data. Figure 3.2 (b) shows the charging process for the step response. The discharging process completes about 300 ms later when the step response returns to zero. It can be seen from this figure that the step response is not suitable for analysing the tank bottom return at 0.600 ms, since the response is saturated.

3.1.1 Bi-static response

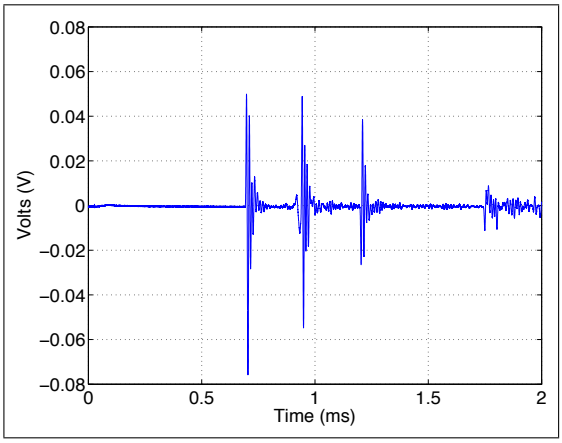

Figure 3.3: The bi-static step response at 47 cm from tank bottom, 66 cm from the water surface, and a 100 cm transducer separation. The direct path occurs at 0.667 ms, the bottom returns at 0.912 ms, the air surface returns at 1.172 ms, and the tank edge reflection at 1.749 ms. The TX is on channel 2, the RX is on channel 1, and the water depth is 113 cm.

The step excitation is used for the bulk of the calibration tests since it has a good signal level and provides the same information as the impulse excitation for all configurations except the mono-static. Figure 3.3 shows the raw bi-static response with the direct path at 0.667 ms, the bottom returns at 0.912 ms, the air return at 1.172 ms, and the tank edge at 1.725 ms. Ignoring the tank edge reflection, the direct path, bottom reflection, and air reflections can be windowed and examined separately. The impulse excitation can be examined by taking the derivative of the

[1] A rectangular pulse is used in place of true impulse excitation. The rectangular pulse is used because an impulse does not produce a large enough signal to be detected due to system bandwidth limitations.

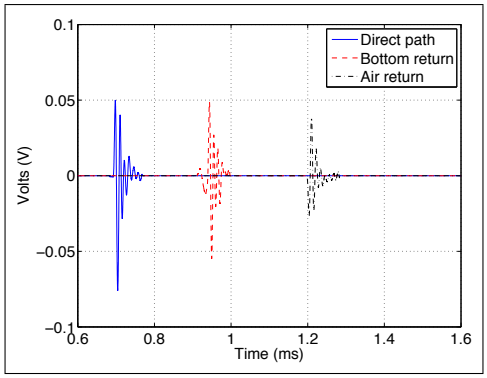

(a) The amplitude response, 47 cm from the tank bottom and 66 cm from the water surface. The direct path is shown at 0.667 ms, bottom return at 0.912 ms, and the air return at 1.172 ms.

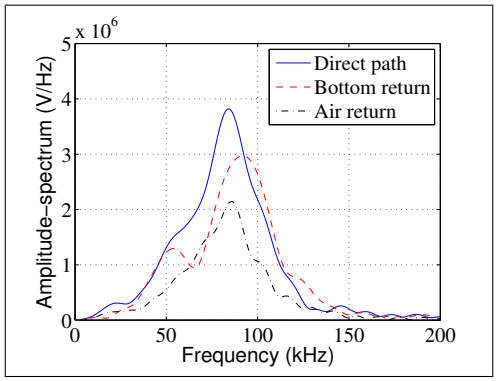

(b) Amplitude-spectrum of the three different returns shown in plot (a). Note this is a plot of the magnitude of the Fourier transform and not the power-spectrum.

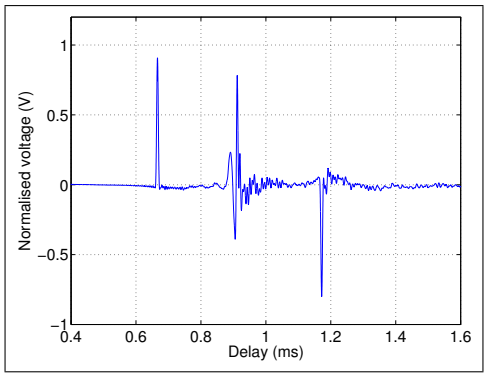

(c) Deconvolution of the transducer response at 47 cm from the tank bottom with the direct path at 0.667 ms, the bottom returns at 0.912 ms, and the air return at 1.172 ms.

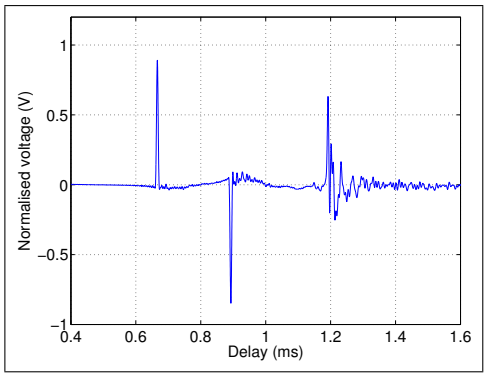

(d) Deconvolution of the transducer response at 75 cm from the tank bottom with the direct path at 0.667 ms, the bottom returns at 1.227 ms, and the air return at 0.873 ms.

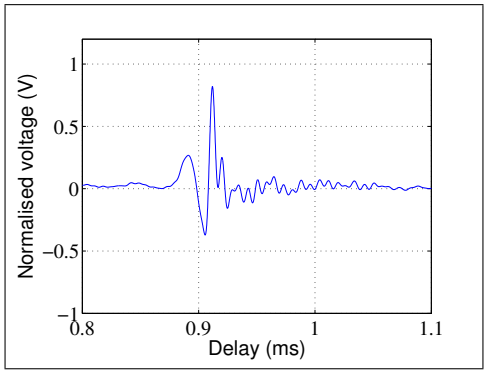

(e) Zoom showing only the deconvolved bottom return at 47 cm from the tank bottom, with the bottom returns at 0.912 ms, the first concrete/air return at 0.905 ms, the second concrete/air return at 0.916 ms, and the third concrete/air return at 0.925 ms.

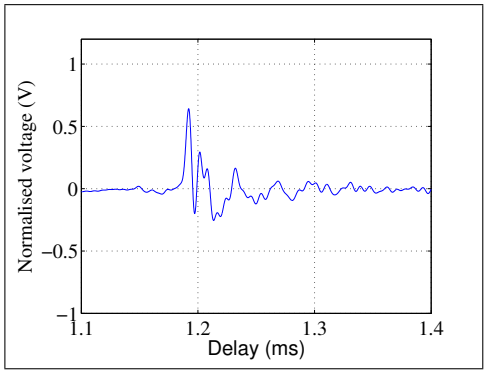

(f) Zoom showing only the deconvolved bottom return at 75 cm from the tank bottom, with the bottom returns at 1.227 ms, the first concrete/air return at 1.198 ms, the second concrete/air return at 1.213 ms, and the third concrete/air return at 1.243 ms.

Figure 3.4: Figures showing the different echo features for test tank with 1 m of water and no sand. Note the differences between figures (e) and (f) are due to multiple responses from the concrete due to head-waves or multiple internal reflections, as described in Section 3.2. The water fall plot shown in Figure 3.12 clearly shows the height dependance head-waves or multiple internal reflections. For clarity, plot (a) is repeated in Figure D.2.

step excitation. Figure 3.4 (a) shows the windowed signals and Figure 3.4 (b) shows the spectrum of each of the signals for a step excitation. Several things can be noted about the waveforms shown in Figure 3.4 (a). Firstly, the air return is inverted with respect to the direct path and secondly, the bottom return seems to have a preamble and some distortion at the end. Two observations can be made looking at the spectra shown in Figure 3.4 (b). Firstly, the air return and direct path spectra are nearly identical, apart from attenuation in the air return[2]. Secondly, the spectrum from the bottom return is different to that of the direct path. These differences are due to multiple responses from the concrete due to head-waves and to multiple internal reflections, as described in Section 3.2.

To better examine these responses, the signals can be deconvolved using a Wiener filter, defined as

$$H_w(f) = \frac{S^*(f)}{|S(f)|^2 + \frac{\Phi_n(f)}{\Phi_o(f)}}, \tag{3.1}$$

where $H_w(f)$ is the transfer function of the Wiener filter [Goodman 2005], $S(f)$ is the transfer function of the ideal waveform, $S^*(f)$ is the complex conjugate of $S(f)$, and $\Phi_n(f)/\Phi_o(f)$ describes the noise to the signal ratio, which is set to 10^{-9} for these experiments. When the spectrum of the ideal waveform is greater than $\Phi_n(f)/\Phi_o(f)$ then the spectrum is normalised. However if the spectrum of the ideal waveform is less than $\Phi_n(f)/\Phi_o(f)$ the spectrum is set to zero. The lower the noise is on the ideal waveform the smaller the $\Phi_n(f)/\Phi_o(f)$ can be thereby meaning less of the spectrum will be set to zero.

The ideal waveform is obtained by either using a signal generated from an air return or the direct path with the transducers at half depth in the tank, i.e., 1 m from any reflective surface. This signal is then averaged over 256 pings. This signal is time-windowed and modelled using MATLAB to generate a parametric model for the waveform using the matrix pencil method [Hua and Sarkar 1990]. The matrix pencil method models a waveform using a series of exponentially damped/undamped sinusoids but limits the number of terms to be used. By limiting the number of terms used the noise should be excluded from the model. The Wiener filter $H_w(f)$ generated from the ideal waveform can then be applied to other waveforms to produce deconvolved waveform. Figure 3.4 (c) shows the deconvolved waveform produced from the waveform in Figure 3.3 with a time varying gain applied.

3.1.2 Mono-static response

The mono-static response cannot use a step transmit waveform like the bi-static configuration. Instead, it uses a rectangular pulse 2.2 μs wide because the transducer

[2]The similarity between the air retrurn and direct path spectra was verified with the electronic data used to generate the figures.

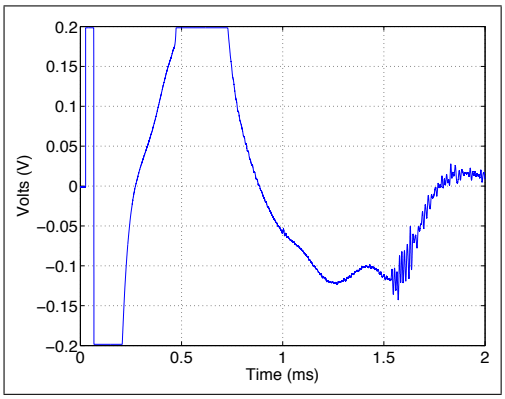

(a) The mono-static amplitude response for a step input.

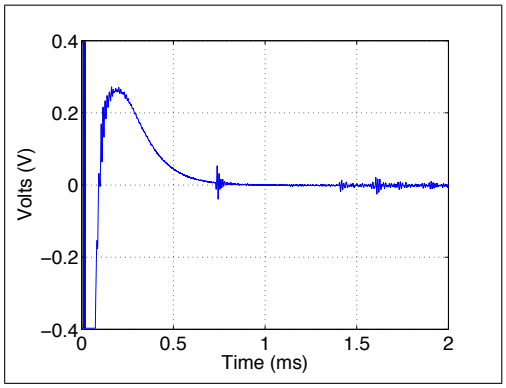

(b) The mono-static amplitude response for a 2.2 μs long pulse. The transducers are 50 cm from the water's surface. The air reflection is at 0.667 ms. The other reflections are from the PVC pipes and the tank edge.

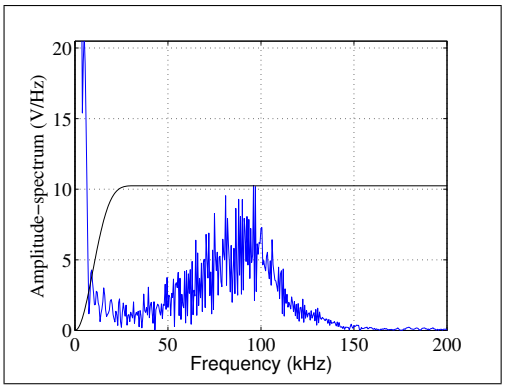

(c) The spectrum of the amplitude response, shown in (b), with the initial 0.2 ms windowed and the high-pass filter overlaid. The filter is a high-pass type 6 Harris window with a cut-off frequency of 15 kHz.

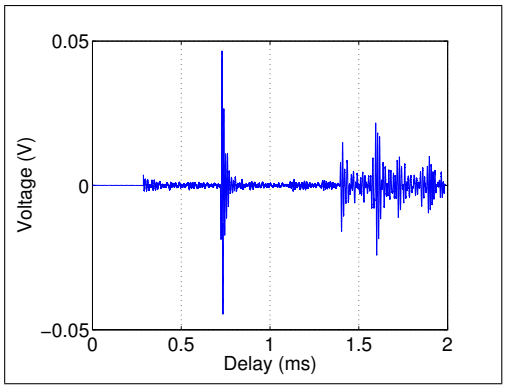

(d) The amplitude response of (b) after the filter has been applied.

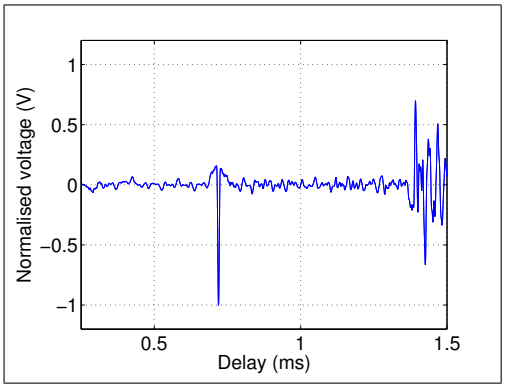

(e) Deconvolution of the transducer response at 50 cm from the water's surface with the air return at 0.667 ms.

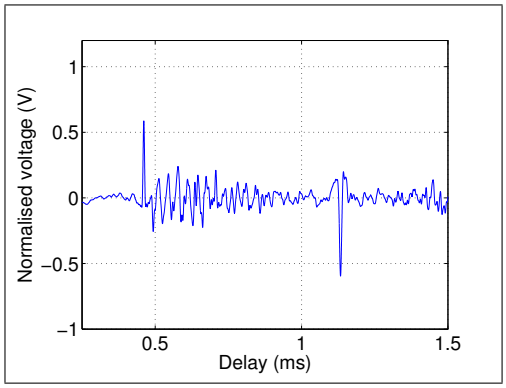

(f) Deconvolution of the transducer response at 34 cm from the tank bottom with the bottom returns at 0.460 ms.

Figure 3.5: The mono-static rectangular pulse responses for transducer 1. Plots (a) and (b) have been repeated from Figure 3.2 for clarity.

discharges too slowly and the data of interest cannot be observed due to saturation as shown in Figure 3.5(a). (Note the saturation occurs at the input diodes of the TX/RX switch, described in Section 3.3, therefore the surface responses cannot be recovered with signal processing.) The main advantage of the pulse excitation over the step excitation is that the mono-static responses can be analysed. The main disadvantage of the 2.2 μs rectangular pulse is that the signal levels are a quarter of the step excitation due to system bandwidth limitations.

When using a rectangular pulse input in a mono-static configuration the system is not in saturation therefore the decaying voltage charge from the transducer can be filtered out with a high pass filter. This is done by windowing out the first 200 μs and filtering the resulting spectrum using a type 6 Harris window. The equation of the Harris window is

$$w[n] = b_0 + b_1 \cos\left(\frac{2\,\pi\,n}{N-1}\right) + b_2 \cos\left(\frac{4\,\pi\,n}{N-1}\right) + b_3 \cos\left(\frac{6\,\pi\,n}{N-1}\right), \qquad (3.2)$$

where $b_0 = 0.355768$, $b_1 = 0.487396$, $b_2 = 0.144232$, and $b_3 = 0.012604$ for a type 6 Harris window, N is the number of sample points, and n is a sample point between 0 and $N-1$ [Ambardar 1999]. The Harris window is applied to the spectrum of the signal as shown in Figure 3.5 (c). The time domain signal resulting from this filtering process is shown in Figure 3.5 (d). This signal, with the exponential decay removed, can then be deconvolved using a Wiener filter as described in Section 3.1.1. The result of deconvolution of the signal shown in Figure 3.5 (c) is shown in Figure 3.5 (e).

As discussed in Section 3.1.1 a reference signal is necessary to deconvolve the response. With the bi-static response, the direct path can be used as the reference signal. In the mono-static configuration there is no direct path therefore the reference signal must be acquired in one of two different ways. Firstly, the transducers can be configured in a upward facing configuration and the air reflection off the surface of the tank can be used as the reference signal. Secondly, a calibration sphere can be lowered below the transducer and the signal it produces can be used as a reference signal, after its frequency response is compensated. Both of these methods require the configuration to be changed to acquire the reference signal and this can cause inaccuracies due to beam pattern issues, as discussed in Section 3.1.3. In this thesis, the air reflection method was used. This method was preferable because the air acts as a mirror with a phase inversion and unlike the calibration sphere no frequency compensation was required. Figure 3.5 (e) and (f) show the result of deconvolving the air reflection and the concrete reflection.

The mono-static configuration produces a simpler return than the bi-static return. The mono-static return is at the incident angle and therefore returns from the layers will occur in order of height. This is unlike the bi-static response, as discussed in Section 3.2, the head-wave or other acoustic paths can occur in an

order other than the height order. The main disadvantages of the mono-static over the bi-static configuration is that the reflection is only measured at the incident angle, this gives a nosier measurement due to reflections from the transducer cable as discussed in Appendix D.2.

3.1.3 Transducer beam-pattern issues

An ideal spherical transducer has no directionality, however in reality, the sensitivity of spherical transducers varies with both frequency and angle. The variation with angle is known as the beam-pattern and the variation with frequency is know as the frequency response. The calibration sheets for the ITC-1042 transducers used for the experiments[3] show a worst case beam pattern variation of -1.2 dB relative to the nominal, rotating the transducer in the xy axis. The transducers also have a 1.5 dB variation in the frequency response along the xy axis, e.g., for the ITC-1042 S/N 1414 at an xy angle of -90°, the attenuation is -0.04, -1.11, and -1.55 dB at 25, 75, and 100 kHz respectively. These differences in frequency response cause minor changes in the width and shape of the deconvolved air reflection over different angles. The calibration sheets provide no information about the transducer performance in the yz or xz planes. Figure 3.6 shows the bi-static transducer performance for the three transducer pairs. None of the transducers achieve exactly the same response for the direct path and the direct reflection. The best response for the direct reflection is an attenuation of -1.4 dB, poorer than the -1.2 dB performance shown in the calibration sheet. The transducer 3-1 pair has a significantly worse air return than for transducer pairs 1-2 and 3-2. This appears to be due to interference with the transducer cable. (Note the transducer cable cannot be easily replaced as it is moulded part of the transducer.) The transducer 3 cable has a kink in it that causes it to slope away from transducer 1. This means that the signal is attenuated for steep upward angles of the bi-static transducer 3-1 pair configuration because the transducer cable is in-between the transducer and the reflecting surface.

The normal transducer configuration has the transducer hanging by their cables 1 m below the PVC frame to avoid reflection from the frame, as discussed in Section 3.1. To test the performance of the transducers' beam-pattern, the transducers' cables were pulled until the transducers were flush with the PVC frame and rotated inwards by 90° with respect to the z axis, shown in Figure 3.7 (a). The results are shown in Figure 3.8. Figure 3.8 (b) shows the reflected signals for the transducers hanging 1 m below the PVC frame, shown in Figure 3.7 (b), with the air reflection coefficient equal to 0.83. Figure 3.8 (a) shows the reflected signals from the rotated transducer configuration, shown in Figure 3.7 (a). The air reflection coefficient is 1.0. The difference based on transducer orientation is 1.83 dB. This orientation variance accounts for the 1.83 dB difference between the air reflection

[3] S/N 1406, 1409, and 1396

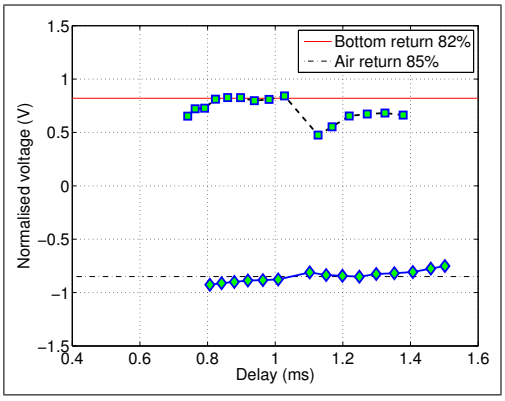

(a) Transducer TX channel 1 RX channel 2 concrete and air reflections.

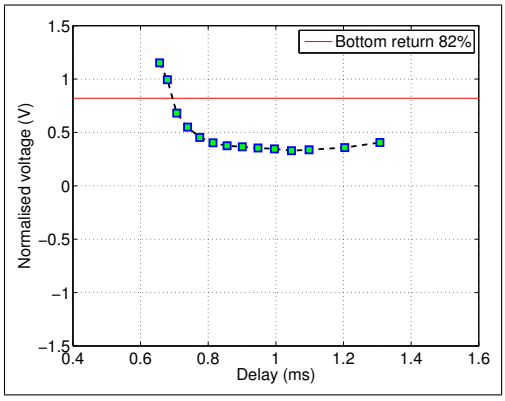

(b) Transducer TX channel 1 RX channel 2 sand reflection.

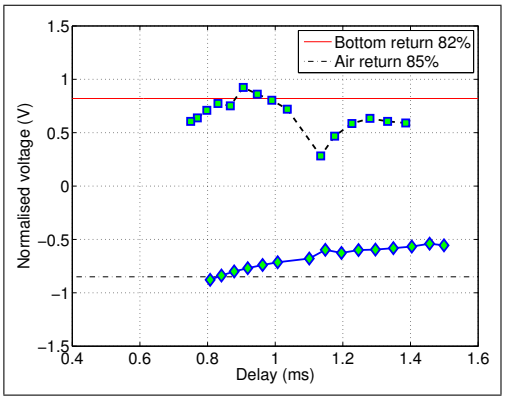

(c) Transducer TX channel 3 RX channel 1 concrete and air reflections.

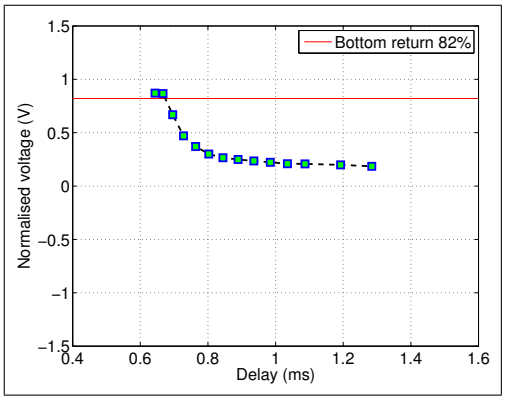

(d) Transducer TX channel 3 RX channel 1 sand reflection.

Figure 3.6: Bi-static transducer configuration with the depth from the bottom varied from 0.2 m to 0.87 m in 5.49 cm increments. These plots show the normalised peak reflection response so the effect of the changing depth and angle can be observed. The reflection coefficient from the water surface should ideally be -1 but the measured values varied between -0.6 and -0.95 depending on the height of the transducers off the reflective surface. If transducer orientation and position did not change the day to day variation was less than 1%. The differences between the ideal and measured air reflection values are due to transducer beam pattern effects as discussed in Section 3.1.3. The differences between ideal and measured concrete reflection values are due to beam pattern and multi-layer reflection, as discussed in Section 3.2.2. The resulting sand reflection is a combination of the beam pattern, the angle-dependent reflection coefficient and the surface roughness, as discussed in Section 4.4. Note the angles measured exceed the concrete's critical angle and the sand critical angle occurs at 65° or 0.65 ms. For clarity plots (a) and (b) are repeated in Figure D.1.

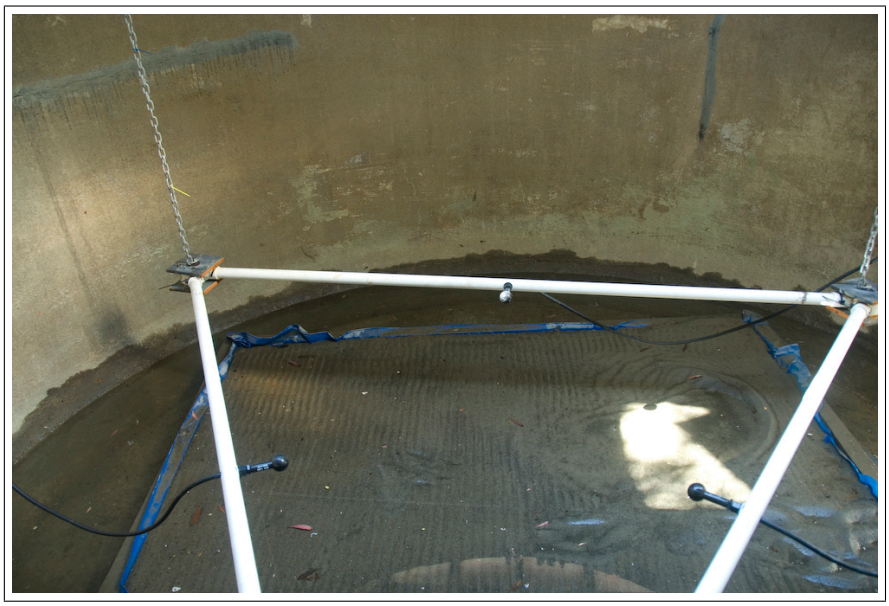

(a) The transducer rotated inwards by 90° from the free hanging configuration with the transducers pulled against the PVC frame.

(b) Free hanging transducer configuration, where transducer 1 is closest, 2 is to the right, and 3 is the farthest to the rear of the tank. Note that a kink in the transducer 3 cable can be seen, causing it to slope away from transducer 2.

Figure 3.7: Photos showing the transducers free hanging and rotated inwards by 90°.

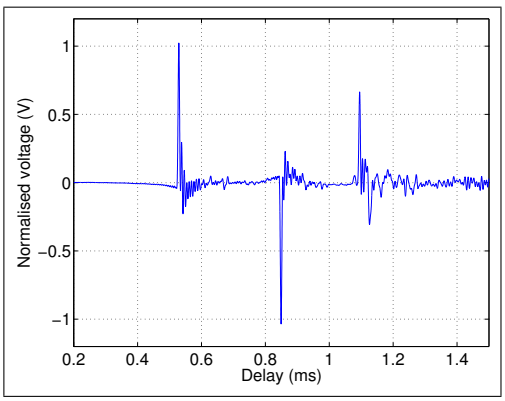

(a) Transducers held by the PVC frame rotated by 90° so that the transducers are pointed towards each other. The separation between the transducers is approximately 0.77 m, with an air reflection of -1.01.

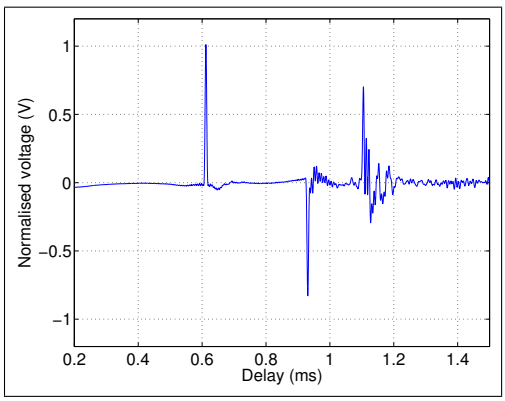

(b) Transducers hanging by cables with approximately 1 m separation between the transducers, with an air reflection of -0.82.

Figure 3.8: Figures showing that the amplitude of the signal received by the transducer varies by 1.83 dB when rotating the transducer about the z axis.

and the direct path seen on all three transducer pairs. This indicates that variations of up to 1.83 dB can occur based on the orientation of the transducers. These variations need to be taken into account when dealing with scattering surfaces where contributions to the received signals can be contrubuted from multiple sources at multiple angles at the same time. Figure 3.8 (a) also shows the effect of the PVC frame on the direct path. The direct path occurs at 0.529 ms, immediately followed by the interference created by the reflections from the PVC pipes.

The interference from the PVC pipe was found to degrade the deconvolved signal for the direct path and the direct reflection for some of the transducer pairs. The PVC pipe interference with respect to the direct reflection seems to be angle dependent. This is due to the PVC pipe acting as a cylindrical scatterer. With spherical transducers, as opposed to directional transducers, small changes to the test structure (cables, PVC frame, etc.) can make significant changes to the signals received. This is because with directional transducer the signal is not transmitted behind the transducer and the test set-up can be located there. Whereas, with spherical transducer in a mono-static configuration the signal is transmitted and received in all directions meaning there is no safe location for the test structure.

Three areas need to be monitored with the tests: firstly, the location and orientation of the cables; secondly, the rotation of the transducers, given that there can be up to a 1.83 dB change due to rotation of the transducers; thirdly, reflective objects in the water, such as the transducer frame. In addition to these beam-pattern issues, any object around the transducer, even the transducer cable, can be a source of interference. This interference problem can be dealt with by minimising the scatterers, directing the scatterers away from the area being imaged or by char-

acterising the scatterers. One method of directing the scattering surfaces away from the areas of interest was used by Cammin [2004]. This method can work in configurations where the transducers are directional, such as a bi-static spherical transducer configurations, but this method does not work well in a mono-static spherical transducer configurations. Since the configuration being used here supports simultaneous bi-static and mono-static acquisition, the methods used were to both minimise the scatterers and to characterise the ones that could not be removed.

To minimise the scatterers, the transducers were hung by their cables 1 m below the frame, i.e., at a maximum distance from all unwanted reflective surfaces/scatters. In the bi-static configuration, no interfering scatterers are produced, but the orientation of the cable can change over time due to bends in the cable as discussed in Appendix D.1. In the mono-static configuration, the cable produces a scatter that interferes with the bottom reflection as discussed in Appendix D.2. Note a rigid sleeve was add to the cable but was found to added interfering scatters to both bi-static and mono-static transducer configurations.

3.2 DIFFERENT PATHS

The different echo features of the bi-static configuration are shown in the deconvolved waveforms in Figure 3.9 (c) and (d). The bi-static transducer echo is made up of two main features: the direct path and the bottom reflection. Figure 3.9 (c) shows these features with the transducers at 30 cm above the tank bottom with the direct path at 0.600 ms and the tank bottom reflection at 0.752 ms. Figure 3.9 (d) shows these same features with the transducers at 50 cm above the tank bottom with the direct path still at 0.600 ms and the tank bottom reflection at 1.062 ms. The differences between the bottom reflection timing in Figure 3.9 (c) and (d) are due to the distances travelled and the sound speeds of the various media. The geometry of the transducers changes these distances and therefore the timings. The tank bottom reflection is made up of five features with different timings. These features are: the head-wave, the water concrete interface (or direct reflection), the concrete rebar interface, the concrete tank to the concrete pad interface, and the concrete pad to dry dirt interface (which behaves like an air interface because the dirt is not water saturated and has air in it.) The rebar for modern concrete tanks is a 15.5 x 15.5 cm mesh which is layered every 2.5 cm. However, it is unknown how the tank was constructed 40 years ago, hence information about the construction is only a guess. Furthermore, the rebar mesh is not necessarily flat, given that there are two places it can be seen protruding through concrete at the bottom of the tank.

The following theoretical timings are based on the physical measurements of the tank and concrete pad thickness and typical concrete sound speed estimates of between 3100 and 3600 $\mathrm{m\,s^{-1}}$ [www.engineeringtoolbox.com]. Figure 3.9 (c)

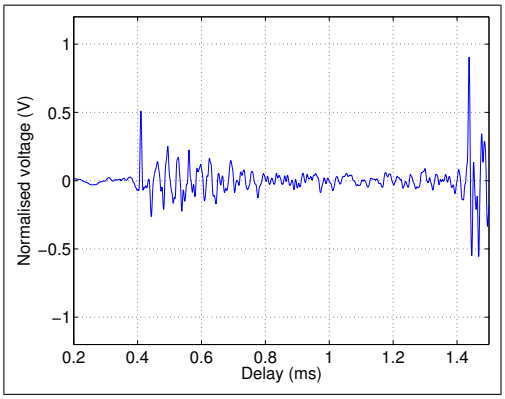

(a) Mono-static transducer response for channel 1 with the transducer 30 cm above the concrete.

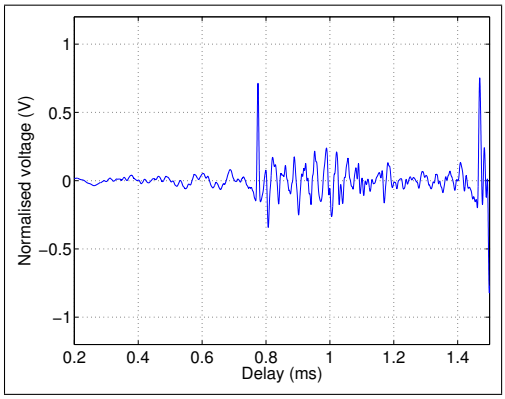

(b) Mono-static transducer response for channel 1 with the transducer 56 cm above the concrete.

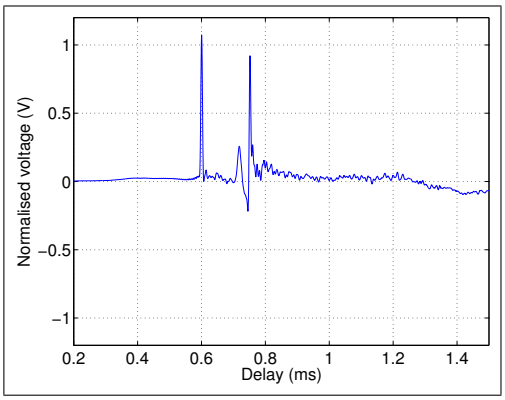

(c) Bi-static transducer response for TX on channel 1 and RX on channel 2 with a transducer separation of 91 cm and the transducers 30 cm above the concrete.

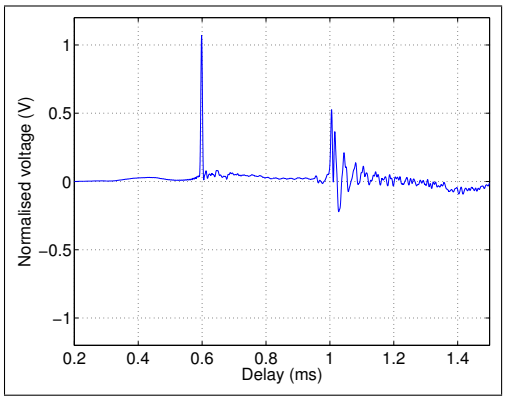

(d) Bi-static transducer response for TX on channel 1 and RX on channel 2 with a transducer separation of 91 cm and the transducers 56 cm above the concrete.

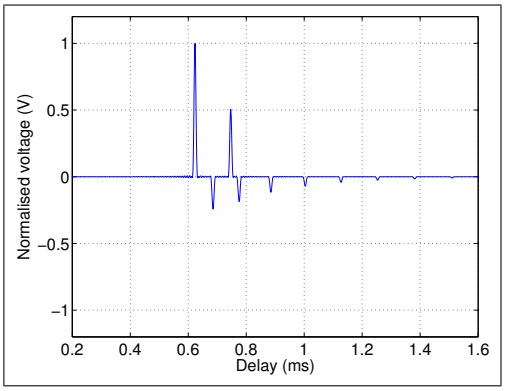

(e) Simulated bi-static transducer response for figure (c).

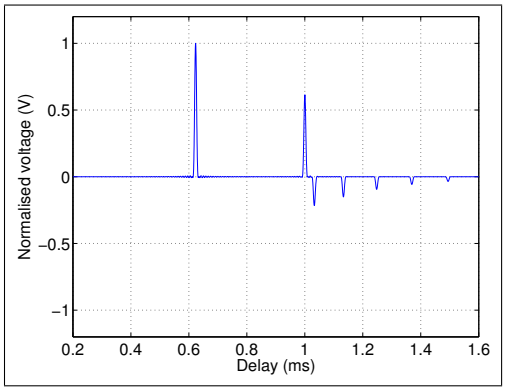

(f) Simulated bi-static transducer response for figure (d).

Figure 3.9: Empirical and simulated impulse responses for three layer reflections. The values for ρ are 1000, 2400, and 1 for water, concrete and air respectively. The values for c are 1462, 3300, and 340 for water, concrete, and air respectively. The transducer height values for the bi-static configuration are determined from the mono-static data shown in figures (a) and (b). The concrete sound speed is also determined from the mono-static data using the measured thickness of the concrete, which is 22.5 cm.

shows the bottom return with the transducers 30 cm above the tank bottom. The first small peak at 0.689 ms is the head-wave, the second peak at 0.718 ms is from the concrete-tank/concrete-pad return, the first negative peak at 0.745 ms is the concrete-pad/dirt return, the third positive peak at 0.752 ms is the concrete/water return followed by scattered returns from the corners of rebar embedded in the concrete and additional echoes from inside the concrete. Note the additional echoes from inside the concrete occur until the end of the trace and are due to multiple internal reflections. Figure 3.9 (d) shows the bottom returns with the transducers 50 cm above the tank bottom. Note the timings have changed. The first return is still the head-wave at 1.235 ms but it is now followed by the tank/water return at 1.255 ms. The returns from concrete-tank/concrete-pad at 1.212 ms and the concrete/dirt at 1.284 ms now follow the concrete/air return. Note due to the geometry of the test set-up these returns are not separated well enough to recognise the sources of all the individual responses.

Although there are many different responses, the timings of the responses can be grouped into three categories: direct path and direct reflection, head-wave, and multi-layer reflection. The rebar/concrete and concrete/air returns are in the multi-layer reflection timings category. The water/concrete return fits into the category of the direct reflection timings. The calculations for the different timings are covered in the following sections: the direct path and the direct reflection timings are described in Section 3.2.1; the head-wave timings are described in Section 3.2.1.1; and the multi-layer reflections timings are described in Section 3.2.2.

3.2.1 Direct path and direct reflection timings

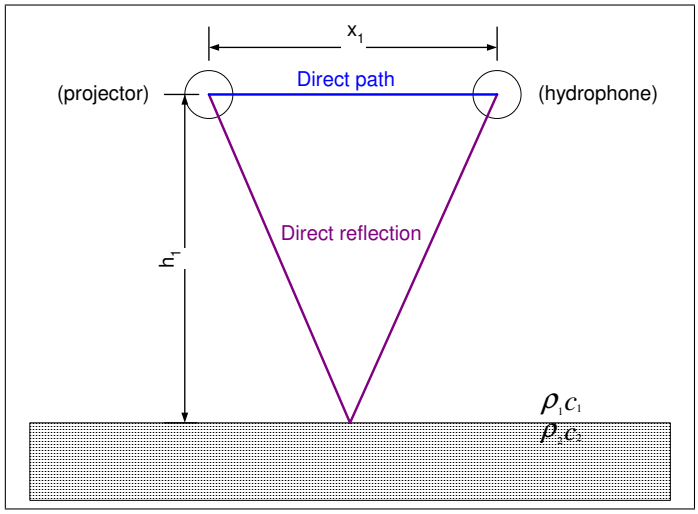

Figure 3.10: Geometry for the direct path and direct reflection. Note this figure is repeated for clarity in Figure 4.1 (a)

The direct path is the path directly between the transducers. The only

effects on the signal are spreading loss and the transducer beam-pattern. The timing for the direct path τ_d is

$$\tau_d = \frac{x_1}{c_1}, \tag{3.3}$$

where c_1 is the speed of sound in the first media and x_1 is the separation between the transducers shown in Figure 3.10. If x_1 and the temperature of the water are known then the speed of sound measurement can be verified using the following equation, which relates the speed of sound to depth, temperature, and salinity as presented by Clay and Medwin [1977],

$$c_w = 1449.2 - 4.6\,T - 0.055\,T^2 + (1.34 - 0.010\,T)(S_w - 35) + 0.016\,Z, \tag{3.4}$$

where c_w ($\mathrm{m\,s^{-1}}$) is the speed of sound in water, S_w is the salinity (ppt), T ($^\circ$ C) is the temperature, and Z (m) is the depth. For the tests performed in the sonar tank, the contribution of the the depth and salinity were found to be negligible.

The direct reflection is the simple two layer reflection as discussed in section Section C.2. The reflection coefficient is -1 for the air/water interface and is between 0.6 and 1 for the concrete/water interface depending on the angle, as described by (C.14). The timing for the direct reflection τ_r is

$$\tau_r = 2\frac{\sqrt{h_1^2 + \left(\frac{x_1}{2}\right)^2}}{c_1} \tag{3.5}$$

where h_1 is the transducer height above the reflecting surface shown in Figure 3.10 [Clay and Medwin 1977].

3.2.1.1 Head-wave timings

A head-wave enters the second medium from the first medium at the critical angle ϕ_c and travels along second medium at its speed speed c_2, as the head-wave travels along second medium interface it reradiates into into the first medium at the critical angle [Brekhovskikh and Lysanov 2003]. The geometry of this interface is shown in Figure 3.11. The critical angle ϕ_c is

$$\phi_c = \arcsin\left(\frac{c_1}{c_2}\right) \tag{3.6}$$

where c_1 and c_2 are the sound speeds in the respective media shown in Figure 3.11. In certain geometries the head-wave will arrive at the hydrophone significantly before the direct reflection. For Head-waves to be received by the hydrophone the sound wave must be transmitted and received at the critical angle. This condition occurs for a direction transducer only when the geometry, i.e., beam-pattern, does not

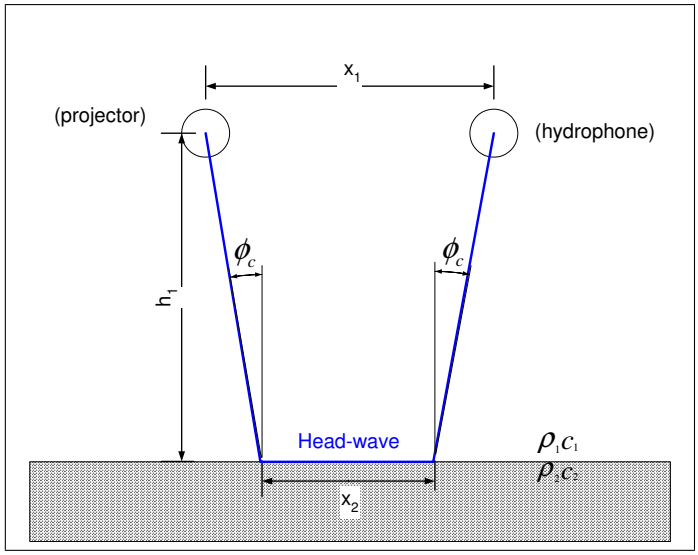

Figure 3.11: Geometry for the head-wave (lateral-wave) with distances defined.

obscure it. Whereas with spherical transducers the head-wave can can be received by the hydrophone as long as there is a critical angle and x_2 is greater than zero. The time delay for a head-wave τ_h is

$$\tau_h = \begin{cases} \frac{2\,h_1}{c_1\,\cos\phi_c} + \frac{x_1 - 2\,h_1\tan\phi_c}{c_2} \\ \\ \frac{2\,h_1\cos\phi_c}{c_1} + \frac{x_1}{c_2} \qquad \text{for} \quad x_1 > \frac{2\,h_1}{c_1\tan\phi_c}, \end{cases} \tag{3.7}$$

where h_1 is the transducer height above the reflecting surface and x_1 is the separation between the transducers shown in Figure 3.11. From Brekhovskikh and Lysanov [2003], the equation for the sound pressure for a monotonic head-wave p_{hw} is

$$p_{hw} = \frac{f\rho_1 p_0\, n}{k_1\, m\,(1-n^2)x_1^{1/2}\,x_2^{3/2}} \exp\left[j\Big(k_2\,x_1 + k_1(1-n^2)^{1/2}\,(2\,h_1)\Big)\right] \exp[-j2\pi ft] \tag{3.8}$$

where x_2 is the distance travelled in the second medium,

$$m = \frac{\rho_2}{\rho_1}, \tag{3.9}$$

and

$$n = \frac{k_2}{k_1}. \tag{3.10}$$

Using (3.7) and (3.8) the timing and amplitude of the head-waves can be verified for concrete. The timings for the head-waves for Figure 3.9 (c) and (d) are estimated to be 0.752 ms and 1.235 ms respectively, with a range and amplitude normalised

value of 0.05, i.e., 100% reflection will give a value of 1.00 independent of range. Although the head-wave can be detected, calculated, and modelled for a perfectly smooth surface, its amplitude is too small to be detected with surface roughness. For this reason the presence of the head-wave is acknowledged but is insignificant compared to the other signals of interest.

3.2.2 Multi-layer reflection timings

The angles that multi-layer reflections occur at are governed by the refractive indexes of the media involved. Like head-waves, multi-layer reflections occur with directional transducers but are unlikely to be detected in the same configuration as the direct reflection. This is because in most geometries the beam-pattern of directional transducers obscures either the multi-layer reflections or the direct reflection. However, spherical transducers do not have a beam-pattern to obscure either the multi-layer reflections or the direct reflection. The waves will only penetrate the concrete when $\phi_1 < \phi_c$, where ϕ_i is the angle of incidence shown in Figure 3.13 (a) and (b), and ϕ_c is the critical angle given by (3.6). To determine the timing for the reflection off the second interface, the distance L_{x1} and angles ϕ_1 and ϕ_2 must be solved by knowing h_1, h_2, and x as defined in Figure 3.13 (a). The relationship between the angles, defined by Snell's law, is

$$\frac{\sin\phi_2}{c_2} = \frac{\sin\phi_1}{c_1}, \tag{3.11}$$

where c_1 and c_2 are the sound speeds in their respective media, ϕ_1 and ϕ_2 are the angles of incidence and transmission, respectively. These parameters are defined in Figure 3.13 (a) and (b). Using simple trigonometry, x_2 can be expressed as

$$x_2 = x_1 - 2h_1 \tan\phi_1 = x_1 - 2h_1 \frac{\sin\phi_1}{\sqrt{1-\sin^2\phi_1}}, \tag{3.12}$$

where x_1 is the separation between transducers, and h_1 is the height of the transducers above the first interface (this assumes the transducers are level with respect to the first interface.) Note that $\tan\phi_1$ is expressed in terms of $\sin\phi_1$ to enable further simplification of the equations. An alternate expression for x_2 using trigonometry is

$$x_2 = 2\,h_2\,\tan\phi_2 = 2\,h_2\,\frac{\sin\phi_2}{\sqrt{1-\sin^2\phi_2}}, \tag{3.13}$$

where h_2 is the thickness of the interface. Substituting (3.11) into (3.13) gives

$$x_2 = 2h_2 \frac{\frac{c_2}{c_1}\sin\phi_1}{\sqrt{1-\left(\frac{c_2}{c_1}\right)^2 \sin^2\phi_1}}. \tag{3.14}$$

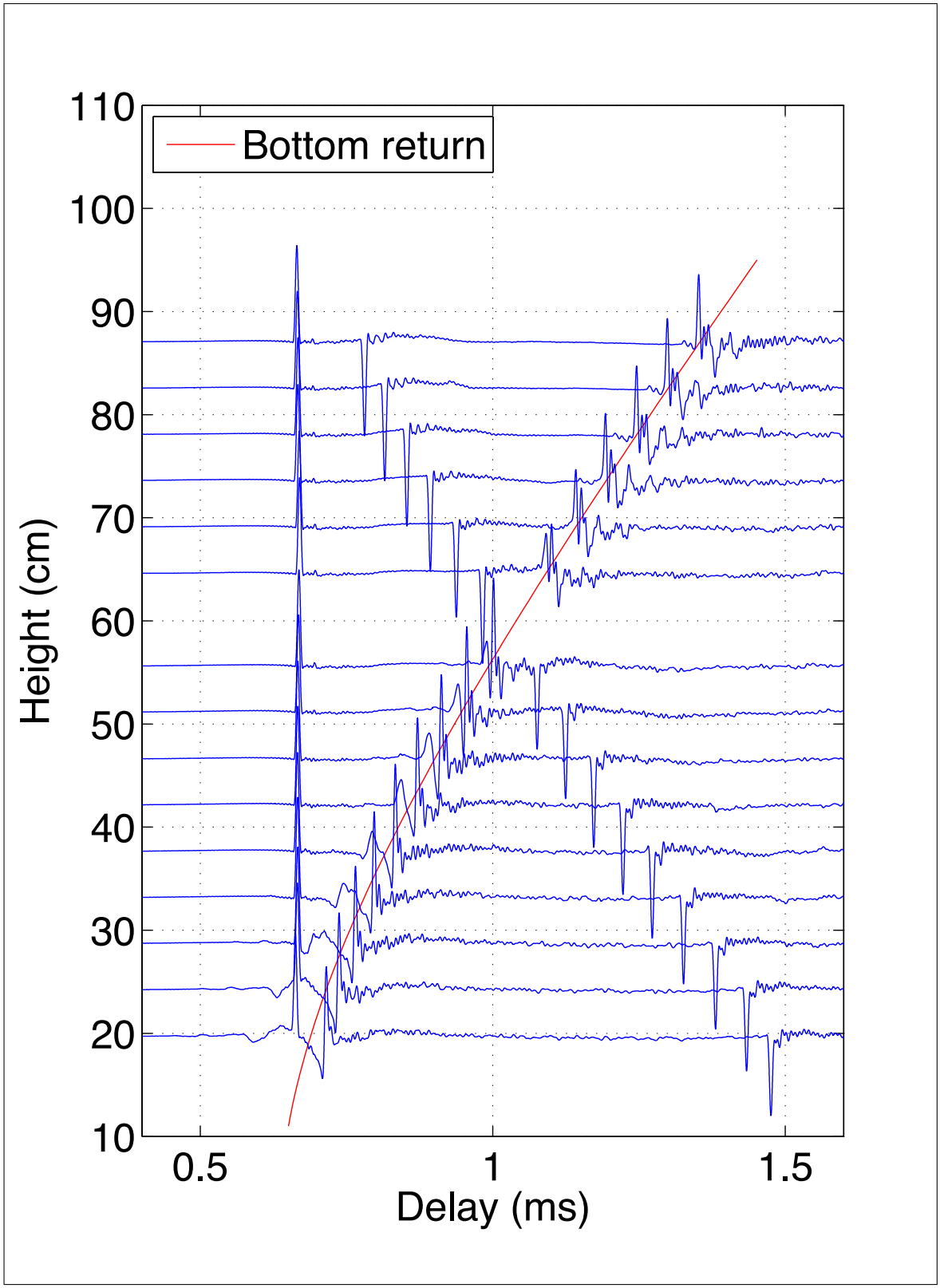

Figure 3.12: Deconvolution of the transducer response for three interface layers made up of water, concrete and air. The TX is on channel 1 and the RX is on channel 2. The height above the concrete was measured between 20 to 87 cm in 4.5 cm increments excluding the 60 cm measurement. Note the curved line is indicating the theoretical timing for the direct reflection from the water/concrete interface based on the transducer separation and height of the transducers above the concrete.

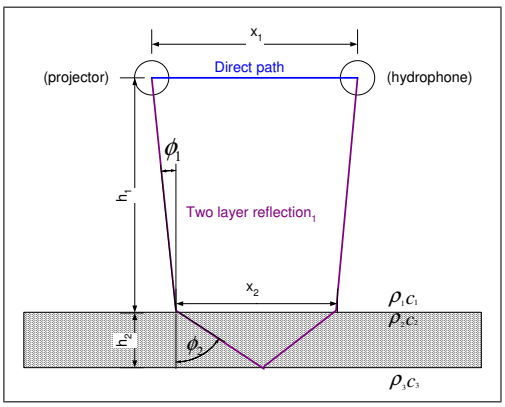

(a) Geometry for the bottom reflection off the concrete/air interface with a single reflection bounce. x_2 is the x component of the length that the wave has travelled in the concrete.

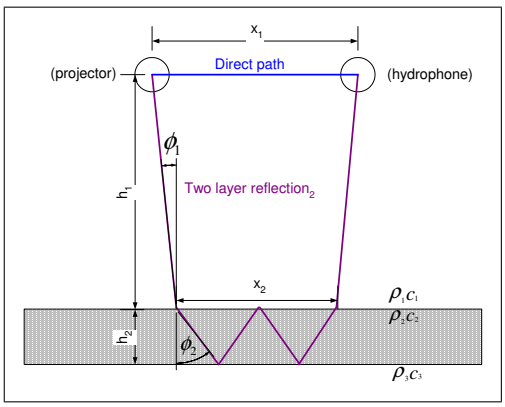

(b) Geometry for the bottom reflection off the concrete/air interface with three reflection bounces. x_2 is the x component of the length that the wave has travelled in the concrete.

Figure 3.13: Geometry for the bottom reflection off the concrete/air interface where x_1 is the distance between the transducer, h_1 is the height of the transducer above the concrete, and h_2 is the thickness of the concrete. Note these figures are repeated for clarity in Figure 4.1 (b) and (c)

Equating (3.12) and (3.14) gives

$$x_1 - 2h_1 \frac{\sin\phi_1}{\sqrt{1-\sin^2\phi_1}} = 2h_2 \frac{\frac{c_2}{c_1}\sin\phi_1}{\sqrt{1-\left(\frac{c_2}{c_1}\right)^2 \sin^2\phi_1}}, \tag{3.15}$$

The roots for this equation are not straightforward so the simplest way to solve for ϕ_1 is to use MATLAB to search where (3.15) is satisfied. Equation (3.15) only solves for the first reflection. Additional reflections can occur when there are multiple bounces off the interface between layers 2 and 3, or the 2-3 interface. The geometry for two bounces off the 2-3 interface is shown in Figure 3.13 (b). For two bounces the geometry will be the same as the one bounce configuration, shown in Figure 3.13 (b), with h_2 doubled. The simplest way to calculate the distances for multiple bounces is to increase h_2 by the number of bounces at the 2-3 interface resulting in

$$x_1 - 2h_1 \frac{\sin\phi_1}{\sqrt{1-\sin^2\phi_1}} = 2\,n\,h_2 \frac{\frac{c_2}{c_1}\sin\phi_1}{\sqrt{1-\left(\frac{c_2}{c_1}\right)^2 \sin^2\phi_1}}, \tag{3.16}$$

where n is the number of 2-3 interface bounces. The time delay for the multi-layer reflection is

$$\tau_{ml} = \frac{L_1}{c_1} + \frac{L_2}{c_2}, \tag{3.17}$$

where L_1 is the distance travelled in the first medium,

$$L_1 = 2\sqrt{h_1^2 + \left(\frac{x - 2\,n\,h_2\tan(\phi_2)}{2}\right)^2}, \tag{3.18}$$

L_2 is the distance travelled in the second medium,

$$L_2 = 2\sqrt{(n\,h_2)^2 + \left(\frac{(2\,n\,h_2\tan(\phi_2)}{2}\right)^2}, \tag{3.19}$$

and ϕ_2 is defined by (3.11). The signal is attenuated by the spreading loss proportional to L and the reflection coefficient. The attenuation is

$$A = L^{-1}\,\mathscr{R} \tag{3.20}$$

where L^{-1} is the spreading loss,

$$L = L_1 + L_2, \tag{3.21}$$

and $\mathscr{R}$ is the total reflection coefficient of all the reflections and transmissions

$$\mathscr{R} = \mathscr{T}_{12}\,\mathscr{T}_{21}\,\mathscr{R}_{23}^{n}\,\mathscr{R}_{21}^{(n-1)}, \tag{3.22}$$

where $\mathscr{R}_{21}$ and $\mathscr{R}_{23}$ are the reflection coefficients and $\mathscr{T}_{12}$ and $\mathscr{T}_{21}$ are the transmission coefficients for the various media. The equations for the reflection and transmission coefficients are defined by (C.14) and (C.18) respectively. Table 3.2 shows a comparison between the empirical and the experimental results. Figure 3.12 shows the trend of the waveform features as the height is changed.

3.2.2.1 Four layer

To determine the timing for the reflection off the second interface, the distances x_2, x_3 and angles ϕ_1, ϕ_2 and ϕ_3 must be solved by knowing h_1, h_2, h_3, and x as defined in Figure 3.16. The relationship between the angles, defined by Snell's law, is

$$\frac{\sin\phi_2}{c_2} = \frac{\sin\phi_3}{c_3} = \frac{\sin\phi_1}{c_1}, \tag{3.23}$$

where c_1, c_2 and c_3 are the sound speeds in their respective media, ϕ_1, ϕ_2 and ϕ_3 are the angles of incidence and transmission as defined in (3.23). These parameters are defined in Figure 3.16. Using simple trigonometry, x_2 can be expressed as

$$x_2 = x_1 - 2h_1\tan\phi_1, \tag{3.24}$$

Data source		Figure 3.9 (a)	Figure 3.9 (b)
Interface	Name	Measured 1	Measured 2
air/concrete	h_2	0.220 m	0.220 m
water/concrete	τ_{hl}	0.411 ms	0.782 ms
water/concrete	$\mathscr{R}$	0.52	0.70
concrete/air	τ_{h2}	0.544 ms	0.724 ms
concrete/air	$\mathscr{R}$	-0.21	-0.20
water	ρ_1	1000 $\mathrm{kg\,m^{-3}}$	1000 $\mathrm{kg\,m^{-3}}$
concrete	ρ_2	2400 $\mathrm{kg\,m^{-3}}$	2400 $\mathrm{kg\,m^{-3}}$
water	c_1	1460 $\mathrm{m\,s^{-1}}$	1460 $\mathrm{m\,s^{-1}}$
		Calculated 1	Calculated 2
concrete/water	h_1	0.300 m	0.571 m
concrete	c_2	3300 $\mathrm{m\,s^{-1}}$	3300 $\mathrm{m\,s^{-1}}$

Table 3.1: Mono-static measurement of the distances and sound speeds for a three layer interface made up of water, concrete, and air. Note the values for Measured 1 and Measured 2 come from Figure 3.9 (a) and (b) respectively. The uncertainties for all distance and time measurements are ± 1 cm and $\pm$ 1 μs, respectively. The timing and amplitude measurements were acquired from the average of 256 stationary measurements.

Data source		Figure 3.9 (e)	Figure 3.9 (c)	Figure 3.9 (f)	Figure 3.9 (d)
Interface	Name	Simulated 1	Measured 1	Simulated 2	Measured 2
-	x	0.91 m	0.91 m	0.91 m	0.91 m
water/concrete $n = 1$	τ_{ml}	0.747 ms	0.752 ms	0.998 ms	0.980 ms
water/concrete $n = 1$	$\mathscr{R}$	0.51	0.92	0.56	0.52
concrete/air $n = 2$	τ_{ml}	0.690 ms	0.716 ms	1.034 ms	1.026 ms
concrete/air $n = 2$	$\mathscr{R}$	-0.24	na	-0.19	-0.20
concrete/air $n = 3$	τ_{ml}	0.776 ms	0.744 ms	1.134 ms	1.056 ms
concrete/air $n = 3$	$\mathscr{R}$	-0.18	-0.20	-0.14	-0.06

Table 3.2: Multi-layer reflection timings (empirical vs. experimental) for a three layer interface. Note the values for h_1, h_2, c_1, c_2, ρ_1, and ρ_2 are taken from Table 3.1. The uncertainties for all distance and time measurements are ± 1 cm and $\pm$ 1 μs respectively. The timing and amplitude measurements were acquired from the average of 256 stationary measurements.

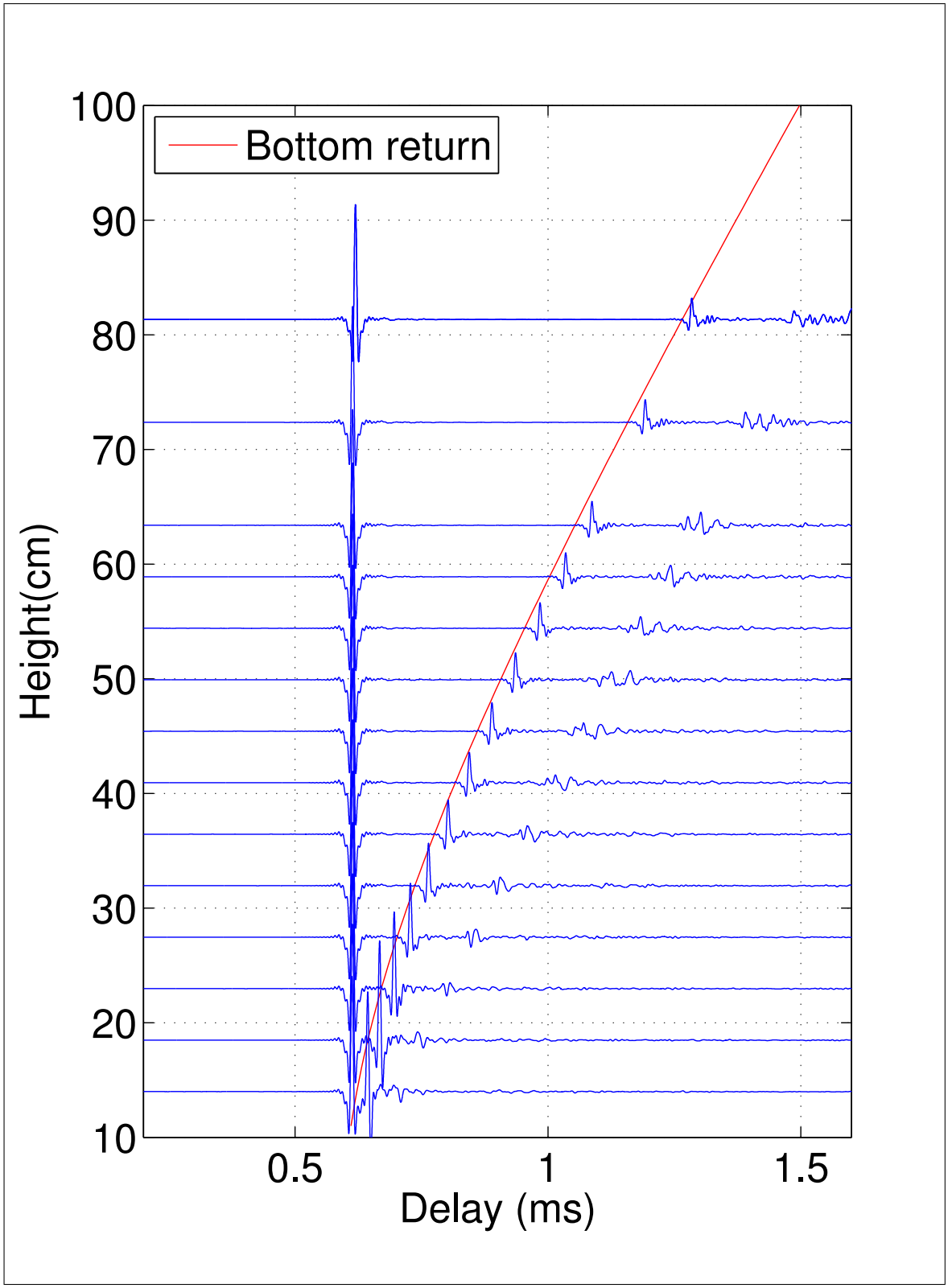

Figure 3.14: Deconvolution of the transducer response for three interface layers made up of water, sand, concrete and air. The TX is on channel 3 and RX is on channel 1. The height above the sand was measured between 14 to 82 cm in 4.5 cm increments excluding the 77 cm and 68 cm measurements. Note the curved line is indicating the theoretical timing for the direct reflection from the water/sand interface based on the transducer separation and height of the transducers above the sand.

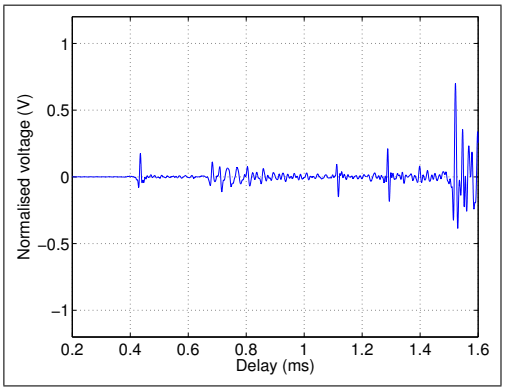

(a) Mono-static transducer response for channel 1 with the transducer 32 cm above the sand.

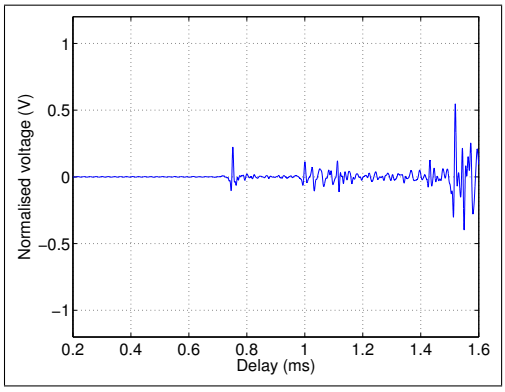

(b) Mono-static transducer response for channel 1 with the transducer 55 cm above the sand.

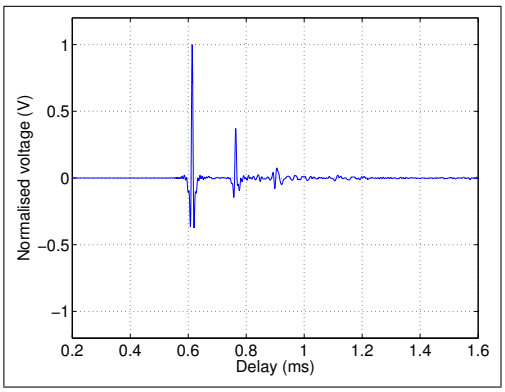

(c) Bi-static transducer response for TX on channel 3 and RX on channel 1 with a transducer separation of 91 cm and the transducers 32 cm above the sand.

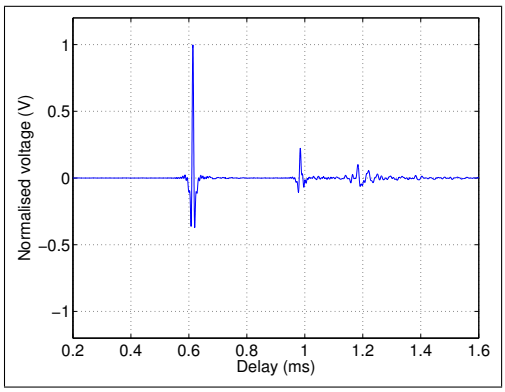

(d) Bi-static transducer response for TX on channel 3 and RX on channel 1 with a transducer separation of 91 cm and the transducers 55 cm above the sand.

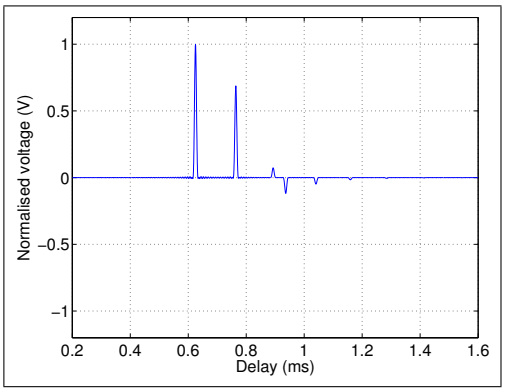

(e) Simulated bi-static transducer response for figure (c).

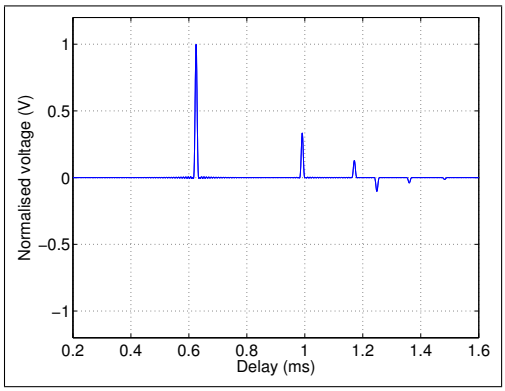

(f) Simulated bi-static transducer response for figure (d).

Figure 3.15: Empirical and simulated impulse responses for three reflection layers. The values for ρ are 1000, 2000, 2400, and 1 for water, sand, concrete and air respectively. The values for c are 1460, 1750, 3300, and 340 for water, sand, concrete and air respectively. The transducer height values of the bi-static configuration are determined from the mono-static data shown in figures (a) and (b). The sand and concrete sound speeds are also determined from the mono-static data using the measured thickness of 21 cm and 22.5 cm for the sand and concrete, respectively.

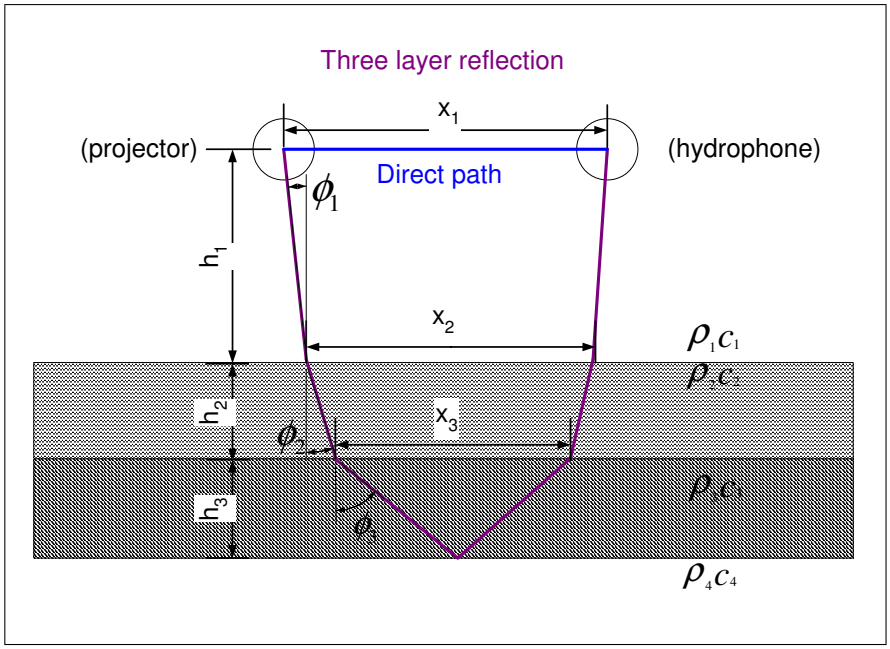

Figure 3.16: Geometry for the bottom reflection off a sand/concrete/air interface with a single reflection bounce. The separation between the two transducers is x_1, x_2 is the separation between entry points into the second media, and x_3 is the separation between entry points in the third media. Note this figure is repeated for clarity in Figure 4.3

where x_1 is the separation between transducers, and h_1 is the height of the transducers above the first interface. (This assumes the transducers are level with respect to the first interface.) Similarly, x_3 can be expressed as

$$x_3 = x_2 - 2\,h_2\,\tan\phi_2, \tag{3.25}$$

where h_2 is the thickness of the first interface. An alternate expression for x_3 is

$$x_3 = 2\,h_3\,\tan\phi_3, \tag{3.26}$$

where h_3 is the thickness of the second interface. Equating (3.24), (3.25) and (3.26) gives

$$0 = x_1 - 2h_1\tan\phi_1 - 2h_2\tan\phi_2 - 2h_3\tan\phi_3\frac{\frac{c_2}{c_1}\sin\phi_1}{\sqrt{1-\left(\frac{c_2}{c_1}\right)^2\sin^2\phi_1}}, \tag{3.27}$$

Using (3.23), all angles can be put in terms of ϕ_1, giving

$$0 = x_1 - 2h_1\frac{\sin\phi_1}{\sqrt{1-\sin^2\phi_1}} - 2h_2\frac{(c_2/c_1)\sin\phi_1}{\sqrt{1-(c_2/c_1)^2\sin^2\phi_1}} - 2h_3\frac{(c_3/c_1)\sin\phi_1}{\sqrt{1-(c_3/c_1)^2\sin^2\phi_1}} \tag{3.28}$$

The roots for this equation are not straightforward so the simplest way to solve for ϕ_1 is to use MATLAB to search where (3.28) is satisfied. The simplest way to calculate these distances for multiple bounces is to increase h_2 by the number of bounces at interface between layers 3 and 4 (the 3-4 interface), resulting in

$$0 = x - 2h_1 \frac{\sin\phi_1}{\sqrt{1-\sin^2\phi_1}} - 2h_2 \frac{(c_2/c_1)\sin\phi_1}{\sqrt{1-\left(c_2/c_1\right)^2\sin^2\phi_1}} - 2\,n\,h_3 \frac{(c_3/c_1)\sin\phi_1}{\sqrt{1-\left(c_3/c_1\right)^2\sin^2\phi_1}} \quad (3.29)$$

where n is the number of 3-4 interface bounces. The time delay for the multi-layer reflection is

$$\tau_{ml} = \frac{L_1}{c_1} + \frac{L_2}{c_2} + \frac{L_3}{c_3}, \quad (3.30)$$

where L_1 is the distance travelled in the first medium,

$$L_1 = 2\,H_1\cos(\phi_1), \quad (3.31)$$

L_2 is the distance travelled in the second medium,

$$L_2 = 2\,H_2\cos(\phi_2), \quad (3.32)$$

L_3 is the distance travelled in the third medium

$$L_3 = 2\,H_3\cos(\phi_3), \quad (3.33)$$

and ϕ_2 and ϕ_3 are defined by (3.23). The attenuation is

$$A = L^{-1}\,\mathscr{R}\,\exp(-L_1\,\alpha_1/8.686)\,\exp(-L_2\,\alpha_2/8.686)\,\exp(-L_3\,\alpha_3/8.686), \quad (3.34)$$

where α_1, α_2, and α_3 are the attenuations in media 1, 2, and 3 in $\mathrm{dB\,m^{-1}}$, L^{-1} is the spreading loss, where

$$L = L_1 + L_2 + L_3, \quad (3.35)$$

and $\mathscr{R}$ is the total reflection coefficient for all the reflections and transmissions:

$$\mathscr{R} = \mathscr{T}_{12}\,\mathscr{T}_{23}\,\mathscr{T}_{32}\,\mathscr{T}_{21}\,\mathscr{R}_{34}^{n}\,\mathscr{R}_{32}^{(n-1)}. \quad (3.36)$$

Here $\mathscr{R}_{34}$ and $\mathscr{R}_{32}$ are the reflection coefficients between various media as defined by (C.14) and $\mathscr{T}_{12}$, $\mathscr{T}_{23}$, $\mathscr{T}_{32}$ and $\mathscr{T}_{21}$ are the transmission coefficients between various media as defined by (C.18).

Data Source		Figure 3.15 (a)	Figure 3.15 (b)
Interface	Name	Measured 1	Measured 2
sand/concrete	h_2	0.210 m	0.210 m
concrete/air	h_3	0.220 m	0.220 m
water/sand	τ_{hl}	0.435 ms	0.752 ms
water/sand	$\mathscr{R}$	0.173	0.216
sand/concrete	τ_{h2}	0.684 ms	1.000 ms
sand/concrete	$\mathscr{R}$	0.110	0.112
concrete/air	τ_{h3}	0.715 ms	1.032 ms
concrete/air	$\mathscr{R}$	-0.105	-0.105
water	ρ_1	1000 $\mathrm{kg\,m^{-3}}$	1000 $\mathrm{kg\,m^{-3}}$
sand	ρ_2	2000 $\mathrm{kg\,m^{-3}}$	2000 $\mathrm{kg\,m^{-3}}$
concrete	ρ_3	2400 $\mathrm{kg\,m^{-3}}$	2400 $\mathrm{kg\,m^{-3}}$
water	c_1	1460 $\mathrm{m\,s^{-1}}$	1460 $\mathrm{m\,s^{-1}}$
		Calculated 1	Calculated 2
concrete/water	h_1	0.318 m	0.549 m
sand	c_2	1686 $\mathrm{m\,s^{-1}}$	1687 $\mathrm{m\,s^{-1}}$
concrete	c_3	3300 $\mathrm{m\,s^{-1}}$	3300 $\mathrm{m\,s^{-1}}$

Table 3.3: Mono-static measurement of the distances and sound speeds for a four layer interface made up of water, sand, concrete, and air. Note the values for the Measured 1 and Measured 2 come from Figure 3.15 (a) and (b) respectively. The uncertainties for all distance and time measurements are ± 1 cm and $\pm$ 1 μs, respectively. The timing and amplitude measurements were acquired from the average of 256 stationary measurements.

Data source		Figure 3.15 (e)	Figure 3.15 (c)	Figure 3.15 (f)	Figure 3.15 (d)
Interface	Name	Simulated 1	Measured 1	Simulated 2	Measured 2
-	x_1	0.91 m	0.91 m	0.91 m	0.91 m
water/sand $n = 1$	τ_{ml}	0.764 ms	0.763 ms	0.980 ms	0.983 ms
water/sand $n = 1$	$\mathscr{R}$	0.68	0.37	0.33	0.21
sand/concrete $n = 1$	τ_{ml}	0.894 ms	0.893 ms	1.158 ms	1.184 ms
sand/concrete $n = 1$	$\mathscr{R}$	0.07	0.04	0.13	0.10
concrete/air $n = 2$	τ_{ml}	0.935 ms	0.898 ms	1.237 ms	1.199 ms
concrete/air $n = 2$	$\mathscr{R}$	-0.11	-0.07	-0.10	-0.05

Table 3.4: Multi-layer reflection timings (empirical vs. experimental) for a four layer interface. Note the values for h_1, h_2, h_3 c_1, c_2, c_3, ρ_1, ρ_2, and ρ_3 are taken from Table 3.3. The uncertainties for all distance and time measurements are ± 1 cm and $\pm$ 1 μs, respectively. The timing and amplitude measurements were acquired from the average of 256 stationary measurements.

3.2.2.2 Multi-layer reflection conclusions

Using the results of the equations in Section 3.2.2.1 the responses for a smooth four layer interface can be analysed. Table 3.4 compares the simulated multi-layer reflection results to the empirical multi-layer results shown in Figure 3.15. For these simulations the attenuations of water and concrete are ignored and the attenuation of sand is set to $20\,\mathrm{dB\,m^{-1}}$[4] based on the measured attenuation of the concrete reflection through the sand (the attenuation values in Jackson and Richardson [2007] for sand vary between $58.0\,\mathrm{dB\,m^{-1}}$ and $632.5\,\mathrm{dB\,m^{-1}}$). For both the simulated results and empirical results the 20 cm of sand on the bottom of the tank is too small to minimise the interference between the surface scattering and the concrete tank bottom reflection. The attenuation of the sand was not accurately measured before the sand was put into the tank due to problems with air being trapped in the sand as discussed in Section 3.2.3. When dealing with sound from a spherical source in a multi-layer environment, sound waves conducted through a buried layer can arrive before the first surface interaction. This occurs when the sound speed in a buried medium is significantly faster than that of the primary medium; as is the case with concrete and water.

In the sonar tank environment, the concrete/air interface acts as a wave guide conducting multiple concrete bottom reflections close to the sand/water reflection. Figures 3.12 and 3.14 show the effect of changing the transducer height on the timing of the reflected signals. The arrival times of the concrete/air reflection are not strictly predictable due to surface roughness of the sand and roughness of the concrete/air interface. For future tests, a pressure release interface under the sand, such as closed-cell foam, would allow better measurements of the bi-static scattered response. In the bi-static configuration only the direct reflection can be analysed due to interference from the concrete/dirt reflection.

3.2.3 Air trapped in sand

Air trapped in sand can distort the reflection coefficient. Generally the reflection coefficient is a property of the acoustic impedance of the seafloor [5]. If the acoustic impedance of the first medium is less than that of the second medium, the reflected signal shows no phase inversion, otherwise, the reflected signal will have a 180° phase inversion[6]. For example, if the first medium is water and the second medium

[4] The attenuation measurement of $20\,\mathrm{dB\,m^{-1}}$ is an average over the 20 kHz-120 kHz range, which is most likely dominated by the lower frequency range. More accurate measurements were hampered by the multiple reflection from the concrete.

[5] The seafloor is defined as the interface at the bottom, which, for most of the experiment is a water/sand interface. The sea-surface is defined as the interface at the top, which, for these experiments is a water/air interface.

[6] Note at very low grazing angles a phase inversion can occur when the acoustic impedance of the first medium is less than that of the second medium. However, this effect is not relevant for the angles used in these experiments.

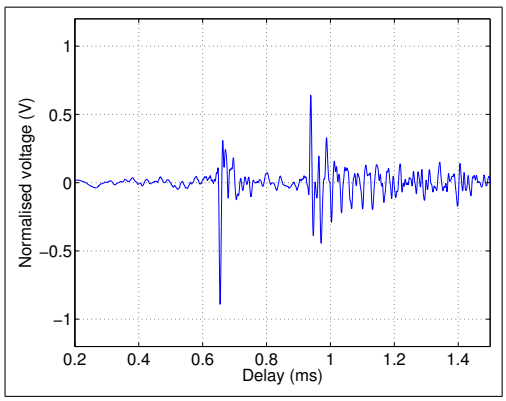

(a) Sand with air mono-static response.

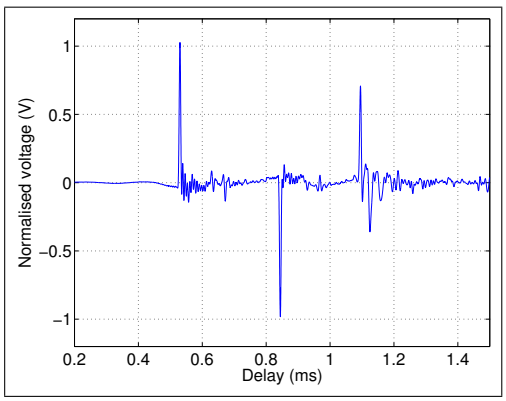

(b) Sand with air bi-static response.

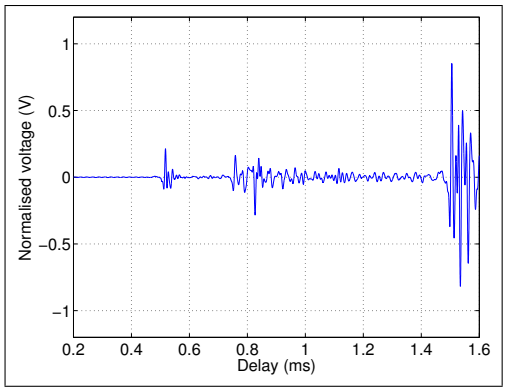

(c) Sand without air mono-static response.

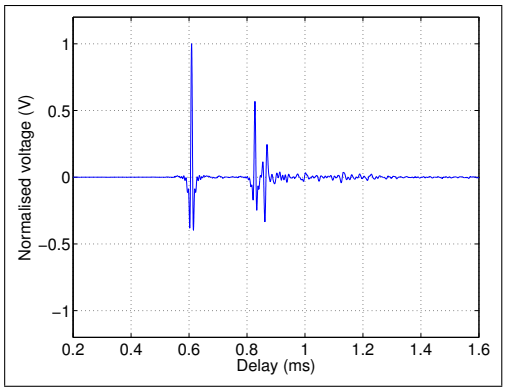

(d) Sand without air bi-static response.

Figure 3.17: Example bottom returns with and without air in the sand 77 cm from the concrete tank bottom. Note the sand reflections do not occur at a fixed location because these readings were taken as sand was being added to the tank.

is sand, given that the acoustic impedance of sand is much greater than that of water, the reflected signal should have no phase inversion. Figure 3.17 (a) and (b) show the deconvolved impulse response of mono-static and bi-static signals reflected from sand with an air inversion present. Figure 3.17 (c) and (d) show the response from the same area after the air has been removed from the sand. Note the bi-static response in Figure 3.17 (b) shows the direct path between the TX and RX transducers at 0.530 ms time delay. This response is positive but the sand response at 0.845 ms time delay is negative, indicating phase inversion. The existence of a phase inversion indicates that there is air trapped in the sand.

Air trapped in the seafloor has always been a problem when making acoustic measurements of the seafloor. In natural environments such as the sea, micro-organisms, sea-animals, and decomposing bio-matter all generate gases that can be trapped in the sand [Jackson and Richardson 2007, Anderson et al. 1998, Anderson and Hampton 1980a, Anderson and Hampton 1980b]. In the tank environment, air can also be trapped in the sand due to decomposing bio-matter, micro-organisms

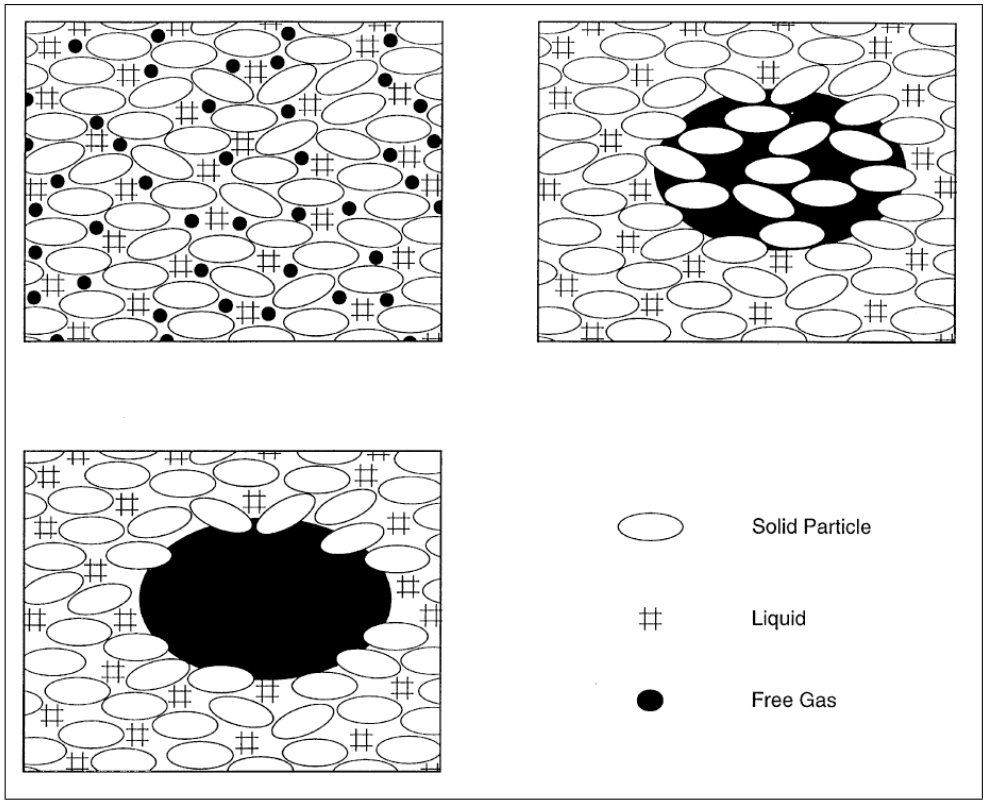

Figure 3.18: The three types of bubbles in sediment, clockwise from the top left: Type I, interstitial bubbles; Type II, reservoir bubbles; and Type III, sediment-displacing bubbles [Anderson et al.1998].

and the method of loading the sand into the test environment [Lyons 2008, Zakharia 2008]. There are three categories of bubbles internal to the sand: interstitial bubbles, reservoir bubbles, and sediment-displacing bubbles, as shown in Figure 3.18 [Anderson et al. 1998]. The primary type of bubbles that were found in the sonar tank were interstitial bubbles and reservoir bubbles (given that no large bubbles or pockets of bubbles were found in the process of removing the bubbles from the sand). In addition to bubbles inside the sand, bubbles can be suspended in the water and on the surface of objects in the water such as the sand, the transducers, and the transducer cables (as observed in the sonar tank over the past two years). These bubbles have been observed in the tank test environment upon refilling or adding water to the tank and when the tank water temperature changes from warm to cold. The cause of these bubbles is the change in the saturation level of water. Tap water is under pressure and therefore can contain more air than water at one atmosphere. Likewise warm water can contain more air than cold water. (A description of saturation level of water and its temperature and pressure dependence can be found in most chemistry text books, e.g., [Ebbing 1987, Nock 2009].)

Modelling of air trapped in sand is difficult, due to the fact that both the

distribution and layering of the air bubbles in the seafloor are unknown. In environments with clear water, such as the sonar tank, the surface of the seafloor can be measured optically using a stereo camera system. These measurements can then be used to generate a surface model that can be simulated and compared to the acoustic results. However, the distribution of the air bubbles in the seafloor may have no correlation with the roughness of the seafloor. More details on statistical analysis of air distribution in sand are covered in Anderson et al. [1998] and Jackson and Richardson [2007]. Measurable physical characteristics of the sand, such as density ρ and sound speed c, seem to have little or no effect on the reflected signal, as seen in Figure 3.17 (c). The effect of these bubbles, in the sonar test tank, has been observed to change over time, as observed over two years of testing in the sonar tank. It is thought that this is due to thermal expansion of the bubbles and migration of the bubbles over time. The air trapped in the sand dominates the reflected signal and marginalises the acoustic proprieties of the sand, making them irrelevant to the model of the seafloor, as seen in Figure 3.17 (c). For this reason it is necessary to remove the bubbles from the test environment.

Different types of bubbles need to be removed in a different manner. For bubbles floating in the water, the best method to remove them is to wait for them to disperse. The more sediment in the tank, the longer it takes for these bubbles to disperse, given that these bubble seem to form around the sediment suspended in the water. Surface bubbles that form on the seafloor can be dispersed by stirring the water but with limited effectiveness, i.e., bubbles that form on the surface of the transducer do not always disperse when the tank is stirred. The only effective way to remove these bubbles is to use detergent on the surface of the transducer. The only effective way to remove the bubbles from the sand was found to be raking. Once the bubbles are trapped in the sand they do not seem to migrate out of the sand on their own. This was verified by filling the tank and running tests over three months and having the bubbles present for the entire time. The process for removing the bubbles was to half drain the tank and then use a garden fork to stir the sand by hand. Care was taken not to stir the sand if air bubbles were seen floating in the water or on the surface of the sand, for fear of stirring additional bubbles into the sand. The only effective way to detect the presence of bubbles in the sand was to look for the phase inversion shown in Figure 3.17 (a) and (b).

3.3 ACOUSTIC HARDWARE OVERVIEW

Figure 3.19 shows the laboratory set-up of a signal generation and a data acquisition system. The signal generation system comprises three signal generators, a power amp, and a TX/RX switch shared with the acquisition system. The data acquisition system consists of an oscilloscope, a pre-amplifier, and the TX/RX switch. Figure 3.20 shows a block diagram of the hardware set-up for one channel. The

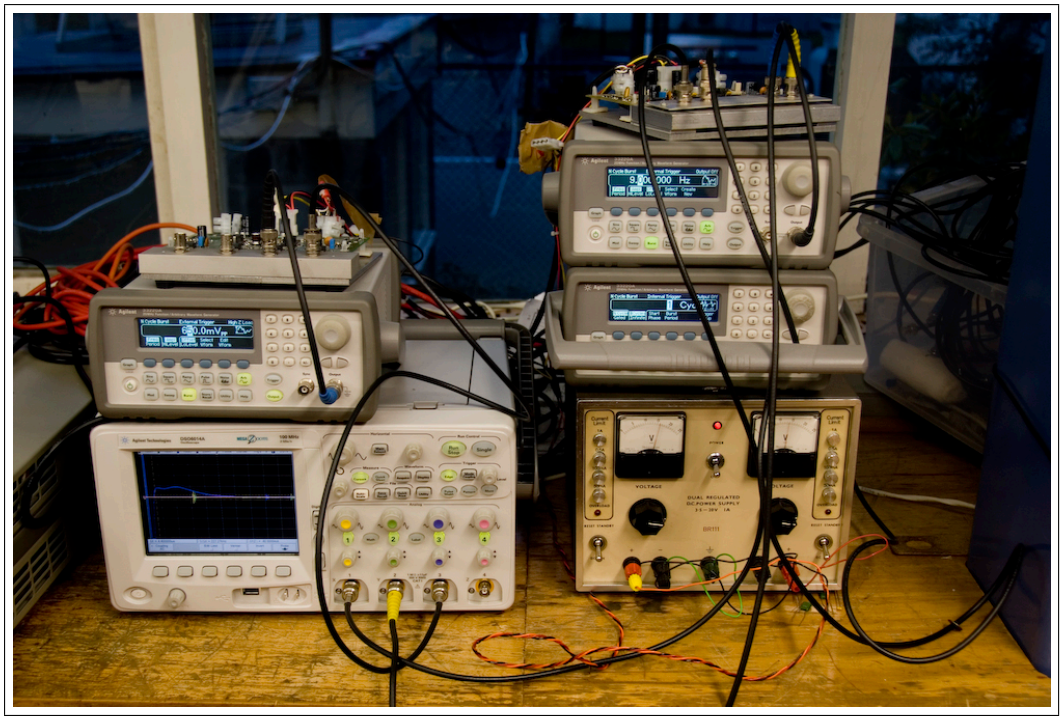

Figure 3.19: Photo of the test set-up showing the power supply, the three signal generators, the oscilloscope, and the two combo pre-amplifier/power-amplifer boards.

entire system is controlled by a laptop computer over the ethernet. The system runs at approximately one ping per second to allow reverberation in the tank to die away.

3.3.1 Signal generation

The signal generation system uses three Agilent arbitrary waveform generators. This set-up allows almost any waveform to be generated by the signal generator. However, what is acoustically reproduced in the tank is limited by the TX/RX switch and the transducers' bandwidth. There are three different categories of signals that are transmitted for the experiments: step excitation, rectangular pulse excitation (impulse excitation), and tone-burst excitation.

The step excitation works well in the bi-static configuration but is not suitable for the mono-static configuration as discussed in Sections 3.1.1 and 3.1.2. The step excitation, with the ITC-1042 transducer, produces a pulse with a bandwidth of approximately 120 kHz with centre frequency of 74 kHz, as shown in Figure 3.4 (b). This pulse can be used to perform broadband analysis of surface reflections. The processing of the step excitation is discussed in Section 3.1.1.

For bi-static applications, the impulse excitation can work almost as well as the step excitation. The main advantage of the impulse excitation over the step excitation is that it can be used in the mono-static configuration. A 2.2 μs wide rectangular pulse (impulse excitation) produces nearly the same signal bandwidth

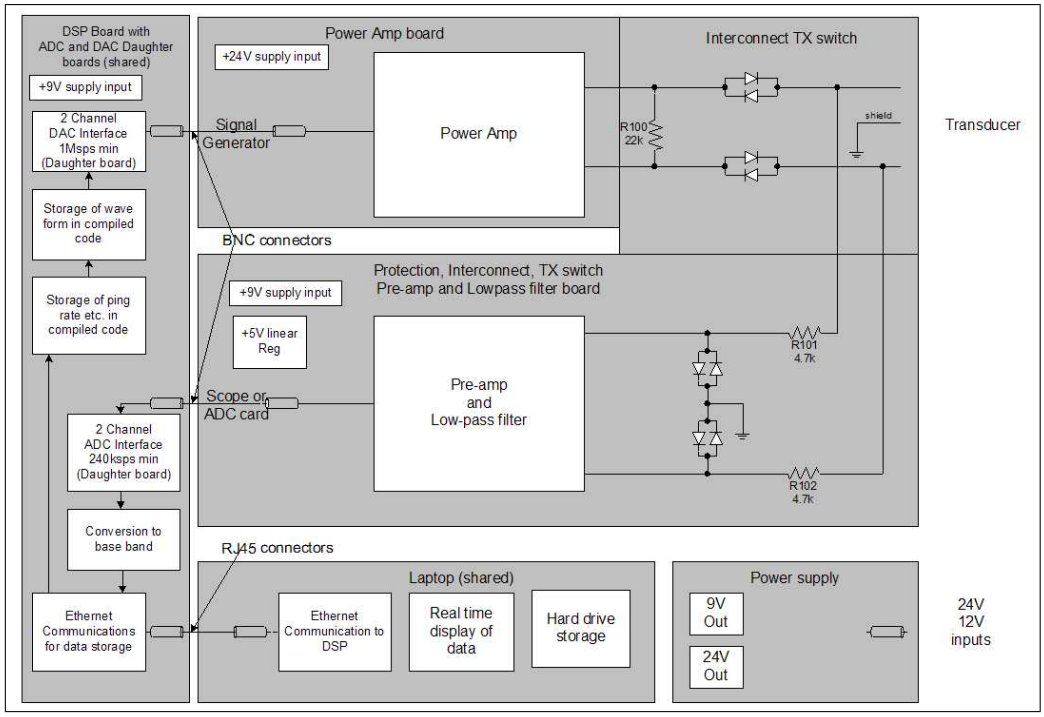

Figure 3.20: The system block diagram showing the data acquisition and sign generation components for one channel. Note the DSP board with daughter board, on the block diagram, although designed was never used because using the oscilloscope with signal generators was found to be adequate for the tests.

as a step excitation with approximately a quarter of the amplitude. Unlike the step excitation, the TX/RX switch has minimal effect on the impulse excitation. The processing of the impulse excitation is described in Sections 3.1.1 and 3.1.2.

The tone-burst waveforms, like the rectangular pulse, can be used in the mono-static configuration. The tone-burst waveforms have the advantages of eight times the amplitude and a specific frequency band, rather than the entire bandwidth of the transducer, as with the step-function and the rectangular pulse. For the tone-burst waveforms, there are limitations on the type of waveform that can be transmitted. To minimise ringing and distortion of the waveform, transmissions were made at a frequency at least 5 kHz away from the resonance frequency of 80 kHz and a ramped waveform was used. A 1/3 ramp up/down ratio worked best for a 3-9 cycle waveform, i.e., a 1/3 of the waveform ramp up, a 1/3 steady state, and a 1/3 ramp down, example 3 and 9 cycle waveforms are shown in Figure 3.21. Above 9 cycles, 3 cycle up and down ramps worked best. This process appeared to help in three ways: having the transducer transmit the correct frequency at the start of the waveform; minimising the ringing at the end of the waveform; and minimising the DC offset at the end of the waveform.

For all three waveform categories, the arbitrary waveform generator is amplified by the power-amplifer which produces a maximum amplitude of 100 V_p. The

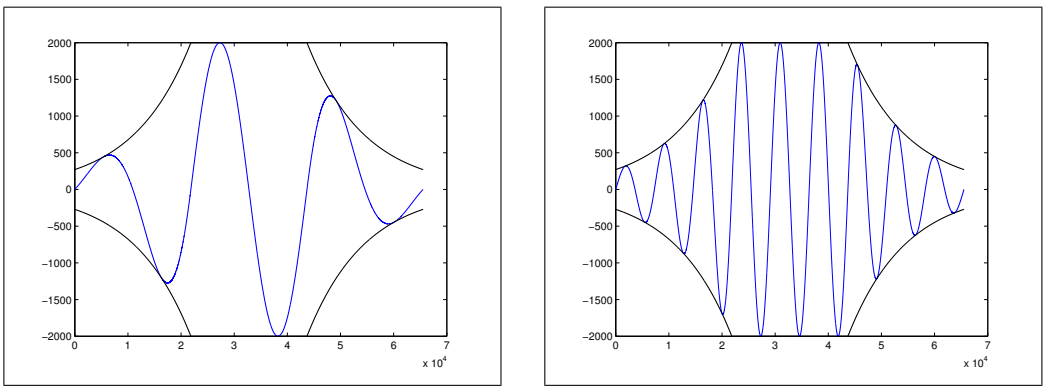

(a) 3 cycle waveform

(b) 9 cycle waveform

Figure 3.21: Example 3 and 9 cycle waveforms with an exponential ramp-up and ramp-down.

power amp connects to the TX/RX switch to drive the transducers. The TX portion of the TX/RX switch goes to a high impedance state when the voltage is between -0.7 V and 0.7 V. This is to allow both transmitting and receiving on the same transducer. The TX/RX switch causes a number of problems when driving the transducer: firstly, there is a dead zone when transmitting between -0.7 V and 0.7 V causing a notch in the transmitted waveform; secondly, the notch is at a fixed voltage so the distortions become greater with smaller output voltage swings; and thirdly, when the waveform generator does not damp the ringing and discharge the transducer below ±0.7 V. When transmission stops, the transducer can ring for up to five cycles at 75 kHz. This is significant when the transmitted waveform is only intended to be three cycles long. The problems with the transducer discharging and the TX/RX are discussed in further detail in Section D.2. Figure 3.22 shows these issues.

3.3.2 Data acquisition

The data acquisition system was chosen to use standard test equipment with an ethernet interface. At the time the Agilent MSO60141A oscilloscope was the best choice. The main advantages of a custom acquisition system over the MSO6014A would be greater dynamic range and faster data storage. The only major drawback of the scope is that the ADC is 12 bits, limiting the dynamic range to 72 dB. Secondly, the pre-amp does minimal pre-processing of the signal. It consists of a 2 kHz high pass filter and a gain of 4. This trade-off reduces the dynamic range of the signal of interest by 12 dB to prevent clipping of the waveform. Most of the filtering and signal processing is carried out after the data has been acquired. This is to allow maximum flexibility of the signal that can be passed through the system. Testing showed that problems, such as clipping of the signals, could be masked if too much

filtering was applied near the beginning of the signal chain.

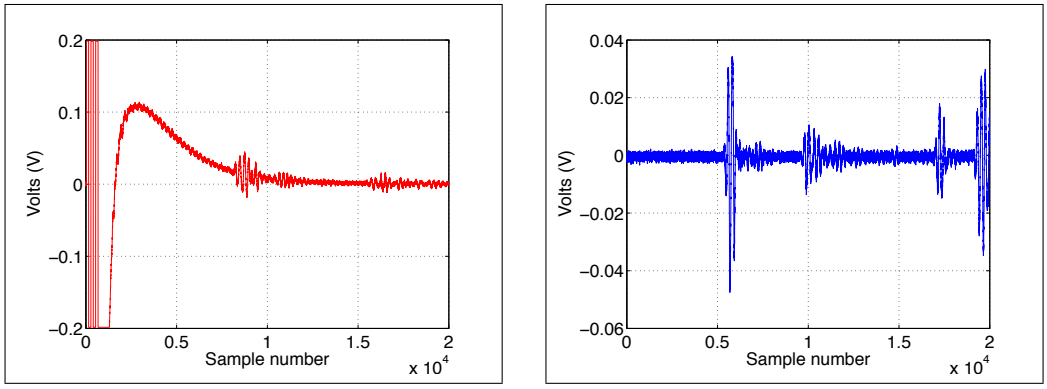

(a) Mono-static channel 1

(b) Bi-static TX on channel 1 and RX on channel 3

Figure 3.22: Raw 38 kHz unprocessed data from the smooth sandy reflection 0.5 m from the transducers.

3.4 STEREO IMAGING SYSTEM OVERVIEW

The stereo imaging system is used to determine the ground-truth of the tank bottom or the seafloor. The ground-truth software portion of the system is based on the work of Gaetano Canepa at the NATO Undersea Research Centre in La Spezia, Italy with modification by Anthony Lyons at the Applied Research Laboratory at the Pennsylvania State University and is an extension of the work described in Lyons et al. [2002]. The software has been developed, previously used and verified [Lyons et al. 2002, Lyons and Pouliquen 2004, Gerig et al. 2009]. Section 3.4.1 describes the hardware and data acquisition. Section 3.4.2 describes the application specific photogrammetry software parameters and a brief overview of the processing trade-offs.

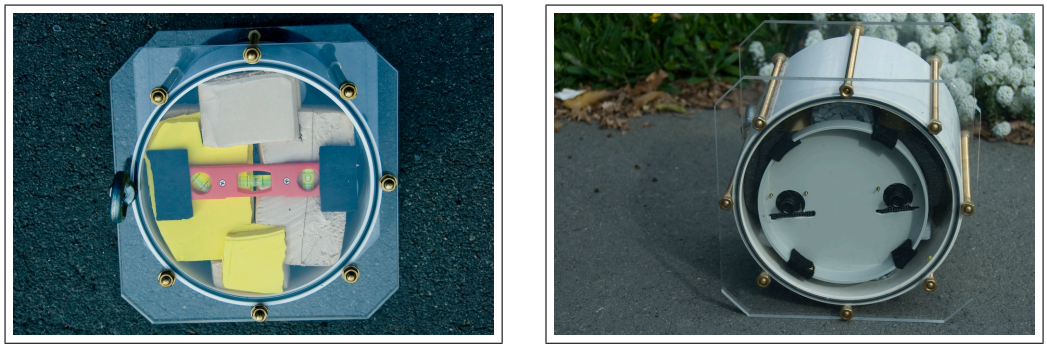

(a) Top view of camera enclosure

(b) Bottom view of camera enclosure

Figure 3.23: Photos showing the underwater stereo camera housing.

3.4.1 Imaging system

The hardware system consists of four parts: a standard laptop for control and data storage; an 802.11n WiFi router with diversity that acts as a repeater for communications between the laptop and the underwater camera; a WiFi antenna inside a sealed air filled tube which is attached to the outside of the camera enclosure; and a camera enclosure with two stereo cameras. (Note the separation limit between the WiFi antenna and the camera housing was 10 cm before wireless communications were interrupted.)

Parameter	Manufacturer Part	Specification
Processor	Analog Devices Blackfin BF537	500MHz (1000 integer MIPS)
Photo-sensor	Omnivision OV9655	1.3 megapixel sensor
Lens	M12 P0.5 format	Aperture f2.0 90-deg FOV (field of view)

Table 3.5: Camera module specification.

The camera system is a Surveyor SVS (Stereo Vision System)[7] consisting of two camera modules separated by 10.75 cm. Each of the camera modules includes the components specified in Table 3.5 and are interfaced to a single WiFi module that communicates to a laptop through the router. These electronics are housed in the waterproof enclosure shown in Figure 3.23.

To keep the enclosure simple and water tight there are no connectors. All communications are wireless through a WiFi antenna inside a sealed air filled tube which is attached to the outside of the camera enclosure. The camera enclosure has a spirit-level attached to the top lid to allow visual verification of the system's orientation (see Figure 3.23 (a)). Figure 3.23 (b) shows the bottom view of the camera enclosure. The two camera modules are mounted to the end-cap of a PVC pipe, braced against the clear bottom of the enclosure. The enclosure contains the electronics, 3 kg of lead to sink the enclosure, and bracing to prevent the cameras from moving. Small movements of the cameras inside the housing were found to invalidate the camera calibration.

The software to control the electronics is separate from the photogrammetry software. This software was written in MATLAB to allow simple access to the other applications, also written in MATLAB. This software configures the camera modules and triggers the image capture. Colour images are captured in a raw format of $3 \times 1024 \times 1280$ pixels. This data is then converted to TIF format, used by the photogrammetry software to generate the height maps.

[7]The SVS is available from www.surveyor.com.

3.4.2 Photogrammetry software

The photogrammetry software, provided by Anthony Lyons, has no formal documentation with the exception of the source code. Although the source code was provided no modifications were required. The software performance optimisation was controlled by four input parameters. The four input parameters are "corr-window", "displac", "max-disp", and the camera calibration parameters. The "corr-window" is the number of pixels in the correlation window, "displac" is the estimated pixel displacement between the cameras for an estimated range, and "max-disp" is the maximum offset (in pixels) between the images in the search window. The search window is the size of the sub-image searched for a correlation match. The camera calibration parameters are a set of values that correct the images for lens aberrations for each camera. This calibration data is valid for approximately $\pm$ 5 cm at range of 50 cm.

The software calibration process needs to be run if there is any change in the cameras' position inside the camera housing. Small movements of the camera inside the housing, i.e., approximately 3 mm, can invalidate the calibration. To verify the calibration of the camera system a single image of the calibration checker board is taken at the beginning of each test run and verified with the calibration software. If the calibration error exceed 60% of a pixel then the calibration is invalid and a new calibration need to be run. A full calibration requires approximately 12 images of the checker board taken at various angles. The software used and the calibration procedures are document on the web sight www.vision.caltech.edu/bouguetj/calib_doc/ [Bouguet 2008].

All stereo camera tests, images and calibrations were preformed underwater given that system behaviour is different between air and water. The performance of the software was verified by imaging a test surface with known heights, slopes, and textures. This test surface was made of nuts, bolts, and sloping bits of angle iron attached to a flat surface. The test surface was covered with a thin layer of sand using contact adhesive to give it the same texture as the sand in the tank. Figure 3.24 shows the resulting height map of the test surface with a correlation window of 11 pixels. The correlation process acts as a filter on the height data. The correlation match gives the range where the largest number of pixels match. The larger the correlation window the greater the filtering of the estimated height values. The smaller the correlation window the more noise there is in the data. A correlation window of 11 pixels was found to be a good trade-off between resolution noise, and outlier filtering.

Figure 3.24 shows the maximum area of overlap between the two cameras, approximately 850×900 pixels of the 1024×1280 pixels available. Figure 3.25 shows the bottom of the sonar test tank in between transducers 2 and 3. This image was taken of sand surface 1 as described in Section 4.2.1. Figure 3.25 has a smaller

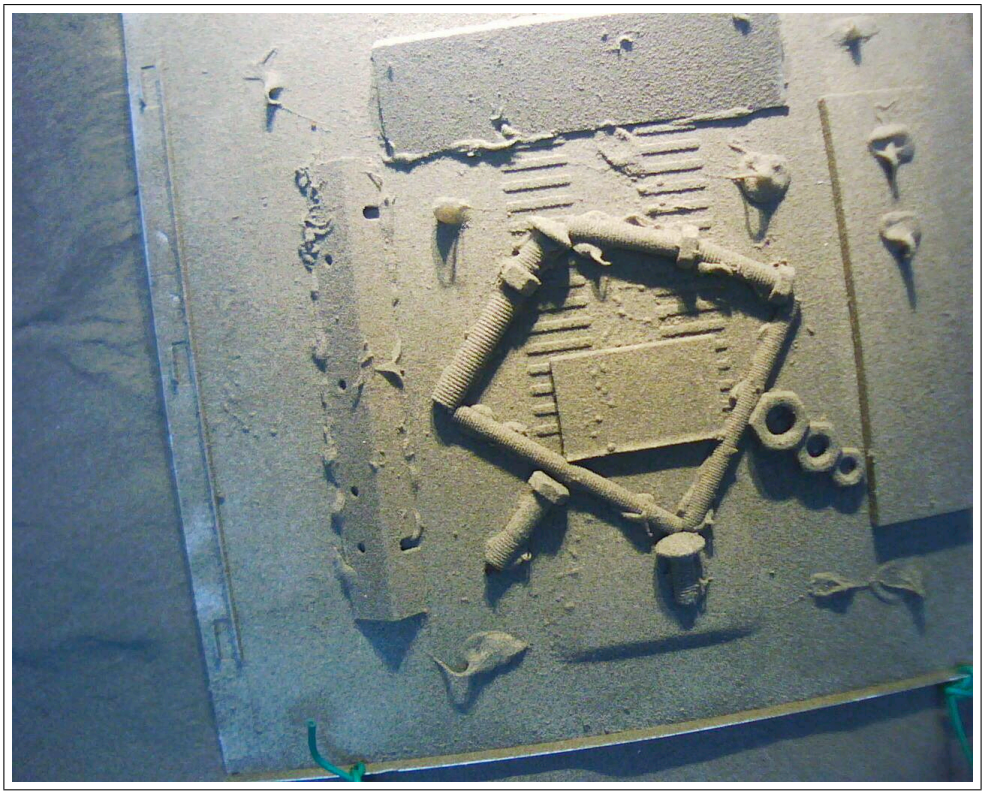

(a) Left camera image

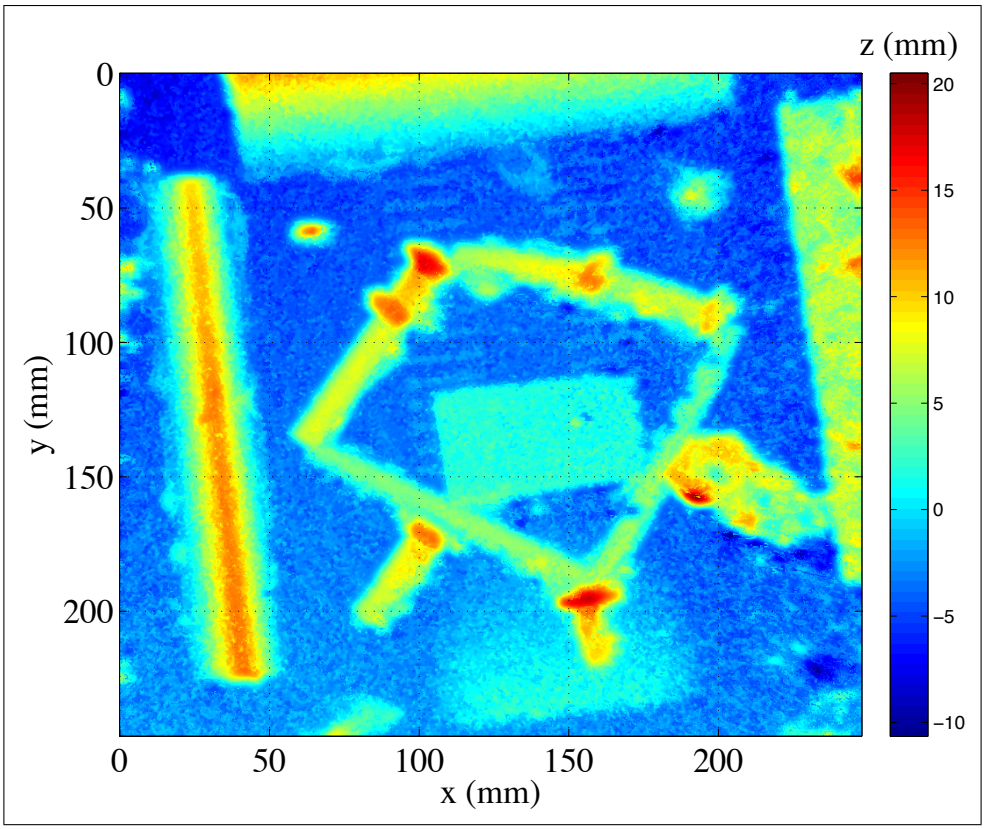

(b) Height map

Figure 3.24: Calibration output from stereo camera set-up. Note, the usable area of overlap between the two cameras is 850×900 pixels, as determined by the camera separation and the height above the surface. Hence, the area shown in (b) is a subset the 1024×1280 pixel image shown in (a) .

usable range of 850×600 pixels, due to poor lighting. The lighting needs to be at a steep enough angle to provide contrast and bright enough not to cause shadows. If there are shadows then the images become noisy and cannot be correlated. Similarly, if the scene is too brightly lit then the area cannot be correlated due to lack of contrast. Lack of contrast can also be caused by uniform objects with no texture such as pieces of shell. If an object has no texture and is bigger than the correlation area (approximately 2 mm), as is the case for the white pieces of shell shown in Figure 3.25 (a), then the area of the object will give erroneous height values. Figure 3.25 (b) shows the height map of the usable area of Figure 3.25 (a).

The erroneous height values given by uniform objects or lack of contrast, i.e., dropouts, generate height values either at the maximum or minimum search range. The area corrupted by these dropouts is dependent on the size of the correlation window and the size of the dropout. If the correlation window is kept small some of dropout can be filtered out by detecting the outliers and replacing them with the average height of the surrounding area. This method was verified by examining height maps of the same area with and without noise. Using this method increased the number of usable height maps. At times it was difficult to get good height maps due to water clarity problems caused by rain.

The height map has an area of 350 mm x 350 mm with a resolution of ± 0.25 mm and an xy resolution of ± 0.13 mm at a standoff of 500 mm. Once the height data is generated then the spectrum of the surface can be examined, as shown in Figure 3.25 (c) and (d). This data can then be used to determine the statistical parameters of the surface, which can then be compared to the statistics of the acoustic response. The results of this analysis are discussed in Chapter 4.

(a) Left camera image

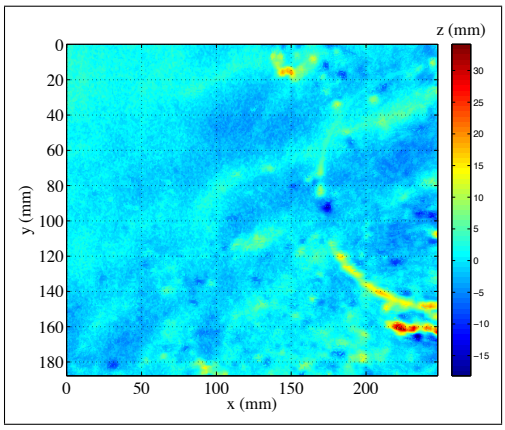

(b) Height map

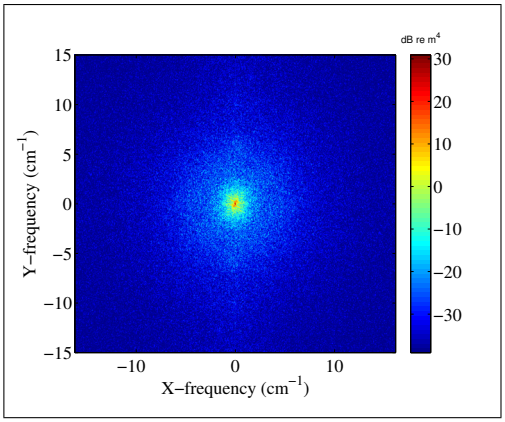

(c) 2-D spectrum

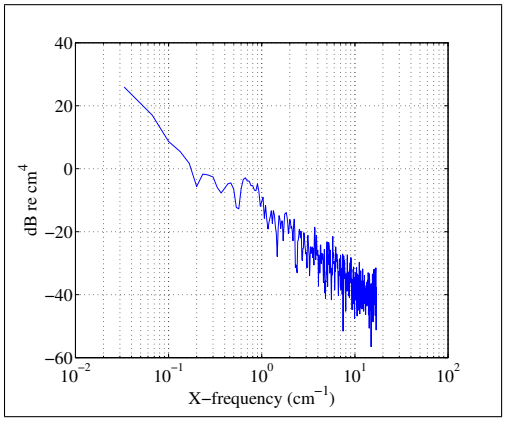

(d) 1-D spectrum of a x-axis cross-section

Figure 3.25: Ground truth of the area between transducers 2 and 3. A number of features can be observed in the spectrum cross section shown in (d). For example the directional ripples seen in figures (a) and (b) cause a peak at 1/5 cm in the spectrum. The overall slope can also be observed to have a power-law roll-off of 25 dB per decade.

Chapter 4

EMPIRICAL AND SIMULATED RESULTS

This chapter describes the empirical results obtained in the sonar test tank and compares them to simulated results. This chapter includes results from six separate test runs. Typical plots to describe specific features are presented here, while additional waterfall plots from these tests are in Appendix E.

The tests presented in this chapter examine sand roughness and its effects on the acoustic signals. This chapter demonstrates how the acoustic impedance, speed of sound, and density of the materiel of the seafloor can be measured, as shown in Section 4.4, provided that there is a critical angle. Then, using the the acoustic impedance to normalise the response, Section 4.5 shows how the roughness spectrum of the seafloor's surface can be analysed; provided there are enough realisations. The test environment where the empirical measurements are made and some of its limitations are described in Section 4.1. The method of analysing the frequency response used throughout this chapter is described in Section 4.3. A summary of the results of this section is provided in Section 4.6.

4.1 OVERVIEW OF THE TANK TESTS

Over the past two and a half years, several different acoustic experiments have been run in the sonar test tank; these experiments are described in Section 3.1. The first tests, which have been excluded from this thesis, were run with river sand that was mixed with fine silt. These tests were problematic given that there was always a phase inversion present in the sand reflection. This inversion was concluded to be caused by air trapped in the sand/silt as discussed in Section 3.2.3. Over a period of 12 months, various unsuccessful methods were used to remove air from the sand. At the end of these experiments, it was concluded that the silt mixed in the sand made it difficult to remove the air from the sand and because of this problem, the sand with silt in it was removed from the tank and the tank was cleaned. After the tank was cleaned, the tests that are included in this thesis were started. These tank tests consist of a series of six tests conducted over approximately one year. The first test was conducted with no sand in the tank in order to characterise the sonar test

tank's acoustic behaviour without sand, which is briefly discussed in Section 3.2.2 and Section 4.1.1. The remaining five tests used different sand surfaces to test the acoustic system's performance with different surface roughness. Each of these sand surfaces has a different surface roughness generated in different manners to simulate the roughness found on a seafloor. The five sand surface tests are described in Section 3.2.2.1 and Section 4.2.1 through Section 4.2.5.

4.1.1 Concrete tank tests

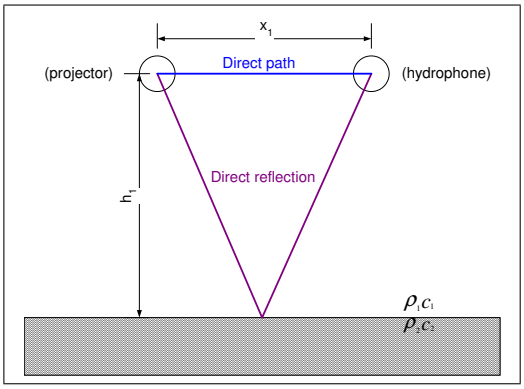

(a) Geometry for the direct reflection off the concrete/water interface.

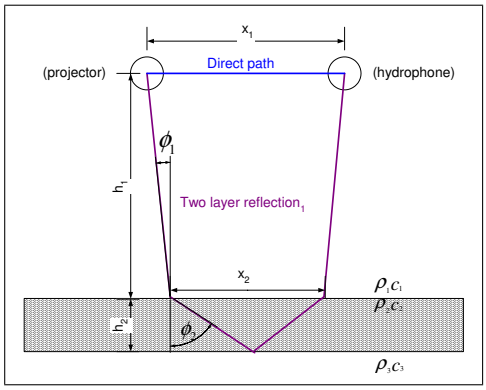

(b) Geometry for an internal concrete reflection with a single reflection bounce.

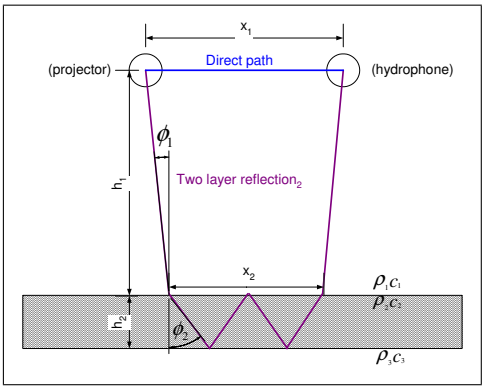

(c) Geometry for an internal concrete reflection with three reflection bounces.

Figure 4.1: These figures show the geometry for the acoustic tests performed in this section. For the mono-static tests x_1, the separation between the two transducers, is zero. For the bi-static tests x_1 is approximately 95 cm and ϕ_1 and ϕ_2 are dictated by h_1, h_2, ρ_1,ρ_2, c_1, and c_2, as discussed in Section 3.2.2. Note for the sonar test tank configuration the reflection shown (c) will arrive before the reflection in (b). This is because the sound speed is concrete is approximately three times faster than that of water and the shorter the distance traveled in water the sooner the reflections arrive. The equations describing the timings are described in Section 3.2.2. Note these diagrams have been repeated for clarity: (a) is from Figure 3.10, (b) and (c) are from Figure 3.13.

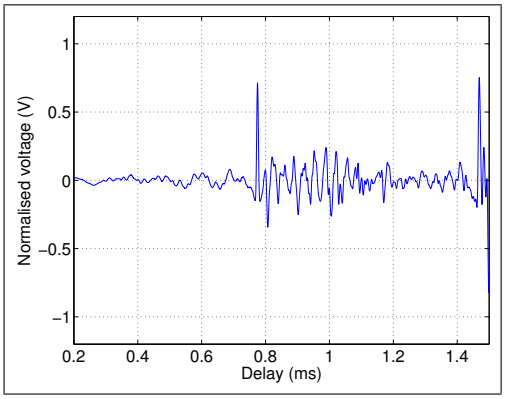

(a) The mono-static transducer response with the transducer 56 cm above the concrete.

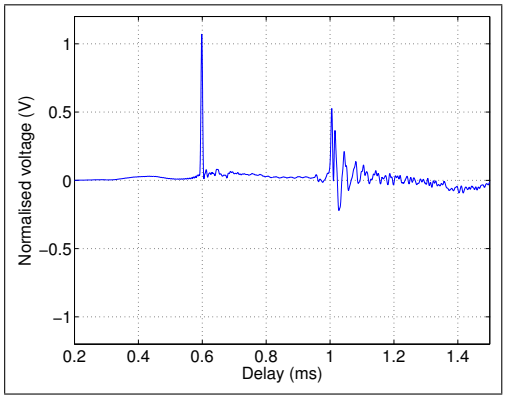

(b) The bi-static transducer response with a transducer separation of 91 cm and the transducers 56 cm above the concrete.

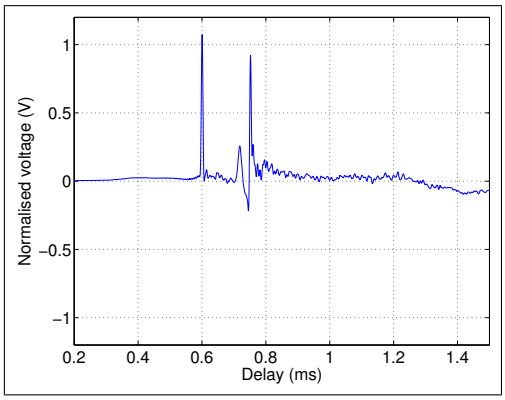

(c) The bi-static transducer response with a transducer separation of 91 cm and the transducers 33 cm above the concrete.

Figure 4.2: Empirical results for the deconvolved acoustic reflection from the sonar test tank. These figures show that if the second medium has a sound speed faster than the first then the internal reflection can occur before the direct reflection. Figure 4.1 shows the geometry of the direct reflection and an internal reflection; (a) shows the mono-static reflection, i.e, the incidence angle $\phi_1 = 0°$, which has the greatest separation between the internal and direct reflections; (b) shows the concrete reflection with the transducers approximately 56 cm above the concrete at approximately 1 ms. At this point, the direct reflection and internal reflections are just starting to interfere; (c) shows the concrete reflection with the transducers approximately 33 cm above the concrete at approximately 0.75 ms. At this point, the internal reflection occurs before direct reflection and the two reflections interfere. The height dependence of the internal reflections can be seen more clearly in the waterfall plot shown in Figure 3.12. Plots b) and c) are individual traces from Figure 3.12 without the air reflection.

The concrete tank tests, i.e., a clean tank without sand, were performed to characterise the tank and to understand the reflection timings. The bottom has a peak roughness of approximately 2 mm over an area of 400 cm^2 and a slope of 4 cm over the 3.5 m tank diameter; the slope is for drainage. For the purposes of these tests the concrete can be considered to be flat and level. Figure 4.1 shows the geometry of a surface that has both a direct reflection and one example of an internal reflection. Internal reflections can only occur if the second medium has minimal attenuation and has acoustic energy transmitted into it. For this reason, a closed-cell foam liner over the concrete (i.e., water/air/concrete interface) does not support multiple internal reflections because almost none of the acoustic energy is transmitted into the air and therefore minimal energy would be reflected from the concrete surface.

Figure 4.2 shows empirical examples of the direct reflection and internal reflections. As discussed in Section 3.2, the tank is not made up of a single homogeneous material. Rather, it is made up of many materials, i.e., concrete, rebar, and even gas bubbles. Each of these materials may act as a reflective surface internal to the concrete. The timings of the tank's internal reflective surfaces occur closer together than they do in water or sand because concrete has sound speed of 3300 $m\,s^{-1}$. For this reason (and because the actual structure of the tank is unknown, as discussed in Section 3.2) the tank's reflections are considered as two groups rather than individual reflections from known reflective surfaces. The two tank reflections groups are: the direct reflection and the internal reflections. The greatest separation between the direct reflection and the internal reflections occurs in the mono-static configuration, shown in Figure 4.2 (a). The direct reflection and the internal reflections start to overlap in the bi-static configuration when the transducers are 56 cm above the tank's bottom; this is because of the geometry of the tank and transducers, as discussed in Section 3.2.2 and shown in Figure 4.2 (b). Figure 4.2 (c) shows the internal reflection occurring before the direct reflection, this is a result of the transducers only being 33 cm away from the concrete.

There are three conclusions that can be made from Figure 4.2 and Section 3.2 for spherical waves: firstly, with this system's resolution the concrete's internal reflections cannot be evaluated independently; secondly, in the bi-static configuration, the closer the transducers are to the concrete, the earlier the internal reflections occur with respect to the direct reflection; and thirdly, in the bi-static configuration, if the sound speed is higher in the second media than the first media, then the internal reflections can occur before the direct reflection. Note, the greater the sound speed in the second media, the sooner the internal reflections overlap with the direct reflection. In general, the acoustic evaluation of the concrete tank with spherical waves was limited by the internal reflections. These same limitations are present with the sand acoustic tests, but are less significant due to the sand's slower

sound speed and greater acoustic attenuation.

4.1.2 Sand tests

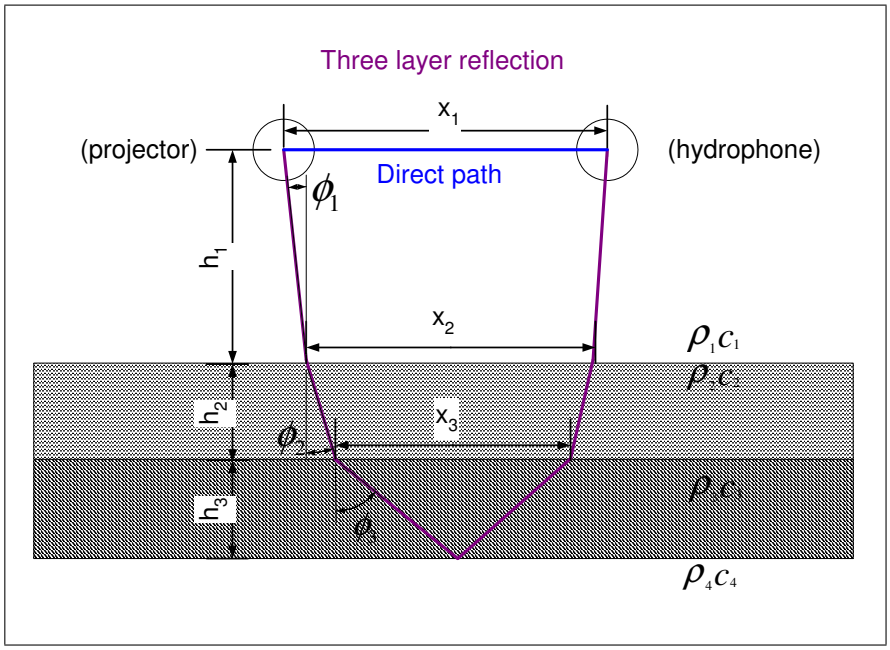

Figure 4.3: Geometry for the bottom reflection off a water/sand/concrete/air interface with a single reflection bounce. x_1 is the separation between the two transducers, x_2 is the separation between the entry/exit points into the second medium, and x_3 is the separation between the entry/exit points in the third medium. Note, for clarity this figure is repeated in Figure 3.16.

When sand is added to the tank, there is an additional layer as shown in Figure 4.3. The equations governing these interfaces are described in more detail in Section 3.2.2.1. The sand layer (unlike the concrete layer) has significant attenuation so the multiple reflections in the sand interface are attenuated enough to be negligible in amplitude. However, the reflections in the concrete layer are not significantly attenuated because the sound waves travel mostly in the concrete with only a short distance travelled in the sand at the entry and exit points, as shown in Figure 4.3.

For the initial test the sand depth, h_2, was only 10 cm. This amount of sand over the concrete was insufficient to prevent internal concrete reflections and the sand direct reflection from interfering. When h_1, the transducer height above the sand, was less than or equal to 40 cm the reflections from the concrete and sand interfere. This, as well as the air trapped in the sand, made the initial test configuration unusable. Hence the sand depth h_2 was increased to approximately 20 cm for the tests recorded in this thesis. For a sand depth h_2 of 20 cm, the concrete reflection does not interfere with the direct reflection until h_1 is below 15 cm. This means the usable range of h_1 is between 15 cm and 80 cm, as shown in Figure 4.4. The

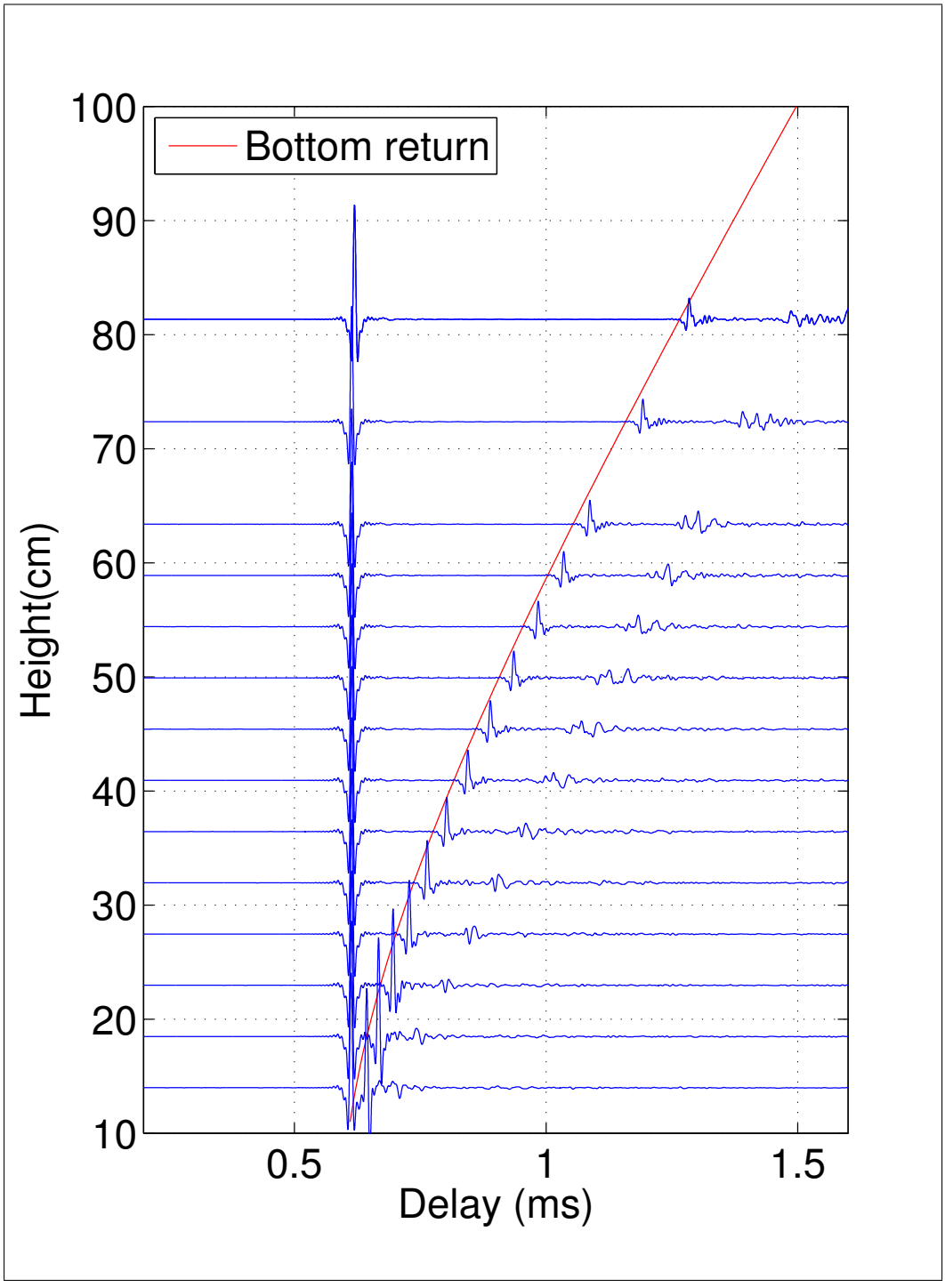

Figure 4.4: Deconvolution of the transducer response for three interface layers made up of water, sand, concrete, and air. The TX is on channel 3 and the RX is on channel 1. The height above the sand was measured between 14 to 82 cm in 4.5 cm increments excluding the 77 cm and 68 cm measurements. Note the curved line indicates the theoretical timing for the direct reflection from the water/sand interface based on the transducer separation and height of the transducers above the sand with a sand depth of 20 cm. This dataset was sand surface 2 from 4th July 2009.

separation between the direct reflection and internal concrete reflections for $h_1 = 15\,\text{cm}$ is 0.020 ms, and at $h_1 = 80\,\text{cm}$, the separation is 0.200 ms. Figure 4.4 clearly shows the trends of direct reflection and internal concrete reflection. The timings shown in Figure 4.4, with the exception of the direct path, are dependent on h_1. The order of the signal returns in Figure 4.4 are constant and their trends can be clearly seen. At 80 cm the direct path, the direct reflection and internal concrete refections, occur at 0.616 ms, 1.286 ms, and 1.486 ms, respectively. The key limitation of this configuration is that the examination of the direct reflection's scattered components is limited by internal concrete reflections. This configuration allows analyses of the critical angle since the specular component is intact for small values of h_1 and the scattered components can be analysed for large values of h_1. Although unnecessary because the sand could be measured at small angles, the angular extent of the scattered components that can be analysed could be improved by placing a pressure release interface, such as closed-cell foam, under the sand, given that the internal concrete reflections occur well before any sand/bottom reflection. The timings of the reflections, and the equations governing them, are described in Section 3.2.2.

4.2 ACOUSTIC AND PHYSICAL PARAMETERS

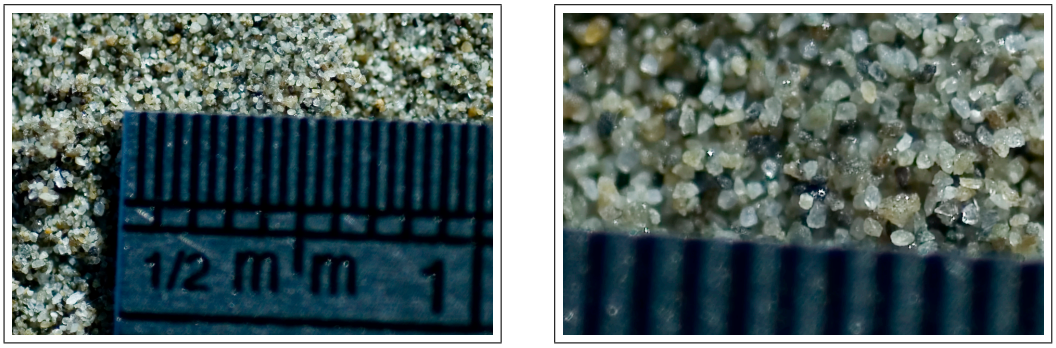

(a) Photo showing the sand over 1 cm with half mm divisions.

(b) Photo showing the sand over 4 mm showing 6 grains per mm, i.e., a grain size of 0.167 mm.

Figure 4.5: Photos showing the sand used in the test tank experiments.

The direct reflection's specular and diffuse components can be used to analyse surface roughness, as described in Section 4.4.1. However to verify the results, the acoustic and physical parameters of the sand should be known, as discussed in Section 4.4. Some of the common physical/acoustic parameters in classifying sand are: grain diameter, M_d, speed of sound, c, bulk density, ρ, and attenuation, α. The average grain diameter of the sand was $0.167\,\text{mm} \pm 0.02\,\text{mm}$. This was determined by taking several photos of a ruler on the sand in different locations and counting the number of grains per mm; a sample photo is shown in Figure 4.5. The speed of sound, c was determined to be $1660\,\text{m}\,\text{s}^{-1}$, by measuring the time delay between

the sand reflection and the concrete reflection. The density, ρ, was determined to be $1950\,\mathrm{kg\,m^{-3}}$ by measuring the weight of a known volume of water saturated sand. The attenuation, α, was determined to be $20\,\mathrm{dB\,m^{-1}}$ by comparing the ideal concrete reflection to the concrete reflection under the sand[1]. These values do not match the parameters shown in Jackson and Richardson [2007] but are similar to the fine sand parameters of $M_d = 0.1593\,\mathrm{mm}$, $\mathrm{c} = 1749\,\mathrm{m\,s^{-1}}$, $\rho = 1941\ \mathrm{kg\,m^{-3}}$, and $\alpha = 25.7\,\mathrm{dB\,m^{-1}}$ found in Hamilton [1980]. Note the difference in the sound speeds between Hamilton [1980] and the tank sand may be the explained by either the pore water being different, i.e., there is fresh water rather than salt in between the grains of sand or that this is different sand.

Knowing these physical/acoustic parameters for the sand allows accurate modelling of the smooth surface reflection coefficient using fluid theory. With knowledge of the smooth surface reflection coefficient, and the surface roughness, the direct reflection can be modelled and analysed. Five different sand surfaces were created in the sonar test tank. The height maps of these surfaces were estimated using the stereo camera setup described in Section 3.4. Before the acoustic test began, approximately two months were spent achieving air-free sand.

The process of achieving air-free sand started when the 20 cm of sand was added to bottom of the sonar test tank. The sand was placed in garbage cans filled with water and allowed to soak for three days. After the sand had soaked it was bucketed up to the tank and swirled into the water. After the sand had settled, the tank was drained and refilled to remove the sediment. At the end of each week, acoustic readings were taken to verify that air was not present in the sand. Towards the end of the filling process an air reflection was detected in the sand. The sand was raked using a garden fork every two days for approximately a month to achieve air-free sand. My conjecture is that the fine silt in the sand trapped air bubbles in the sand because the sand's air-free readings coincided with the reduction of sediments in the tank, however this cannot be substantiated, given that the bubbles in the sand could not be directly observed. It is recommend that for future tank experiments, the sand be fully washed before it is added to the tank.

After air-free sand was achieved, five different sand surfaces were created. To keep the sand air-free, the tank was never fully drained and the surfaces were added to the sand with between 1 m and 0.3 m of water in the tank. For all the surfaces, the process of filling the tank was found to add ripples to the sand. The shallower the water in the bottom of the tank, the higher the ripple peaks and

[1]This reading is the least accurate acoustic parameter used in these experiments and is based on the assumption that for the concrete $\mathrm{c} = 3300\,\mathrm{m\,s^{-1}}$ and ρ= 2400 $\mathrm{kg\,m^{-3}}$. Note these readings are based only on typical concrete parameters. Actual measurement of the concrete parameters was not possible due to the unknowns in the tank construction. The attenuation measurement of $20\,\mathrm{dB\,m^{-1}}$ is an average over the 20 kHz-120 kHz range which is most likely dominated by the lower frequency range. More accurate frequency specific attenuation measurements were hampered by the multiple reflection from the concrete.

the shorter the distance between the peaks. During sand surfaces 1, 2, and 3, the water was approximately 1 m; for sand surfaces 4 and 5, the water depth was approximately 0.3 m, to avoid hypothermia caused by water temperatures between 5°C and 10°C. A description of the surface plus representative height maps are provided in Section 4.2.1 - Section 4.2.5.

Two methods of filling the tank were used. The first process filled the tank using a bucket to diffuse the water from a hose. This process was found to generate currents that caused significant ripples on the surface of the sand. The final solution was a 9.5 m loop of 2 cm diameter pipe placed on top of the sand. This pipe had upward pointing risers inserted every 50 cm. This worked to fill the tank without causing significant roughness on the bottom of the tank. However, when the tank was drained to 30 cm some roughness was still generated by the filling process. This roughness was 1 cm diameter by 0.4 mm deep and located around the edges of the tank. This roughness is visible in some of the height map photos.

4.2.1 Sand surface 1

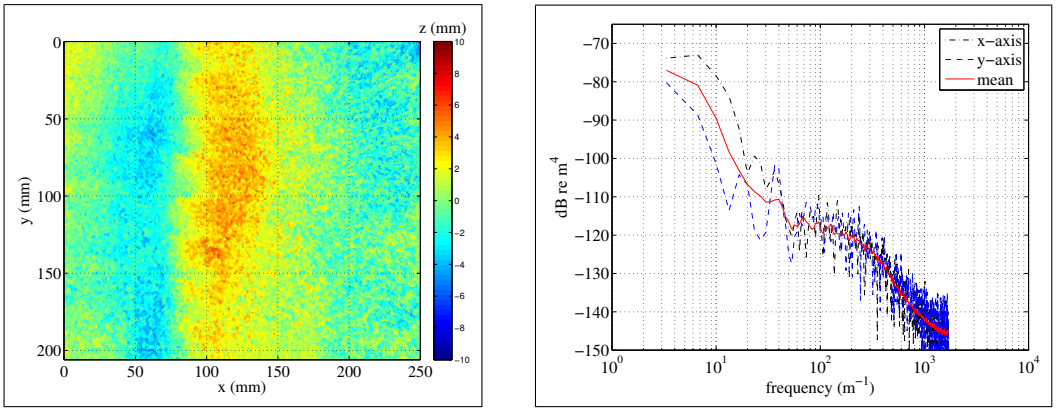

(a) Height map

(b) Roughness spectra in x-direction, y-direction, and average of the cross-sections.

Figure 4.6: Ground truth of the area between the transducer 3 - 1 pair for sand surface 1. The directional ripple seen in (a) produces a peak in the spectrum at 37 cycles m^{-1}. The high frequency spectral slope can also be observed to have a power-law roll-off of -23 dB per decade with an amplitude of -90 dB at 10 cycles m^{-1}.

The first sand test was performed on the 23rd of March 2009. This was an unsuccessful attempt at generating a smooth sand interface. The sand for these tests was smoothed with 1 metre of water in the tank. The tank was then filled slowly using a bucket to diffuse the water. The filling process took approximately 12 hours to complete. During this process the water pressure changed and the hose dislodged from the bucket disturbing the sand on the bottom of the tank. The hose spraying on the sand caused ripples and holes to form in the sand. The water

took approximately two weeks to clear enough to see the damage caused by the hose. Rather than drain the tank and repeat the smoothing and filling process, this surface was used as the first rough surface. The height map and the spectrum of the area between the transducer 3 - 1 pair are shown in Figure 4.6. It was found that the surface reading under all the transducers had minimal relation to the areas under other transducer areas. For this reason, the hydro-dynamic method of adding surface roughness was not used on the other sand surfaces.

4.2.2 Sand surface 2

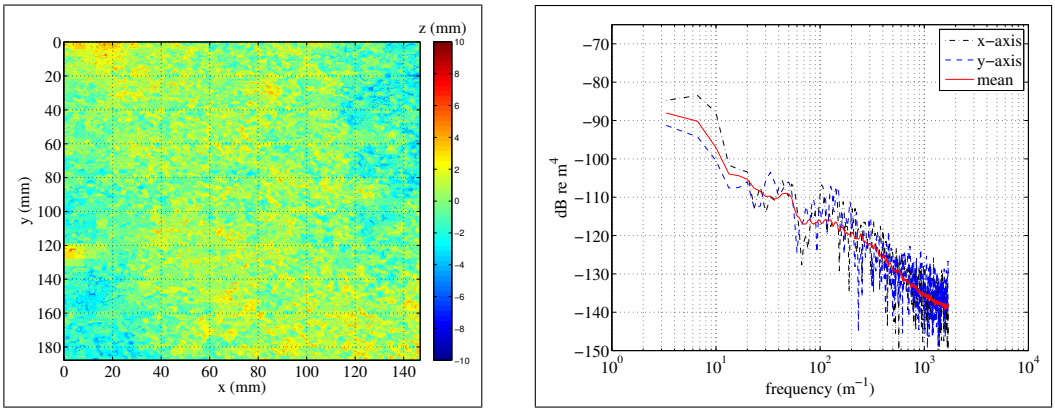

(a) Height map

(b) Roughness spectra in x-direction, y-direction, and average of the cross-sections.

Figure 4.7: Ground truth of the area between the transducer 3 - 1 pair for sand surface 2. The high frequency spectral slope can also be observed to have a power-law roll-off of -25 dB per decade with an amplitude of -100 dB at 10 cycles m^{-1}.

The second set of tank tests were performed on the 4th of July 2009. The pipe system, described in Section 4.2, was used to fill the tank. The process of filling the tank still added some roughness to the sand on the tank bottom that is detected by the bi-static measurements. However, the area between transducers 3 - 1 pair was smooth, both acoustically and optically. The height map is shown in Figure 4.7 and the acoustic response is shown in Figure 4.4. Note, not all of the acoustic and optical readings were valid for this test run. At the end of the first test run the tank cover collapsed. Small bits of wood paint and other debris were scattered over the surface of the sand which caused problems with both the acoustic and optical measurements. The cover of the tank was replaced and the surface of the sand was cleaned. However, not all of the debris was cleared from the tank bottom and this caused problems with the area between the transducer 2 - 3 pair, as discussed in Section 4.4.2. After this test run was complete, the sand surface was cleaned and these problems did not reoccur.

4.2.3 Sand surface 3

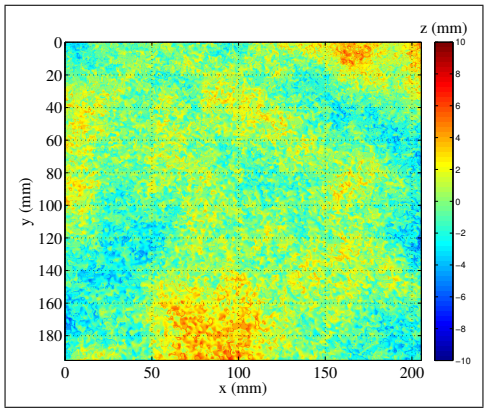

(a) Height map

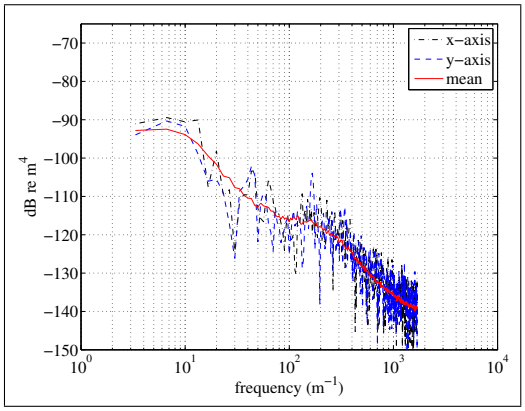

(b) [Roughness spectra in x-direction, y-direction, and average of the cross-sections.

Figure 4.8: Ground truth of the area between the transducer 3 - 1 pair for sand surface 3. The directional ripples seen in (a) produce a peak at 50 cycles m^{-1} in the spectrum. The high frequency spectral slope can also be observed to have a power-law roll-off of -25 dB per decade with an amplitude of -92 dB at 10 cycles m^{-1}.

The third set of tank tests were performed on the 24th of July 2009. To avoid ripples caused by filling the tank, the tank was left full and the roughness was added using a 3 m long pole with a flat block attached to the end. The goal for this sand surface was to achieve a randomly rough surface. This goal was met, however the major problem with this method was that packed sand is difficult to move in a controlled manner using a long pole under the edge of the tank cover. If the tank had a fully removable cover, then adding surfaces to the sand with the tank fully filled would have been the best method. The resulting height map and spectrum produced using this method are shown in Figure 4.8.

4.2.4 Sand surface 4

The fourth set of tank tests were performed on the 31st of July 2009. The goal for this surface was a periodic surface with period of 5 cm. For these tests, the tank was drained to 50 cm and a single 50 mm by 100 mm plank with the end sharpened was used to plough rows in the sand. It was found that the sand did not support much in the way of sharp edges and returned to its previous shape. This method worked better than the sheet metal plough or the rake but a better method would be useful. The general problem was that narrow troughs were created with flat areas in-between them. The resulting height map and spectrum are shown in Figure 4.9.

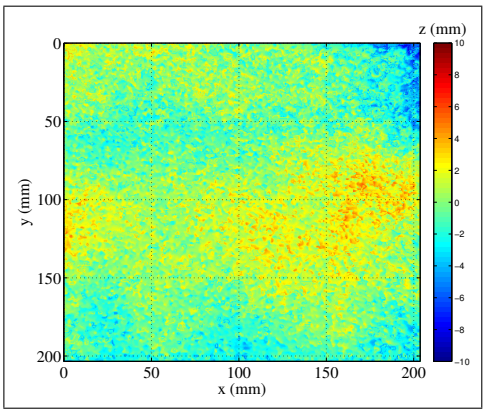

(a) Height map

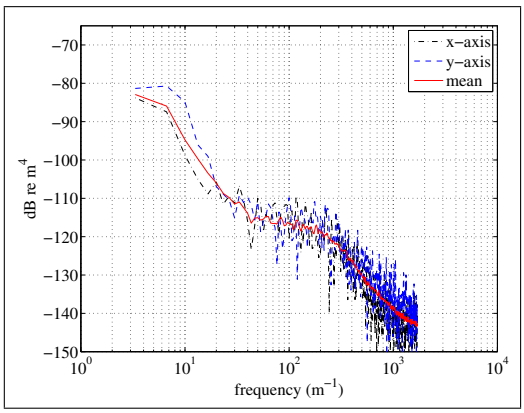

(b) [Roughness spectra in x-direction, y-direction, and average of the cross-sections.

Figure 4.9: Ground truth of the area between the transducer 3 - 1 pair for sand surface 4. The high frequency spectral slope can be observed to have a power-law roll-off of -25 dB per decade with an amplitude of -95 dB at 10 cycles m^{-1}.

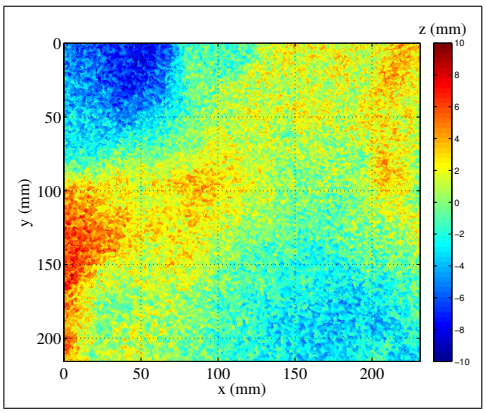

(a) Height map

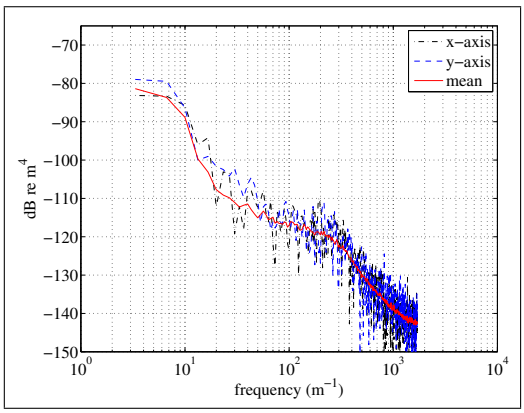

(b) [Roughness spectra in x-direction, y-direction, and average of the cross-sections.

Figure 4.10: Ground truth of the area between the transducer 3 - 1 pair for sand surface 5. The high frequency spectral slope can be observed to have a power-law roll-off of -25 dB per decade with an amplitude of -90 dB at 10 cycles m^{-1}.

4.2.5 Sand surface 5

The fifth set of tank tests were performed on the 14th of August 2009. The goal for this surface was a randomly rough surface. This surface was generated by draining the tank to 30 cm of water over the sand and then using the sharpened end of the 50 mm by 100 mm plank to jab holes in the sand. The process was to jab and turn the 50 mm by 100 mm plank every 10 cm to 15 cm. The resulting height map and spectrum are shown in Figure 4.10.

4.3 FREQUENCY ANALYSIS OF ACOUSTIC RESPONSES

One of the main advantages of spherical transducers is that their frequency and angular dependant beam pattern effects are minimal. Additionally the ITC-1042 transducer used in these experiments has a wide usable bandwidth 30 kHz to 130 kHz, a representative transducer data sheet is shown in Appendix D.4. The spectral plots are produced by windowing the deconvolved time domain responses, shown in Figure 4.11 (b). The deconvolution process, described in Section 3.1.1, normalises the usable spectrum, shown in Figure 4.11 (c). If the plane wave reflection coefficient is valid for the spherical waves, then any deviation from the flat response is caused by either the reflection coefficient or surface roughness. Note, the plane reflection coefficient is not valid for spherical waves when the ranges are close, near the critical angle, or in the case of total internal reflection, i.e., when ϕ_i >critical angle, as discussed in Section 1.3 and Appendix C.2.4.

Two different time windows were used to analyse the reflection coefficient: 460 μs and 256 μs. These window sizes trade time domain resolution for frequency domain resolution. The 460 μs window allows the deconvolved signal to be analysed without affecting the shape of the resulting spectrum. The 256 μs window allows two non overlapping windows to be fitted between the reflected signal and the concrete return. The spectra for the 460 μs and 256 μs windows for a smooth sand surface are shown in Figure 4.11 (c) and (d), respectively.

Using the spectral response from the 460 μs window as well as the deconvolved time domain waveform, the reflection coefficient can be determined as described in Section 4.4.1. Using the spectral responses from the 460 μs and 256 μs windows, the roughness of the surface can be analysed as described in Section 4.5.1. A general overview of the separation of the reflection coefficient from the roughness is described in following two Sections 4.4 and 4.5.1.

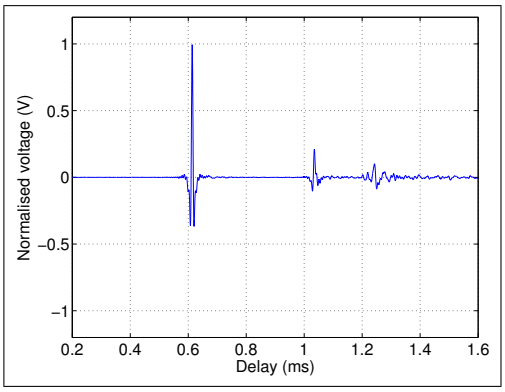

(a) The deconvolved bi-static returns for sand surface 2 from the transducer 3 - 1 pair with the transducers 60 cm from the sand. The signal returns are: the direct path, the specular reflection, and internal concrete refections. These occur at: 0.613 ms, 1.034 ms, and 1.242 ms respectively.

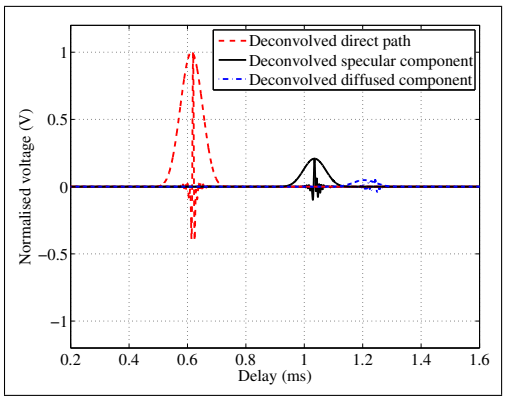

(b) The direct path, specular reflection and diffused reflection shown in (a) windowed separately with a 460 μs window. Note the concrete return interferes with the diffused component and a smaller window is required to analyse it.

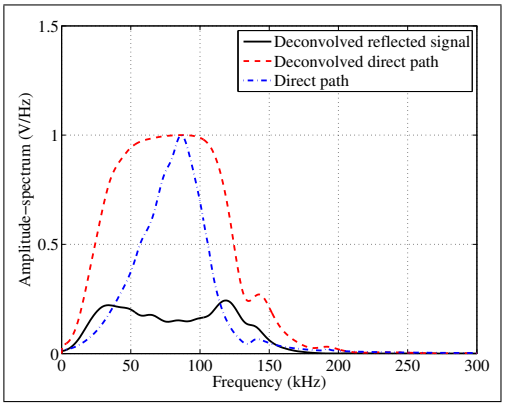

(c) The spectrum of the direct reflection before it has been deconvolved (impulse direct path), the deconvolved direct path, and the deconvolved direct reflection with a 460 μs window.

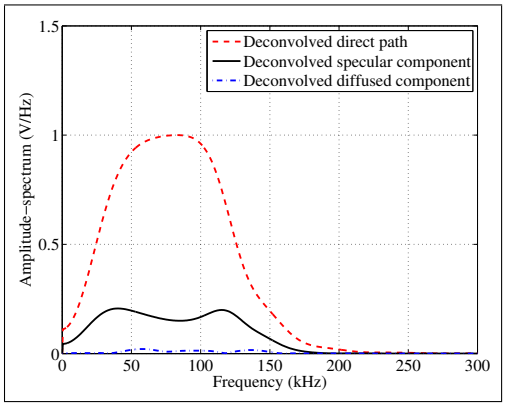

(d) The spectrum of the deconvolved direct path, the deconvolved specular reflection, and the deconvolved diffused reflection with a 256 μs window.

Figure 4.11: These plots show the process used to examine the spectrum of the surface reflection. With a 460 μs window, only a single non-overlapping window of the reflected signal can be made without including the concrete reflection, as shown in (b) and (c). Using a 256 μs window, two non-overlapping windows of the reflected signal can be made without including the concrete reflection. The resulting spectrum is shown in (d).

4.4 REFLECTED SIGNAL WITH ROUGHNESS

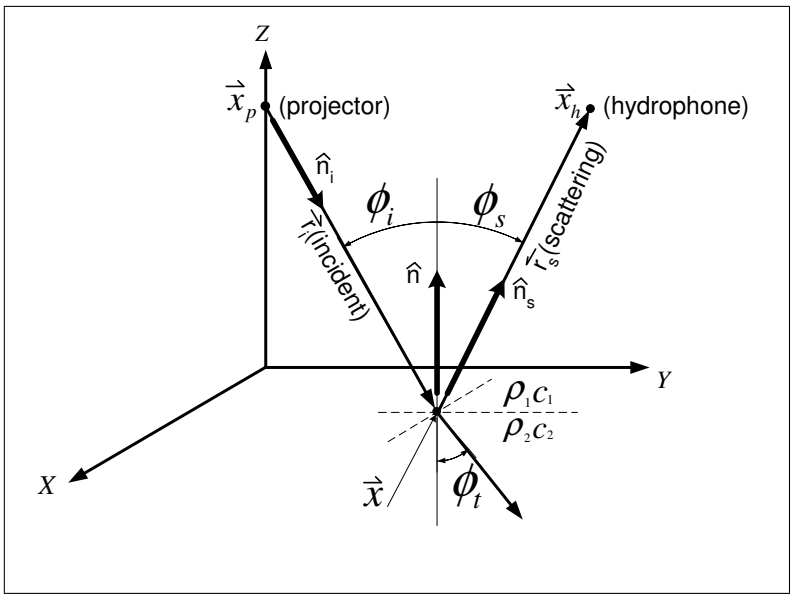

Figure 4.12: Projector and hydrophone configuration.

The reflection of spherical waves from a rough surface can be broken into three aspects: the angular dependence of the plane wave reflecting from a smooth surface as described in Appendix C.1 and Section 2.1, the plane wave to spherical wave conversion as described in Appendix C.2, and the degradation of the reflection coefficient due to roughness as described in Section 2.3.1 and Section 2.3.2. To simplify the problem, it can be broken into two parts: the reflection coefficient with plane wave to spherical conversion and the roughness degradation of the reflection coefficient.

4.4.1 Reflection coefficient with spherical waves

In many applications of the Kirchhoff approximation, the reflection coefficient is separated from the surface statistics. Therefore, for surfaces where this applies, the reflection coefficient can be calculated independently of surface roughness. In these applications the reflection coefficient $\mathscr{R}_{12}$ is moved outside the integral of the general Kirchhoff equation (2.20) [Clay and Medwin 1977]. The major difference to (2.20) is that it uses the average reflection coefficient rather than the continuous reflection coefficient evaluated over the entire surface. The average value of $\mathscr{R}_{12}$ can be used, rather than calculating $\mathscr{R}_{12}$ for all angles of the surface if $\mathscr{R}_{12}$ is slowly changing and if the changes in $\mathscr{R}_{12}$ are minimal [Clay and Medwin 1977]. This indicates that for a surface that can be accurately modelled using the Kirchhoff approximation, the slope and critical angle can be examined independent of the roughness. Figure 4.13 (a) and (b) show the angle dependent peak surface response for the transducer 3 - 1 pair for five different surfaces with the angular measurement of $\phi_i = \phi_s$ varied from

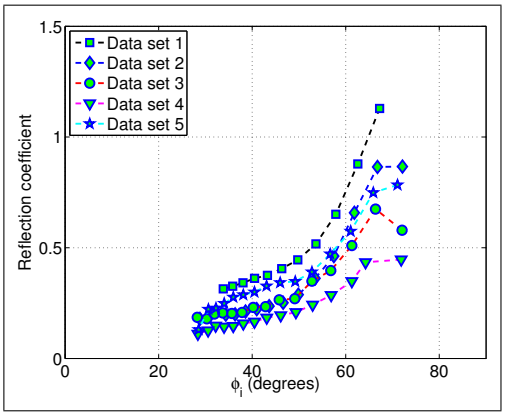

(a) Pre-normalisation sand reflection from the transducer 3 - 1 pair.

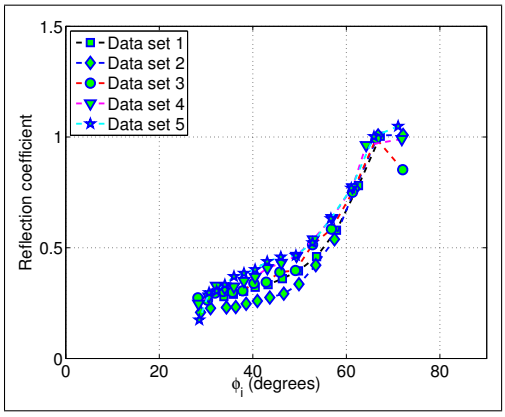

(b) Normalised sand reflection the from transducer 3 - 1 pair.

Figure 4.13: The peak sand response of the bi-static deconvolution for the transducer 1-3 pair. The distance between the transducers is fixed at approximately 95 cm. The height of the transducers above the sand is varied between 15 cm and 80 cm producing angular measurement of $\phi_i = \phi_s$ between 70° and 30°. These plots show the angular dependence of the reflection coefficient on 5 different surfaces; (a) shows the plots for all 5 sand surfaces without normalisation; (b) shows the plots normalised to the reflection coefficient at the critical angle, i.e. approximately 65° for all 5 sand surfaces. The normalisation angle was determined by determining common peak reflection angle on the normalisation plots. The geometry of the test setup is shown in Figure 4.12. Note each data set is from a single bottom realisation.

29° to 73°. These plots show a consistent critical angle at 65° ±2.5°, which translates to a sand sound speed of 1611 $\mathrm{m\,s^{-1}}$, which is consistent with the measured sound speed of 1650 $\mathrm{m\,s^{-1}}$; this measurement assumes a water sound speed of 1460 $\mathrm{m\,s^{-1}}$. The critical angle is consistent over 14 of 15 acoustic measurements. There are two data sets that are outliers: the transducer 1 - 2 pair for test surface 5, and the transducer 3 - 2 pair for test surface 2. The transducer 1 - 2 pair for test surface 5 does not show the critical angle. The transducer pair 3 - 2 for test surface 2 has inconstant levels. These outliers are discussed in further detail in Section 4.4.2.

Excluding the outliers, the critical angle and angle dependent reflection coefficient curves are consistent, as shown in Figure 4.13. Figure 4.13 shows the plots for each transducer pair for all five test surfaces overlaid. Figure 4.13 (a) shows the pre-normalised peak surface reflections. Figure 4.13 (b) shows the peak surface reflections normalised by the critical angle reflection. The pre-normalised plot shows one return level above unity; this is due to constructive interference. Figure 4.14 shows the frequency dependence of spherical waves using the stationary phase approximation as described in Appendix C.2.4. Although this approximation is inaccurate close to the critical angle due to a divide by zero, the frequency dependence before and after the critical angle exists [Brekhovskikh and Lysanov 2003]. Figure 4.14 (a) shows the reflection coefficient for spherical waves at 30 kHz, com-

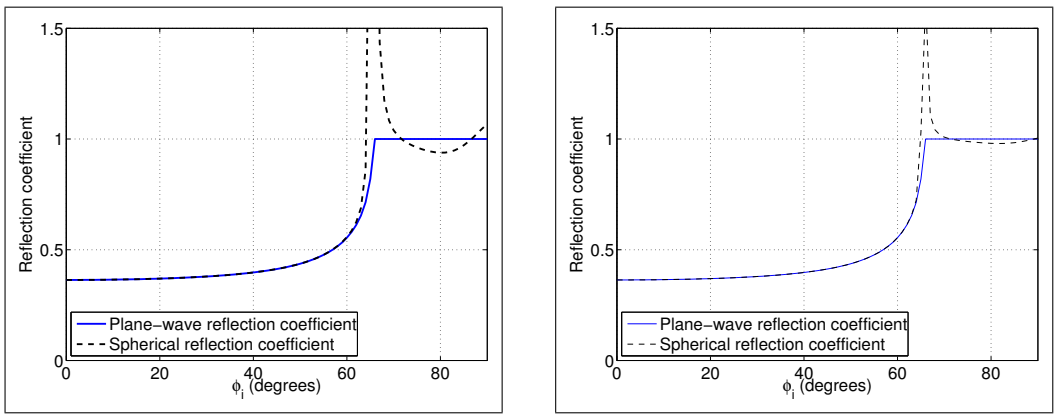

(a) f = 30 kHz (b) f = 120 kHz

Figure 4.14: The reflection coefficient of spherical waves at 30 kHz and 120 kHz using the stationary phase approximation as described in Section C.2.4. These simulations use a density and sound speed of $\rho_1 = 1000\,\mathrm{kg\,m^{-3}}$, $c_1 = 1460\,\mathrm{m\,s^{-1}}$ for the water, $\rho_2 = 1950\,\mathrm{kg\,m^{-3}}$, $c_2 = 1650\,\mathrm{m\,s^{-1}}$ for the sand, and a transducer separation of 95 cm. The primary effect that frequency has on the reflection coefficient is that at lower frequencies the critical angle occurs earlier and the spherical waves cause a larger attenuation after the critical angle, as seen in (a) and (b).

pared to the plane wave reflection coefficient. According to this approximation, at 30 kHz the spherical reflection coefficient exceeds unity 3° before the critical angle, and then dips below unity 7° after. Likewise, at 120 kHz the spherical reflection coefficient exceeds unity 1° before the critical angle, and then dips below unity 4° after, as shown in Figure 4.14 (b). The spherical wave frequency dependent behaviour is shown in the spectral plots in Figure 4.15 (a) through (f). Note, the generation of the spectral plots are described in Section 4.3. The high frequency peak is shown in Figure 4.15 (d) and it starts to decrease in Figure 4.15 (e) which indicates a critical angle between 62° and 65°. Across the 13 measurements, the 120 kHz peak is consistently between 62° and 65°. Although this data set has a high frequency peak at 62°, some of the other rough surfaces have the peaks at 65°. This indicates an uncertainty of 3° for the critical angle which translates to a sound speed uncertainty of $43\,\mathrm{m\,s^{-1}}$, i.e., a sound speed between $1611\,\mathrm{m\,s^{-1}}$ and $1654\,\mathrm{m\,s^{-1}}$.

Given that the sound speed in the second medium is $1650\,\mathrm{m\,s^{-1}}$, the density of the second medium can be calculated by matching the reflection coefficient curve. Figure 4.16 shows the effect of changing ρ_2 on the reflection coefficient. Looking at these plots, it is obvious that the major effect of changing ρ_2 is in amplitude before the critical angle, e.g., at 57° for $\rho_2 = 2250$, 2050, 1950, and $1750\,\mathrm{kg\,m^{-3}}$ the reflection coefficient is 0.55, 0.52, 0.50, and 0.46, as shown Figure 4.16 (c). If the surface was perfectly smooth and the transducer had no beam-pattern, then determining ρ_2 would be as simple as measuring return strength at a specific angle. In reality, the surface is not perfectly smooth and the transducers have a beam-

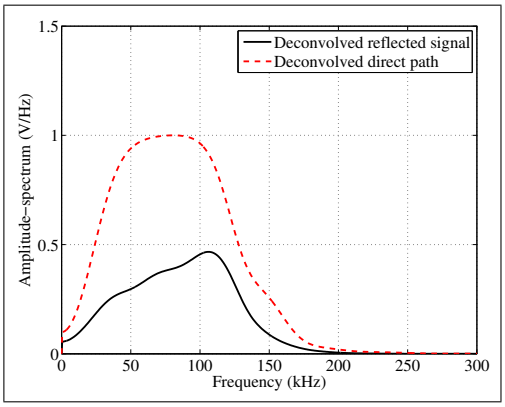

(a) $\phi_i = \phi_s$ =52°.

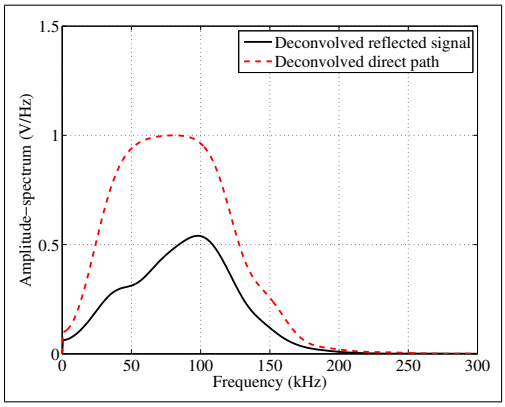

(b) $\phi_i = \phi_s$ =55°.

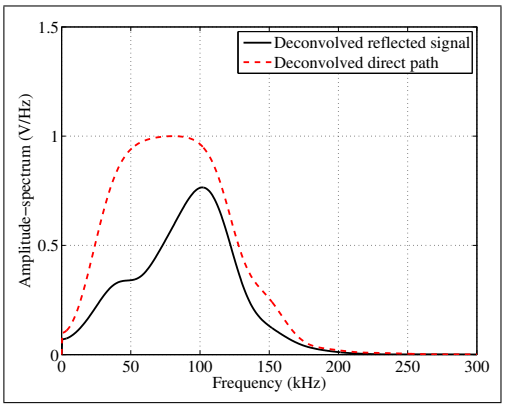

(c) $\phi_i = \phi_s$ =58°.

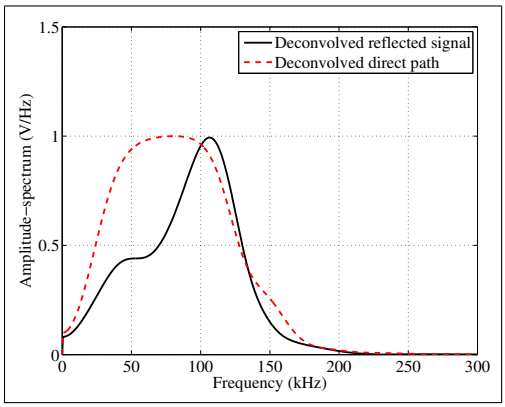

(d) $\phi_i = \phi_s$ =62°.

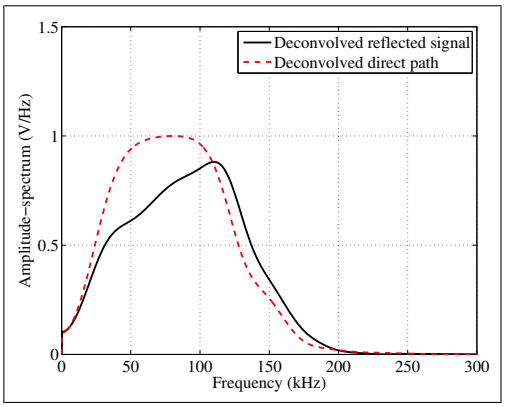

(e) $\phi_i = \phi_s$ =65°.

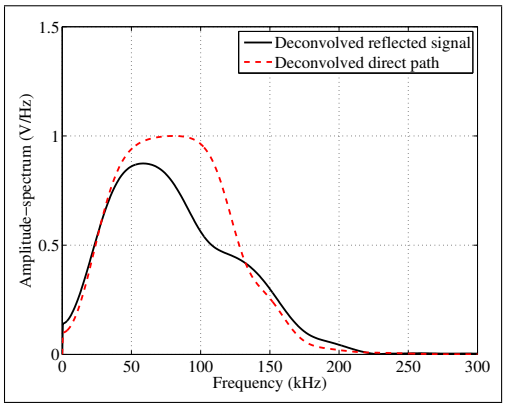

(f) $\phi_i = \phi_s$ =70°.

Figure 4.15: The spectrum of the bi-static deconvolution of sand surface 5 for the transducer response for the transducer 3 - 1 pair. These plots show the spherical wave frequency and angular dependence. As seen in Figure 4.14, spherical waves have a frequency dependence around the critical angle. This can be seen by by examining the spectral response of the reflected signal around the critical angle. These plots show that the dependence around the critical angle ends at approximately 55°. For this reason, the bi-static analysis of the reflection coefficient should be 55° or less. The method for generating the spectrum of the specular reflection is described in Section 4.3. Note the spectrum of the reflected signal in (a) through (e) are single realisations and increase with frequency, contrary to what is expected for an average signal. The trends of a single realisation are not statistically relevant as explained Section 4.5.1.

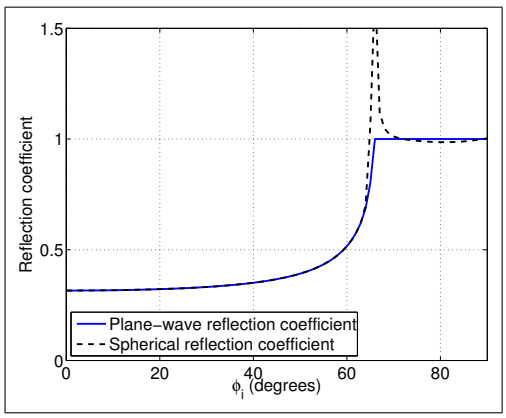

(a) ρ =1750 kg m^{-3}

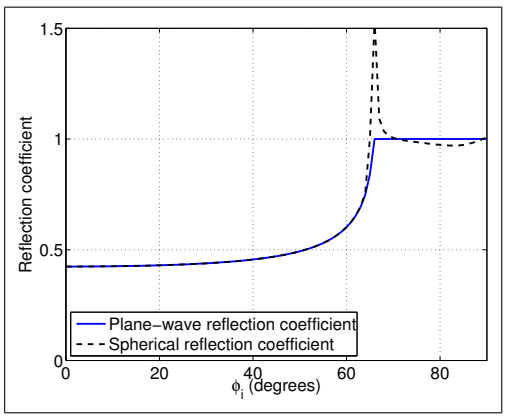

(b) ρ =2250 kg m^{-3}

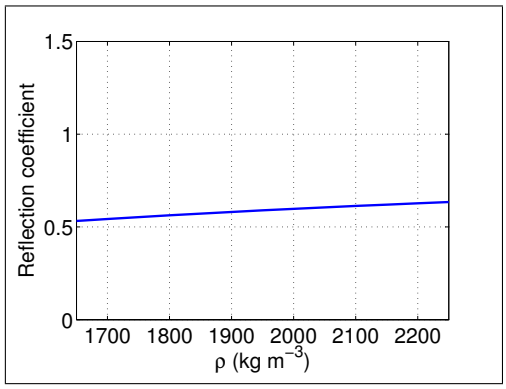

(c) $\phi_i = 57°$

Figure 4.16: These plots show that ρ only affects the amplitude of the pre-critical angle reflection coefficient. The reflection coefficient is generated using stationary phase approximation as described in Section C.2.4. These simulations are at 120 kHz and use sound density and sound speed of $\rho_1 = 1000\,\mathrm{kg\,m^{-3}}$, $c_1 = 1460\,\mathrm{m\,s^{-1}}$ for the water, ρ_2 varied between 1750 kg m^{-3} and 2250 kg m^{-3}, $c_2 = 1650\,\mathrm{m\,s^{-1}}$ for the sand, and a transducer separation of 95 cm.

pattern. The beam-pattern issues are described in Section 3.1.3 and Appendix D.1. Examining the normalised peak of three bi-static transducers at 57° indicated a reflection coefficient ranging from 0.43 to 0.56. This translates to a value of ρ between 1700 kg m^{-3} and 2300 kg m^{-3}. The measured value of $\rho_2 = 1941\,\mathrm{kg\,m^{-3}}$ indicating ±15% error[2].

This method has several sources of error. Firstly, the normalisation at the critical angle is a source of error. This is because the angular measurements are sparse and small angular changes can significantly change the normalisation amplitude, e.g., if the critical angle is early or late then this peak can be low. Secondly, the beam pattern of the transducers can change the amplitude by 1 dB over 10° or 2 dB over 30°. A -1 dB variation in the reflection coefficient from 0.5 to 0.44 which

[2]The density of the sand was measured by filling a 330 cm x 330 cm x 200 cm container with water saturated sand and measuring its mass and then subtracting the mass of the container.

translates to a ρ_2 value of 1650 or an error of 25% in the density reading. By taking more readings, ambiguities in the critical angle can be reduced and normalisation can be improved. The beam pattern ambiguity is more problematic. This is because correcting for the transducer beam pattern requires them to be rigid to make their characterisation repeatable and therefore useful. Solutions to the beam pattern problem are discussed in more detail in Chapter 5.

4.4.2 Test surface outliers

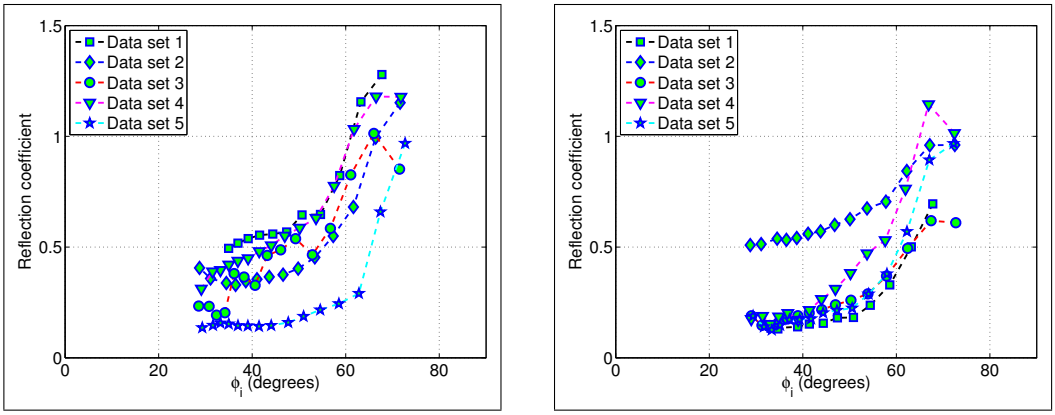

(a) Sand reflections from transducer 1 - 2 pair.

(b) Sand reflection from transducer 3 - 2 pair.

Figure 4.17: The pre-normalised peak response of the bi-static deconvolution for transducer 1 - 2 and 3 - 2 pairs. The outlier for the transducer 1-2 pair is data set 5 (sand surface 5), and the outlier for the transducer 3-2 pair is data set 2 (sand surface 2).

The real world empirical results are never as simple as simulated results and there are always outliers that need to be excluded from the data set. The two outlying data sets that were excluded are: test surface 2 transducer pair 3-2 and test surface 5 transducer pair 1-2 , as shown in Figure 4.17.

The outlier shown in Figure 4.17 (b) transducer pair 3 - 2 test surface 2 still has the critical angle at the correct location, however, the overall reflection coefficient is higher than any of the other plots. The deconvolved waterfall plot shown in Figure E.8 shows a ringing on the deconvolved direct reflection that is not present on the direct path. This is consistent with two signal sources causing constructive interference but the height map of the surface did not show any features that would generate this return. A possible explanation was that the wood or pieces of shell lying on the sand may have caused this problem. The surface of the sand was cleaned before any additional tests were performed and this problem did not reoccur after the sand surface was cleaned. Note, the effect of cleaning the sand could not be verified because the surface roughness of the sand was changed during the process of cleaning the sand.

The outlier shown in Figure 4.17 (a) transducer pair 1 - 2 test surface 5 is a periodic surface with a geometry that produces constructive interference at the critical angle. Near the critical angle the two reflections merge, doubling the amplitude. The deconvolved waterfall plot shown in Figure E.9 shows the two reflections merging near the critical angle. This outlier masks the effects of the reflection coefficient. Both of these data sets have been excluded from the results.

4.5 SURFACE ROUGHNESS ANALYSIS

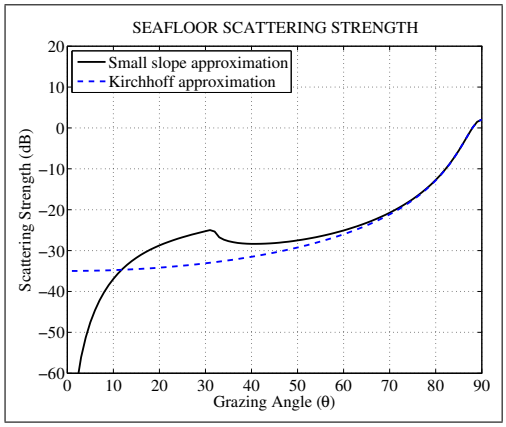

(a) Mono-static comparison between the Kirchhoff and the small slope approximations.

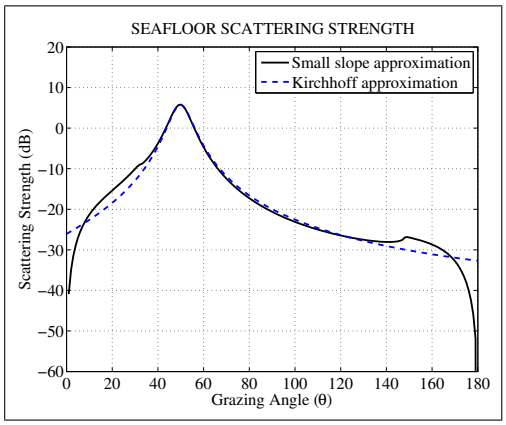

(b) Bi-static comparison between the Kirchhoff and the small slope approximations with $\phi_i = 40°$.

Figure 4.18: Assuming the small slope approximation to be the more accurate, these plots show the region of validity for the Kirchhoff approximation. For the mono-static configuration, shown in (a), the Kirchhoff approximation is only accurate for grazing angles between 55° and 90° degrees. For the bi-static configuration, shown in (b), the Kirchhoff approximation is only accurate for grazing angles between 30° and 130°. These simulations were run for: a_ρ=1.845, v_p=1.1782, δ_ρ=0.01624, γ_2=3.00, and ω_2=0.0000141, at 80 kHz.

The Kirchhoff approximation, described by (2.67) in Section 2.3.2, separates the roughness from the surface statistics. Figure 4.18 shows the region of validity for the Kirchhoff approximation assuming that the small slope approximation is the more accurate [Jackson and Richardson 2007]. The limitations of the Kirchhoff approximation, for the mono-static configuration, can be seen in Figure 4.18 (a). Note the mono-static configuration is discussed because it is simpler to understand, but the same principles apply to the bi-static configuration. There are two key differences in the results of the Kirchhoff and small slope approximations: the first difference occurs at the critical-angle which causes a peak at approximately 30°, this is because the Kirchhoff approximation does not account for the critical angle; the second difference is below 10° where the Kirchhoff approximation gives a high returns at small grazing angles. For Figure 4.18 (a), these differences in the diffused reflection

are 25 dB below the specular reflection and therefore have a small contribution to the reflected signal. However, as roughness increases, the contribution of diffused scattering increases and therefore these errors become more significant.

The angles sampled in the mono-static geometry with a window time of 256 μs are 43°, 39°, 37°, and 35° for transducer heights of 45 cm, 55 cm, 65 cm, and 75 cm, respectively. This indicates that rough surfaces at close ranges exceeded the validity of the Kirchhoff approximation. For this reason, heights of 55 cm or greater are used to evaluate the surfaces.

The reason that the Kirchhoff approximation was chosen for this roughness analysis is that the reflection coefficient and the roughness can be treated as two separate parameters. Using this method allows the surface to be normalised by the reflection coefficient and then the surface roughness can be analysed independently. The spectrum of the rough surface scattering can be generated either by using the roughness statistics, as described in Section 2.3.2, or by using the mean of 12 or more simulated surfaces responses using the simulation process described in Section 2.2.2. Note, multiple realisations are required for the spectrum to converge to a consistent result, this is described in more detail in Section 4.5.1. The statistical analysis described in Section 2.3.2 is valid for $2 < \gamma_2 < 4$ [Jackson and Richardson 2007]. This limitation is due to exponents in (2.3.2) exceeding 0 when $\gamma_2 < 2$ and the numeric integration (2.67) becomes erroneous. The surfaces generated in the sonar test tank had values of $2 < \gamma_2 < 3$ (spectral roll-off between 20 dB per decade and 30 dB per decade). Figure 4.18 was generated using MATLAB software based on Jackson [2000].

4.5.1 Rough surface frequency response

To understand how the roughness characteristics (γ_2 and ω_2 defined in Section 2.3.4) can be determined, it is useful to look at scattering strength and its frequency dependence as shown Figure 4.19. Figure 4.19 shows that the greatest spectral difference created by changes in γ_2 occurs during the transition between specular and diffused reflection, i.e., 70° to 90°. Note, Figure 4.19 was generated using MATLAB software based on Mourad and Jackson [1989]. After the transition to diffused scattering (0° to 70°), the roughness has minimal effect on spectral slope with the main difference being in amplitude. With a directional transducer, these plots could be reproduced with a single transducer and sweeping the angle. This would require multiple readings at both different angles and different locations. The frequency ambiguity would be based on the length of the pulse and the angular ambiguity would be determined by the beam-pattern of the transducer.

With a single spherical transducer in the mono-static configuration, the same plot can be reproduced with a single test producing the angular data, provided it is moved to acquire additional realisations. However, the angular ambiguity, frequency

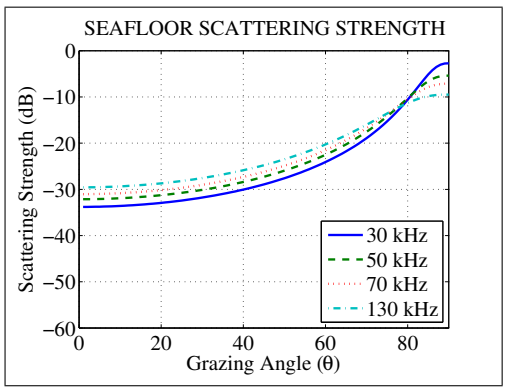

(a) γ_2=3.25 and ω_2=0.00014.

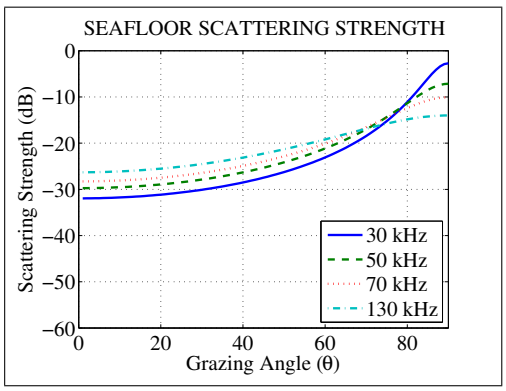

(b) γ_2=3.00 and ω_2=0.0000684.

Figure 4.19: These plots use Kirchhoff approximation and the acoustic parameters for the sand used in the sonar test tank . The parameter for the sand are: a_ρ=1.845, v_p=1.1782, and δ_ρ=0.01624. The values of ω_2 were chosen to normalise the spectral response at 30 kHz. These plots show the effect of changing γ_2 on the scattering strength for a mono-static configuration.

ambiguity, and distance of the transducer above the seafloor are now all linked. Figure 4.20 shows the results of two individual realisations and the average of 12 realisations. The simulations generate an impulse response and the spectrum of the waveform of interest is then applied. The resulting signal is then converted to baseband and the magnitude of the envelope can then be evaluated. The timing was set up to use the centre of the waveform as the zero time. Any waveform can be applied to the impulse response provided the bandwidth of the waveform does not exceed the bandwidth of the impulse response that was generated. The waveform used to generate these plots was a 120 kHz, three-cycle waveform with an exponential ramp-up and ramp-down. This same process has been successfully applied to the deconvolved signal in the sonar tank test environment with the bandwidth of the waveform limited to be between 30 kHz and 130 kHz.

Figure 4.20 shows the envelopes for two different simulated seafloors. Figure 4.20 (a) is for a seafloor with the roughness spectrum described in Figure 4.21(a) and (b). Figure 4.20 (b) is the response for a seafloor with the roughness spectrum described in Figure 4.21 (c). All of the simulations are of a 3 m by 3 m surface with the transducers equally spaced; this means that for each simulated surface there are three transducer locations, as there are in the sonar tank described in Section 3.1. For these simulations, the transducers were 65 cm above the seafloor and a minimum of 1 m from the seafloor edge. Figure 4.20 (c) and (d) show the average amplitude response mapped onto the seafloor. The round spot is the specular component from the area directly under the transducer. The transducer is 1 m from the edge of the seafloor. This limits the valid angular range to 57°. Note, the size of the seafloor was chosen to roughly correspond to the tank edge interference for a tank diameter

of 3.5 m. Figure 4.20 (a) and (b) compare an individual realisation with the average of 12 realisations. It has been seen in the simulated responses that a single realisation of diffused scattering component (between 20° and 57°) can deviate from the average by 17 dB.

Figure 4.20 (a) shows that the specular component (between 0° and 15°), deviates by 6 dB. Although individual realisations follow the trend, they are variable and to acquire accurate measurements the average must be examined. Note, the individual realisations are representative plots, i.e., the worst case plots had deviations of up to 12 dB for the specular components. This method gives a good view of the angular dependence of the seafloor, although its response is a weighted frequency average[3].

With these plots it can be seen that the fewer the cycles in the pulse, the better the spatial resolution and the worse the frequency resolution. If the extreme case is taken and the entire available spectrum is used, i.e., the impulse response or deconvolved signal would be used, then the signals would be an average of the entire frequency range. The spectrum of the impulse response can be analysed by windowing a range of angles. This is accomplished by using the windowing method described in Section 4.3. Figure 4.22 (a) and (b) show a single realisation from two different surfaces. Both of these surfaces show an increase in the specular component of reflected signal with frequency. This contradicts the expected results shown in Figure 4.19 (a) and (b), which show that the reflected signal should decrease with frequency. After examining all the spectra of the reflected signals, the only ones that match are the smooth surface reflections from sand surface 2, shown in Figure 4.11 (c) and (d). There are two reasons for this: firstly, this window includes both the specular and diffused component of the reflected signal averaged from 0° to 25°, and secondly, a single realisation of the specular component of the reflection is meaningless, given that it can vary by up to 12 dB between different realisation of a surface with the same roughness statistics. This was found to be true of both the tank test results and the simulated results. The diffused component of the reflection, the dash dot line, shown in Figure 4.22 (a) and (b), follows the expected trends better; however, it is still inaccurate.

The sonar tank test configuration samples only three realisations of each seafloor. It was found that averaging these realisations was insufficient to observe the spectral trends of the seafloors generated in the test tank. For this reason, simulated seafloors are used to show the behaviour of averaging the responses. Figure 4.23 shows the specular response and Figure 4.24 shows the diffused response for three different seafloor roughness spectrums. Figure 4.25 shows the specular responses for simulated surface 4 using 1, 3, 12, and 48 realisations. As can be seen by comparing

[3]During early tests these plots were generated by performing three cycle tests at 30 kHz, 40 kHz, 70 kHz, and 110 kHz. It was later discovered that the same results could be obtained with a single test using the deconvolved impulse response.

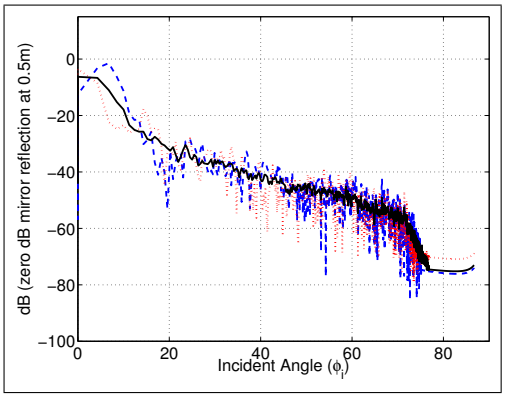

(a) The envelope of a 120 kHz three cycle pulse for a mono-static configuration. The pulse has an exponential ramp-up and ramp down. The surfaces simulated had a roll-off of 30dB per decade and a 10 cycle amplitude of -90 dB.

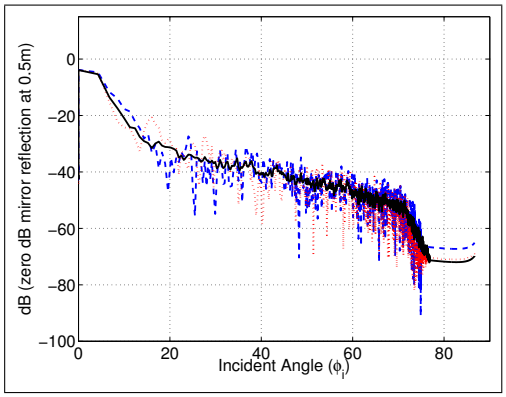

(b) The envelope of a 120 kHz three cycle pulse for a mono-static configuration. The pulse has an exponential ramp-up and ramp down. The surfaces simulated had a roll-off of 20dB per decade and a 10 cycle amplitude of -108 dB.

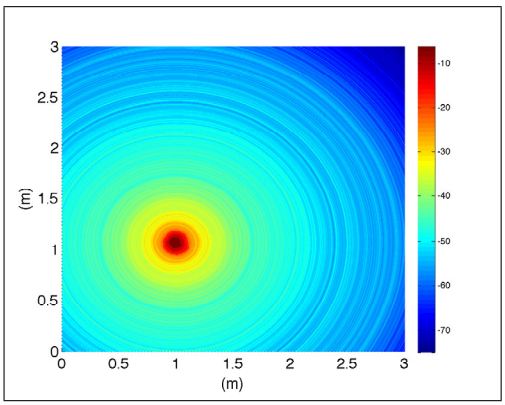

(c) The average of 12 envelopes shown in (a) mapped onto a 3 m x 3 m surface based on the timing.

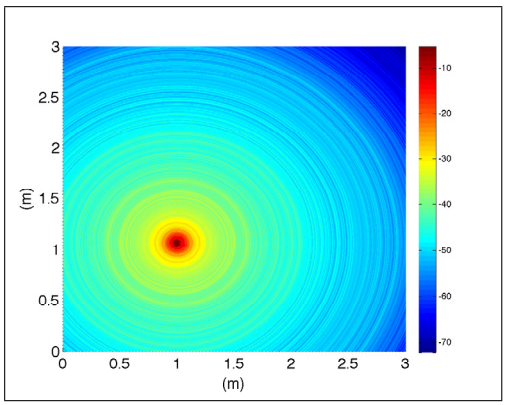

(d) The average of 12 envelopes shown in (b) mapped onto a 3 m x 3 m surface based on the timing.

Figure 4.20: Shows an alternate method of analysing the frequency dependant roughness response using the envelope of a three cycle pulse. Once the signal has been deconvolved then any signal can be applied to the spectrum provided there is adequate bandwidth. Although only the 120 kHz response is shown the 70 kHz, 50 kHz, and 30 kHz responses can easily be generated allowing the frequency dependance to be analysed. The key observations that can be made is that the 12 realisations (the solid line) are enough to see the trends of the reflection and that although the individual realisations (the dashed and dotted lines) follow the trend of the average values, they have variations of greater than 10 dB.

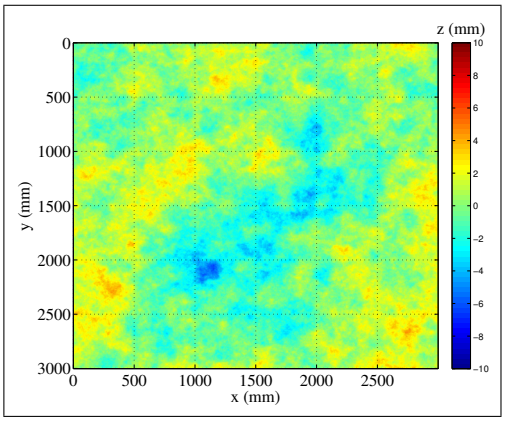

(a) Typical height map for a simulated surface with the spectrum shown in figure (b).

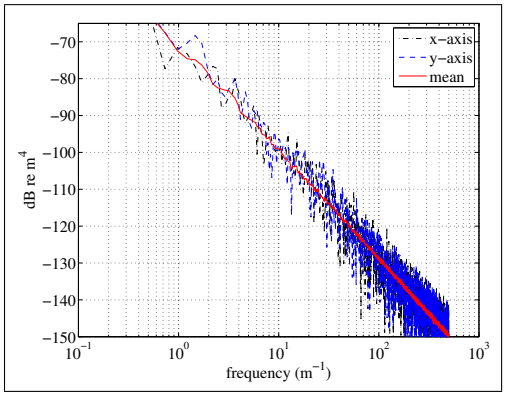

(b) Power spectrum of a surface with a roll-off of 30dB per decade and a 10 cycle amplitude of -100 dB. This spectrum was used in simulation set 1.

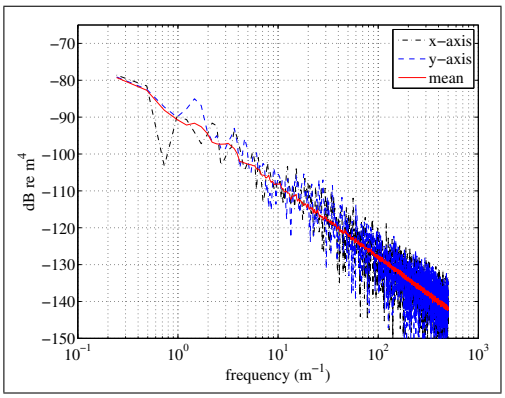

(c) Power spectrum of a surface with a roll-off of 20dB per decade and a 10 cycle amplitude of -108 dB. This spectrum was used in simulation set 2.

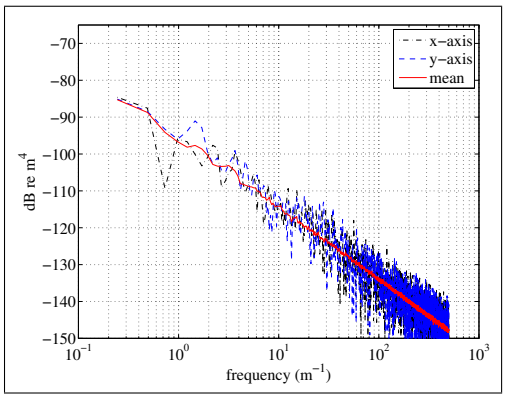

(d) Power spectrum of a surface with a roll-off of 20dB per decade and a 10 cycle amplitude of -114 dB. This spectrum was used in simulation set 3.

Figure 4.21: The spectrum of the simulated surfaces used in simulation sets 1, 2, and 3. These surfaces were generated using the techniques described in Section 2.3.4.

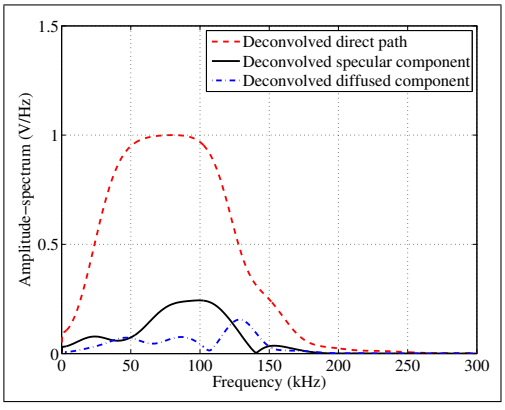

(a) Sand set 4.

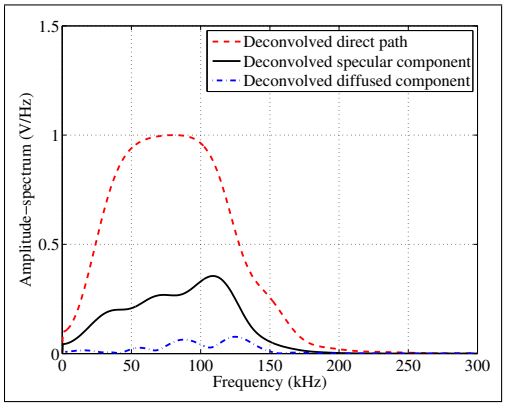

(b) Sand set 5.

Figure 4.22: The spectrum of bi-static deconvolution of the transducer 3 - 1 pair for sand surfaces 4 and 5 at 35°.

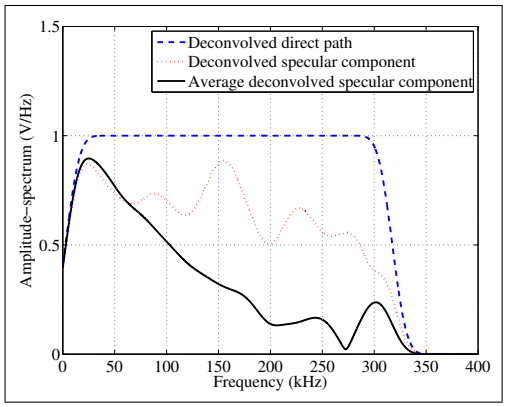

(a) The bi-static configuration using simulation set 1 surfaces.

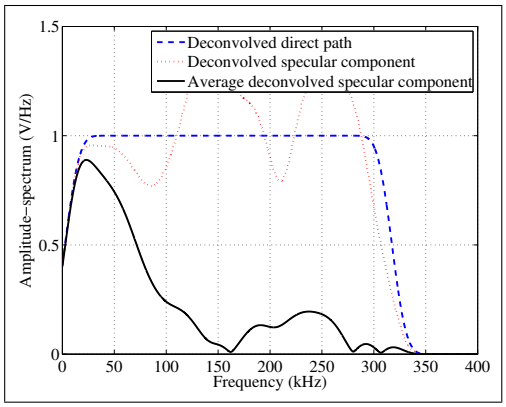

(b) The mono-static configuration using simulation set 1 surfaces.

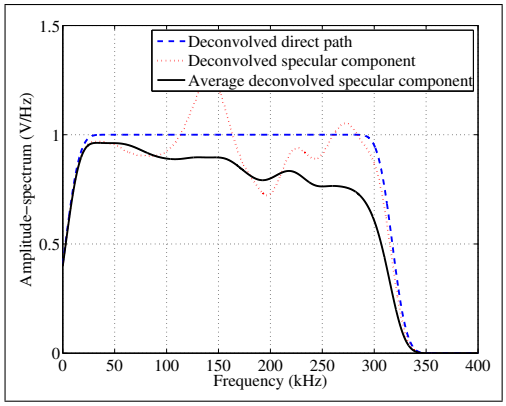

(c) The mono-static configuration using simulation set 2 surfaces.

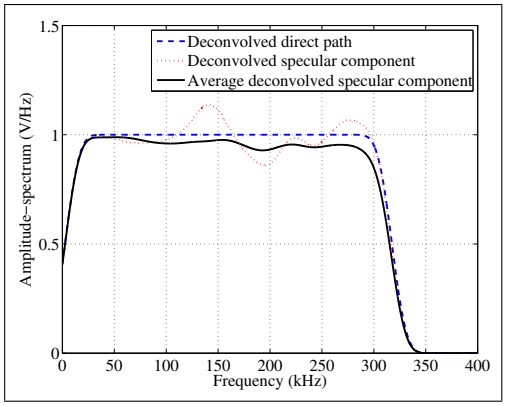

(d) The mon-static configuration using simulation set 3 surfaces.

Figure 4.23: These plots show the spectrum of the specular component of the direct reflection. The spectrum of the direct path is the dashed line. There are two versions of the specular component of the direct reflection shown. The first version (the dotted line) is a single realisation of the specular component. The second version (the solid line) is the average of 12 realisations of the specular component. The time domain signal for the diffused and specular components uses a 256 μs window as described in Section 4.3. The two key things to be observed in these figures are: firstly, a single realisation of the specular components does not resemble the average value; secondly, the average values of the specular components decreases as the frequency increases. The roughness spectrum used to simulate these responses is described in Figure 4.21.

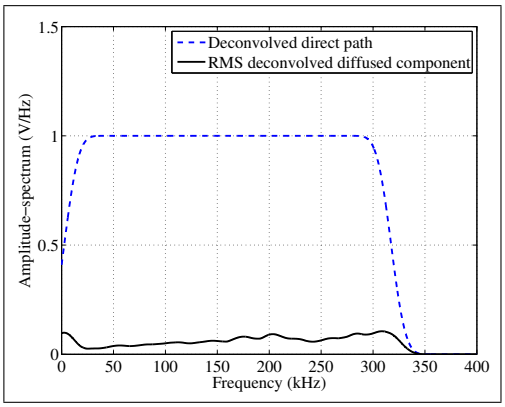

(a) The bi-static configuration using simulation set 1 surfaces.

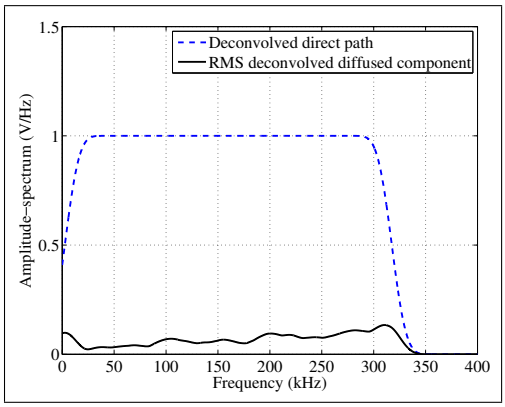

(b) The mono-static configuration using simulation set 1 surfaces.

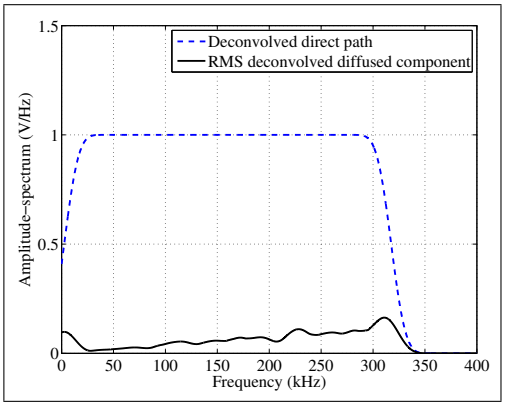

(c) The mono-static configuration using simulation set 2 surfaces.

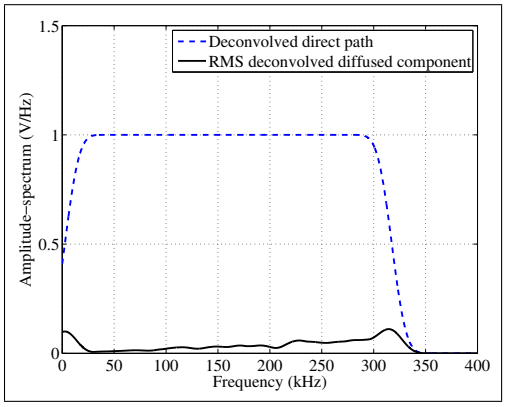

(d) The mono-static configuration using simulation set 3 surfaces.

Figure 4.24: These plots show the spectrum of the diffused component of the direct reflection. The spectrum of the direct path is the dashed line. The rms average of 12 realisations of the diffused component of the direct reflection is the solid line. The time domain signal for the diffused component uses a 256 μs window as described in Section 4.3. The key things to be observed are as follows: firstly, that the rms value, rather than the average value is used since the diffused component is incoherent; and secondly, the rms values of the diffused components increases as the frequency increases. The roughness spectrum used to simulate these responses is described in Figure 4.21.

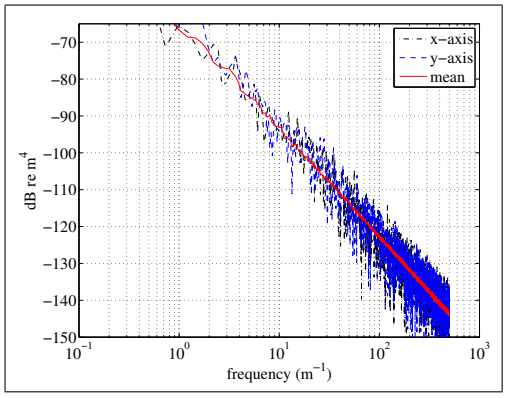

(a) The spectrum of simulation set 4. The simulated roughness spectrum has a roll-off of 30 dB per decade and a 10 cycle amplitude of 94 dB.

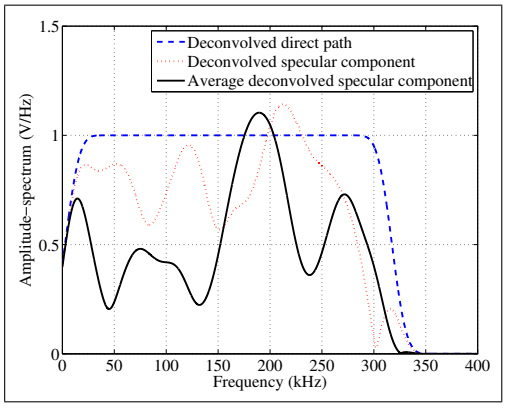

(b) The spectrum of the specular component using 3 realisations of simulation set 4 surfaces.

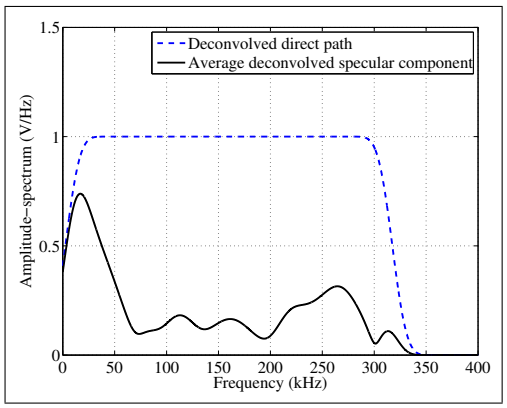

(c) The spectrum of the specular component using 12 realisations of simulation set 4 surfaces.

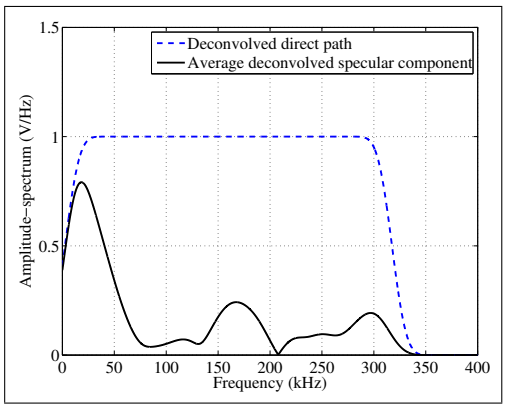

(d) The spectrum of the specular component using 48 realisations of simulation set 4 surfaces.

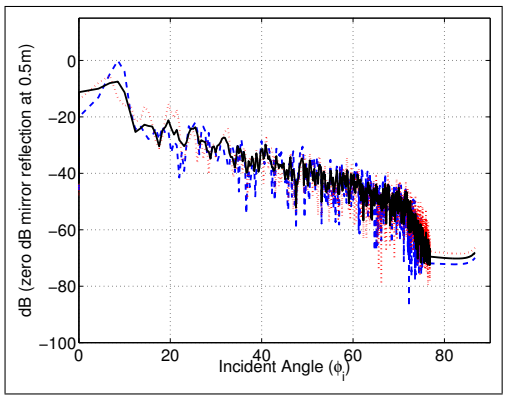

(e) The envelope of a 120 kHz three cycle pulse for a mono-static configuration using 3 realisations of simulation set 4 surfaces.

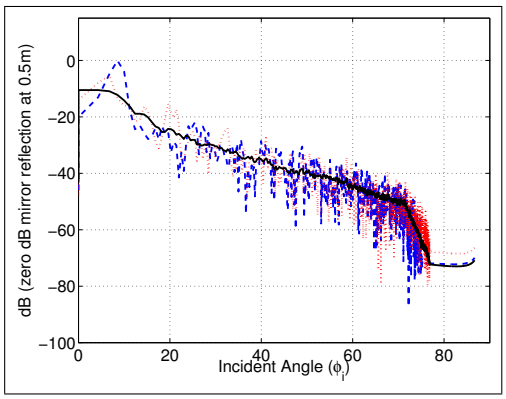

(f) The envelope of a 120 kHz three cycle pulse for a mono-static configuration using 48 realisations of simulation set 4 surfaces.

Figure 4.25: (a) shows the spectrum of simulation set 4; (b), (c), and (d) show the spectrum of mono-static response for the specular component of the direct reflection for averages of 3, 12, and 48 realisations. (e) and (f) show the 120 kHz envelopes for 3 and 48 realisations. The spectrum shown in plot (b) has minimal resemblance to that shown in (d), this was found to be true except for relatively smooth surfaces. From this it can be concluded that 3 realisations are insufficient for the spectral responses to converge.

the results of Figure 4.23 (c) and Figure 4.25 (d), the spectral response converged at 12 realisations. The simulations of surfaces 1, 2, and 3 only had 12 realisations generated to minimise the time required to run the simulations. It was found that the greater the roughness, the more seafloor realisations that were required for the spectra of the specular and diffused component to converge.

The deconvolved specular component needs different processing than a waveform or waveform envelope because it is an impulse. Since it is coherent, it can be averaged and the average response of the incoherent (the diffused component) signal is reduced as the number of averages increases. Likewise, the diffused component must be analysed using an rms average because it is incoherent. Because the specular component is coming from a single angle and can be analysed independently of the diffused component, there is no angular ambiguity. However, the greater the amplitude of the diffused component, the greater the number of realisations required to minimise its effect.

4.6 RESULTS SUMMARY

The acoustic impedance of the seafloor can be analysed and determined using a single realisation of the seafloor measured at multiple angles using a bi-static configuration, as described in Section 4.4.1. The analysis of the seafloor roughness is not practical with the current spherical transducer test configuration, as described in Section 3.1. Using spherical transducers, the specular and diffused component of a rough surface reflection can be analysed over a large range of frequencies and angles without changing the configuration. However, for this data to be meaningful, multiple realisations of the rough surface are required. Both the mono-static and bi-static configurations are useful for analysing the specular component. Furthermore, the mono-static configuration can be used to analyse the angular-dependent diffused scattering component. The bi-static configuration is unsuitable for this purpose, because the diffused scattering component is simultaneously received from multiple angles in this configuration, as discussed in Section 2.3.3.2.

Figure 4.26 shows the simulated results for a mono-static configuration with surfaces roll-offs of 20 dB and 30 dB per decade. If the Kirchhoff approximation is valid for the region being evaluated then the surfaces can be normalised by their reflection coefficient. This then allows the surface roughness to be analysed independent of the reflection coefficient. These simulated surfaces have a 10 cycle m^{-1} amplitude range of -90 dB re m^4 to -108 dB re m^4 for the 20 dB per decade roll-off and 10 cycle m^{-1} amplitude range of -94 dB re m^4 to -112 dB re m^4 for the 30 dB per decade roll-off. These ranges are roughly equivalent to the roughness found during the tank tests. From Figure 4.26 (c) and (d) it can be seen that, for the tank tests had there been sufficient realisations, the acoustic frequency response dif-

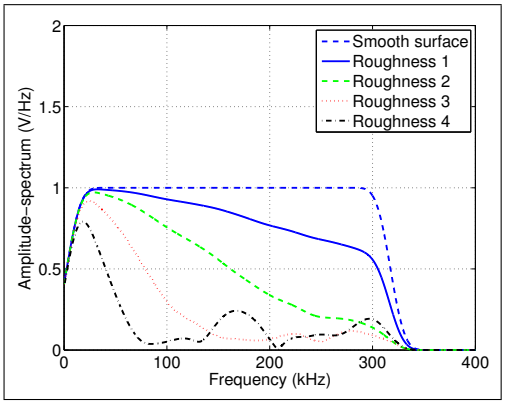

(a) Roughness 1 has a surface roughness spectrum with 30 dB per decade roll-off and a 10 cycle m^{-1} amplitude of -112 dB re m^4. The amplitude of each additional roughness increases by 6 dB re m^4.

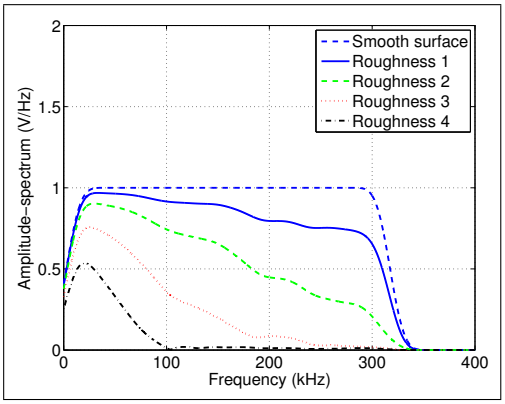

(b) Roughness 1 has a surface roughness spectrum with 20 dB per decade roll-off and a 10 cycle m^{-1} amplitude of -108 dB re m^4. The amplitude of each additional roughness increases by 6 dB re m^4.

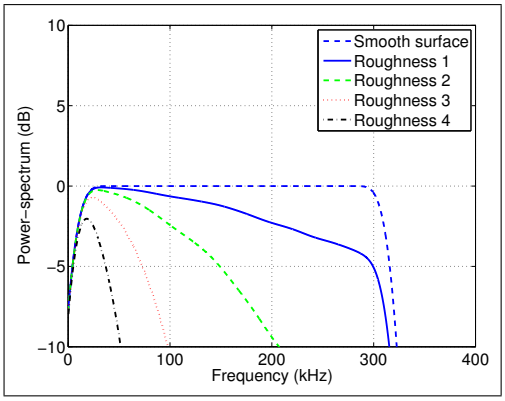

(c) Power spectrum of (a)

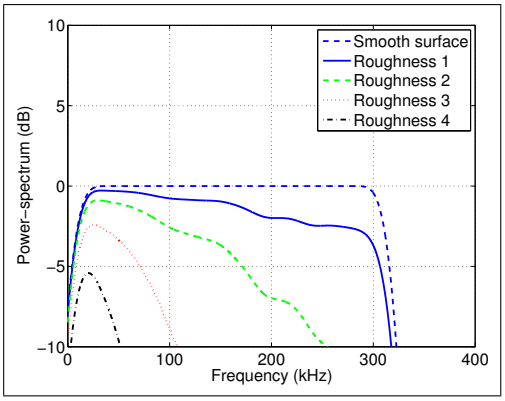

(d) Power spectrum of (b)

Figure 4.26: These plots show the difference between surface roll-offs of 20 dB and 30 dB per decade for a mono-static configuration 65 cm from the seafloor. These plots show that similar acoustic frequency responses can be achieved with both surface roll-offs. However, the amplitude is different depending on the surface roll-off. This is shown clearly with surface roughness 4 where there is a 4 dB difference in the power spectrum between the surface roll-offs of 20 dB and 30 dB per decade. The other surface roughnesses also show this difference; however, it is not as large. All plots shown are averages of 48 surface realisations. Surface roughness 4 in plot (a) is reaching the limit of average 48 surface realisations and surfaces with greater roughness will require a larger number of realisations. Note the spectrum has been shown as (V Hz^{-1}) for most of the plots because the frequency response is closer to a linear response in this form. For these plots the power spectrum is also shown because most acoustic signals are measured in dB and it is easer to evaluate the scales.

ferences would have been sufficient to provide an indication for both the roughness amplitude and roll-off for surfaces with 10 cycle m^{-1} amplitude ranges of -94 dB re m^4 (Roughness 4) or greater. For surface roughness with 10 cycle m^{-1} amplitude ranges of less than -100 dB re m^4 (Roughnesses 1-3), the acoustic amplitude differences would have been less than 2 dB, which is in the range of the transducer beam pattern variations and would have been insufficient to determine the surface roll-off.

However, this system in its present form cannot provide an adequate number of realisations. There were two primary reasons the system could not provide 48 or more realisations: firstly, the transducer's sensitivity to movement required a recalibration each time the transducers were moved as well as time for the system to stabilise; secondly, the system was not designed to provide multiple realisations due to the initial design constraints and once the system was functional there was not enough time to redesign the system. It was therefore decided to gather as much information with the system in its present form so a better system could be designed in the future. There are applications for this system but not in its present form for analysing surface roughness. A system using spherical transducers could be used to analyse the roughness spectrum of the seafloor, but there are other systems that provide more information as described in Section 1.2.1. Some of the potential applications and improvements to this system are described in Chapter 5.

Chapter 5

CONCLUSIONS

The spherical transducer system described in this thesis can meet the project goals, namely, to non-invasively measure the acoustic impedance and the roughness characteristics of the seafloor. If the seafloor's acoustic impedance has a critical angle, then the method described in Section 4.4.1 can determine the acoustic impedance. The measurement of the acoustic impedance of the seafloor is demonstrated by both simulated results and empirical results from the experiments conducted in the sonar test tank. However, the determination of seafloor roughness can only be demonstrated with simulation due to limitations in the sonar test tank configuration. In order to determine the roughness of the seafloor, 12 or more realisations of the seafloor are required (depending on the roughness spectrum of the seafloor). The sonar test tank configuration can only provide three realisations of the seafloor which limits the analysis of surface roughness. These experiments have succeeded as a proof of concept for using spherical transducers with broadband acoustics to study seafloor roughness. The experiments also identified some of the advantages and disadvantages of using spherical transducers.

The main advantage of using a spherical transducer is that it has minimal beam pattern effects over a wide frequency range. This allows the use of a single broadband pulse to analyse the roughness spectrum of the seafloor. The bi-static configuration can be used to analyse the angular dependent specular reflection by simply raising and lowering two spherical transducers. The mono-static configuration can be used to analyse the specular scattering components at the incident angle and diffused scattering component of the reflected signal. Some of the potential applications of the bi-static and mono-static configurations are discussed in Section 5.1.

The main disadvantage of using a spherical transducer is that it radiates in all directions. This means that anything around the transducer can scatter and be a source of interference; even the cable attached to the transducer (as discussed in Section 3.1.3 and Appendix D). Additionally, the plane wave reflection coefficient is invalid for spherical waves: at close ranges relative to the wavelength, near the critical angle, and in the case of total internal reflection, i.e., when the incident angle

is greater than the critical angle, as discussed in Section 1.3 and Appendix C.2.4. When the plane wave reflection coefficient is invalid for spherical waves, the Kirchhoff approximation also becomes invalid. This is because the Kirchhoff approximation uses the plane wave reflection coefficient [Brekhovskikh and Lysanov 2003]. Methods of reducing the close range limitation are discussed in Section 5.2.

The work in the sonar test tank was more challenging than expected. There were three key problems: Firstly, there was the problem of a surface layer of air trapped in the sand. In a natural environment, this would not occur due to tidal action constantly moving the sand. However, in the sonar test tank, the air bubbles in the sand were not only possible, but were difficult to eliminate. For future tank tests, it is recommended: firstly, to use clean washed sand and to allow for at least one month of raking to eliminate air bubbles; secondly, to allow for internal reflections, the timing of these reflections can vary due to surface roughness changing the geometry, i.e., if there are holes in the sand then they can occur sooner; thirdly, to find a better method for rough surface generation, the generation of rough surfaces was problematic in that the generation and measurement process could take up to a month to verify due to the time required for water turbidity to clear.

Stereo photogrammetry worked well in clear water with good lighting. However, light filtering through the water from the surface and inhomogeneous surfaces can be problematic. A simple filtering algorithm was used to remove the outliers from the height maps generated by the stereo photogrammetry. Much of the work with the stereo photogrammetry could not be automated and required optimisation depending on the conditions that changed from day to day, such as external lighting and water clarity. Towards the end of the tank testing process, it was found that water clarity and lighting were key to generating good height maps. If there were any problems with water clarity, then closer the lighting and the more settled the water, the better the images. These problems were caused by shadows generated by material suspended in the water. If the water was clear, then the process was trivial and the farther (up to 1 m) the lights were from the surface being imaged, the more even the lighting and therefore better the images. If stereo photogrammetry is to be used in the future, better water clarity is required. Additionally, synchronising the cameras could reduce the height map errors due to changing shadows. A water filtration system could be employed to reduce the time for the for water turbidity to clear. To maintain the water clarity, sealing the openings on the tank to prevent leaves and other objects from entering the water would help this process.

Automated test equipment controlled using MATLAB was found to be useful in that testing and data processing could be combined. This allowed quick validation of the results and a common language for analysis and equipment control. MATLAB was found to work well with both off the shelf equipment, such as the Agilent oscilloscopes and arbitrary waveform generators, as well as custom equipment, such

as the Surveyor SVS. In general, I can recommend employing MATLAB for equipment control and to apply additional data processing realtime. The key method to access custom equipment is to write a JAVA interface to the ethernet socket or other interface. Once this is done, then the system will work, however, MATLAB exception handling was problematic.

5.1 APPLICATIONS

A spherical (or hemispherical) transducer system could be of use to measure the acoustic properties of the seafloor using: an AUV, a ROV, a free hanging system deployed from a boat, or a towed system. However, for any of these systems to be useful, the transducer mounting problem, discussed in Section 5.2, must be solved. If the range is sufficient, i.e., 65 cm or greater, this system would be useful in studying angle and frequency dependent roughness scattering effects. Note, at 65 cm the frequency dependance of the reflection due to spherical waves is negligible as discussed in Section 4.4.1. The bi-static configuration is useful primarily for studying the specular scattering. The diffused scattering component of the bi-static configuration is of limited value because it is an average of many different angles, as shown in Section 2.3.3.2. However, bi-static configuration is useful in examining the angular dependence as well as the directional dependence of the specular reflection. The mono-static configuration is useful for specular and diffused back-scattered components of surface reflection, as shown in Section 2.3.3.1. For the mono-static configuration, the diffused scattered component of the reflection only comes from one angle for any given range. Using the omnidirectional properties of the bi-static transducer configuration and the directional properties of the mono-static configurations, the effects of surface directionality could be studied. With most transducer systems, the transducer's directionality biases the surface response. This is not the case with the mono-static transducer. The spherical transducer system could be of use for a number of different applications, but not in its current form. Improvements must be made to the existing system configurations to conduct further research, as discussed in Section 5.2.

The AUV, ROV, and towed systems are all envisaged as using hemispherical transducers rigidly mounted to the vehicle. All three systems would have two transducers mounted in line on the vehicle. One transducer would be mounted fore and the other aft, with a metre separation. This system would depend on the beampattern of the hemispherical transducer to minimise the interference from reflections from the vehicle. The use of the hemispherical transducer is discussed in more detail in Section 5.2.1.

5.2 IMPROVEMENTS

The improvements that need to be made are dependent on the application. If the system were to be used in a laboratory environment, the hardware improvements in Section 5.2.3 will be unnecessary. If the system is to be used in a field environment, the improvements to tank test environment in Section 5.2.4 will be unnecessary. However, two issues must be solved before this system can be useful: firstly, the system must be configured in such a way that 12 or more realisations can be taken of the seafloor without difficulty; one solution to this problem is discussed in Section 5.2.4. Note the number of realisation required to analyse the roughness spectrum is dependant on how rough the surface is, as discussed in Section 4.5.1. Secondly, the transducers must be rigidly mounted without causing significant interference from the mounting apparatus; two solutions to this problem are discussed in Section 5.2.1.

5.2.1 Transducer configuration

The use of spherical transducers has been problematic due to scattering from the mounting apparatus or variability of the system due to the transducers being free-hanging. There are two potential solutions to these problems: the most promising is to use a hemispherical transducer; a more complicated solution that uses the existing transducers is to mount the transducers on pipes.

Replacing the spherical transducer with hemispherical transducers could greatly simplify the configuration and allow it to be used on an AUV or ROV. In the test tank environment, this could potentially double the usable vertical range in the tank. However, there is a compromise. A hemispherical transducer will have a frequency dependent beam pattern. How this will effect the acoustic measurements has yet to be determined. The construction and some of the differences between spherical and hemispherical transducers are discussed in Sherman and Butler [2007]. If new transducers are purchased to perform further tests, use of a higher frequency transducer should be considered to reduce the effective size limitations of the sonar test tank by reducing the wavelengths used in experiments.

Mounting the transducers on rigid pipes is a potential solution. This solution was tried with limited success. A PVC pipe was placed over the transducer cable. The end of the pipe fitted tightly over a ridge on the transducer making a rigid structure for the transducers. This structure was found to increase unwanted received signals on the transducers. One suggestion for this is that the PVC pipe conducted the sound into the mounting structure and then back into the transducers. In experiments requiring the transducer to be held in place in water, the most effective solution was to use cotton string. Once the string was water saturated, it had no acoustic effect on the measurements.

5.2.2 Simulation software

The simulation software, although functional, could be expanded in two areas. This work used some of the work done by Hunter [2006] and likewise used the Kirchhoff approximation. There are two areas where the simulation software could be improved. Firstly, by using the small slope approximation rather than the Kirchhoff approximation could increase the range of angles over which the simulations are accurate. Secondly, adding compensation for shadowing would increase the accuracy of the simulations.

5.2.3 Hardware

There are several areas of improvement that can be made to the electronic hardware. These improvements were not made because they were unnecessary in the laboratory environment but in a field environment they would greatly enhance the system's usability. The data acquisition and signal generations systems could be replaced by semi-custom hardware that would fit in a small waterproof case and run directly off a battery supply. The data acquisition system could be improved by replacing the Agilent MSO6014A oscilloscope with some semi-custom hardware. The requirements for the hardware would be 1.0 MSPS (mega sample per second) with 16 bit or better resolution. The AD7760 analog to digital converter (24 bit 2.5 MSPS) with a Blackfin DSP could meet these requirements. The signal generation system could be simplified by replacing the Agilent arbitrary waveform generators with a simple square pulse generator. The square pulse generator could be run off a timer output from the DSP that runs the acquisition system. There may be commercial hardware that can perform these functions but when this research was initially undertaken there were none that met the cost requirements. As a result the semi-custom hardware appeared to be the best choice for field work.

5.2.4 Sonar test tank environment

There were positive and negative aspects of using the sonar test tank. The positive aspects of using the sonar test tank were: it was a controlled environment and the tests could be repeated once configured; the sonar test tank was close to a building with a dry environment that provided power and heat; this allowed standard test equipment to be used and the tests could be run over a number of different angles without the test environment changing.

The negative aspects of using the sonar test tank were: no water filtration system, so clearing the water requires the tank to be flushed multiple times; the transducers were mounted in fixed locations allowing only three realisations per test surface; the internal reflections of the concrete interfered with the surface reflections limiting the acoustic measurements; it was not possible to add test surfaces to sand

without draining the tank; and the most significant problem was that there was no controlled way of adding an isotropic roughness to the the surface of the sand, i.e., if a surface with specific values of ω_2 and γ_2 was required, the only way to add this roughness was through trial and error.

To improve the sonar test tank setup, three things could be done: a water filtration system could be added using the 9.5 m loop of 2 cm diameter pipe placed on top of the sand and an overflow pipe could be added to the top of the tank. This system would reduce the time required for the water to clear from up to a month to approximately a week; the transducers could be mounted on a rotating system allowing multiple realisations of the sand surface to be acquired; a weighted rig of some sort could be developed to allow roughness to be added to the surface of the sand without draining the tank. These improvements could greatly increase the usefulness of the sonar test tank.

5.3 ADDITIONAL WORK

In addition to the improvements of the current system, there were several ideas that were never fully explored. One of the more interesting ideas, that limited the number of experiments that were performed, was rough surface generation. For rough surface generation, two areas were explored but never completed. The first used two-part expanding foam to generate rough surfaces. The foam was used to generate rough surfaces up to 2 m x 1.5 m in size. For the bi-static system, these surfaces did not provide enough realisations to be useful. However, a surface this size could be useful for mono-static scattering experiments. Given that the goal of this project included the measurement of the acoustic impedance of the surface, working with a pressure release surface was not appropriate for this project. The second idea was a controlled method of adding isotropic roughness to the sand on the bottom of the sonar test tank. Both of these projects could be included to support additional scattering experiments (using a spherical transducer system) provided that the required improvements from Section 5.2 are implemented.

Appendix A

COORDINATE SYSTEMS

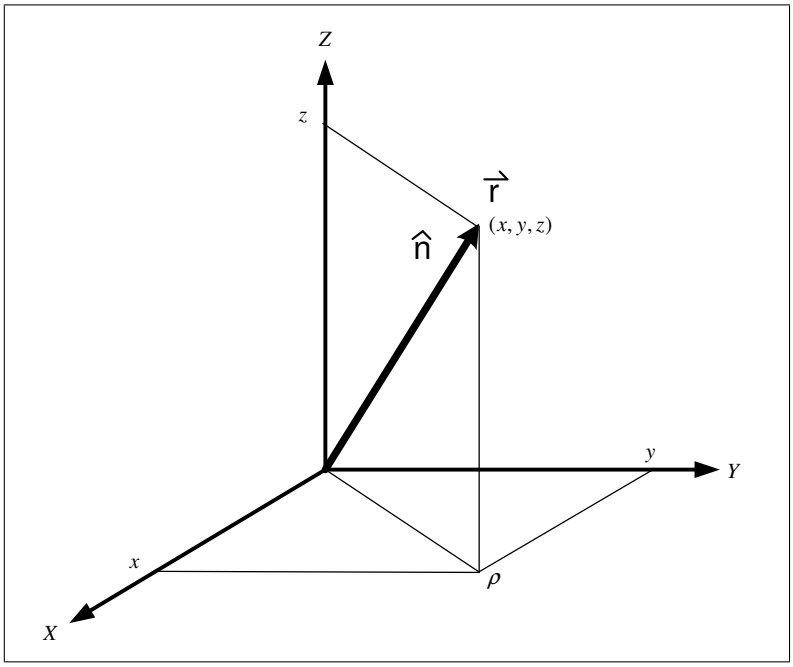

Figure A.1: The unit vector $\widehat{\boldsymbol{n}}$ shown in rectangular coordinates.

There are three basic coordinate systems: rectangular, cylindrical, and spherical. All three of these systems can describe the vector $\vec{\boldsymbol{r}}$. For example the vector $\vec{\boldsymbol{r}}$ described using rectangular coordinates is given by

$$\vec{\boldsymbol{r}} = x\,\widehat{\boldsymbol{x}} + y\,\widehat{\boldsymbol{y}} + z\,\widehat{\boldsymbol{z}}, \tag{A.1}$$

where x, y, and z are the rectangular coordinates shown in Figure A.1 and $\widehat{\boldsymbol{x}}$, $\widehat{\boldsymbol{y}}$, $\widehat{\boldsymbol{z}}$ are the orthogonal unit vectors.

The vector $\vec{\boldsymbol{r}}$ described using cylindrical coordinates is given by

$$\vec{\boldsymbol{r}} = \rho\cos\theta\,\widehat{\boldsymbol{x}} + \rho\sin\theta\,\widehat{\boldsymbol{y}} + z\,\widehat{\boldsymbol{z}}, \tag{A.2}$$

where θ is the angle between x and y shown in Figure A.2 (a), and ρ is xy radius

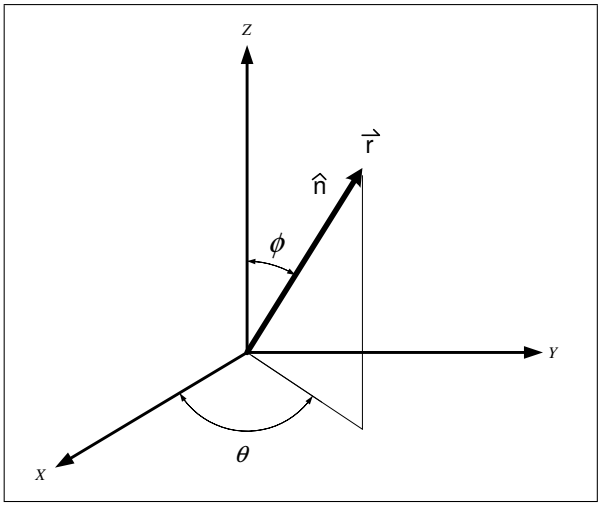

(a) The unit vector $\widehat{\boldsymbol{n}}$ with respect to angles(θ, ψ).

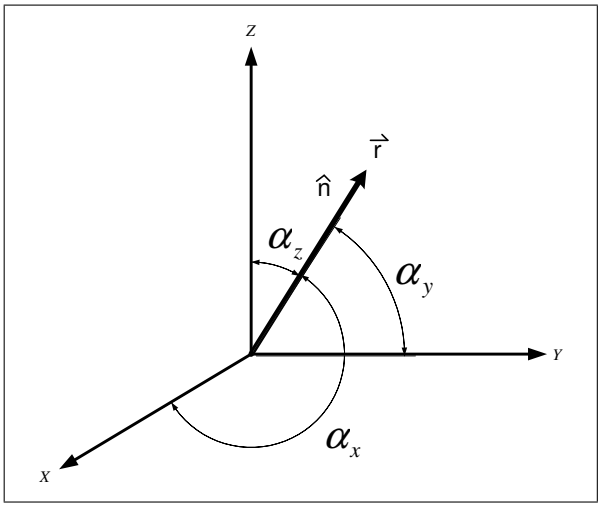

(b) The unit vector $\widehat{\boldsymbol{n}}$ with respect to angles$(\alpha_x, \alpha_y, \alpha_z)$.

Figure A.2: The unit vector $\widehat{\boldsymbol{n}}$ and the two different angle sets.

shown in Figure A.1. It can be calculated using

$$\rho = \sqrt{x^2 + y^2}. \tag{A.3}$$

The vector $\vec{\boldsymbol{r}}$, described using polar coordinates, is given by

$$\vec{\boldsymbol{r}} = r\, \sin\phi \cos\theta\, \widehat{\boldsymbol{x}} + r\, \sin\phi \sin\theta\, \widehat{\boldsymbol{y}} + r\, \cos\phi\, \widehat{\boldsymbol{z}}, \tag{A.4}$$

where ϕ is the angle between z and the x, y plane, θ is the angle between x and y (shown in Figure A.2 (a)), and r is the radius. The radius is described by

$$r = |\vec{\boldsymbol{r}}| = \sqrt{x^2 + y^2 + z^2} = \sqrt{\rho^2 + z^2}. \tag{A.5}$$

The unit vector described using rectangular coordinates is given by

$$\widehat{\boldsymbol{n}} = \frac{\vec{\boldsymbol{r}}}{|\vec{\boldsymbol{r}}|} = \frac{x\,\widehat{\boldsymbol{x}} + y\,\widehat{\boldsymbol{y}} + z\,\widehat{\boldsymbol{z}}}{\sqrt{x^2+y^2+z^2}} = n_x\,\widehat{\boldsymbol{x}} + n_y\,\widehat{\boldsymbol{y}} + n_z\,\widehat{\boldsymbol{z}}, \tag{A.6}$$

where

$$n_x = \frac{x}{|\vec{\boldsymbol{r}}|}, \tag{A.7}$$

$$n_y = \frac{y}{|\vec{\boldsymbol{r}}|}, \tag{A.8}$$

$$\text{and } n_z = \frac{z}{|\vec{\boldsymbol{r}}|}. \tag{A.9}$$

For cylindrical coordinates the unit vector is defined as

$$\widehat{\boldsymbol{n}} = \frac{\vec{\boldsymbol{r}}}{|\vec{\boldsymbol{r}}|} = \frac{\rho\,\widehat{\boldsymbol{\rho}} + z\,\widehat{\boldsymbol{z}}}{\sqrt{\rho^2+z^2}} = n_\rho\,\widehat{\boldsymbol{\rho}} + n_z\,\widehat{\boldsymbol{z}} \tag{A.10}$$

where

$$n_z = \frac{z}{|\vec{\boldsymbol{r}}|}, \tag{A.11}$$

$$\text{and } n_\rho = \frac{\rho}{|\vec{\boldsymbol{r}}|}. \tag{A.12}$$

The unit vector described using polar coordinates is

$$\widehat{\boldsymbol{n}} = n_x\,\widehat{\boldsymbol{x}} + n_y\,\widehat{\boldsymbol{y}} + n_z\,\widehat{\boldsymbol{z}} \tag{A.13}$$

with

$$n_x = \sin\phi\cos\theta = \cos\alpha_x, \tag{A.14}$$

$$n_y = \sin\phi\sin\theta = \cos\alpha_y, \tag{A.15}$$

$$\text{and } n_z = \cos\phi = \cos\alpha_z, \tag{A.16}$$

with ϕ and θ being defined in Figure A.2 (a), and α_x, α_y, and α_z being defined in Figure A.2 (b).

The wave number for a plane wave with direction $\widehat{\boldsymbol{n}}$ is

$$\vec{\boldsymbol{k}} = k\,\widehat{\boldsymbol{n}} \tag{A.17}$$

which can also be written as

$$\vec{\boldsymbol{k}} = k\,n_x\,\widehat{\boldsymbol{x}} + k\,n_y\,\widehat{\boldsymbol{y}} + k\,n_z\,\widehat{\boldsymbol{z}}, \tag{A.18}$$

or

$$\vec{\boldsymbol{k}} = k_x\,\widehat{\boldsymbol{x}} + k_y\,\widehat{\boldsymbol{y}} + k_z\,\widehat{\boldsymbol{z}}. \tag{A.19}$$

Likewise the wave number is described using cylindrical coordinates as

$$\vec{\boldsymbol{k}} = k_\rho\,\widehat{\boldsymbol{\rho}} + k_z\,\widehat{\boldsymbol{z}} \tag{A.20}$$

with k_x, k_y, k_z and k_ρ from (A.14) – (A.16) and (A.19) defined as:

$$k_x = k\,n_x = k\,\sin\phi\cos\theta, \tag{A.21}$$

$$k_y = k\,n_y = k\,\sin\phi\sin\theta, \tag{A.22}$$

$$k_z = k\,n_z = k\,\cos\phi, \tag{A.23}$$

$$\text{and } k_\rho = k\,n_\rho = k\,\sin\phi. \tag{A.24}$$

Appendix B

SIGNAL NOTATION

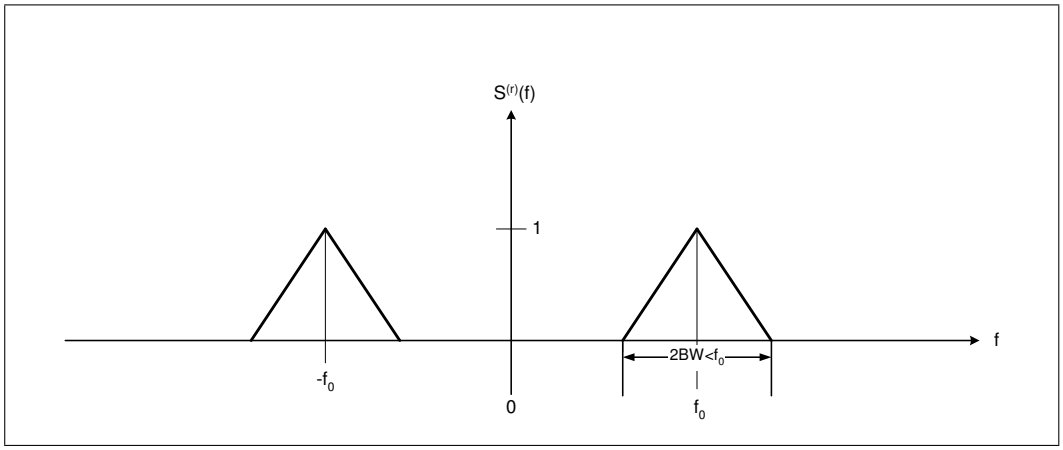

Figure B.1: This figure shows a representative spectrum of a band pass signal, $S^{(r)}(f)$, described by (B.2). The time domain representation of this signal, the real signal $s^{(r)}(t)$ is described by (B.1) .

The sonar system used in this application generates a pulse with a centre frequency f_0 and a bandwidth BW. The signal can be represented as a modulated signal of the form

$$s^{(r)}(t) = a(t)\cos\big(2\,\pi\,f_0\,t + \phi(t)\big), \tag{B.1}$$

where $s^{(r)}(t)$ is known as the real signal (representing a general form for all modulated signals), $a(t)$ is the amplitude envelope, and $\phi(t)$ is the time varying phase term [Ambardar 1999]. The spectrum of this signal is given by a Fourier transform

$$S^{(r)}(f) = \mathscr{F}\{s^{(r)}(t)\} = \int_{-\infty}^{\infty} s^{(r)}(t)\exp[-j\,2\,\pi\,f\,t]dt, \tag{B.2}$$

where $\mathscr{F}\{s^{(r)}(t)\}$ denotes the Fourier transform of $s^{(r)}(t)$ and $S^{(r)}(f)$ is the resulting spectrum. A representative spectrum is shown in Figure B.1 [Ambardar 1999].

The single sided spectrum of the real signal is the pre-envelope (or analytic

signal) and can be represented as

$$s_+(t) = s^{(r)}(t) + j\,\mathscr{H}\{s^{(r)}(t)\} = s^{(r)}(t) + j\,\widehat{s}(t), \tag{B.3}$$

where $\widehat{s}(t) \equiv \mathscr{H}\{s^{(r)}(t)\}$ is the Hilbert transform of $s^{(r)}(t)$ [Ambardar 1999]. The spectrum of $s_+(t)$ is

$$S_+(f) = \mathscr{F}\{s_+(t)\} = \begin{cases} 2S^{(r)}(f), & f > 0, \\ S^{(r)}(0), & f = 0, \\ 0, & f < 0. \end{cases} \tag{B.4}$$

This spectrum is shown in Figure B.2 [Haykin 1994]. When the pre-envelope has its

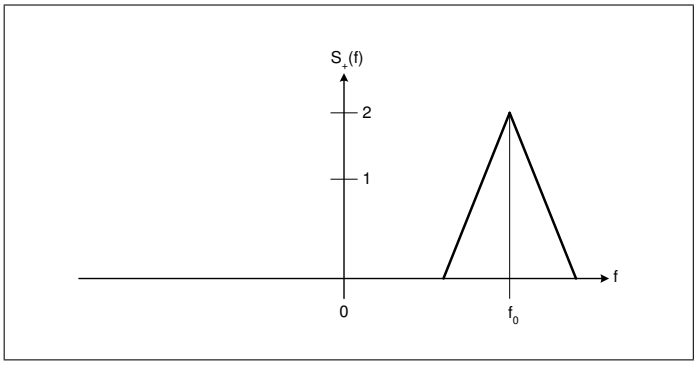

Figure B.2: This figure shows a representative spectrum of a bandpass single sided spectrum $S_+(f)$ as described by (B.4). The time domain representation of the single sided real signal $s^+(t)$ is described by (B.3) .

centre frequency f_0 shifted to 0, the resulting signal is called the complex envelope (or base-band signal) and can be represented as

$$s(t) = s_+(t)\exp[-j\,2\,\pi\,f_0\,t]. \tag{B.5}$$

The real signal can be derived from the complex envelope using

$$s^{(r)}(t) = \mathrm{Re}\big\{s_+(t)\exp\big[-j\,2\,\pi\,f_0\,t\big]\big\}. \tag{B.6}$$

The spectrum of the complex envelope is

$$S(f) = S_+(f - f_0), \tag{B.7}$$

shown in Figure B.3 [Ambardar 1999].

Another signal representation is the monochromatic signal. A waveform can be decomposed into monochromatic signals using Fourier transform. A monochromatic signal is a time domain representation of a pure sinusoid. Many acoustic parameters are more easily understood at a single frequency rather than over a

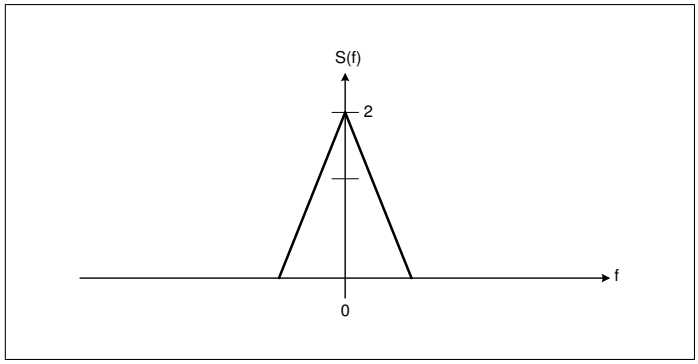

Figure B.3: This figure shows a representative spectrum of a base-band signal $S(f)$ described by (B.7). The time domain representation of this signal, the base-band signal $s(t)$ is described by (B.5) .

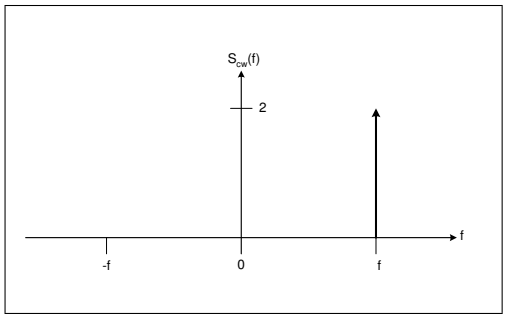

(a) This plot show a representative spectrum of a CW signal $S_{cw}(f)$.

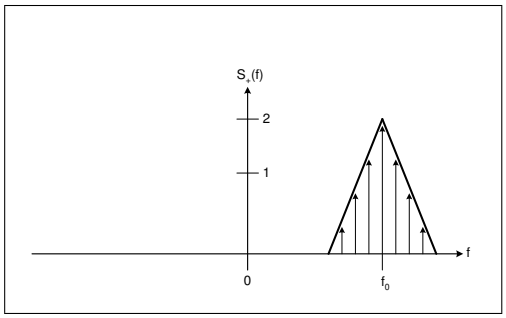

(b) this plot representative spectrum of $S_+(f)$ using a sum of monochromatic signals $S_{cw}(f)$.

Figure B.4: These figures show the relationship of the monotonic signal with a single sided spectrum.

band of frequencies, such as the reflection-coefficient, as shown in Section C.1. For these parameters the monotonic CW (or continuous-waveform) signal is used. The time domain representation of CW signal is

$$s_{cw}(t, f) = \exp[-j\,2\,\pi\,f\,t] = \cos(2\,\pi\,f\,t) + j\sin(2\,\pi\,f\,t). \tag{B.8}$$

The spectrum of this signal is shown in Figure B.4 (a). The pre-envelope can be formed from a sum of CW signals, shown in Figure B.4 (b). When analysing CW representations, such as the reflection-coefficient, where bandwidth BW > 0, it must be taken into account that the response is the sum of the CW signals present in the transmitted signal,

$$s_+(t) = \int_{-\infty}^{\infty} S_+(f)\exp[-j\,2\,\pi\,f\,t]\,df = \int_{-\infty}^{\infty} S_+(f)\,s_{cw}(t, f)\,df, \tag{B.9}$$

where $S_+(f)$ is the pre-envelope of a modulated signal and $s_{cw}(t, f)$ is the monochromatic signal.

B.1 NARROWBAND APPROXIMATIONS

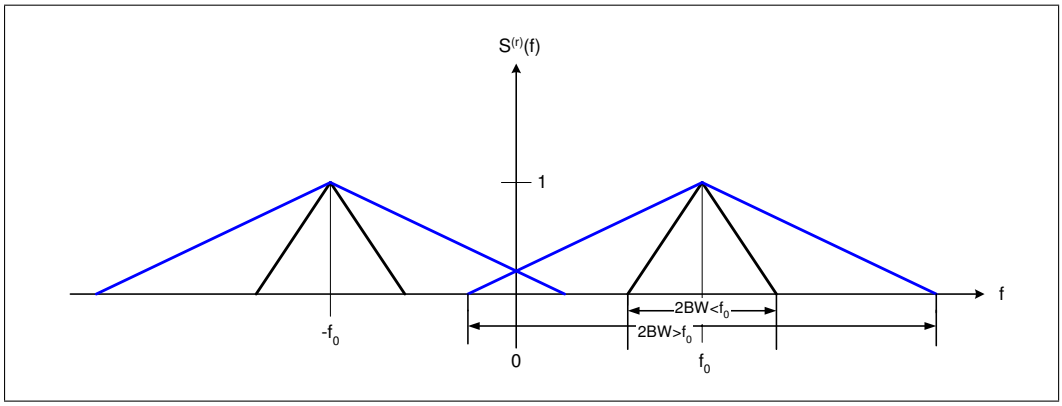

Figure B.5: This figure shows a representative spectrum of a narrow band and wide band signal, $S^{(r)}(f)$, described by (B.2).

Signals are considered narrow band when $f_0 \ggg \text{BW}$ and the signal can be represented in exponential form by the narrow band pre-envelop approximation, as described by (B.10) and (B.11). However, this approximation is not valid if the $f_0 < \text{BW}$ because there can be spectral overlaps of the positive and negative frequencies, as shown in Figure B.5. The narrow band pre-envelop approximation is

$$\begin{aligned} s_+(t) &\approx a(t)\cos\big(2\,\pi\,f_0\,t+\phi(t)\big)+j\,a(t)\sin\big(2\,\pi\,f_0\,t+\phi(t)\big), \\ &\approx a(t)\exp\big[j\,2\,\pi\,f_0\,t+\phi(t)\big], \end{aligned} \tag{B.10}$$

and likewise the narrowband complex envelope approximation is

$$\begin{aligned} s(t) &\approx a(t)\exp\big[j\,2\,\pi\,f_0\,t+\phi(t)\big]\exp\big[-j\,2\,\pi\,f_0\,t\big], \\ &\approx a(t)\exp\big[\phi(t)\big]. \end{aligned} \tag{B.11}$$

In most sonar applications, there is significant spectral spill-over. If f_0 is significantly greater than the BW, then the spectral spill-over can be ignored or dealt with by using an appropriate filter [Ambardar 1999].

Appendix C

WAVE EQUATIONS

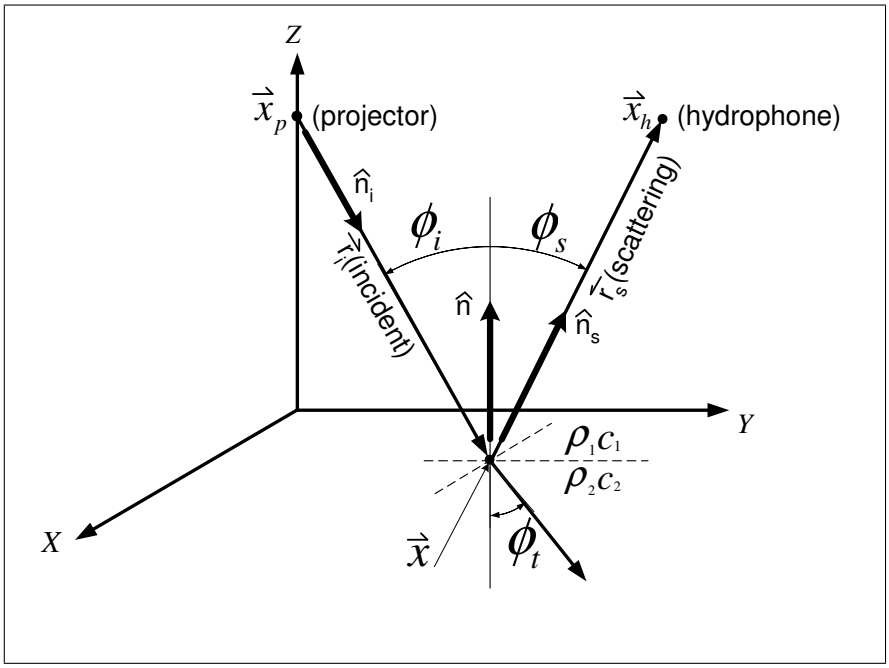

Figure C.1: Projector and hydrophone configuration showing the vectors $\vec{\boldsymbol{x}}_p$, $\vec{\boldsymbol{x}}_h$, $\vec{\boldsymbol{r}}_i$, and $\vec{\boldsymbol{r}}_s$ and normals $\widehat{\boldsymbol{n}}_i$, $\widehat{\boldsymbol{n}}_s$, and $\widehat{\boldsymbol{n}}$.

Sonar systems detect sound waves and infer their interaction with the environment. The voltage produced by and applied to the transducer is proportional to the transmitted and received sound pressure $p(\vec{\boldsymbol{x}}, t)$, with the units of Pa = $\mathrm{N\,m^{-2}}$ = $\mathrm{kg\,m^{-1}\,s^{-2}}$. The sound pressure at an arbitrary location $\vec{\boldsymbol{x}}$ from a projector at a location $\vec{\boldsymbol{x}}_p$ is defined as

$$p_i(\vec{\boldsymbol{x}}|\vec{\boldsymbol{x}}_p, t) = -\rho_w \frac{\partial}{\partial t}\varphi_i(\vec{\boldsymbol{x}}|\vec{\boldsymbol{x}}_p,\, t) \quad \left(\frac{\mathrm{kg}}{\mathrm{m\ s^2}}\right) \text{ or } \big(\mathrm{Pa}\big), \tag{C.1}$$

where $\varphi_i(\vec{\boldsymbol{x}}|\vec{\boldsymbol{x}}_p, t)$ ($\mathrm{m^2 s^{-1}}$) is the acoustic velocity potential of the incident field at a position $\vec{\boldsymbol{x}}$ due to a source at $\vec{\boldsymbol{x}}_p$; $\vec{\boldsymbol{x}}$ and $\vec{\boldsymbol{x}}_p$ are vectors defined in Figure C.1 and ρ_w

is the density of water:

$$\rho_w \approx 1000 \left(\frac{\text{kg}}{\text{m}^3}\right).$$

The sound pressure in the frequency domain is

$$p_i(\vec{\boldsymbol{x}}|\vec{\boldsymbol{x}}_p, f) = \rho_w \, j \, 2\pi f \, \varphi_i(\vec{\boldsymbol{x}}|\vec{\boldsymbol{x}}_p, f) = \rho_w \, j \, k_w \, c_w \, \varphi_i(\vec{\boldsymbol{x}}|\vec{\boldsymbol{x}}_p, f), \quad \left(\frac{\text{kg}}{\text{m } s}\right) \text{ or } \left(\frac{\text{Pa}}{\text{Hz}}\right) \tag{C.2}$$

where c_w is the speed of sound in water:

$$c_w = c_1 \approx 1500 \left(\frac{\text{m}}{\text{s}}\right),$$

the wave number of water, k_w, or the first media, k_1, is:

$$k_w = k_1 = \frac{\omega}{c_w} = \frac{2\,\pi\,f}{c_w},$$

and $\varphi_i(\vec{\boldsymbol{x}}|\vec{\boldsymbol{x}}_p, f)$ $(\text{m}^2 f^{-1})$ is the acoustic velocity potential in the frequency domain. The acoustic velocity potential $\varphi(\vec{\boldsymbol{x}}, f)$ is used rather than the sound pressure $p(\vec{\boldsymbol{x}}, t)$, in many applications, because it is easy to relate to velocity $\vec{\boldsymbol{u}}(\vec{\boldsymbol{x}}, t)$ and pressure $p(\vec{\boldsymbol{x}}, t)$. The relationship between $\vec{\boldsymbol{u}}(\vec{\boldsymbol{x}}, t)$ and $\varphi(\vec{\boldsymbol{x}}, t)$ is given by

$$\vec{\boldsymbol{u}}_i(\vec{\boldsymbol{x}}|\vec{\boldsymbol{x}}_p, t) = \nabla \varphi_i(\vec{\boldsymbol{x}}|\vec{\boldsymbol{x}}_p, t) \left(\frac{\text{m}}{\text{s}}\right), \tag{C.3}$$

where

$$\nabla = \frac{\partial}{\partial\, x}\widehat{\boldsymbol{x}} + \frac{\partial}{\partial\, y}\widehat{\boldsymbol{y}} + \frac{\partial}{\partial\, z}\widehat{\boldsymbol{z}} \tag{C.4}$$

is the gradient operator expressed in rectangular coordinates. The frequency domain relationship between $\vec{\boldsymbol{u}}_i(\vec{\boldsymbol{x}}|\vec{\boldsymbol{x}}_p, f)$ and $\varphi_i(\vec{\boldsymbol{x}}|\vec{\boldsymbol{x}}_p, f)$ is given by

$$\vec{\boldsymbol{u}}_i(\vec{\boldsymbol{x}}|\vec{\boldsymbol{x}}_p, f) = \frac{j\,2\,\pi\,f}{c_w} \, \varphi_i(\vec{\boldsymbol{x}}|\vec{\boldsymbol{x}}_p, f) \, \widehat{\boldsymbol{n}}_i = j \, \varphi_i(\vec{\boldsymbol{x}}|\vec{\boldsymbol{x}}_p, f) \, \widehat{\boldsymbol{k}}_{wi} \qquad \left(\text{m}\right) \tag{C.5}$$

where the incident normal is

$$\widehat{\boldsymbol{n}}_i = \frac{\vec{\boldsymbol{x}}_p - \vec{\boldsymbol{x}}}{|\vec{\boldsymbol{x}}_p - \vec{\boldsymbol{x}}|}, \tag{C.6}$$

$\vec{\boldsymbol{x}}$ is an arbitrary location, $\vec{\boldsymbol{x}}_p$ is the location of the projector as shown in Figure C.1, and $\widehat{\boldsymbol{k}}_{wi}$ is the wave number for water with the incident normal, i.e., $\widehat{\boldsymbol{k}}_{wi} = k_w \, \widehat{\boldsymbol{n}}_i$ [Ziomek 1995].

The acoustic velocity potential for a spherical incident wave $\varphi_i(\vec{\boldsymbol{x}}|\vec{\boldsymbol{x}}_p, f)$ is

$$\varphi_i(\vec{\boldsymbol{x}}|\vec{\boldsymbol{x}}_p, f) = -S(f) \, g_f\big(\vec{\boldsymbol{x}}_p - \vec{\boldsymbol{x}}, f)\big) = -S(f) \, g_f(\vec{\boldsymbol{r}}_i, f) \qquad \left(\text{m}^2\right) \tag{C.7}$$

where $S(f)$ is the spectrum of the signal that has the units (m^2) for plane waves and the units (m^3) for spherical waves, $\vec{\boldsymbol{r}}_i = \vec{\boldsymbol{x}}_p - \vec{\boldsymbol{x}}$, and $g_f(\vec{\boldsymbol{r}}_i, f)$ is the time-independent free-space Green's function for a loss-less, homogeneous media:

$$g_f(\vec{\boldsymbol{r}}_i, f) = -\frac{\exp\Big[-j\,k\,|\vec{\boldsymbol{r}}_i|\Big]}{4\,\pi\,|\vec{\boldsymbol{r}}_i|} \qquad \left(\frac{1}{\mathrm{m}}\right). \tag{C.8}$$

The time-dependent Green's function equation is

$$g_f(\vec{\boldsymbol{r}}_i, t) = \frac{1}{4\,\pi\,|\vec{\boldsymbol{r}}_i|}\,\delta\!\left(t - \frac{|\vec{\boldsymbol{r}}_i|}{c}\right) \qquad \left(\frac{s}{\mathrm{m}}\right). \tag{C.9}$$

Substituting (C.8) into (C.7) yields

$$\varphi_i(\vec{\boldsymbol{r}}_i, f) = S(f)\,\frac{\exp\Big[-j\,k\,|\vec{\boldsymbol{r}}_i|\Big]}{4\,\pi\,|\vec{\boldsymbol{r}}_i|} \qquad \Big(\mathrm{m}^2\Big). \tag{C.10}$$

If the signal from a point source is reflected by an ideal point scatterer, the acoustic velocity potential for the scattered field is

$$\varphi_s(\vec{\boldsymbol{r}}_i, \vec{\boldsymbol{r}}_s, f) = A\,S(f)\,g_f(\vec{\boldsymbol{r}}_i, f)\,g_f(\vec{\boldsymbol{r}}_s, f) = A\,S(f)\,\frac{\exp\Big[-j\,k\,\big(|\vec{\boldsymbol{r}}_i| + |\vec{\boldsymbol{r}}_s|\big)\Big]}{(4\,\pi)^2\,|\vec{\boldsymbol{r}}_i|\cdot|\vec{\boldsymbol{r}}_s|}\,\Big(\mathrm{m}^2\Big) \tag{C.11}$$

where $\vec{\boldsymbol{r}}_s$ is $\vec{\boldsymbol{r}}_s = \vec{\boldsymbol{x}} - \vec{\boldsymbol{x}}_h$ and $\vec{\boldsymbol{x}}_h$ is the location of an omni-directional hydrophone, and A is the equivalent scattering area of the point.

C.1 SCATTERING FROM A PLANE INTERFACE BY A PLANE WAVE

The point source acoustic velocity potential from (C.7) can be used as the starting point for the plane-wave acoustic velocity potential equation. Assuming the transmitted wave is a plane wave, then symmetry around the z axis can be assumed, simplifying (C.7) to

$$\varphi_i(\vec{\boldsymbol{r}}_i, f) = S(f)\,\exp\big[-j\,k\,\widehat{\boldsymbol{n}}_i\cdot\vec{\boldsymbol{r}}_i\big] \qquad \Big(\mathrm{m}^2\Big) \tag{C.12}$$

Note that there is no spreading loss; this is because an ideal plane wave does not spread. The plane-wave acoustic velocity potential for the scattered waveform is

$$\varphi_s(\vec{\boldsymbol{x}}, f) = S(f)\,\mathscr{R}_{12}(k_{z1}, k_{z2})\exp\big[-j\,k\,\widehat{\boldsymbol{n}}_s\cdot\vec{\boldsymbol{r}}_s\big] \qquad \Big(\mathrm{m}^2\Big) \tag{C.13}$$

The plane-wave reflection coefficient $\mathscr{R}_{12}(k_{z1}, k_{z2})$, as derived in Ziomek [1995], is

$$\mathscr{R}_{12}(k_{z1}, k_{z2}) = \frac{\varphi_s}{\varphi_i} = \frac{\rho_2 k_1\cos\phi_i - \rho_1 k_2\cos\phi_t}{\rho_2 k_1\cos\phi_i + \rho_1 k_2\cos\phi_t} = \frac{\rho_2 k_{z_1} - \rho_1 k_{z_2}}{\rho_2 k_{z_1} + \rho_1 k_{z_2}} \quad \text{for } (\phi_i < \phi_c). \tag{C.14}$$

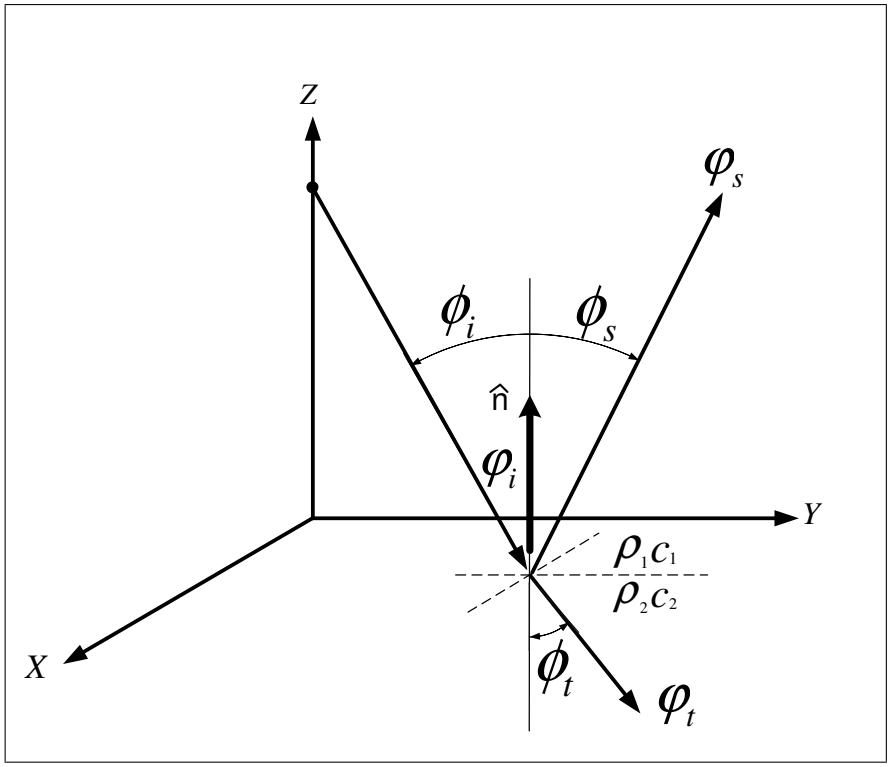

Figure C.2: A plane wave scattered from a smooth surface as described by equations (C.12) - (C.21).

where $k_{z1} = k_1 \cos\phi_i$, $k_{z2} = k_2 \cos\phi_t$, k_2 is the wave number of the second media, and the relationship between ϕ_i and ϕ_t, as defined by Snell's Law, is

$$\frac{\sin\phi_i}{c_1} = \frac{\sin\phi_t}{c_2}, \tag{C.15}$$

and the critical angle ϕ_c, i.e., the angle above which the entire signal is reflected at the 1, 2 interface ($|\mathscr{R}_{12}| = 1$) is

$$\phi_c = \arcsin\left(\frac{c_1}{c_2}\right). \tag{C.16}$$

Note that, there can only be a critical angle when $c_1 < c_2$. The plane wave acoustic velocity potential for the transmitted waveform is

$$\varphi_t(\vec{\boldsymbol{x}}, f) = S(f)\, \mathscr{T}_{12}(k_{z1}, k_{z2}) \exp\left[-j\, k\, \hat{\boldsymbol{n}}_t \cdot \vec{\boldsymbol{r}}_t \right] \qquad \left(\mathrm{m}^2\right) \tag{C.17}$$

where the plane-wave transmission coefficient $\mathscr{T}_{12}(k_{z1}, k_{z2})$, as derived in Ziomek [1995], is

$$\mathscr{T}_{12}(k_{z1}, k_{z2}) = \frac{\varphi_t}{\varphi_i} = \frac{2\,\rho_1 k_1 \cos\phi_i}{\rho_2 k_1 \cos\phi_i + \rho_1 k_2 \cos\phi_t} = \frac{2\,\rho_1 k_{z_1}}{\rho_2 k_{z_1} + \rho_1 k_{z_2}} \quad \text{for } (\phi_i < \phi_c) \tag{C.18}$$

When $\phi_i > \phi_c$, then $\mathscr{T}_{12} = 0$ and $|\mathscr{R}_{12}| = 1$ and the phase of the reflected signal is

$$\mathscr{R}_{12} = \exp[+2j\Phi] \qquad \text{for } \phi_i > \phi_c, \tag{C.19}$$

where

$$\Phi = \arctan\left(\frac{p_1 c_1 b_2}{p_2 c_2 \cos\phi_i}\right) \qquad \text{for } \phi_i > \phi_c, \tag{C.20}$$

and

$$-jb_2 = \left[1 - \left(\frac{c_2}{c_1}\right)^2 \sin^2\phi_i\right]^{\frac{1}{2}} \qquad \text{for } \phi_i > \phi_c, \tag{C.21}$$

as described by Clay et al. [1973]. Note that $\mathscr{R}_{12}$, $\mathscr{R}_{12}^{(P)}$, and $\mathscr{R}_{12}^{(U)}$ are the reflection coefficients for acoustic velocity potential, pressure, and velocity respectively, and likewise, $\mathscr{T}_{12}$, $\mathscr{T}_{12}^{(P)}$, and $\mathscr{T}_{12}^{(U)}$ are the transmission coefficients, shown in Table C.1.

$\mathscr{R}_{12}$	$\mathscr{R}_{12}^{(P)}$	$\mathscr{R}_{12}^{(U)}$	$\mathscr{T}_{12}$	$\mathscr{T}_{12}^{(P)}$	$\mathscr{T}_{12}^{(U)}$
1	1	-1	$2\frac{\rho_1}{\rho_2}$	2	0
-1	-1	1	0	0	2
0	0	0	$\frac{\rho_1}{\rho_2}$	1	1
R	R	-R	$\frac{\rho_1}{\rho_2}$(1+R)	1+R	1-R

Table C.1: Relationship between reflection $\mathscr{R}_{12}$ and transmission $\mathscr{T}_{12}$ amplitude coefficients for acoustic velocity potential, pressure, and velocity.

C.2 SPHERICAL WAVES

Spherical transducers have advantages over planar transducers; the most notable is that they approximate a point source. A point source has no frequency dependent beam pattern and no directionality. This allows the examination of a reflecting surface over a range of frequencies independent of the transducer. One of the major disadvantages of spherical transducers is that acoustic velocity potential equations are more complicated for the scattered field $\varphi_s(\vec{\boldsymbol{x}}|\vec{\boldsymbol{x}}_p, f)$ and transmitted field $\varphi_t(\vec{\boldsymbol{x}}|\vec{\boldsymbol{x}}_t, f)$ equations. The point source acoustic velocity potential is

$$\varphi_i(\vec{\boldsymbol{r}}_i, f) = -S(f)\, g_f(\vec{\boldsymbol{r}}_i, f) = S(f)\, \frac{\exp\Big[-j\,k\,|\vec{\boldsymbol{r}}_i|\Big]}{4\,\pi\,|\vec{\boldsymbol{r}}_i|} \qquad \Big(\mathrm{m}^2\Big). \tag{C.22}$$

(Note now $S(f)$ for the acoustic velocity potential for a spherical wave has the units (m^3).) Equation (C.22) can be related to plane waves using the Hankel transform

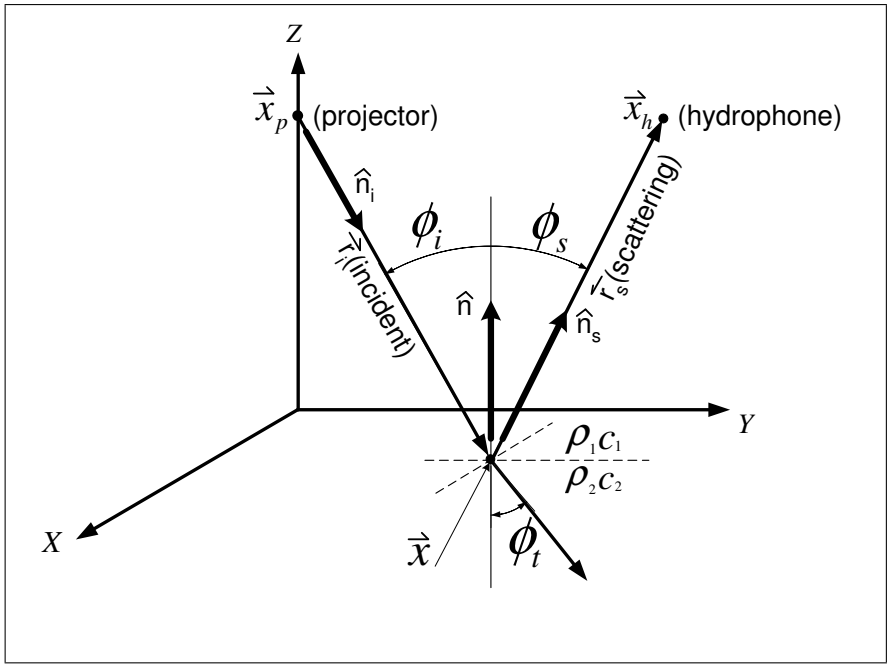

Figure C.3: Projector and hydrophone configuration defining $\vec{\boldsymbol{x}}_p$, $\vec{\boldsymbol{x}}_h$, $\vec{\boldsymbol{r}}_i$, $\vec{\boldsymbol{r}}_s$, $\widehat{\boldsymbol{n}}_i$, $\widehat{\boldsymbol{n}}_i$, and $\widehat{\boldsymbol{n}}$.

(C.33) or the double integral (C.38). Relating spherical waves to plane waves allows the plane wave reflection coefficient to be related to the spherical wave reflection coefficient. The Hankel transform is valid when circular symmetry applies and the double integral approach is the general solution which is valid for all cases. The simplest way to examine these approaches is to examine the integral representation of the free-space Green's function.

C.2.1 Integral representations of the free-space Green's function

The free-space Green's function is

$$g_f(\vec{\boldsymbol{r}}_i, f) = -\frac{\exp\Big[-j\,k\,|\vec{\boldsymbol{r}}_i|\Big]}{4\,\pi\,|\vec{\boldsymbol{r}}_i|} = -\frac{\exp\Big[-j\,k\,|\vec{\boldsymbol{x}}-\vec{\boldsymbol{x}}_p|\Big]}{4\,\pi\,|\vec{\boldsymbol{x}}-\vec{\boldsymbol{x}}_p|} \qquad \left(\frac{1}{\mathrm{m}}\right) \qquad \text{(C.23)}$$

[Duffy 2001]. Transforming (C.23) into the spatial frequency domain gives

$$g_f(\vec{\boldsymbol{r}}_i, f) = -\frac{1}{(2\pi)^4}\iiint_{-\infty}^{+\infty}\frac{\exp\Big[-j\Big(k_x(x-x_p)+k_y(y-y_p)+k_y(z-z_p)\Big)\Big]}{k^2-\big(k_x^2+k_y^2+k_z^2\big)}\mathrm{d}k_x\mathrm{d}k_y\mathrm{d}k_z. \qquad \text{(C.24)}$$

Equation (C.24) can be rearranged so that z can be integrated independently of x and y giving

$$\begin{aligned} g_f(\vec{\boldsymbol{r}}_i, f) = -\frac{1}{(2\pi)^4} \iint_{-\infty}^{+\infty} \exp\Big[-j\Big(k_x(x-x_p) + k_y(y-y_p)\Big)\Big] \\ \times \int_{-\infty}^{+\infty} \frac{\exp\big[+j\, k_z\, z_p\big]}{k_z^2 - \big[k^2 - (k_x^2 + k_y^2)\big]} \exp[-j2\pi k_z\, z]\, \mathrm{d}k_z\, \mathrm{d}k_x\, \mathrm{d}k_y. \end{aligned} \tag{C.25}$$

Integrating (C.25) with respect to k_z reduces it into a two dimensional integral giving

$$\begin{aligned} g_f(\vec{\boldsymbol{r}}_i, f) = +j\frac{1}{8\pi^2} \iint_{-\infty}^{\infty} \exp\Big[-j\big(k_x(x-x_p) + k_y(y-y_p)\big)\Big] \times \\ \frac{\exp\Big[-j\, k_z\, |z - z_p|\Big]}{k_z} \mathrm{d}k_x\, \mathrm{d}k_y. \end{aligned} \tag{C.26}$$

Equation (C.26) is the general solution which is valid for all cases it can be used to solve for the $\varphi_i(\vec{\boldsymbol{r}}_i, f)$, $\varphi_s(\vec{\boldsymbol{r}}_s, f)$, and $\varphi_t(\vec{\boldsymbol{r}}_t, f)$, as shown in Section C.2.3. If circular symmetric can be applied to the interface, then (C.26) can be further simplified using the Hankel transform [Ziomek 1995]. The Hankel transform is a two-dimensional Fourier transform assuming the axes have the relationship of $\rho = \sqrt{x^2 + y^2}$, i.e. circular symmetry [Bracewell 1986]. The Hankel transform with respect to wave-number k rather than frequency f is

$$\begin{aligned} \mathscr{H}\big[g_f(x,y,z,f)\big] &= (2\,\pi)^2 \iint_{-\infty}^{\infty} g_f(x,y,f) \exp[-j(x\,k_x + y\,k_y)] \mathrm{d}k_x\, \mathrm{d}k_y \\ &= (2\,\pi)^2 \int_0^{\infty} \int_0^{2\pi} G_f(\rho, f) \exp\big[-j\,\rho\, k_\rho\, \cos(\psi - \phi)\big] \rho\, \mathrm{d}k_\psi\, \mathrm{d}k_\rho \\ &= 2\pi \int_0^{\infty} G(\rho)\, J_0(k_\rho\, \rho) \rho\, \mathrm{d}k_\rho, \end{aligned} \tag{C.27}$$

where $g_f(x, y, f)$ is the two-dimensional free-space Green's function, $G(\rho, f)$, is the two-dimensional free-space Green's function in the spatial domain in cylindrical quadrants, and $J_0(k_\rho, \rho)$ is the zeroth-order Bessel function of the first kind described as

$$J_0(k_\rho \rho) = \frac{1}{2\,\pi} \int_0^{2\,\pi} \exp\big[-j\, k_\rho\, \rho\, \cos(\psi - \phi)\big] \mathrm{d}k_\psi. \tag{C.28}$$

Substituting (C.27) into (C.26) gives

$$g_f(\vec{\boldsymbol{r}}_i, f) = +j\frac{1}{4\,\pi} \int_0^{\infty} J_0(k_\rho \rho) \frac{\exp\big[-j\, k_{z_1} |z - z_p|\big]}{k_{z_1}} k_\rho\, \mathrm{d}k_\rho. \tag{C.29}$$

The integral representation of the Green's function can be alternatively solved using $H_0^{(2)}(k_\rho \rho)$, the Hankel function of the second kind. This integral representation of

the Green's function is

$$g_f(\vec{\boldsymbol{r}}_i, f) = +j\frac{1}{8\,\pi}\int_{-\infty}^{\infty} H_0^{(2)}(k_\rho\rho)\frac{\exp\left[-j\,k_{z_1}|z-z_p|\right]}{k_{z_1}}k_\rho\,dk_\rho \tag{C.30}$$

given that

$$J_0(k_\rho\rho) = \frac{1}{2}\big(H_0^{(1)}(k_\rho\rho) + H_0^{(2)}(k_\rho\rho)\big) \tag{C.31}$$

and finally

$$H_0^{(1)}(k_\rho\rho) = H_0^{(2)}(-k_\rho\rho) \tag{C.32}$$

[Ziomek 1995].

C.2.2 Spherical wave acoustic velocity potential assuming spherical symmetry and a planar interface

If circular symmetry can be assumed, substituting (C.29) into (C.22) gives the incident acoustic velocity potential as,

$$\begin{aligned}\varphi_i(\vec{\boldsymbol{r}}_i, f) &= S(f)\,G_f(\vec{\boldsymbol{r}}_i, f)\\ &= S(f)\,\frac{j}{4\,\pi}\int_0^{\infty} J_0(k_\rho\rho)\frac{\exp\left[-j\,k_{z_1}|z-z_p|\right]}{k_{z_1}}k_\rho\,\mathrm{d}k_\rho\end{aligned} \tag{C.33}$$

where $z \le 0$ and

$$k_{z1} = \begin{cases}\sqrt{k_1^2 - k_\rho}, & k_\rho^2 \le k_1^2\\ -j\sqrt{k_\rho - k_1^2}, & k_\rho^2 > k_1^2\end{cases}\quad. \tag{C.34}$$

From (C.34) the acoustic velocity potential of the scattered field for a smooth plane is derived as

$$\varphi_s(\vec{\boldsymbol{r}}_s, f) = S(f)\,\frac{j}{4\,\pi}\int_0^{\infty} \mathscr{R}_{12}(k_{z_1}, k_{z_2})\,J_0(k_\rho\rho)\frac{\exp\left[-j\,k_{z_1}(z+z_p)\right]}{k_{z_1}}k_\rho\,\mathrm{d}k_\rho, \tag{C.35}$$

where $z \ge 0$ and $\mathscr{R}_{12}(k_{z_1}, k_{z_2})$ is the plane wave reflection coefficient from (C.14) [Ziomek 1995]. Likewise the acoustic velocity potential for the transmitted field is

$$\varphi_t(\vec{\boldsymbol{r}}_t, f) = S(f)\,\frac{j}{4\,\pi}\int_0^{\infty} \mathscr{T}_{12}(k_{z_1}, k_{z_2})\,J_0(k_\rho\rho)\frac{\exp\left[j\,(k_{z_2}z + k_{z_1}z_p)\right]}{k_{z_1}}k_\rho\,\mathrm{d}k_\rho, \tag{C.36}$$

where $z \leq 0$ and $\mathscr{T}_{12}(k_{z_1}, k_{z_2})$ is the plane wave transmission coefficient from (C.18) and

$$k_{z1} = \begin{cases} \sqrt{k_2^2 - k_\rho}, & k_\rho^2 \leq k_2^2 \\ -j\sqrt{k_\rho - k_2^2}, & k_\rho^2 > k_2^2 \end{cases} . \tag{C.37}$$

The full derivation of the acoustic velocity potential for spherical waves can be found in Ziomek [1995].

C.2.3 Plane wave decomposition of a spherical wave using a double integral

The Hankel transform cannot be used when modelling surfaces where symmetry cannot be assumed. In these cases, the double integral can be used [Ziomek 1995]. Substituting (C.26) into (C.22) gives

$$\varphi_i(\vec{\boldsymbol{r}}_i, f) = +S(f)\, j\frac{1}{8\pi^2} \iint_{-\infty}^{\infty} \exp\Big[-j\big(k_x(x - x_p) + k_y(y - y_p)\big)\Big] k_\rho \times \frac{\exp\big[-j\, k_{z_1}(z + z_p)\big]}{k_{z_1}}\, \mathrm{d}k_x\, \mathrm{d}k_y \tag{C.38}$$

for the acoustic velocity potential for the scattered field, where $k_\rho = \sqrt{k_x^2 + k_y^2}$ and

$$k_{z1} = \begin{cases} \sqrt{k_1^2 - k_\rho}, & k_\rho^2 \leq k_1^2 \\ -j\sqrt{k_\rho - k_1^2}, & k_\rho^2 > k_1^2 \end{cases} . \tag{C.39}$$

From (C.39) the scattered field is derived as

$$\varphi_s(\vec{\boldsymbol{r}}_s, f) = +S(f)\, j\frac{1}{8\,\pi^2} \iint_{-\infty}^{\infty} \mathscr{R}_{12}(k_{z_1}, k_{z_2}) \exp\Big[-j\big(k_x(x - x_p) + k_y(y - y_p)\big)\Big] k_\rho \times \frac{\exp\big[-j\, k_{z_1}(z + z_p)\big]}{k_{z_1}}\, \mathrm{d}k_x\, \mathrm{d}k_y, \tag{C.40}$$

where $\mathscr{R}_{12}(k_{z_1}, k_{z_2})$ is the plane wave reflection coefficient from (C.14). Likewise the acoustic velocity potential for the transmitted field is

$$\varphi_t(\vec{\boldsymbol{r}}_t, f) = +S(f)\, j\frac{1}{8\,\pi^2} \iint_{-\infty}^{\infty} \mathscr{T}_{12}(k_{z_1}, k_{z_2}) \exp\Big[-j\big(k_x(x - x_p) + k_y(y - y_p)\big)\Big] k_\rho \times \frac{\exp\big[+j\,(k_{z_2} z + k_{z_1} z_p)\big]}{k_{z_1}}\, \mathrm{d}k_x\, \mathrm{d}k_y, \tag{C.41}$$

where $\mathscr{T}_{12}(k_{z_1}, k_{z_2})$ is the plane wave transmission coefficient from (C.18) and

$$k_{z1} = \begin{cases} \sqrt{k_2^2 - k_\rho}, & k_\rho^2 \leq k_2^2 \\ -j\sqrt{k_\rho - k_2^2}, & k_\rho^2 > k_2^2 \end{cases}, \tag{C.42}$$

[Ziomek 1995]. These equations are a general solution for spherical wave interacting with a surface and are required if symmetry cannot be applied. However if symmetry can be applied, the solution described in Section C.2.2 is just as accurate. Circular symmetry can be applied to the problem of spherical waves interacting with a planar interface. For this problem the equations in Section C.2.2 can be further simplified using the stationary phase approximation.

C.2.4 Spherical waves interacting with a smooth planar interface using the stationary phase approximation

The Bessel function and Hankel function integrals in (C.29) and (C.33) can be evaluated to give

$$\begin{aligned} g_f(\vec{\boldsymbol{r}}_i, f) &= \frac{\exp\left[-j\,k\,|\vec{\boldsymbol{r}}_i|\right]}{4\,\pi\,|\vec{\boldsymbol{r}}_i|} \\ &= \frac{j}{8\,\pi}\int_{-\infty}^{\infty} H_0^{(2)}(k_\rho \rho)\frac{\exp\left[-j\,k_{z_1}|z - z_p|\right]}{k_{z_1}} k_\rho\,\mathrm{d}k_\rho, \end{aligned} \tag{C.43}$$

however, when used to evaluate the acoustic velocity potential for the scattered field

$$\begin{aligned} \varphi_s(\vec{\boldsymbol{r}}_s, f) = S(f)\,\frac{j}{8\,\pi}\int_{-\infty}^{\infty} \mathscr{R}_{12}(k_{z_1}, k_{z_2})\,H_0^{(2)}(k_\rho\rho) \\ \frac{\exp\left[-j\,k_{z_1}(z + z_p)\right]}{k_{z_1}} k_\rho\,dk_\rho, \end{aligned} \tag{C.44}$$

there is not a closed form solution for the integral. The integral in (C.44) can be approximated using the stationary phase method [Brekhovskikh and Lysanov 2003, Brekhovskikh 1980, Aki and Richards 2002] giving

$$\varphi_s(\vec{\boldsymbol{r}}_s, \phi_0, f) = S(f)\,\frac{1}{r}\left[\mathscr{R}_{12}(\phi_0) - j\frac{N}{k_1 r}\right], \tag{C.45}$$

where ϕ_0 is the angle of stationary phase and it can be assumed that $\phi_0 = \phi_i$[1]. The geometry is defined by Figure C.3 and, r is the range or distance travelled by the sound waves, given by

$$r = \sqrt{(2H)^2 + S^2}, \tag{C.46}$$

[1]The stationary phase method is used because the result approximates a closed form solution of (C.44). However, at close ranges the stationary phase method is invalid at the critical angle. This limitation is present in other solutions of (C.44) as well as the stationary phase approximation.

with S being the separation between the transducer which is fixed at 1 m, H is the height of the transducers above the interface and is defined as

$$H = \frac{S}{2\tan(\phi_0)}, \tag{C.47}$$

and

$$N = \frac{1}{2}\left[\mathscr{R}''_{12}(\phi_0) + \mathscr{R}'_{12}(\phi_0)\cot(\phi_0)\right], \tag{C.48}$$

with $'$ representing the derivative with the respect to ϕ_0 and $\mathscr{R}_{12}(\phi_0)$ the planar reflection coefficients. Note that, this equation works for both fluid and elastic theory reflection coefficients. For simplicity, the fluid theory reflection coefficient is chosen (C.14) and put in terms of ϕ_i, giving

$$\mathscr{R}_{12}(\phi_i) = \frac{m\cos\phi_i - \sqrt{n^2 - \sin^2\phi_i}}{m\cos\phi_i + \sqrt{n^2 - \sin^2\phi_i}} = \mathscr{R}_{12}(k_{z1}, k_{z2}), \tag{C.49}$$

where

$$n = \frac{k_2}{k_1} = \frac{c_1}{c_2}, \text{ and} \qquad m = \frac{\rho_2}{\rho_1}. \tag{C.50}$$

Equating (C.49) and (C.48) gives

$$N = \frac{m(1-n^2)}{q_0^3(m\gamma_0 + q_0)^3}\left[2m(n^2-1) + 3m\gamma_0^2 + q_0\gamma_0(2n^2 - \gamma_0^2 + 1) - m\gamma_0^4\right], \tag{C.51}$$

where

$$\gamma_0 = \cos(\phi_i), \text{ and} \qquad q_0 = \sqrt{n^2 - \sin^2(\phi_i)}. \tag{C.52}$$

From (C.45) the spherical reflection coefficient can be calculated as

$$\mathscr{R}_s = \frac{\varphi_s}{\varphi_i} = \mathscr{R}_{12}(\phi_0) - j\frac{N}{k_1 r}. \tag{C.53}$$

This approximation is not valid as $\phi_0 \to n$, i.e., as ϕ_0 approaches the critical angle, q_0 approaches zero and N (C.51) approaches ∞ due to the shrinking denominator. At high frequencies or large distances, the approximation (C.45) simplifies to

$$\varphi_s(\vec{\boldsymbol{r}}_s, \phi_0, f) = \frac{1}{r}\left[\mathscr{R}_{12}(\phi_0)\right] S(f). \tag{C.54}$$

[Brekhovskikh and Lysanov 2003].

Figure C.4 shows a comparison between a planar reflection coefficient and the approximated spherical reflection coefficient for sand and concrete. The set-up

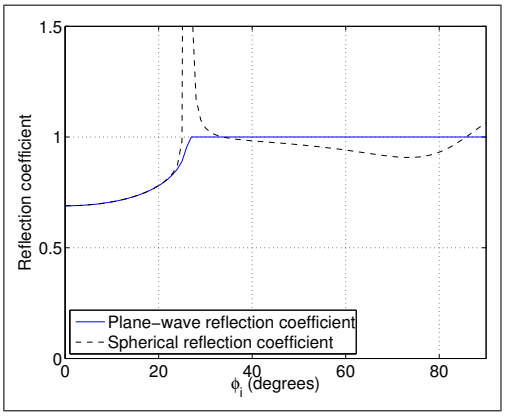

(a) The plane wave and spherical wave reflection coefficients for concrete compared at 10 kHz. The parameters for the first and second media are $\rho_1 = 1000$, $c_1 = 1456$ and $\rho_2 = 2400$, $c_2 = 3300$.

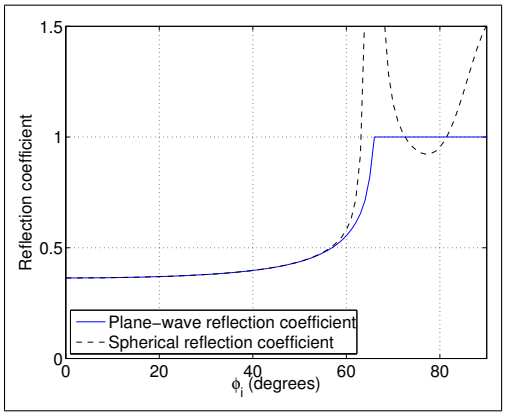

(b) The plane wave and spherical reflection coefficients for sand compared at 10 kHz. The parameters for the first and second media are $\rho_1 = 1000$, $c_1 = 1456$ and $\rho_2 = 2000$, $c_2 = 1750$.

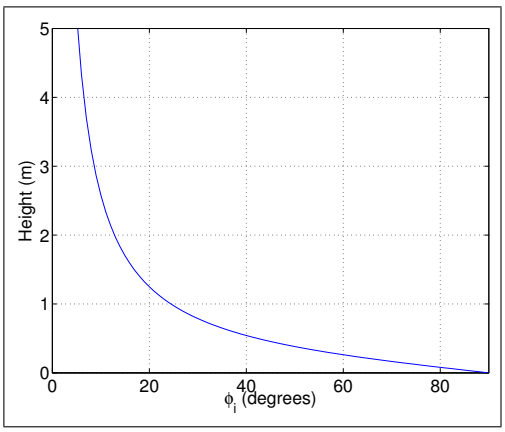

(c) The transducer separation is fixed at 1 m the transducer height is varied to produce the appropriate value of ϕ_i.

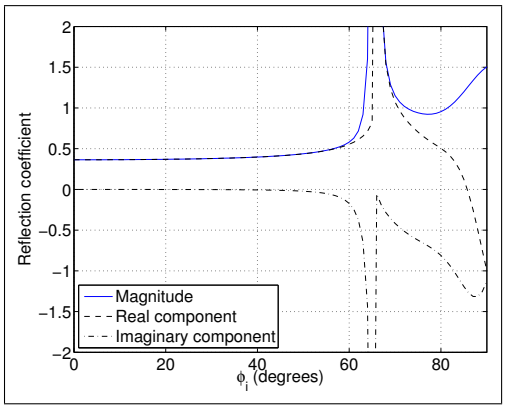

(d) The spherical reflection coefficient for sand at 10 kHz with real and imaginary components separated.

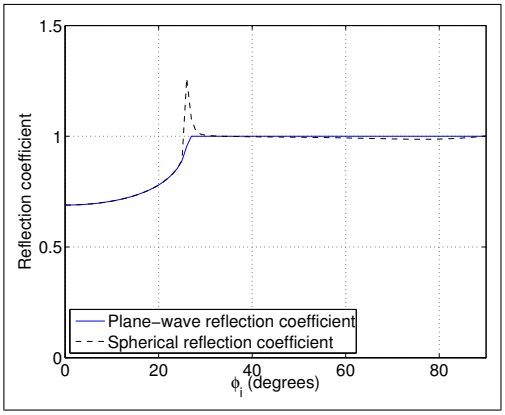

(e) The plane wave and spherical reflection coefficients for concrete compared at 80 kHz.

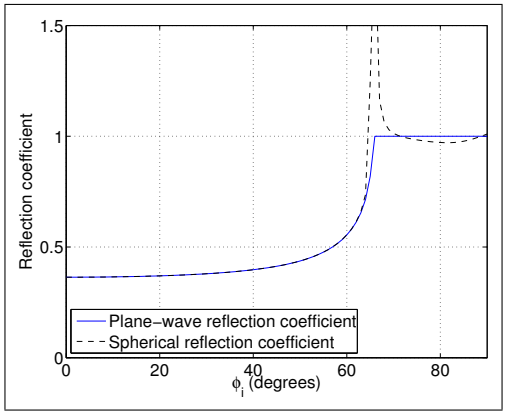

(f) The plane wave and spherical reflection coefficients for sand compared at 80 kHz.

Figure C.4: Spherical-wave reflection coefficients derived using the stationary phase approximation and compared to plane-wave reflection coefficients. Note this figure is a repeat of Figure 1.3.

has the transducers at a fixed separation of 1 m. Their height is varied to produce the required incidence angle. A plot of the resulting height-angle relationship is shown in Figure C.4 (c). Figure C.4 (a), (b), (e), and (f) have several points where the approximated reflection coefficient is greater than 1. These points are invalid points for the approximation. The reflection coefficient exceeds 1 at points near 90°, where height approaches the wave length, and at the critical angles of 26.2° and 56.3° for concrete and sand. Excluding the invalid regions, the maximum differences between the spherical and planar reflection coefficients for concrete and sand are -0.08 and -0.10 for 10 kHz and 0.01 and 0.02 for 80 kHz as shown in Figure C.4 (a), (b), (e), and (f). The difference between spherical and planar reflection coefficients, although interesting and easy to compensate for, in most cases can be ignored. At 45°, where most of the tank testing is done there is very little error using plane wave reflection coefficient for spherical waves.

Appendix D

TRANSDUCER BEHAVIOUR

The major advantage of using a spherical transducer is that the frequency dependent beam-pattern effects are much smaller than that of a directional transducer. These beam-pattern issues, as discussed in Section 3.1.3, can be dealt with to some extent by characterising the transducers. The beam-pattern changes are not gradual, as shown in the calibration data sheets shown in Figures D.12, D.13, D.14, and D.15. These calibration sheets show variations over both frequency and angle. Figure D.14 shows a 1 dB variation over 10°(0 to 10°) and a 2 dB variation over 60° (90 to 140°). These variations are not symmetric over frequency as shown in Figures D.12, D.13, D.14, and D.15.

D.1 BI-STATIC CONFIGURATION

The bi-static configuration allows the analysis of the angular effect on the returned signal. Figures D.1 (a) and (b) show the effect of changing height on the return signal strength. The signals shown in these figures are normalised to the signal strength of the direct path and have been corrected for the r^{-1} spreading loss. Figure D.1 (a) shows both the concrete and air returns with the tank half full. If the transducer had no beam-pattern the air return should have a return strength of -1. The concrete return should be 1 below the critical of 25°, i.e., when the transducer height above the concrete is less than 1 m. In both cases this is not true: the maximum air and concrete returns are 0.82 and -0.85 respectively. Figure D.1 (b) shows the response on a different transducer pair where the maximum air and concrete return are -1.1 and 0.77, respectively.[1]

Figures D.1 (c) and (d) show the sand response for the same transducer pairs as Figure D.1 (a) and (b). The critical angle for this sand response occurs at 60°, which is close to an area where the transducer has a beam-pattern change. If the sonar test tank were larger then the transducers could be separated by a greater distance. These effects have been found to be consistent over time provided

[1]Note the concrete return variation above 1 ms are due to interference with the air return under the concrete pad as discussed in Section 3.2.2.

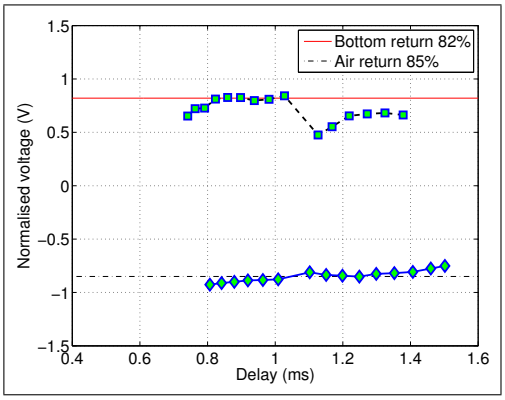

(a) Deconvolution of the transducer concrete and air responses for TX on channel 2 and RX on channel 1 with the height from bottom swept from 16 - 62 cm. The tank was half full to allow both the concrete and air responses to be seen at the same time.

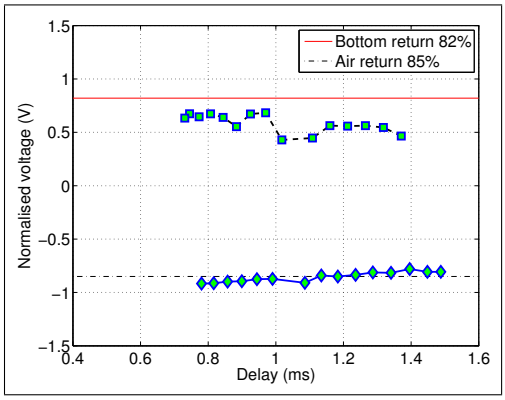

(b) Same as (a) except that the TX is on channel 2 and RX is on channel 3.

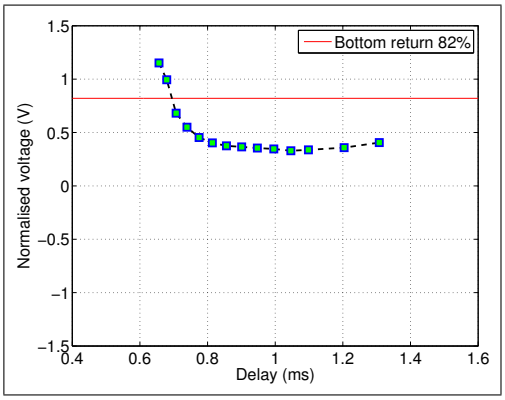

(c) Deconvolution of the transducer response for TX on channel 2 and RX on channel 1 with the height from bottom swept from 16 - 62 cm.

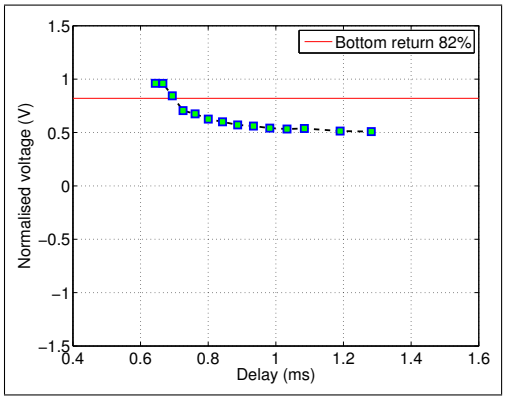

(d) The same as (c) except that the TX is on channel 2 and RX is on channel 3.

Figure D.1: Bi-static transducer responses and beam-pattern effects. These plots have been repeated from Figure 3.6 for clarity.

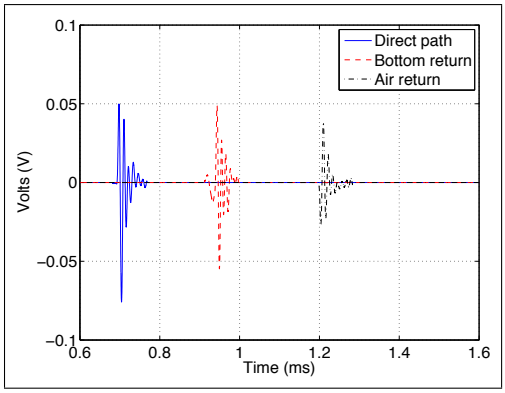

Figure D.2: The amplitude response, 47 cm from the tank bottom and 66 cm from the water surface. The direct path is shown at 0.667 ms, bottom return at 0.912 ms, and the air return at 1.172 ms. For clarity this figure is a repeat of Figure 3.4 (a).

the transducer orientation does not change. However, because the transducers are hung by their cables, there is nothing to prevent their orientation from changing. Transducer 2 has a kink in its cable and the direct path timing and beam-pattern of transducer 2 vary over time independent of temperature.

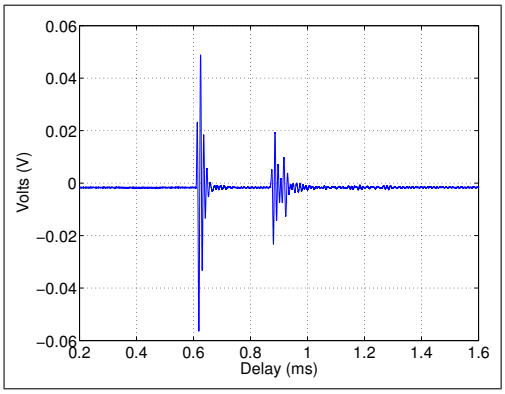

(a) The amplitude response for TX on channel 2 RX on channel 1 with the transducers 47 cm above the sand. The direct refection is at 0.621 ms and the sand reflection is at 0.886 ms. The other reflections are from the concrete under the sand, the PVC pipes and the tank edge.

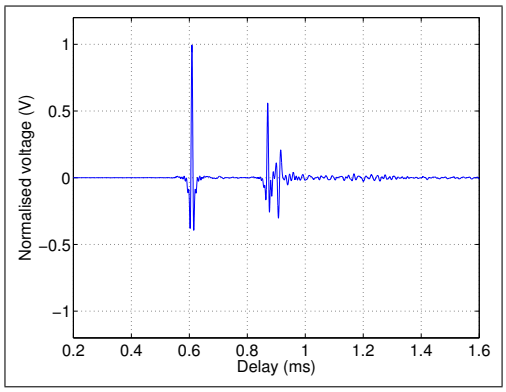

(b) The deconvolution of the transducer response shown in (b).

Figure D.3: Single trace bi-static transducer responses.

These dependencies can be seen in the air returns in shown in Figures D.1 (a) and (b). Figure D.2 show the bi-static return with the sonar test tank half full. The first pulse in this figures is the direct path. If the transducers do not move and the temperature is constant then the timing of the direct path should be constant. If the variation in the timing was only due to temperature dependencies then variation should be consistent between transducer pairs. This is not the case as interactions

between transducer 2 and the other transducers tend to have more variation than that between the other transducers.

The variations are not only with the timings of the return but also with the frequency response of the direct path. Figure D.3 (a) shows the raw waveform with the direct path at 0.621 ms. The deconvolved waveform is shown in Figure D.3 (b) with a slight ripple on the direct path after the main pulse. This ripple is due to variations in the spectrum of the direct path. At first these differences were thought to be temperature dependent. With this in mind spectra of the direct path at various temperatures and different dates were compared in Figures D.4 (a) though (e). These figures show no correlation between temperature and spectrum. Because of these variations it seems to be necessary to calibrate the signal used for deconvolution at least once a day. These differences between days minimises the accuracy of a detailed system calibration that requires several days to perform, given that the system can change during the calibration process. Two out of the three transducer pairs give consistent results given that most of the variations occur between the transducer 2-3 pair. For this system to be usable in sea trials the transducers will need to be hard mounted in some way. This is discussed in Chapter 5.

D.2 MONO-STATIC CONFIGURATION

Achieving a noise free signal in a mono-static configuration is more complex than in a bi-static configuration. There are several ways to implement the bi-static configuration. Using two transducers close to each other was found to produce more acoustic reverberation than using a single transducer. This acoustic reverberation is from the extra transducer and the cable. The method that has the least acoustic reverberation is to use a single transducer with a TX/RX switch. The single transducer method still has reverberation from the transducer cable, shown in Figure D.5 (b) from 0.300 us.

The single transducer configuration complicates the electrical response due to the TX/RX switch. To better understand these interactions the transducer, and driving circuit were modelled and simulated using SPICE. The following timings have been verified by using this simulation. The model of the transducer is described in Section D.3. Figure D.5 (a) shows the raw signal captured by the oscilloscope. This signal is made up of four main features. From 0 to 0.02 ms there is ringing from the transducer. From 0.02 ms to 0.2 ms there is a low frequency oscillation created by the interaction of the power-amplifer step-up inductor with the TX/RX switch. From 0.2 ms to 0.8 ms there is an exponential decay created by the high-pass filter in the oscilloscope's AC coupling circuitry. Finally, there is a less obvious clipping issue with the pre-amp caused by the charge on the transducer. This clipping ends between 0.400 ms and 0.460 ms, depending on the transducer channel. This clipping

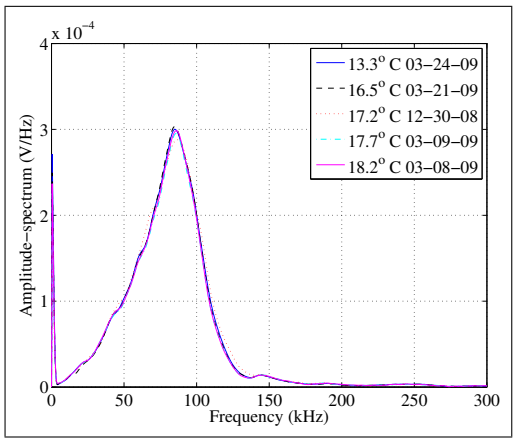

(a) The bi-static spectrum of TX 1 RX 2.

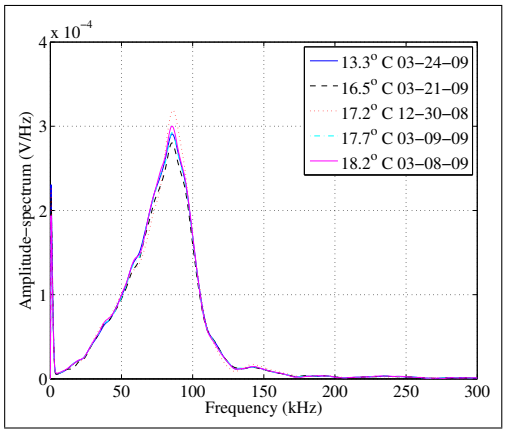

(b) The bi-static spectrum of TX 1 RX 3.

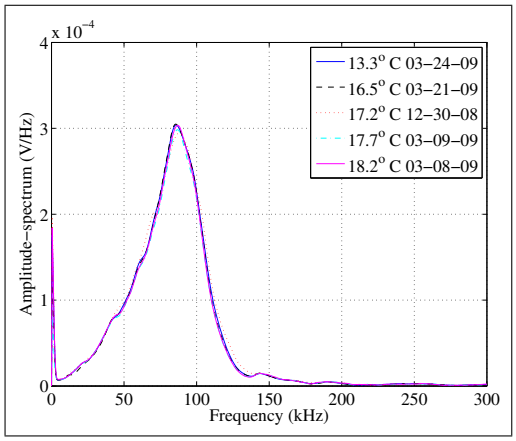

(c) The bi-static spectrum of TX 2 RX 1.

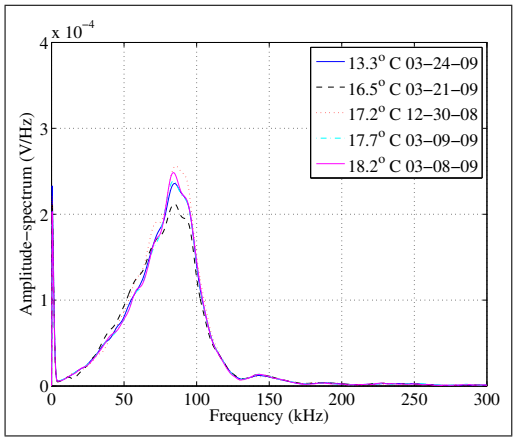

(d) The bi-static spectrum of TX 2 RX 3.

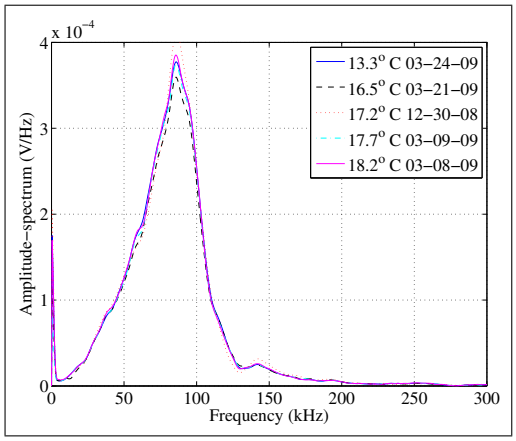

(e) The bi-static spectrum of TX 3 RX 1.

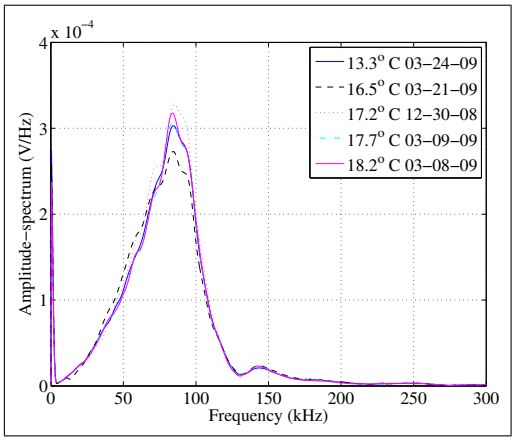

(f) The bi-static spectrum of TX 3 RX 2.

Figure D.4: The spectrum of the direct path of the transducers windowed to exclude any other reflections with the transducers 1 m from the tank bottom. These plots show the changes in the spectrum on different days at different temperatures. Note the spectrum of the transducer 3 2 pair shown in (f) and (d) has the least consistency. This is most likely caused by interference due to the bend in the transducer 2 cable.

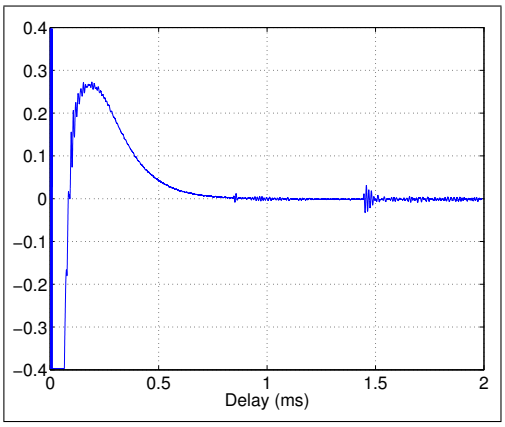

(a) The amplitude response with the transducers 50 cm from the water's surface. The air reflection is at 0.667 ms. The other reflections are from the PVC pipes and the tank edge.

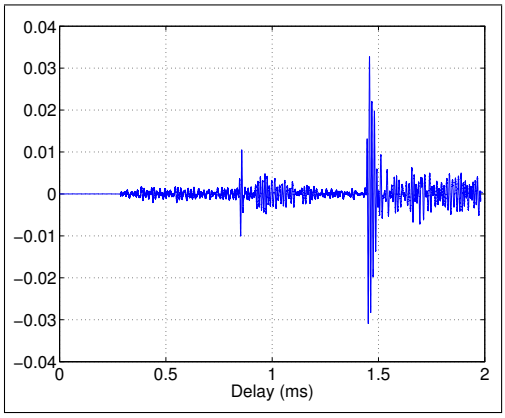

(b) The amplitude response of (b) after the filter has been applied.

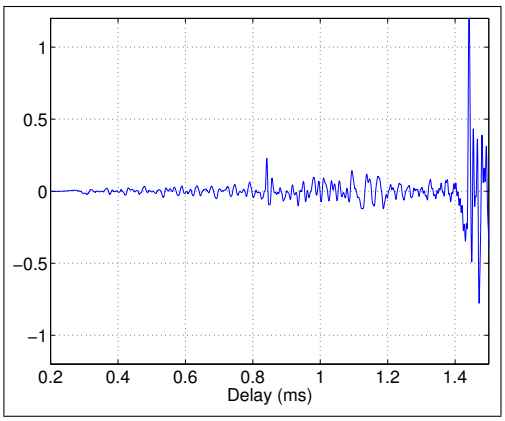

(c) Deconvolution of the transducer response at 50 cm from the water's surface with the air return at 0.667 ms.

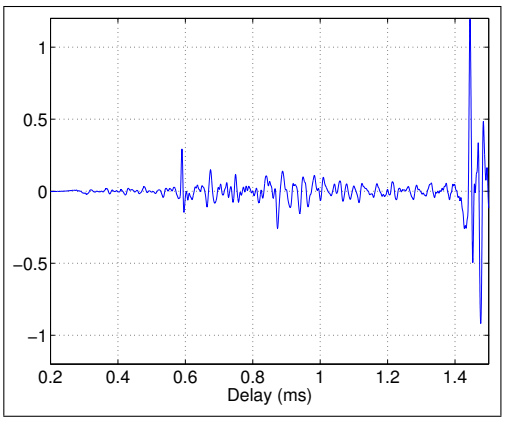

(d) Deconvolution of the transducer response at 48 cm from the tank bottom, 28 cm from the sand. The sand response is at 0.380 ms and the bottom returns are at 0.622 ms.

Figure D.5: The mono-static square pulse responses for transducer 1.

can be observed in Figure D.8. The clipping issue limits the minimum range in the mono-static configuration to 33 cm. Except for the clipping issue, all of the effects from 0.2 ms on can be eliminated with a high-pass filter. This filtering process is described Section 3.1.2.

The waveform resulting from the filtering process is shown in Figure D.5 (b). This figure shows reverberation on the transducer from 0.3 ms on. This reverberation is from the transducer cable. The reverberation can be isolated and subtracted from the main signal by taking a reading with the transducer 1m from the sand and tank surface and using it as a reference signal. This process has reduced the reverberation between 6 dB and 30 dB depending on how well the reference signal matches. Figures D.6 (a) - (e) shows the spectrum of the reverberation with the transducer 1 m from the sand over a period of months. It can be seen that both the amplitude and the spectrum change over time. This is thought to be due to changes in how the cable hangs after the transducers are soaped to remove bubbles from their surface. Tests have been run over a period of a week showing that the reverberation is constant if the transducer cables are not flexed. These tests have also shown that the reverberation will change if the frame holding the transducers is not level, i.e., two adjustment chains are lowered by 4 links one chain is lowered by 6 links.

It appears that the changes in the reverberation can be minimised by keeping the orientation of the cables consistent. It also appears that soaping the transducers at the start of each day causes changes in the cable orientation. Transducer 2 is under the edge of the tank and to reach this transducer to soap it requires the cable to be flexed more than the other transducers and thereby makes the reading of this transducer the most variable. For this reason movement of the transducers should be avoided and the practice of soaping the transducers each day is not recommended. It is also obvious that this configuration is not realistic for field work where the transducers will move. For this system to be usable in sea trials the transducers will need to be hard mounted in some way. This is discussed in Chapter 5.

D.3 TRANSDUCER MODELS

The electrical and mechanical behavior of a transducer can be represented by the model shown in Figure D.9 (b) [Wilson 1988, Sherman and Butler 2007]. R_1, C_1, and L_1 represent the mechanical components of the transducer model with the power dissipated in R_1 being proportional to the power dissipated in the water. R_2 and C_2 represent the electrical component of the transducer model. The transducer manufacturer provided a plot showing the conductance and susceptance of the transducers in water for 10 kHz to 100 kHz. The transducer provided by the manufacture has 2 m of cable. To use these transducers in the sonar test tank 20 m of cable was

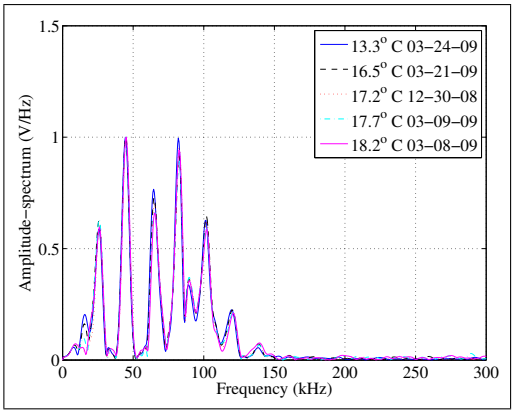

(a) The mono-static spectrum of transducer 1 normalised at 50 kHz.

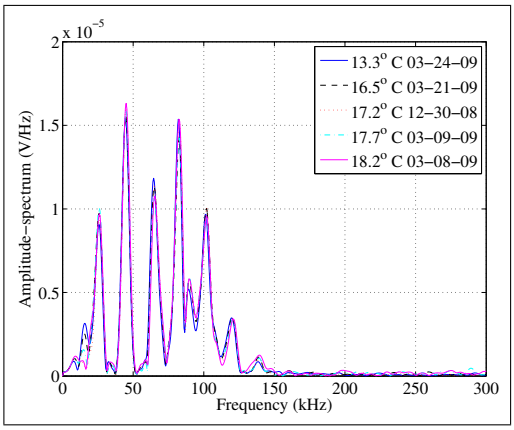

(b) The mono-static spectrum of transducer 1.

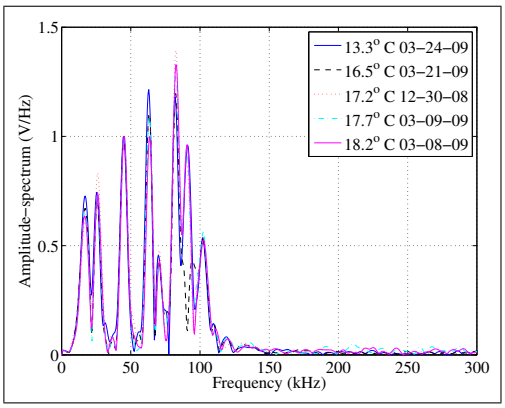

(c) The mono-static spectrum of transducer 2 normalised at 50 kHz.

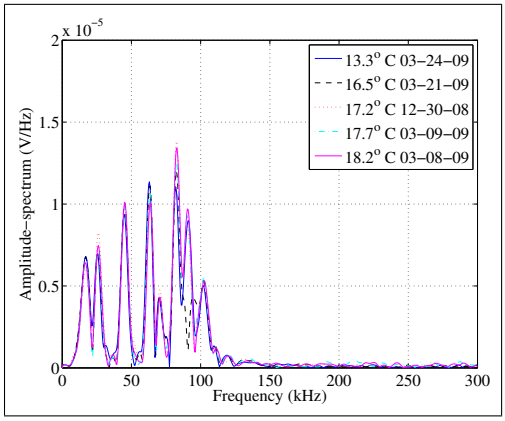

(d) The mono-static spectrum of transducer 2.

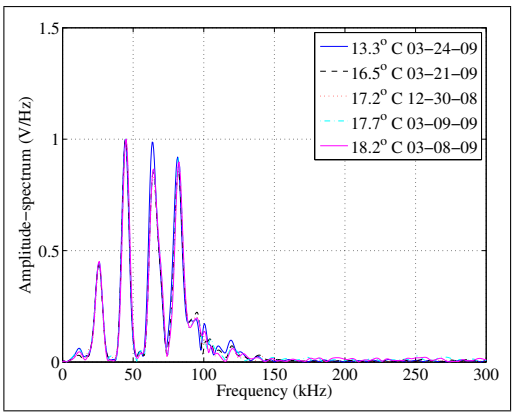

(e) The mono-static spectrum of transducer 3 normalised at 50 kHz.

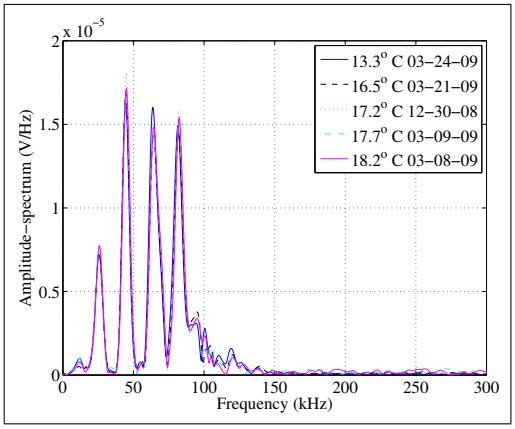

(f) The mono-static spectrum of transducer 3.

Figure D.6: The spectrum of the ringing of the transducers windowed to exclude any reflections or saturation, i.e., 400 us to 600 us with the transducers 1 m from the tank bottom. These plots show the changes in the spectrum on different days at different temperatures.

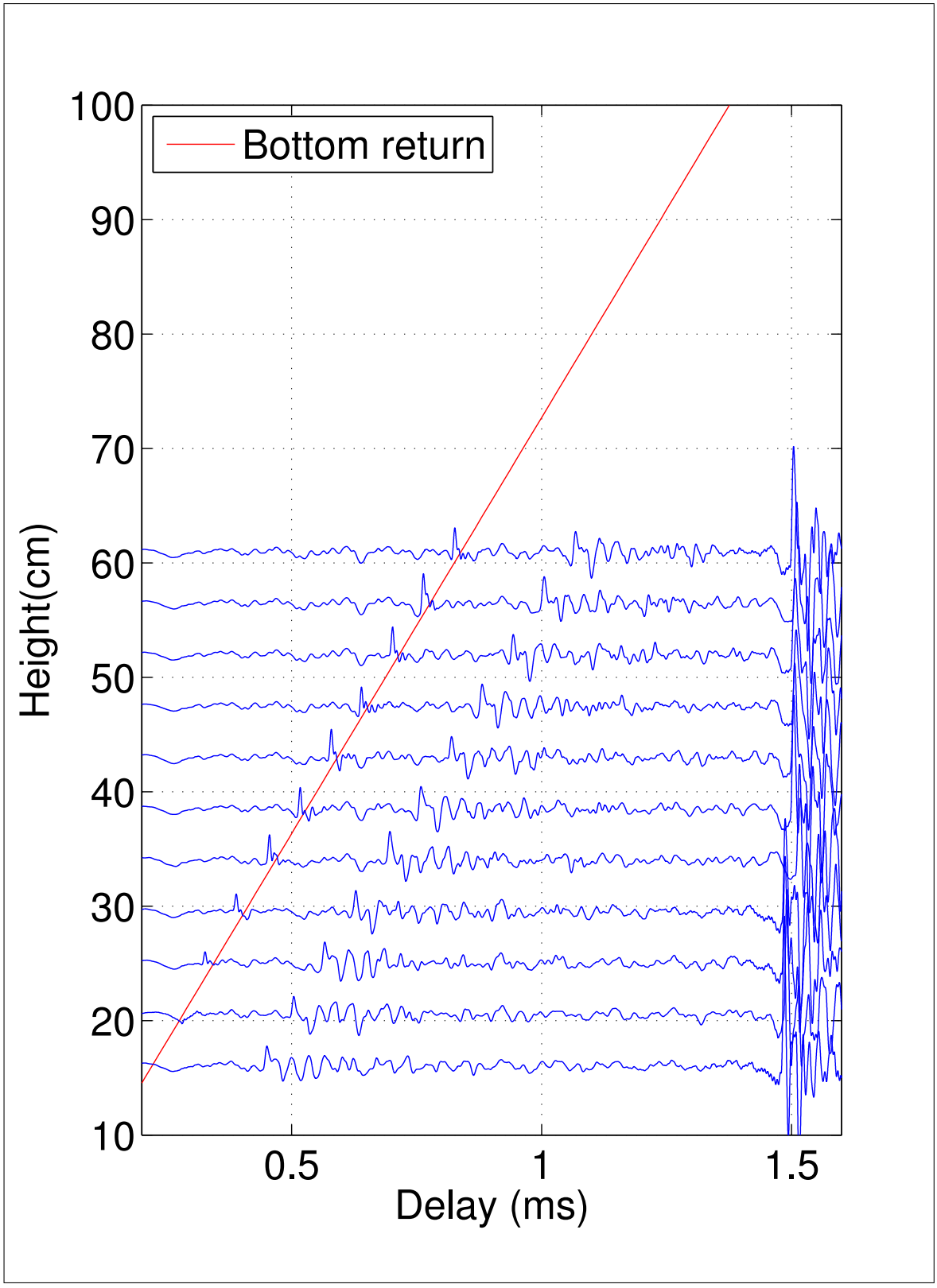

Figure D.7: Deconvolution of the transducer response for TX on channel 1 and RX on channel 1. The height above the sand was measured between 14 to 62 cm in 4.5 cm increments. Cable reverberation not filtered out. Data set from 23rd March 2009.

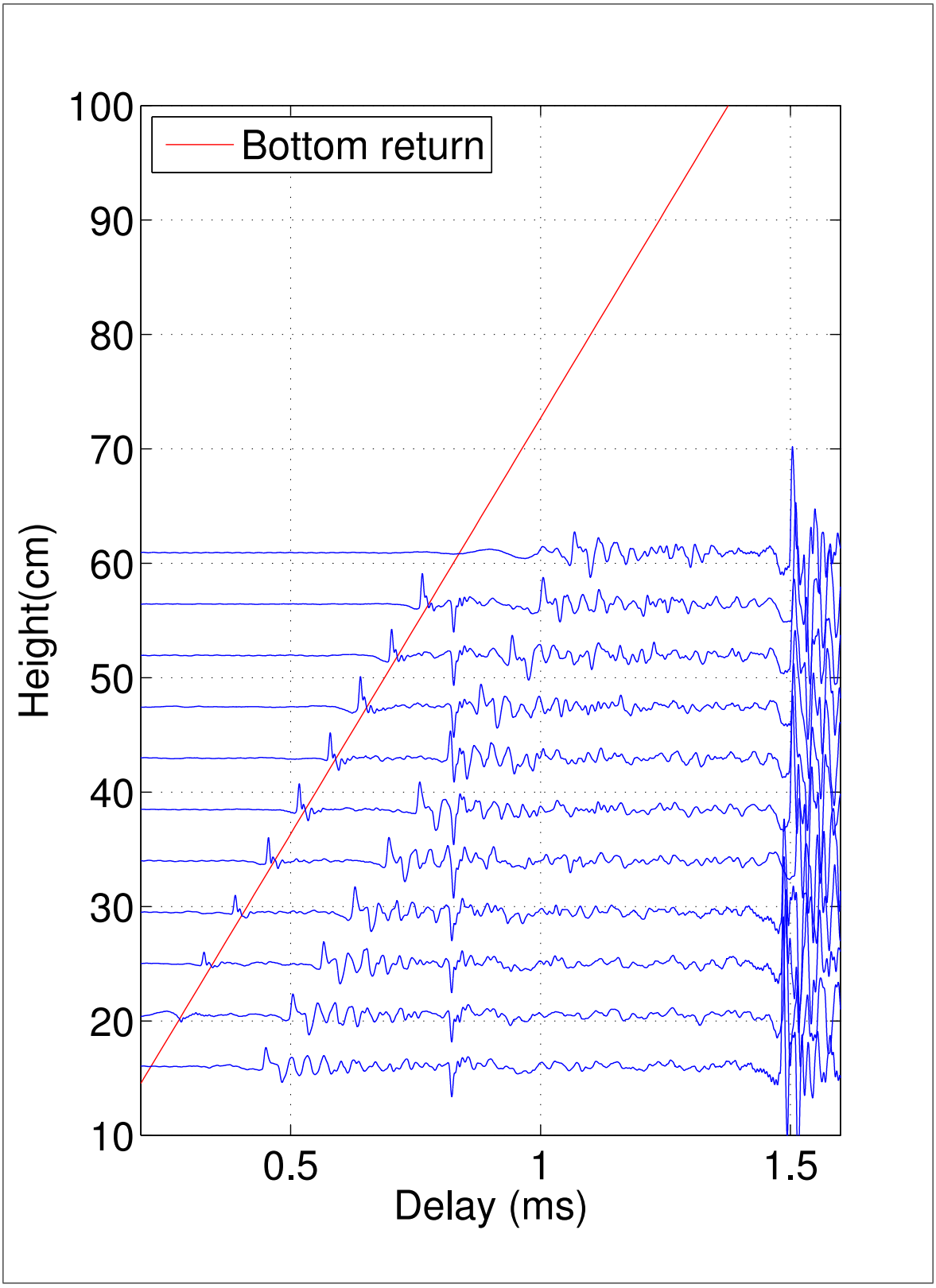

Figure D.8: Deconvolution of the transducer response for TX on channel 1 and RX on channel 1.The height above the sand was measured between 14 to 62 cm in 4.5 cm increments. Data set from 23rd March 2009.

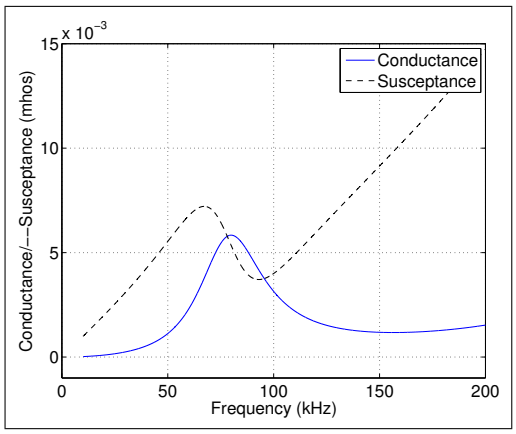

(a) Frequency response showing conductance and susceptance for the 1 kHz to 200 kHz model.

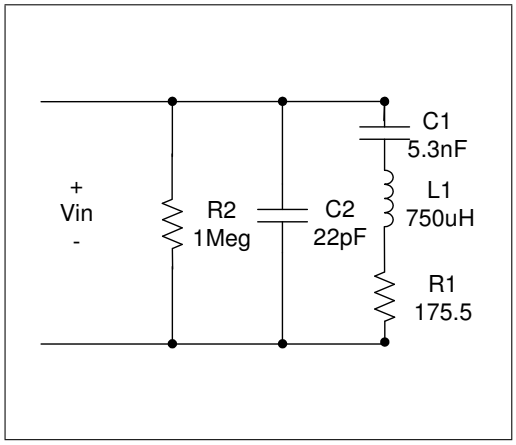

(b) Projector electrical model for transducer 1 kHz to 200 kHz.

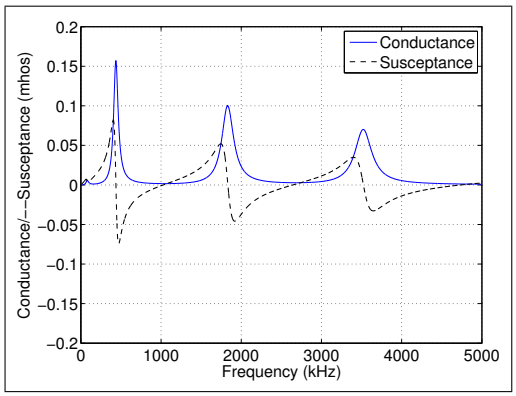

(c) Frequency response showing conductance and susceptance for the 1 kHz to 5 MHz.

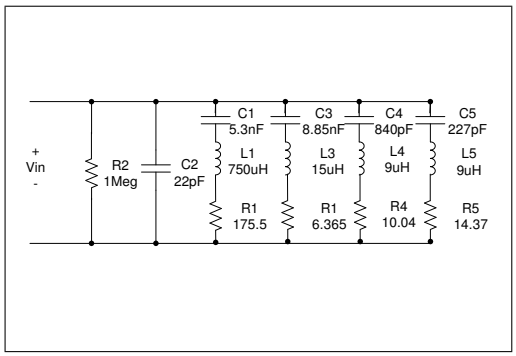

(d) Projector electrical model for transducer 1 kHz to 5 MHz.

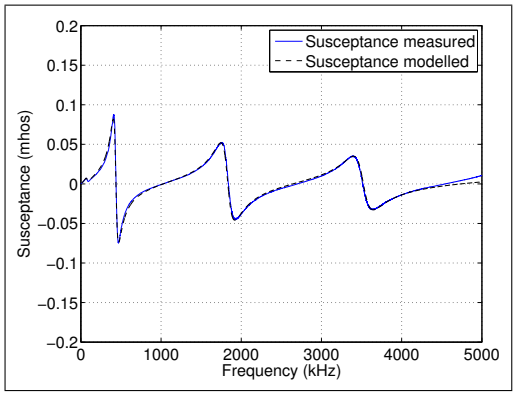

(e) Comparison between the model and measured susceptance.

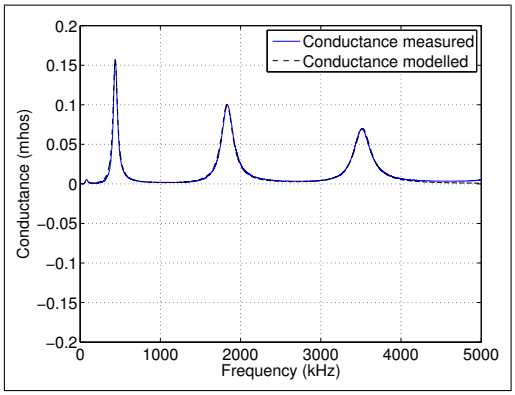

(f) Comparison between the model and measured conductance.

Figure D.9: Typical model for a ITC-1042 transducer with a 20 m cable attached. Note the additional peaks above 200 kHz have minimal effect on the transducer response but have been included to be complete.

added to allow the equipment to be operated in the lab. The addition of the cable changed the performance of the transducer. For this reason the transducer was characterised with the cable attached. A MATLAB model for Figure D.9 (b) was made to show the conductance and susceptance based on the values of R_1, C_1, L_1, R_2, and C_2, these values were varied to match the measured curve resulting in Figure D.9. The values for R_1, C_1, L_1, R_2, and C_2 were then used to model the behaviour and performance of the transducers and cable in the system.

While making the measurements of the transducer impedance it was noted that there are additional peaks at higher frequencies. To include these peaks a more complicated transducer model was made, shown in Figure D.9 (d). A comparison between the measured and simulated impedance is shown in Figures D.9 (e) and (f). It was found that although more complicated, the additional components do not add or subtract from the accuracy of the SPICE simulation. However, the length and amplitude of the ringing of the transmitted signal does change between the models of the transducer with cable and without the cable.

The transducer models were used to characterise the behaviour of the TX/RX switch. Making real world measurements in the mono-static configuration is difficult as transmit and receive voltages are simultaneously present. (The transmit voltage is 200 V and the receive voltage is 5 mV to 10 mV.) In general the SPICE models of the system provided a good indication of its real-world performance.

D.4 TYPICAL TRANSDUCER DATA SHEETS

These are the manufacturer calibration data sheets for one of the three transducers. These are included to give a feeling of the typical receive and transmit response and to show the beam-pattern issues. Each of the transducers had different performance. These calibration data sheets provided the beam-patterns for XY plane. The configuration that the transducers are being used for in these experiments use all the planes. For this reason these beam-patterns are only considered indicative of the transducer performance.

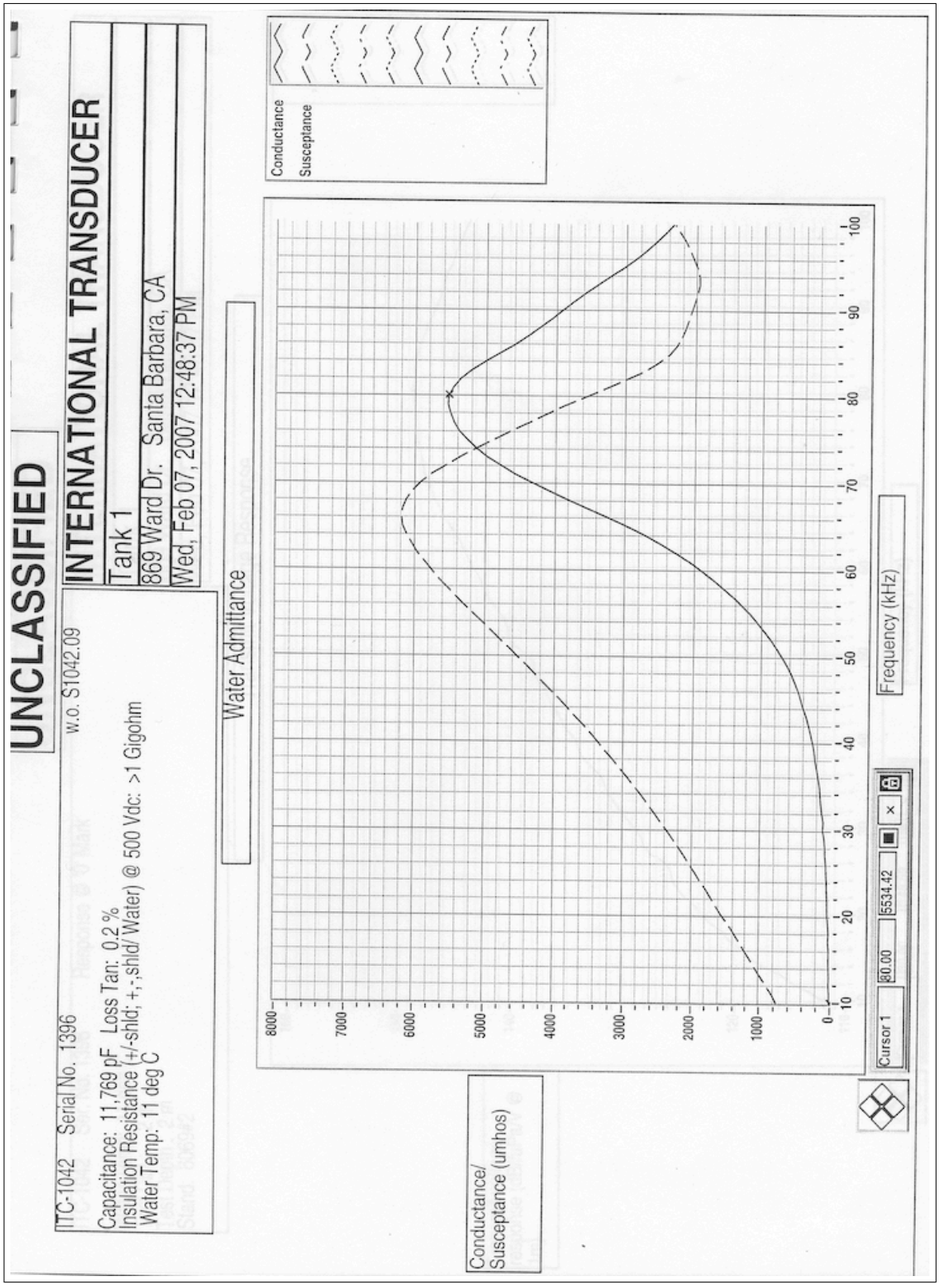

Figure D.10: Admittance for Transducer 1406

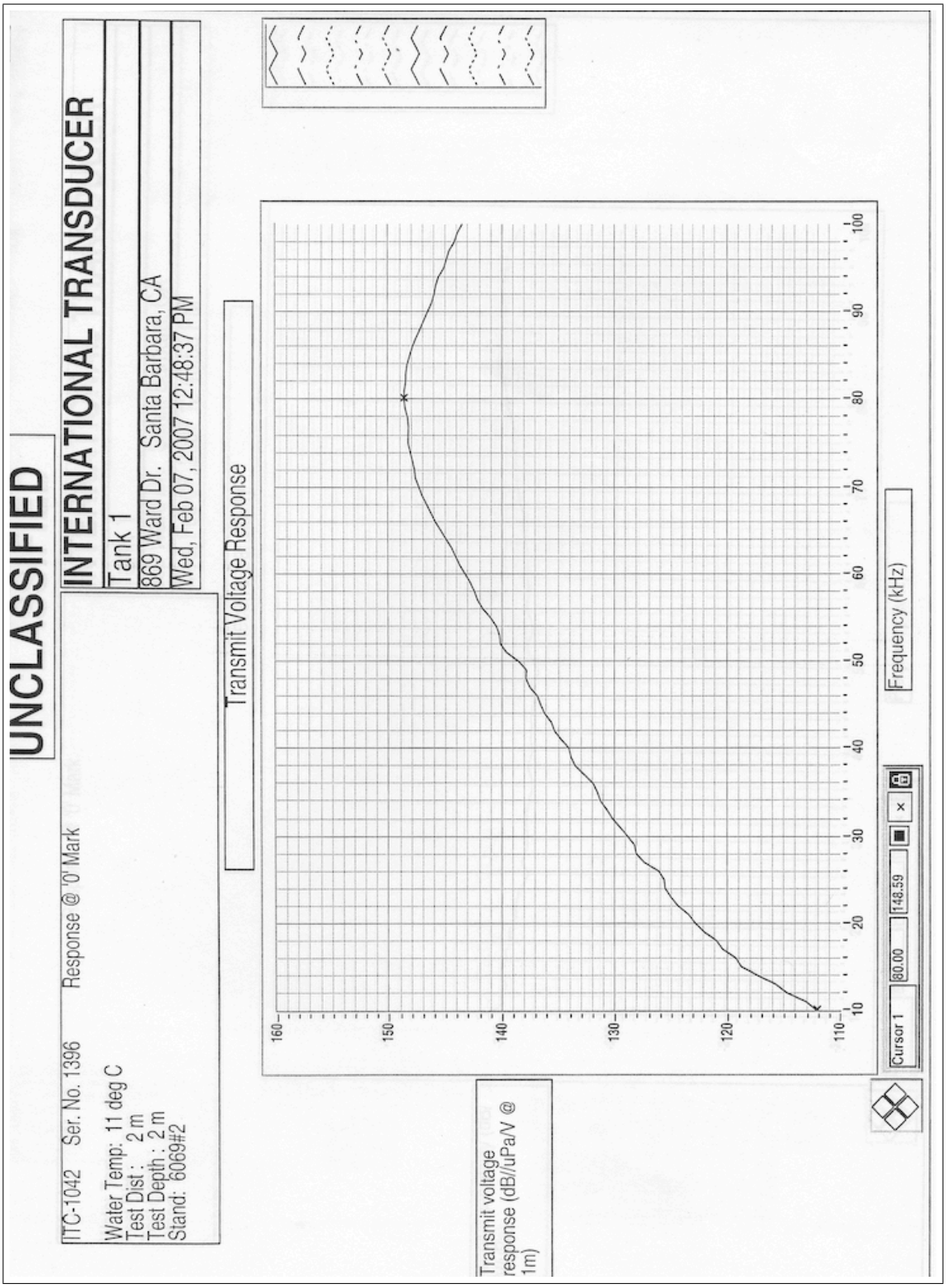

Figure D.11: Transmit Voltage Response for Transducer 1406

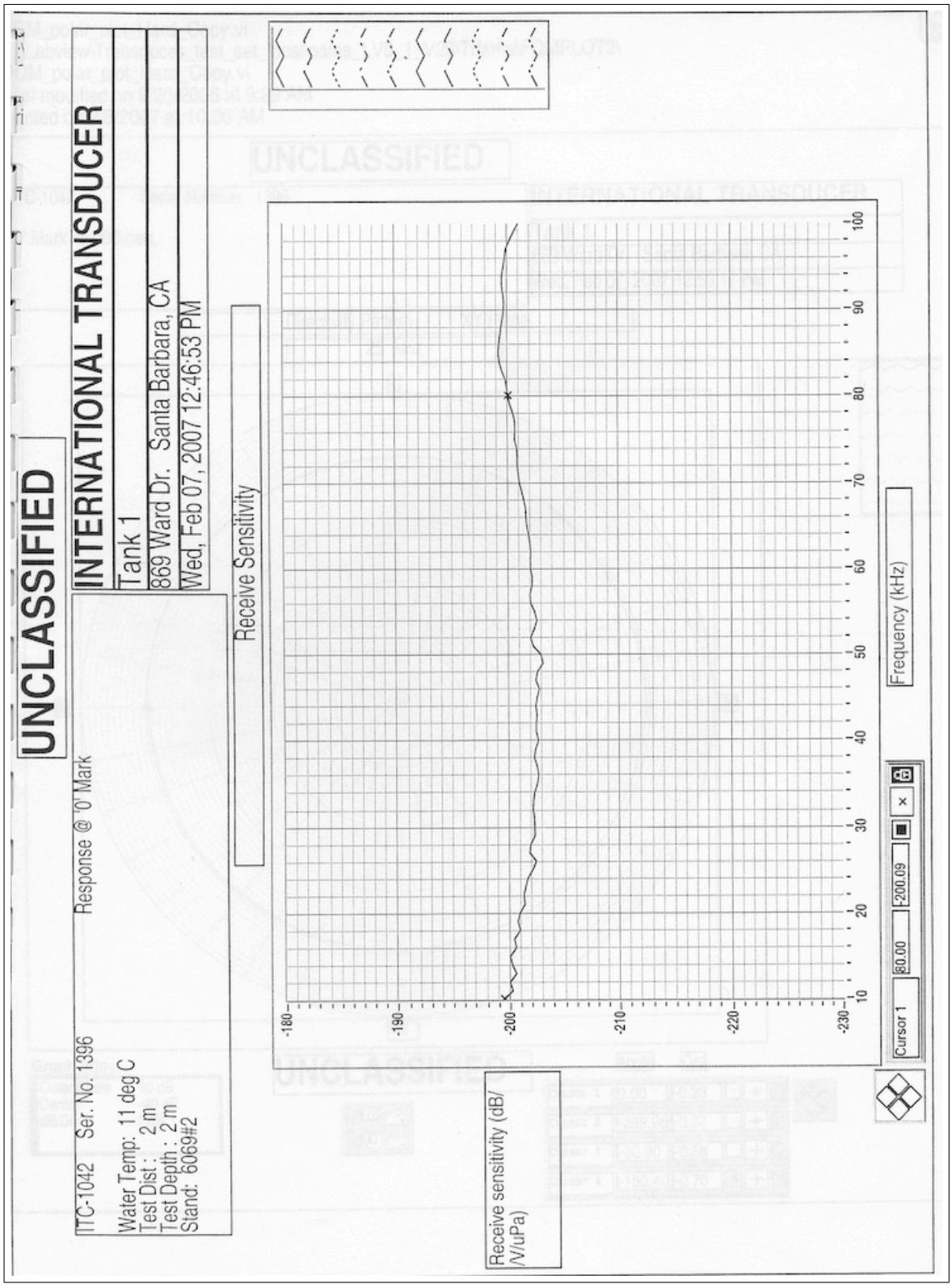

Figure D.12: Receive Sensitivity for Transducer 1406

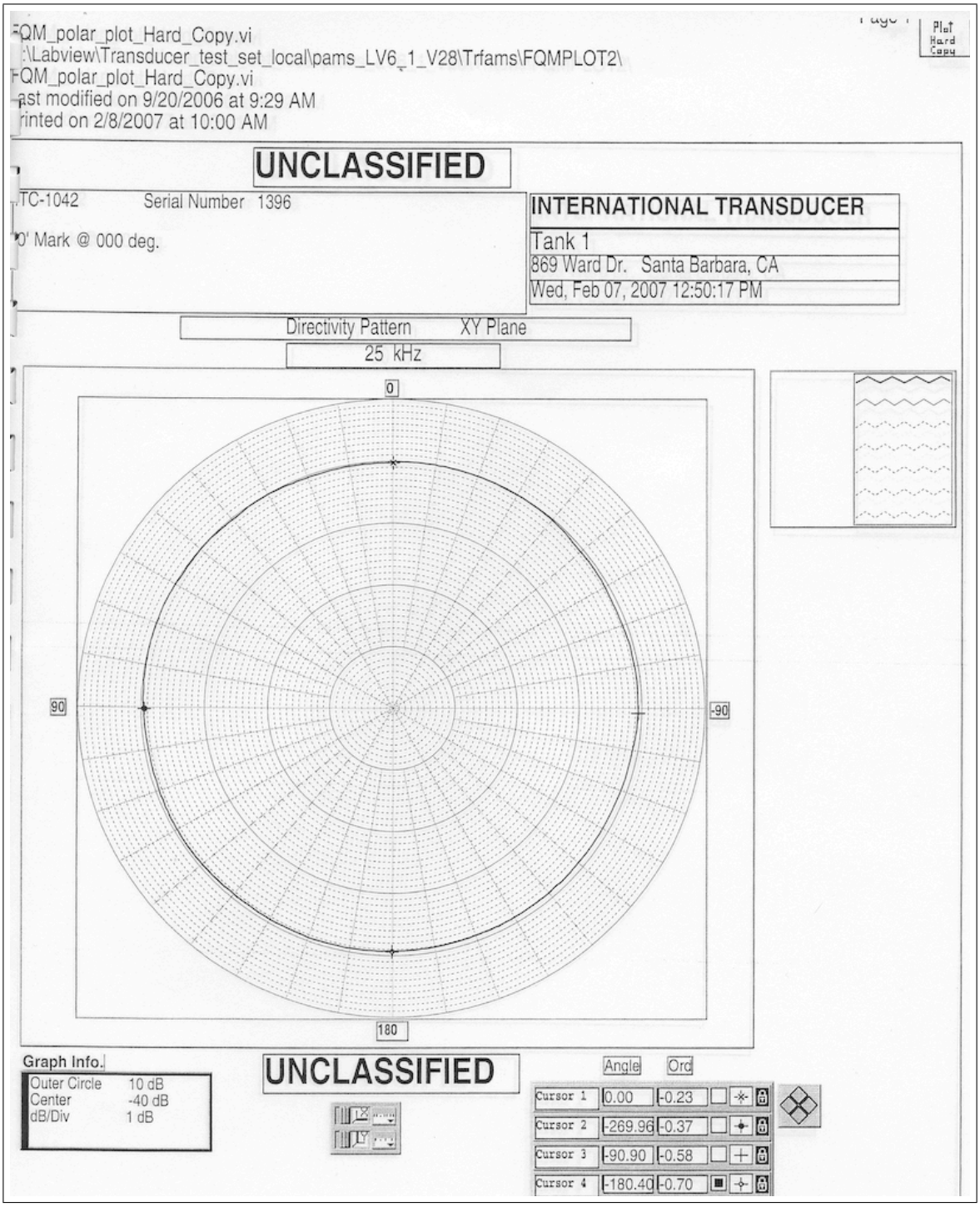

Figure D.13: Beam-pattern at 25 kHz for Transducer 1406

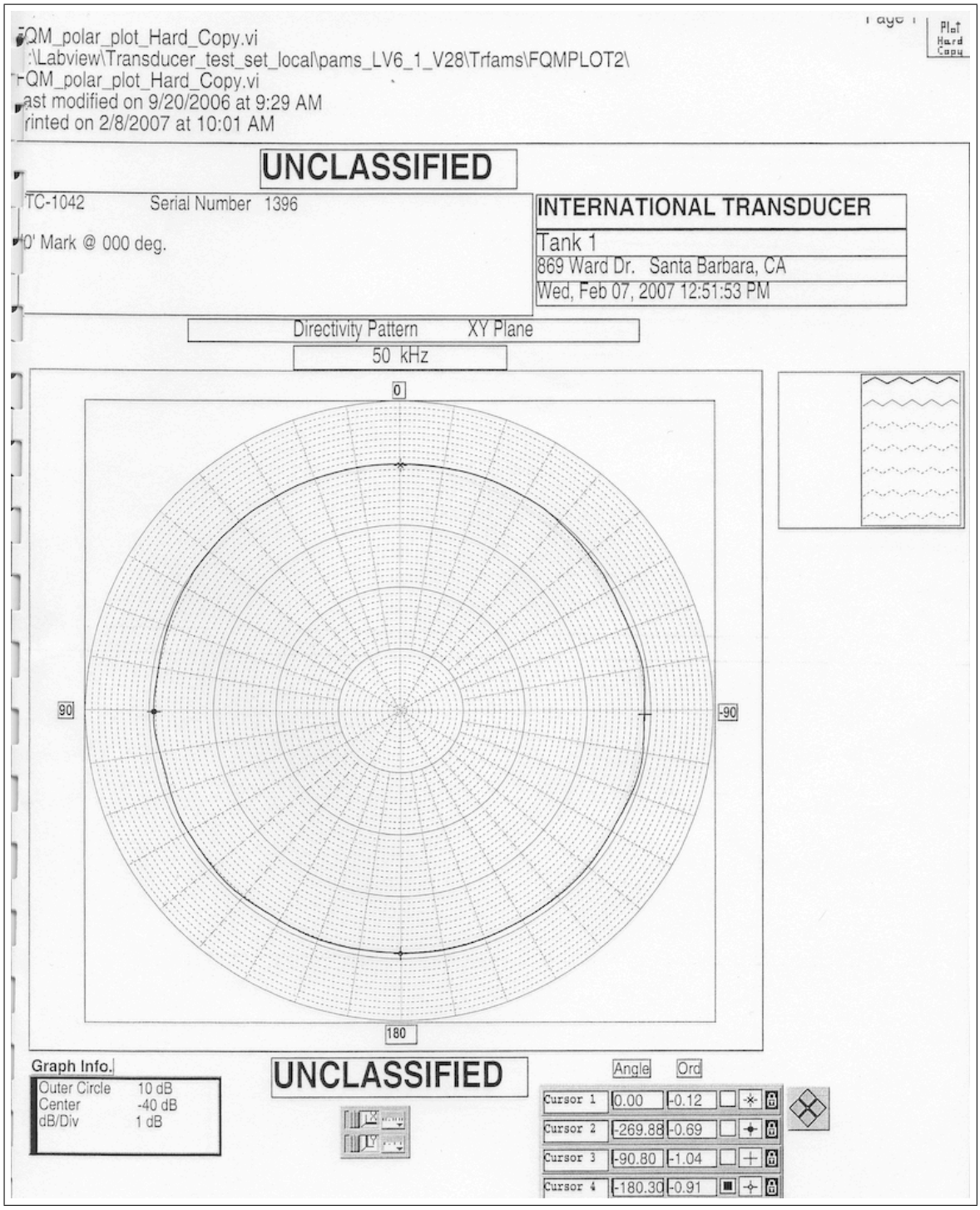

Figure D.14: Beam-pattern at 50 kHz for Transducer 1406

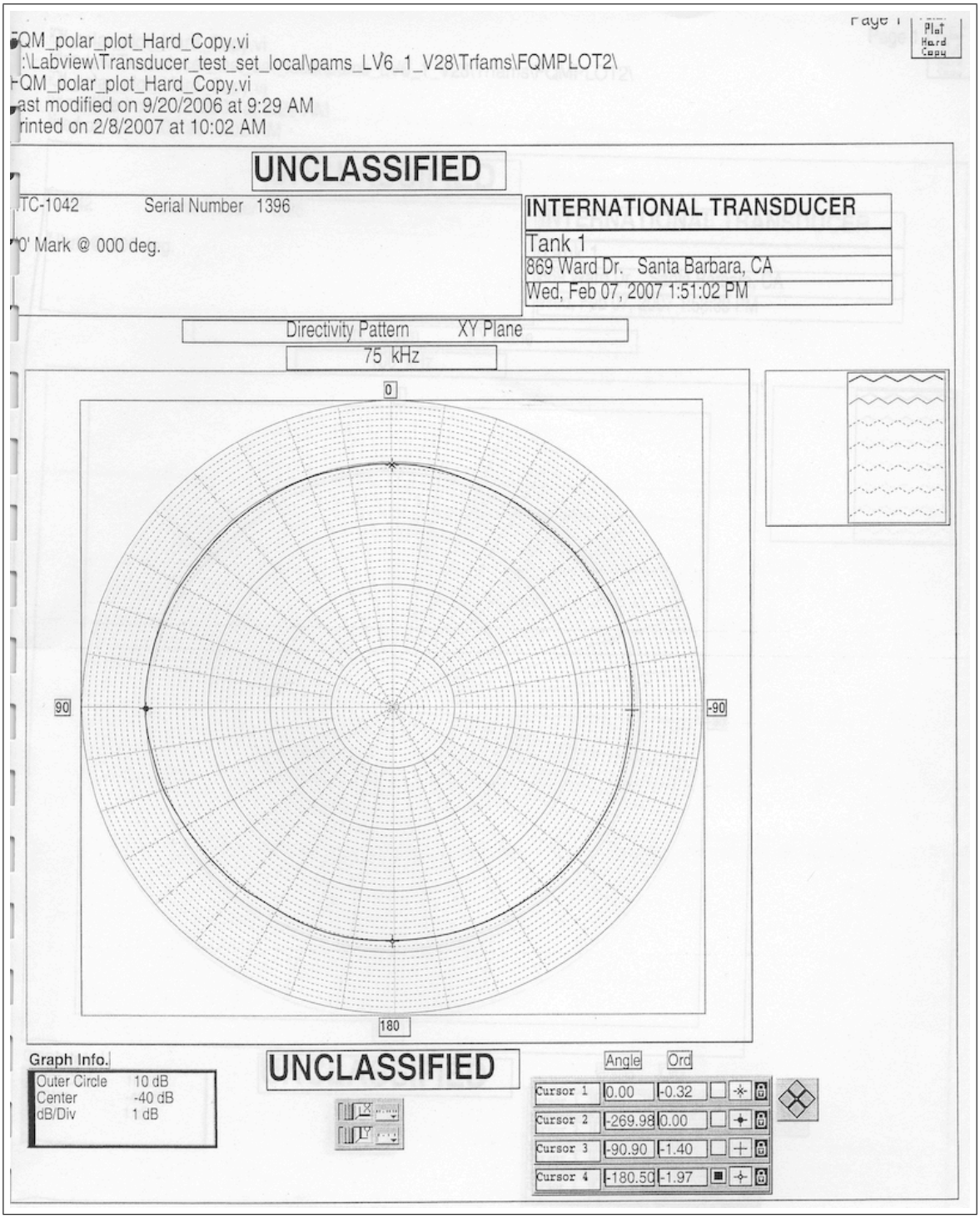

Figure D.15: Beam-pattern at 75 kHz for Transducer 1406

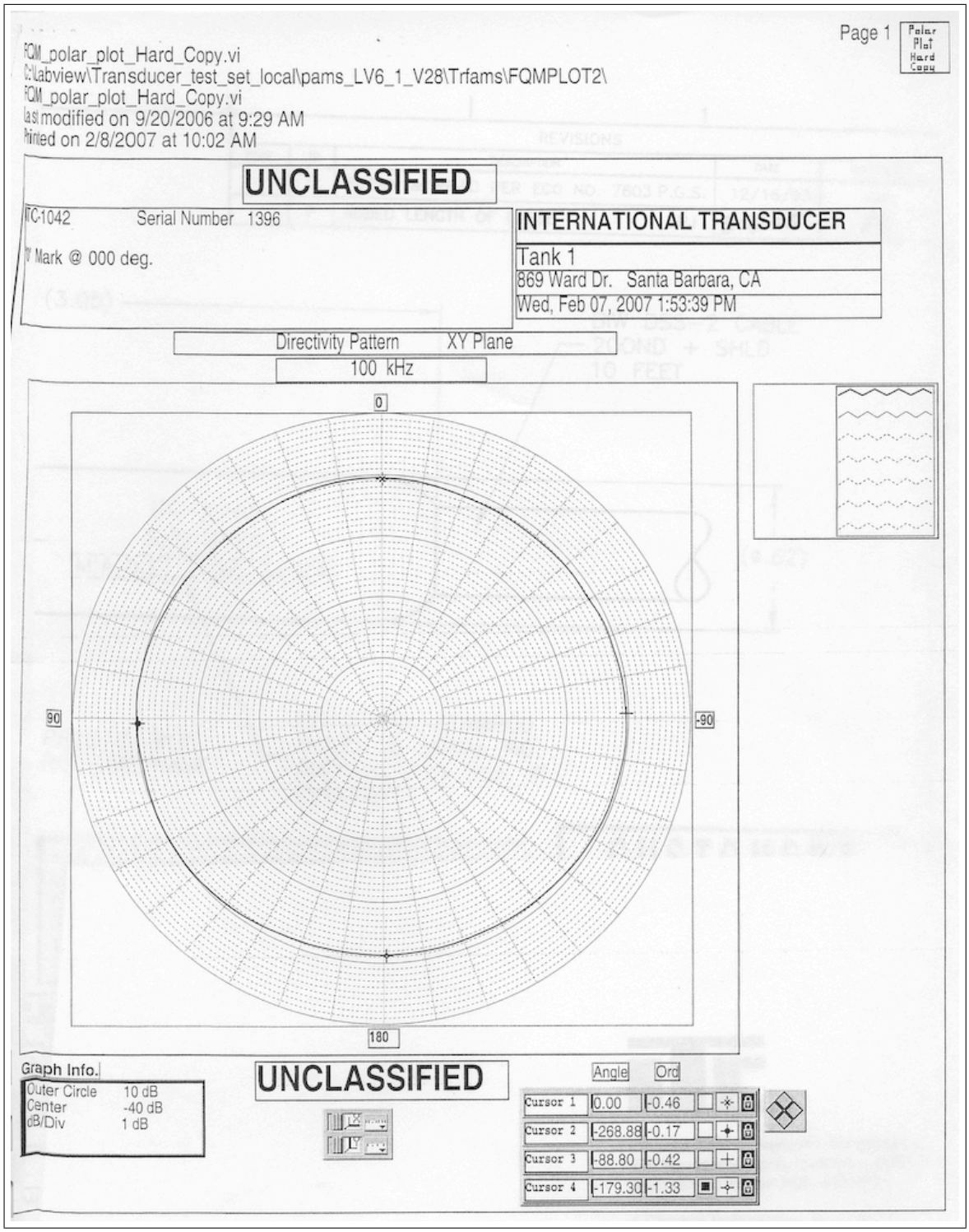

Figure D.16: Beam-pattern at 100 kHz for Transducer 1406

Appendix E

WATERFALL PLOTS

Seven representative waterfall plots have been included. The first plots are the bi-static transducer responses for the transducer 3-1 pair for all five surfaces, Figures E.1 through E.5. The surfaces for these five waterfall plots are described in Section 4.1. Figures E.6 and E.7 are representative mono-static plots for transducer 1. Figure E.6 shows the mono-static response for a smooth surface. Figure E.7 shows the mono-static response for a rough surface. Figures E.8 and E.9 are the two outliers discussed in Section 4.4.2. These plots have been included to clearly show the trends in the data.

The waterfall plots were used like photographic proof sheets to get an overview of the surface behaviour at various heights. The initial test did not raise the transducers to 82 cm above the sand because it did not seem necessary. After the initial test data was analysed it was realised that the readings at 82 cm were valuable and were include from this point forward. The detailed analysis of these acoustic reading is described in Chapter 4.

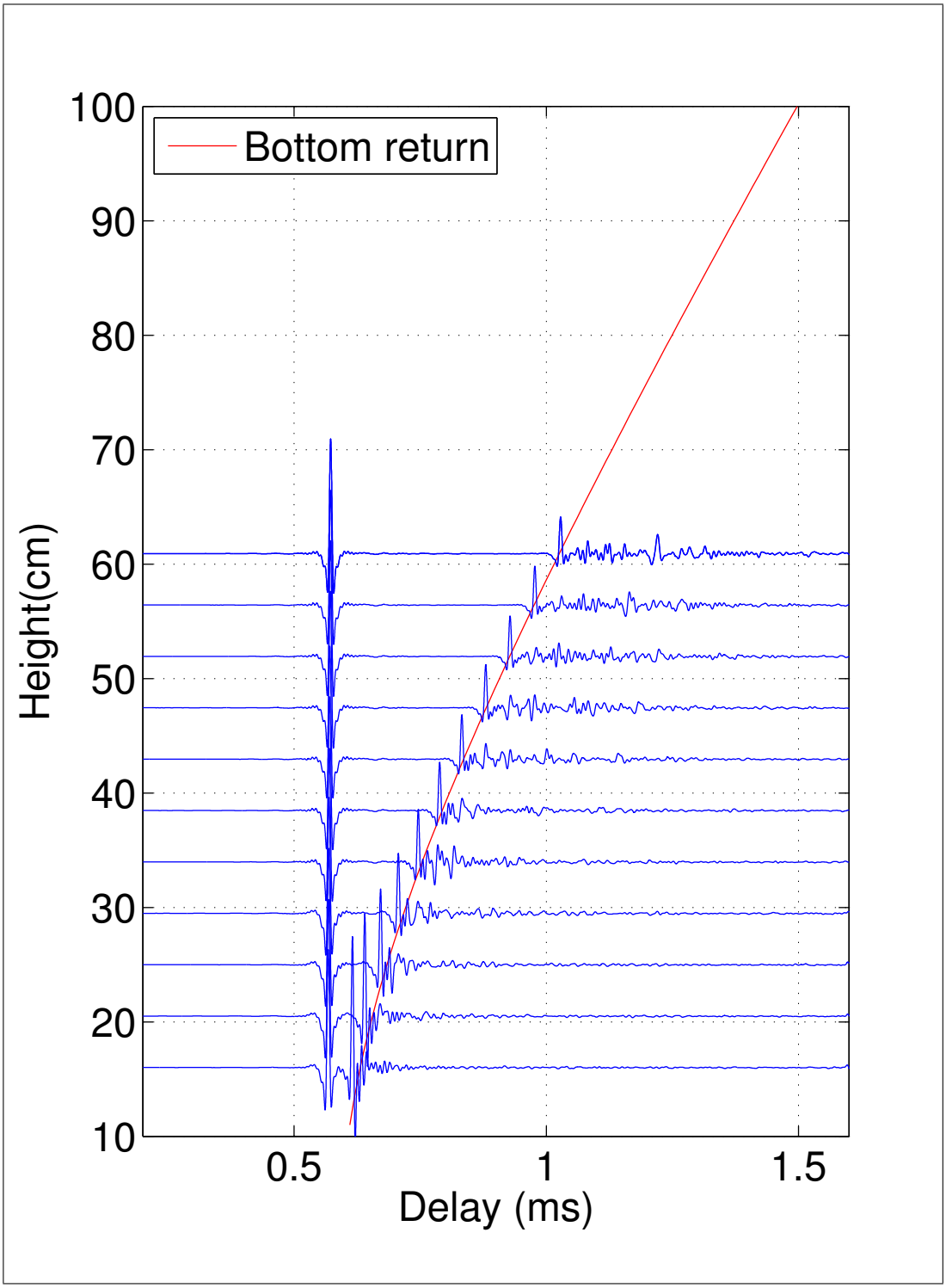

Figure E.1: Deconvolution of the transducer response for TX on channel 3 and RX on channel 1. The height above the sand was measured between 14 to 62 cm in 4.5 cm increments. Data set from 23rd March 2009.

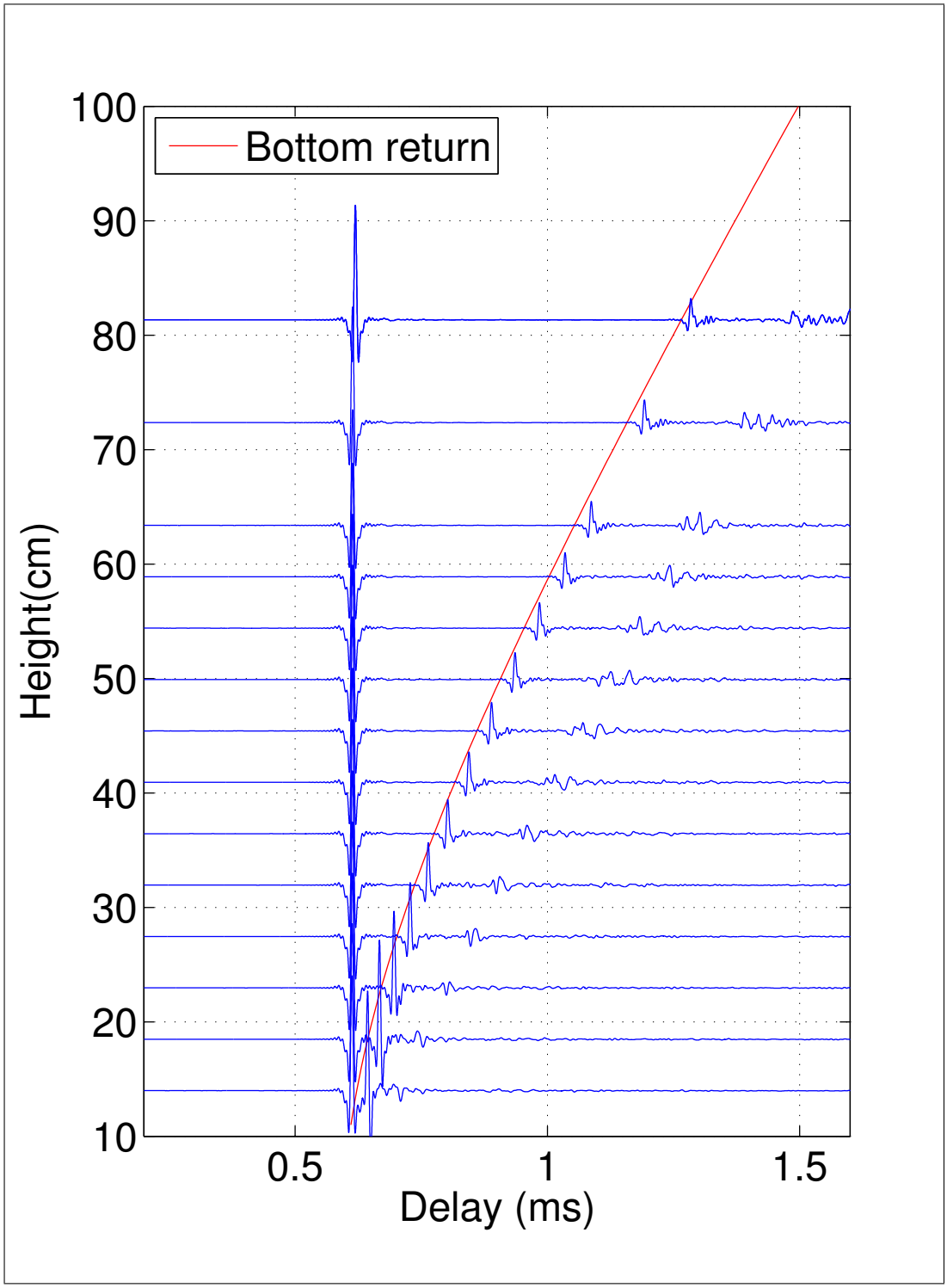

Figure E.2: Deconvolution of the transducer response for TX on channel 3 and RX on channel 1. The height above the sand was measured between 14 to 82 cm in 4.5 cm increments excluding the 77 cm and 68 cm measurements. Data set from 4th July 2009.

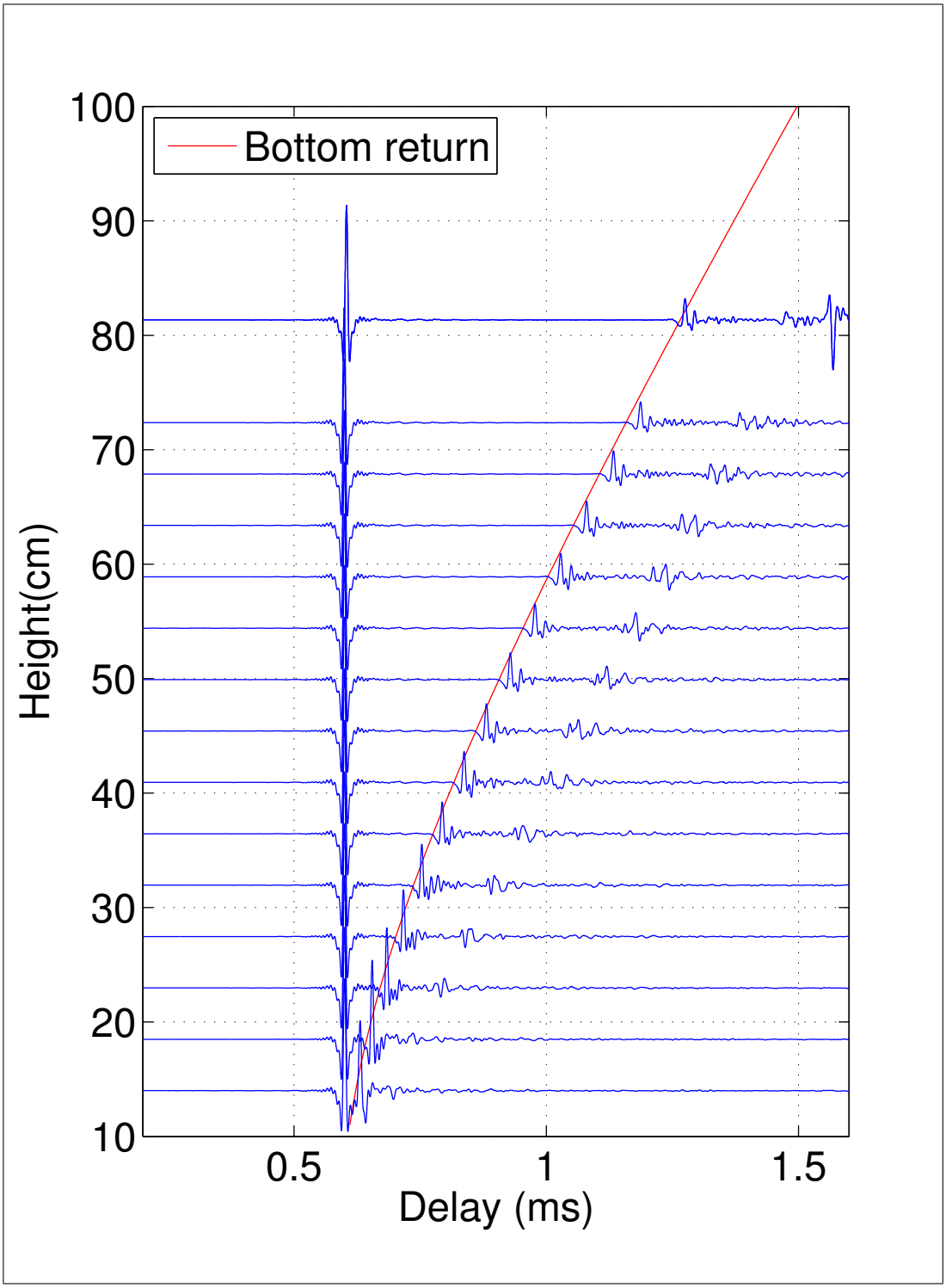

Figure E.3: Deconvolution of the transducer response for TX on channel 3 and RX on channel 1. The height above the sand was measured between 14 to 82 cm in 4.5 cm increments excluding the 77 cm measurement. Data set from 24th July 2009.

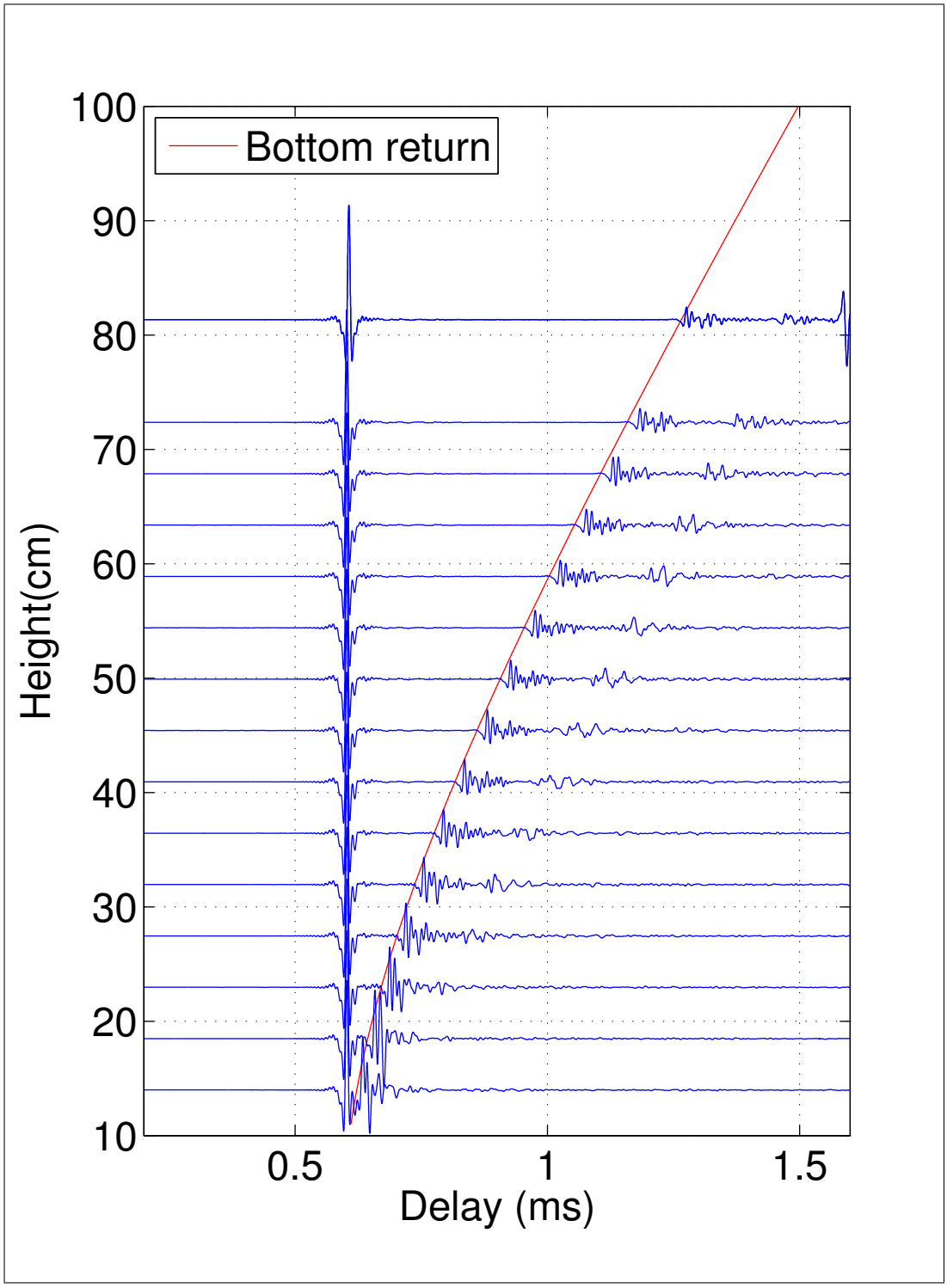

Figure E.4: Deconvolution of the transducer response for TX on channel 3 and RX on channel 1. The height above the sand was measured between 14 to 82 cm in 4.5 cm increments excluding the 77 cm measurement. Data set from 31st July 2009.

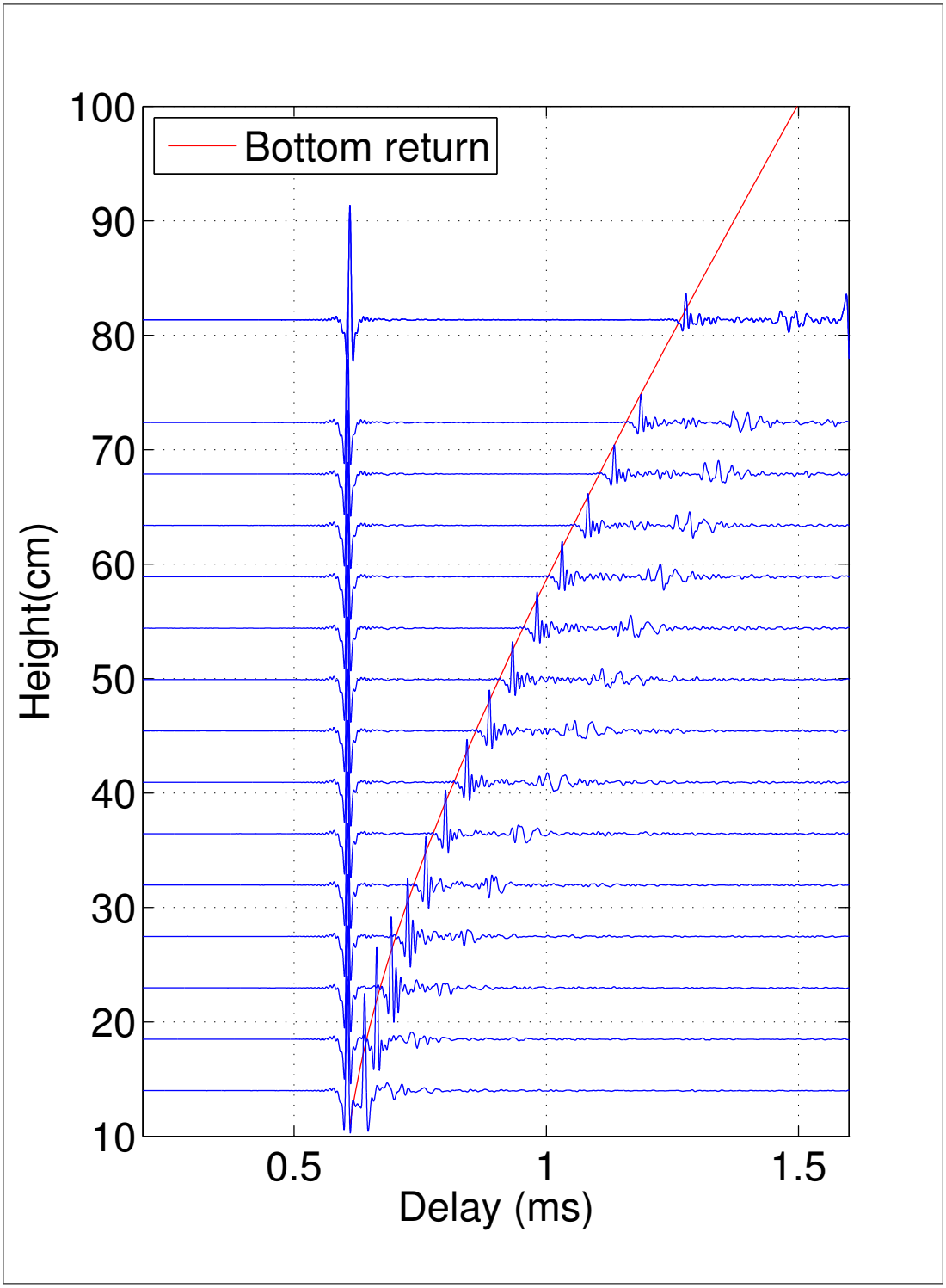

Figure E.5: Deconvolution of the transducer response for TX on channel 3 and RX on channel 1. The height above the sand was measured between 14 to 82 cm in 4.5 cm increments excluding the 77 cm measurement. Data set from 14th August 2009.

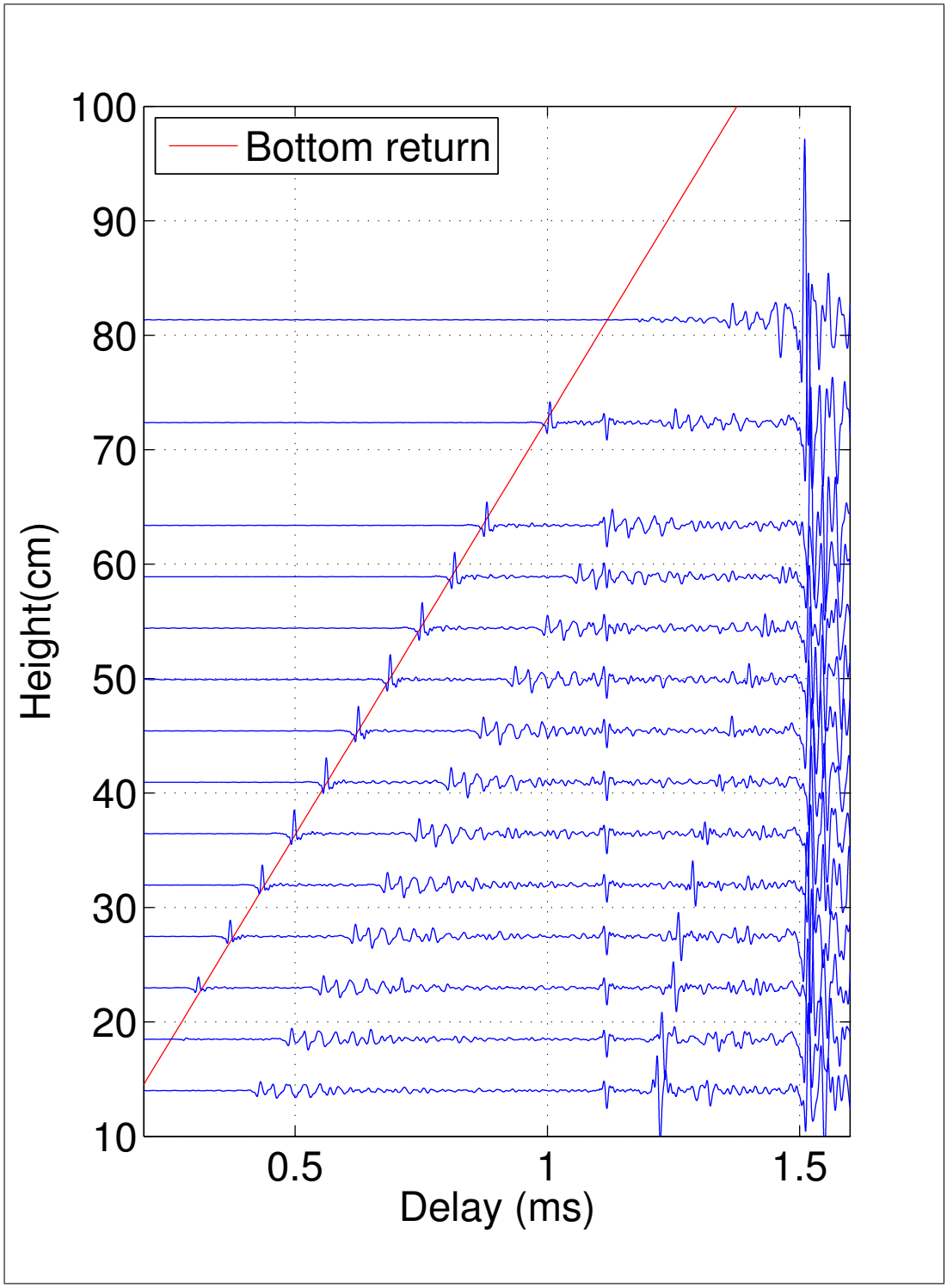

Figure E.6: Deconvolution of the transducer response for TX on channel 1 and RX on channel 1. The height above the sand was measured between 14 to 82 cm in 4.5 cm increments excluding the 77 cm and 68 cm measurements. Data set from 4th July 2009.

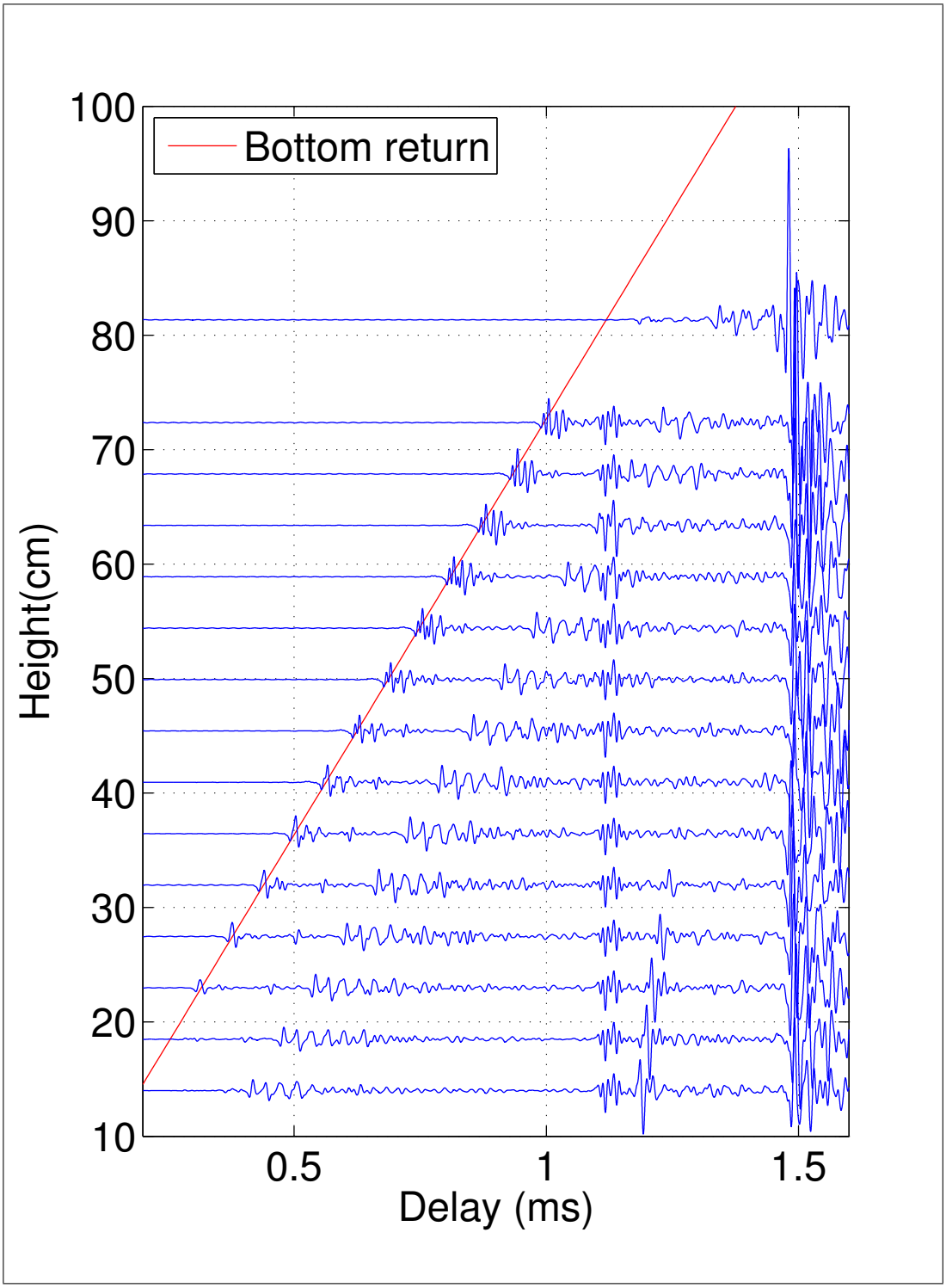

Figure E.7: Deconvolution of the transducer response for TX on channel 1 and RX on channel 1. The height above the sand was measured between 14 to 82 cm in 4.5 cm increments excluding the 77 cm measurement. Data set from 14th August 2009.

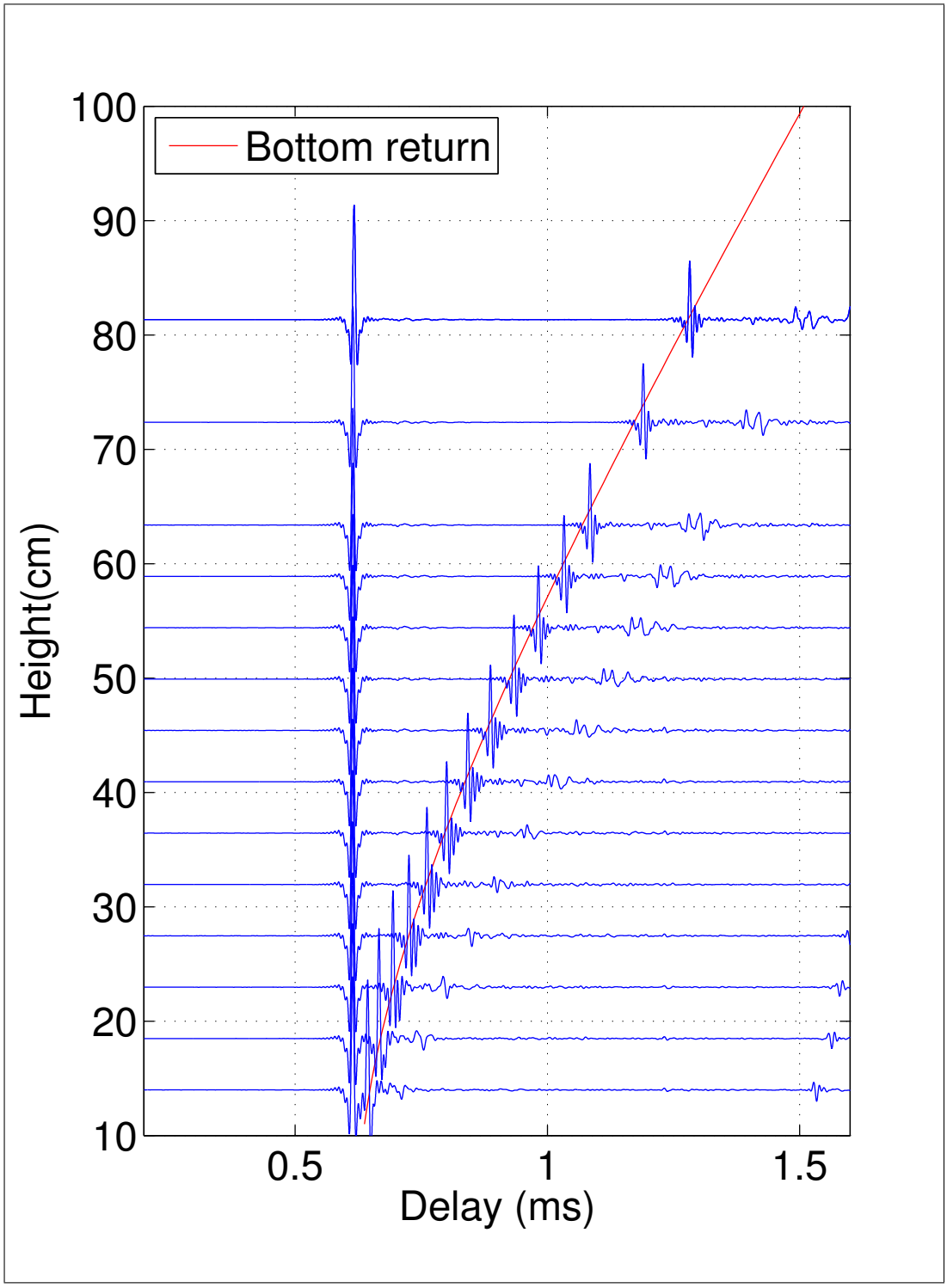

Figure E.8: Deconvolution of the transducer response for TX on channel 3 and RX on channel 2. The height above the sand was measured between 14 to 82 cm in 4.5 cm increments excluding the 77 cm and 68 cm measurements. Data set from July 4th 2009.

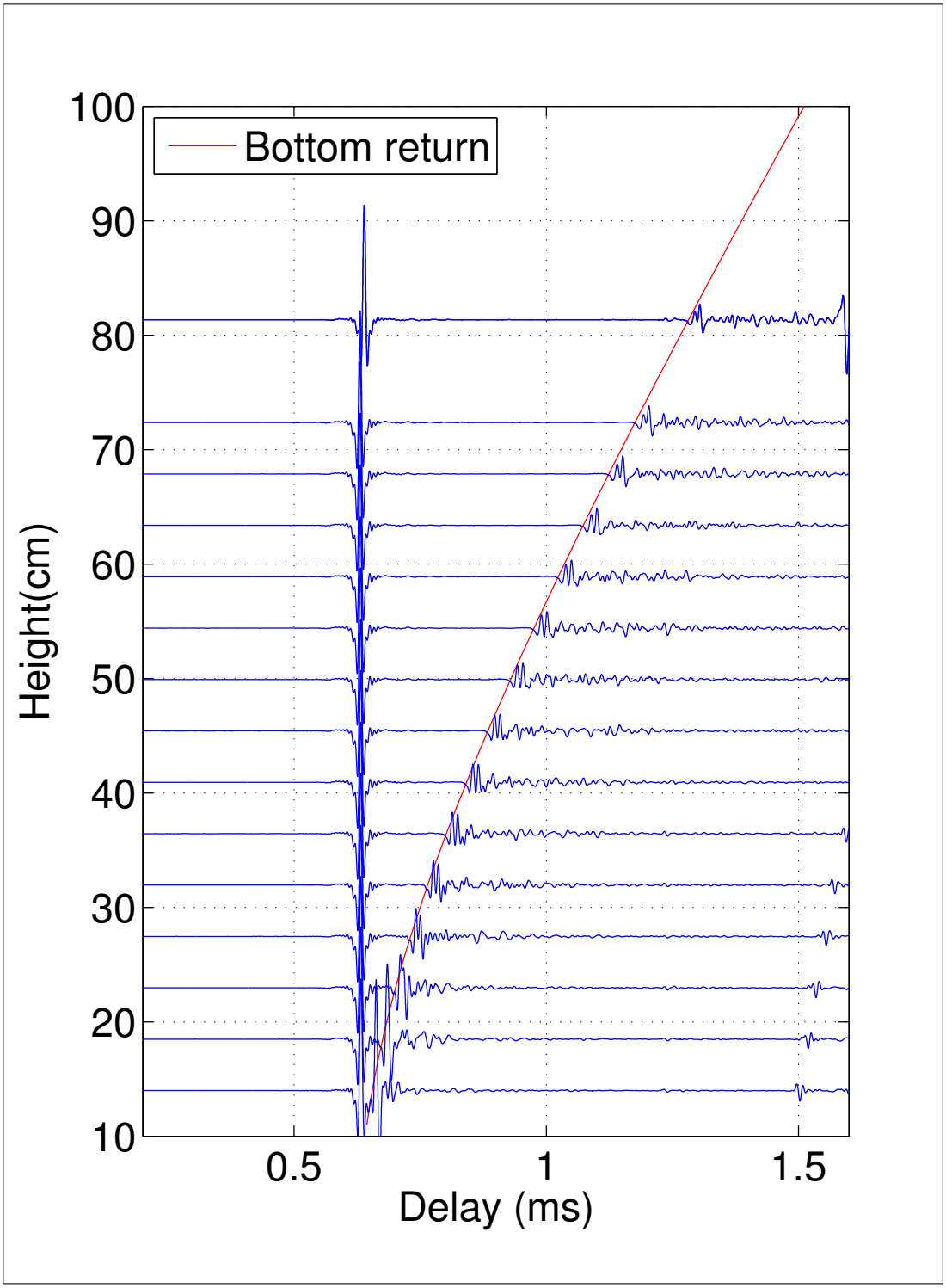

Figure E.9: Deconvolution of the transducer response for TX on channel 1 and RX on channel 2. The height above the sand was measured between 14 to 82 cm in 4.5 cm increments excluding the 77 cm measurement. Data set from 14th August 2009.

Appendix F

COPYRIGHT PERMISSIONS

The flowing figures have been used with permission from their authors and if required the publisher.

Figure 2.14 from [Briggs et al. 2005] has been used with permissions from Briggs [2009].

Figure 3.18 from [Anderson et al. 1998] has been used with permissions from Lyons [2009] and Elsevier [2009].

REFERENCES

Aki, K. and Richards, P.G. (2002), *Quantitative Seismology*, University Science Books, Sausalito, CA, USA, 2nd ed.

Ambardar, A. (1999), *Analog and digital signal processing*, Brooks/Cole Publishing Co., Pacific Grove, CA, USA, 2nd ed.

Anderson, A.L. and Hampton, L.D. (1980a), 'Acoustics of gas-bearing sediments i. background', *The Journal of the Acoustical Society of America*, Vol. 67, No. 6, pp. 1865–1889.

Anderson, A.L. and Hampton, L.D. (1980b), 'Acoustics of gas-bearing sediments. ii. measurements and models', *The Journal of the Acoustical Society of America*, Vol. 67, No. 6, pp. 1890–1903.

Anderson, A.L., Abegg, F., Hawkins, J.A., Duncan, M.E. and Lyons, A.P. (1998), 'Bubble populations and acoustic interaction with the gassy floor of Eckernforde bay', *Continental Shelf Research*, Vol. 18, No. 14-15, Dec, pp. 1807–1838.

Beckmann, P. and Spizzichino, A. (1963), *The Scattering of Electromagnetic Waves from Rough Surfaces*, Artech House, Inc, Norwood, MA, USA.

Bergem, O., Pouliquen, E., Canepa, G. and Pace, N.G. (1999), 'Time-evolution modeling of seafloor scatter. ii. numerical and experimental evaluation', *The Journal of the Acoustical Society of America*, Vol. 105, No. 6, pp. 3142–3150.

Berkson, J.M. and Matthews, J.E. (1983), 'Statistical properties of seafloor roughness', In Pace, N.G. (Ed.), *Acoustics of the Sea Bed*, Oxford University Press Oxford, pp. 215–223.

Bouguet, J. (2008), 'www.vision.caltech.edu/bouguetj/calib_doc/', Web page, June.

Bracewell, R.N. (1986), *The Fourier Transform and its Applications*, McGraw-Hill, Inc, New York, NY, USA, 2nd ed.

Brekhovskikh, L.M. (1980), *Waves in Layered Media*, Academic Press, New York, NY, USA, 2nd ed.

Brekhovskikh, L.M. and Lysanov, Y.P. (2003), *Fundamentals of Ocean Acoustics*, Springer Science and Business Media, LLC, New York, NY, USA, 3rd ed.

Briggs, K. (1989), 'Microtopographical roughness of shallow-water continental shelves', *Oceanic Engineering, IEEE Journal of*, Vol. 14, No. 4, Oct, pp. 360–367.

Briggs, K.B. (2009), 'Copyright permission to use Figure 4 from Briggs et al.[2005] by Kevin Briggs.', email, December.

Briggs, K.B., Williams, K.L., Richardson, M.D. and Jackson, D.R. (2001), 'Effects of changing roughness on acoustic scattering: (1) natural changes', In Leighton, T.G., Heald, G.J., Griffiths, H.D. and Griffths, G. (Eds.), *Proceedings of the Institute of Acoustic Conference*, South Hampton, UK.

Briggs, K.B., Lyons, A.P., Pouliquen, E., Mayer, L.M. and Richardson, M.D. (2005), 'Seafloor roughness, sediment grain size, and temporal stability', In Papadakis, J.P. and Bjorno, L. (Eds.), *Underwater acoustic measurements: Technologies and Results*, Proceedings of a conference held in Heraklion, Crete, pp. 337–343.

Cammin, H.J. (2004), *A comparison of spherical wave sediment reflection coefficient measurements to plane wave models*, Master's thesis, The University of Texas, Austin, TX, December.

Chotiros, N., Isakson, M., Piper, J. and Zampolli, M. (2007), 'Seafloor roughness measurement from a ROV', In *Underwater Technology and Workshop on Scientific Use of Submarine Cables and Related Technologies, 2007. Symposium on*, April, pp. 52–57.

Clay, C.S. and Medwin, H. (1970), 'Dependence of spatial and temporal correlation of forward-scattered underwater sound on the surface statistics. i. theory', *The Journal of the Acoustical Society of America*, Vol. 47, No. 5B, pp. 1412–1418.

Clay, C.S. and Medwin, H. (1977), *Acoustical Oceanography: Principles and Applications*, John Wiley and Sons, Inc, Hoboken, NJ, USA.

Clay, C.S., Medwin, H. and Wright, W.M. (1973), 'Specularly scattered sound and the probability density function of a rough surface', *The Journal of the Acoustical Society of America*, Vol. 53, No. 6, pp. 1677–1682.

Dacol, D.K. (1990), 'The Kirchhoff approximation for acoustic scattering from a rough fluid–elastic solid interface', *The Journal of the Acoustical Society of America*, Vol. 88, No. 2, pp. 978–983.

Duffy, D.G. (2001), *Green's functions with applications*, Chapman and Hall/CRC, New York, NY, USA.

Ebbing, D.D. (1987), *General Chemistry*, Houghton Mifflin Co., Boston, MA, USA, 2nd ed.

Eckart, C. (1953), 'The scattering of sound from the sea surface', *The Journal of the Acoustical Society of America*, Vol. 25, No. 3, pp. 566–570.

Elsevier (2009), 'Copyright permission to use Figure 1 from Anderson et al.[1998] by Elsevier publishing.', email, December.

Fox, C.G. and Hayes, D.E. (1985), 'Quantitative methods for analyzing the roughness of the seafloor', *Reviews of Geophysics*, Vol. 23, No. 1, February, pp. 1 – 48.

Gerig, A.L., Lyons, A.P., Pouliquen, E. and Williams, K.L. (2009), 'Comparison of seafloor roughness and scattered acoustic temporal decorrelation', *Oceanic Engineering, IEEE Journal of*, Vol. 34, No. 4, Oct., pp. 423–430.

Goodman, J.W. (1968), *Introduction to Fourier Optics*, McGraw-Hill, Inc, Englewood, CO, USA, 1st ed.

Goodman, J.W. (2005), *Introduction to Fourier Optics*, Roberts and Company, Englewood, CO, USA, 3rd ed.

Gough, P.T., Hayes, M.P. and Noonchester, M.A. (2006a), 'Towards the imaging of targets buried beneath the seafloor using a two band, interferometric synthetic aperture sonar', In *Proc. Eighth Euro. Conf. Underwater Acoust. (ECUA)*, Carvoeiro, Portugal, June. CDROM.

Gough, P.T., Noonchester, M.A., Hunter, A.J. and Hayes, M.P. (2006b), 'Imagery from a multifrequency sas: A comparison of simulated and experimental results', In *Institute of Acoustics Preceedings Int. Conf. on SAS and SAR*, Institute of Acoustics, Lerici, Italy, September, pp. 31–38.

Gough, P., Noonchester, M., Hunter, A. and Hayes, M. (2006c), 'Towards multi-frequency imaging and analysis of sub-surface targets using sas', In *OCEANS 2006*, Sept., pp. 1–6.

Hamilton, E.L. (1980), 'Geoacoustic modeling of the sea floor', *The Journal of the Acoustical Society of America*, Vol. 68, No. 5, pp. 1313–1340.

Hamilton, E.L., Shumway, G., Menard, H.W. and Shipek, C.J. (1956), 'Acoustic and other physical properties of shallow-water sediments off San Diego', *The Journal of the Acoustical Society of America*, Vol. 28, No. 1, pp. 1–15.

Hawkins, D.W. (1996), *Synthetic Aperture Imaging Algorithms: with application to wide bandwidth sonar.*, PhD thesis, Department of Electrical and Electronic Engineering, University of Canterbury, October.

Hay, A.E. (2008), 'Near-bed turbulence and relict waveformed sand ripples: Observations from the inner shelf', *Journal of Geophysical Research*, Vol. 113, April.

Haykin, S. (1994), *Communication System*, John Wiley and Sons, Inc, Hoboken, NJ, USA, 3rd ed.

Hua, Y. and Sarkar, T. (1990), 'Matrix pencil method for estimating parameters of exponentially damped/undamped sinusoids in noise', *Acoustics, Speech and Signal Processing, IEEE Transactions on*, Vol. 38, No. 5, May, pp. 814–824.

Hunter, A.J. (2006), *Underwater Acoustic Modelling for Synthetic Aperture Sonar*, PhD thesis, Department of Electrical and Electronic Engineering, University of Canterbury, June.

Hunter, A. (2007), 'Personal communications', January.

Irish, J.D., Lynch, J.F., Traykovski, P.A., Newhall, A.E., Prada, K. and Hay, A.E. (1999), 'A self-contained sector-scanning sonar for bottom roughness observations as part of sediment transport studies', *Journal of Atmospheric and Oceanic Technology*, Vol. 16, November, pp. 1830–1841.

Ishimaru, A. (1997), *Wave Progagation and Scattering in Random Media*, IEEE Press, New York, NY, USA.

Jackson, D.R. (2000), *High-Frequency Bistatic scatterin model for elastic seafloors*, Technical Report APL-UW TM 2-00, Applied Physics Laboratory, University of Washington, 1013 NE 40th St, Seattle, WA, February.

Jackson, D.R. and Richardson, M.D. (2007), *High-Frequency Seafloor Acoustics*, Springer Science and Business Media, LLC, New York, NY, USA.

Jackson, D.R., Baird, A.M., Crisp, J.J. and Thomson, P.A.G. (1986a), 'High-frequency bottom backscatter measurements in shallow water', *The Journal of the Acoustical Society of America*, Vol. 80, No. 4, pp. 1188–1199.

Jackson, D.R., Winebrenner, D.P. and Ishimaru, A. (1986b), 'Application of the composite roughness model to high-frequency bottom backscattering', *The Journal of the Acoustical Society of America*, Vol. 79, No. 5, pp. 1410–1422.

Jackson, D., Briggs, K., Williams, K. and Richardson, M. (1996), 'Tests of models for high-frequency seafloor backscatter', *Oceanic Engineering, IEEE Journal of*, Vol. 21, No. 4, Oct, pp. 458–470.

Jackson, D.R., Richardson, M.D., Williams, K.L., Lyons, A.P., Jones, C.D., Briggs, K.B. and Tang, D. (2009), 'Acoustic observation of the time dependence of the roughness of sandy seafloors', *Oceanic Engineering, IEEE Journal of*, Vol. 34, No. 4, Oct., pp. 407–422.

Kaharl, V.A. (2003), 'Sounding out the ocean's secrets', Web page. Adapted from an artical written by Victora A. Kaharl for the National Academy of Sciences' Beyond Discovery: The Path from Research to Human Benefit.

Katz, M., Papadopoulos, P. and Bruno, G. (2002), 'Leveraging standard core technologies to programmatically build linux cluster appliances', In *Cluster Computing, 2002. Proceedings. 2002 IEEE International Conference on*, pp. 47–53.

Lyons, A.P. (2008), 'Personal communications', September.

Lyons, A.P. (2009), 'Copyright permission to use Figure 1 from Anderson et al.[1998] given by Anthony for the deceased anderson.', email, December.

Lyons, A.P. and Pouliquen, E. (2004), 'Advances in high-resolution seafloor characterization in support of high-frequency underwater acoustics studies: techniques and examples', *Measurement Science and Technology*, Vol. 15, October, pp. R59–R72.

Lyons, A., Fox, W., Hasiotis, T. and Pouliquen, E. (2002), 'Characterization of the two-dimensional roughness of wave-rippled sea floors using digital photogrammetry', *Oceanic Engineering, IEEE Journal of*, Vol. 27, No. 3, Jul, pp. 515–524.

Medwin, H. (1967), 'Specular scattering of underwater sound from a wind-driven surface', *The Journal of the Acoustical Society of America*, Vol. 41, No. 6, pp. 1485–1495.

Medwin, H. and Clay, C.S. (1970), 'Dependence of spatial and temporal correlation of forward-scattered underwater sound on the surface statistics. ii. experiment', *The Journal of the Acoustical Society of America*, Vol. 47, No. 5B, pp. 1419–1429.

Moore, K. and Jaffe, J. (2002), 'Time-evolution of high-resolution topographic measurements of the sea floor using a 3-d laser line scan mapping system', *Oceanic Engineering, IEEE Journal of*, Vol. 27, No. 3, Jul, pp. 525–545.

Mourad, P. and Jackson, D. (1989), 'High frequency sonar equation models for bottom backscatter and forward loss', In *OCEANS '89. Proceedings*, Sep, pp. 1168–1175.

Nock, V. (2009), *Control and measurment of oxygen in microfluidic bioreactors*, PhD thesis, University of Canterbury, Chirstchurch NZ, January.

Nooncheste r, M.A., Hayes, M.P. and Gough, P.T. (2007), 'Seafloor roughness measurement with forward and backscattering', In *Proceedings of the Fourteenth Electronics New Zealand Conference*, pp. 159–164.

Ogilvy, J.A. (1991), *Theory of Wave Scattering from Random Rough Surfaces*, Taylor and Francis, Boston, MA, USA, 1st ed.

Pouliquen, E. and Lyons, A. (2002), 'Backscattering from bioturbated sediments at very high frequency', *Oceanic Engineering, IEEE Journal of*, Vol. 27, No. 3, Jul, pp. 388–402.

Pouliquen, E., Bergem, O. and Pace, N.G. (1999), 'Time-evolution modeling of seafloor scatter. i. concept', *The Journal of the Acoustical Society of America*, Vol. 105, No. 6, pp. 3136–3141.

Richardson, M., Briggs, K., Bibee, L., Jumars, P., Sawyer, W., Albert, D., Bennett, R., Berger, T., Buckingham, M., Chotiros, N., Dahl, P., Dewitt, N., Fleischer, P., Flood, R., Greenlaw, C., Holliday, D., Hulbert, M., Hutnak, M., Jackson, P., Jaffe, J., Johnson, H., Lavoie, D., Lyons, A., Martens, C., McGehee, D., Moore, K., Orsi, T., Piper, J., Ray, R., Reed, A., Self, R., Schmidt, J., Schock, S., Simonet, F., Stoll, R., Tang, D., Thistle, D., Thorsos, E., Walter, D. and Wheatcroft, R. (2001), 'Overview of sax99: environmental considerations', *Oceanic Engineering, IEEE Journal of*, Vol. 26, No. 1, Jan, pp. 26–53.

Sacerdoti, F., Chandra, S. and Bhatia, K. (2004), 'Grid systems deployment and management using rocks', In *Cluster Computing, 2004 IEEE International Conference on*, Sept., pp. 337–345.

Sherman, C.H. and Butler, J.L. (2007), *Transducers and Arrays for Underwater Sound*, Springer Science and Business Media, LLC, New York, NY, USA, 2nd ed.

Simmons, G. (1975), *Calculus with Analytic Geometry*, McGraw-Hill, Inc, New York, NY, USA.

Spindel, R.C. and Schultheiss, P.M. (1972), 'Acoustic surface-reflection channel characterization through impulse response measurements', *The Journal of the Acoustical Society of America*, Vol. 51, No. 6A, pp. 1812–1824.

Stanton, T.K. (1984), 'Sonar estimates of seafloor microroughness', *The Journal of the Acoustical Society of America*, Vol. 75, No. 3, pp. 809–818.

Stewart, W., Chu, D., Malik, S., Lerner, S. and Singh, H. (1994), 'Quantitative seafloor characterization using a bathymetric sidescan sonar', *Oceanic Engineering, IEEE Journal of*, Vol. 19, No. 4, Oct, pp. 599–610.

Stoll, R.D. and Bautista, E.O. (1998), 'Using the Biot theory to establish a baseline geoacoustic model for seafloor sediments', *Continental Shelf Research*, Vol. 18, No. 14, December, pp. 1839–1857.

Tang, D. (2004), 'Fine-scale measurements of sediment roughness and subbottom variability', *Oceanic Engineering, IEEE Journal of*, Vol. 29, No. 4, Oct., pp. 929–939.

Thorsos, E.I. (1988), 'The validity of the Kirchhoff approximation for rough surface scattering using a Gaussian roughness spectrum', *The Journal of the Acoustical Society of America*, Vol. 83, No. 1, pp. 78–92.

Thorsos, E.I. (1990), 'Acoustic scattering from a "Pierson–Moskowitz" sea surface', *The Journal of the Acoustical Society of America*, Vol. 88, No. 1, pp. 335–349.

Thorsos, E.I. and Jackson, D.R. (1989), 'The validity of the perturbation approximation for rough surface scattering using a Gaussian roughness spectrum', *The Journal of the Acoustical Society of America*, Vol. 86, No. 1, pp. 261–277.

Urick, R.J. (1983), *Principles of Underwater Sound*, McGraw-Hill, Inc, New York, NY, USA, 2nd ed.

Williams, E.G. (1999), *Fourier acoustics Sound radiation and nearfield acoustical holography.*, Academic Press, New York, NY, USA.

Williams, K., Jackson, D., Thorsos, E., Tang, D. and Briggs, K. (2002a), 'Acoustic backscattering experiments in a well characterized sand sediment: data/model comparisons using sediment fluid and Biot models', *Oceanic Engineering, IEEE Journal of*, Vol. 27, No. 3, Jul, pp. 376–387.

Williams, K., Jackson, D., Thorsos, E., Tang, D. and Schock, S. (2002b), 'Comparison of sound speed and attenuation measured in a sandy sediment to predictions based on the Biot theory of porous media', *Oceanic Engineering, IEEE Journal of*, Vol. 27, No. 3, Jul, pp. 413–428.

Wilson, O.B. (1988), *Introduction to theory and design of sonar transducers*, Peninusular Publishing, Los Altos, CA, USA.

www.engineeringtoolbox.com 'Concrete sound speed estimates', Web page:.

Zakharia, M. (2008), 'Personal communications', February.

Ziomek, L. (1995), *Fundamentals of Acoustic Field Theory and Space-Time Signal Processing*, CRC Press Inc, Boca Raton, Florida, USA.